

TGB

8200

.M58

DEPARTMENT OF
TRANSPORTATION

JUN 14 1973

**REVIEW OF EFFECTS OF HYPERVELOCITY
JETS AND PROJECTILES ON ROCK**

June 1968

FINAL REPORT

George B. Clark
Charles J. Haas

by

John W. Brown
Clifford D. Muir

for

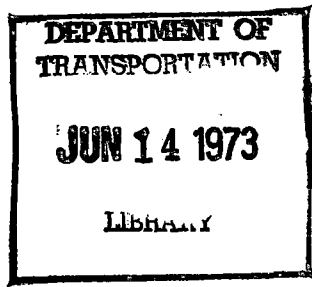
OFFICE OF HIGH SPEED GROUND TRANSPORTATION
U.S. DEPARTMENT OF TRANSPORTATION
WASHINGTON D.C. 20591

CONTRACT NO. DC7-35511

Rock Mechanics & Explosives Research Center
UNIVERSITY OF MISSOURI - ROLLA
Rolla, Missouri 65401

09-Materials Science

TGB
8200
MS8



✓
REVIEW OF EFFECTS OF HYPERVELOCITY
JETS AND PROJECTILES ON ROCK;

June 1968

✓
FINAL REPORT,

by

George B. Clark
Charles J. Haas
John W. Brown
Clifford D. Muir

for

OFFICE OF HIGH SPEED GROUND TRANSPORTATION
U.S. DEPARTMENT OF TRANSPORTATION
WASHINGTON, D.C. 20591

CONTRACT NO. DC7-35511

Missouri, University.
Rock Mechanics & Explosives Research Center.

UNIVERSITY OF MISSOURI-ROLLA

Rolla, Missouri 65401

PB179 022

TABLE OF CONTENTS

Chapter		Page
I	Introduction	1
	General	1
	Objective	1
	History	2
	Report Organization	4
II	Equations of State	6
	Shock Waves	8
III	Water Jets	15
	Jet Stability-Theory	15
	Summary	26
	Jet Stability-Experimentation	26
	Pulsed Jets-Theory and Experiment	44
	Nozzles	45
	Summary-Nozzles	57
	Compressors	57
	Water Jet Production	60
	Fluid Jet Augmentation	81
	High Pressure Freezing of Water	87
	Calculation of Shock Front Parameters	88
	Extrapolation of p-V-T Data	91
	Discussion	98
IV	Water Jet Impact on Rock	102
V	Projectile Acceleration and Impact	142
	Introduction	142
	Limitations-High Velocity Guns	142
	Cratering and Penetration Theories	150
	Thermal Penetration	158
	Explosive Analogy	158
	Empirical Relations	159
	Penetration-General	159
	Impact Experiments-Metals	162
	Impact Data-Metal Targets	171
	Dimensional Analysis	184
	Impact Experiments-Rock	192
	Comminution	207

TABLE OF CONTENTS

Chapter		Page
VI	Explosive Shaped Charges and Cumulation	209
	Design of Shaped Charges with Conical Liners	218
	Jet Penetration of Rock	221
	Energy Partitioning	231
	Cumulation-Tubular Booster	234
	Miscellaneous	238
VII	Pressure Vessels	242
	Introduction	242
	Dynamic Pressure Vessels	242
	Static Pressure Vessels	246
	Material Considerations	278
VIII	Conclusions and Recommendations	286
	General	286
	Equations of State	287
	Water Jets	288
	Water Jet Impact	289
	Hypervelocity Projectiles	292
	Pressure Vessels	294
	Shaped Charges and Cumulation	296
	Discussion	297
	Summary-Status of Research and Development	300
	Recommendations	305
Appendices		
A	Theory of Single Stage Light Gas Guns	307
	Projectile Velocity	307
	Velocity-Constant Base Pressure	307
	Pressure Disturbances	308
	Characteristic Theory	314
	Simple Wave Region-Constant Diameter	314
	Numerical Calculations	319
	First Reflected Wave	324
	Projectile Path-Post-Reflection	326
	Isentropic Expansion-Constant Diameter	327
	Infinite Chamber	328
	Acoustic Inertia-Infinite Chamber	329
	Ideal Gas	329
	Projectile Equations	333
	Finite Length Chamber	335
	Chambered Gun	342
	Back Pressure of Gas in Barrel	347
	Heating Propellant Gas	350

TABLE OF CONTENTS

Appendices		Page
B	Pressure Vessels	351
B-I	Stress Analysis	351
	Thin-Walled Vessels, Elastic Analysis	351
	Thick-Walled Vessels, Elastic Analysis	351
	Autofrettage-Theoretical Analysis	355
B-II	Tabulation of Material Properties	361
C	Shock Waves-Water Cannon	383
	Piston-Water Impact	383
	Piston-Water Impact with Air	393
	References	413

CHAPTER I

INTRODUCTION

General

Although many advances have been made in tunnel excavation in rock in the past few decades, improvements have been built around established practices of drilling, blasting, loading and haulage of broken rock. Loading and haulage, as well as drilling and blasting have been improved until little feasible increase in efficiency or time saving appears possible. New and faster methods of tunneling are necessary if planned high speed ground transportation is to become a reality.

One of the current disadvantages of conventional explosive excavation systems is that they are cyclic in nature, involving individual operations which cannot be performed simultaneously. Some factors which cause delays include: (1) The method does not permit simultaneous and continuous breakage, loading and haulage; (2) There is a delay to clear out gases from explosives; (3) Turnaround time is required in moving drilling equipment; (4) There are delays in track haulage due to moving in empties; (5) Other delays.

Objective

Several approaches have been made to solve the basic and engineering problems of devising new rapid tunnel excavation systems. Tunnel boring machines have been developed which will excavate tunnels of circular cross-section at rapid rates in soft rock such as shale. Conventional drilling,

blasting and loading methods have been improved by ingenious mechanization. Low velocity jets are in use for rapid mining of soft materials such as bituminous coal. However, each of these methods appears to be reaching an economic or technical limit of improvement.

New methods are being continuously sought, which will not have some of the disadvantages of the above systems, and which will radically increase the rates of tunnel excavation. Attention has turned to the use of hypervelocity impact as a means of cutting and breaking rock, as well as the use of lasers, electric current, explosive drilling, high frequency vibration, etc. Many of these techniques are currently under investigation.

The information in this report was assembled and analyzed to give a state of the art summary of hypervelocity techniques which show promise for use in cutting and breaking rock. These include the use of water jets, metallic jets and hypervelocity projectiles.

History

Investigation of water jets has been carried on extensively in the USSR for well over a decade. Low velocity jets are used successfully to mine coal, and high velocity capillary jets have been employed to cut and break rocks under laboratory conditions. Velocity ranges for breaking and cutting are dependent upon rock properties, while pulsed jets appear to break some rocks more easily than continuous jets. Spectacular results have been reported for breakage of some rocks. Several agencies in the USSR have reported results. Compressors, pressure multipliers, gas explosion chambers

and water cannons have been used to generate jets.

Jet properties, including continuity, unit pressure, total pressure, and stability have been measured by various means. Results appear to agree with theory, although the latter has been established only for low velocity flow. Speed of traversing and frequency of pulsed jets are items of basic interest.

Investigations have also been carried out in Britain, but this work was limited to somewhat softer rock and lower velocities. Interesting discoveries have been made concerning the continuity of jets, i. e., the core is more continuous than previously believed. Lower limits of velocity for rock cutting were found for the rock investigated.

Shaped charge jets were discovered in 1888 by Charles Munroe, and have long been known as the Munroe effect in the United States and England. Early shaped charges were unlined and produced only indentations.

With the emphasis on armor in World War II there was a need to develop anti-tank weapons. The "Bazooka," employing lined shaped charge projectiles, proved very effective for armor penetration. A great deal of research has been done with them, primarily for military applications. They have found industrial application in tapping iron furnaces and perforating oil well casings. Attempts to use them for mining or excavating rock in the late 1940's failed, largely because of the cost of their use.

Hypervelocity projectile studies developed mainly because of the interest in the impact of meteorites on metals and rocks. One concern has been with the effect of particle impact on aluminum space vehicles. A second area

of interest is the effect of meteorite impact on rock on the moon. The phenomena of impact on rock and metal are similar in many respects, although craters in rock are larger because of the brittleness and low tensile strength of rock. Most projectiles are accelerated by means of the light gas gun which was developed at the New Mexico School of Mines in the 1950's.

Report Organization

The use of hypervelocity agents for excavation purposes has been under investigation for only a relatively short time, and research results are somewhat fragmentary. Hence, in most cases the investigations are described by the author under the appropriate subject. Summaries and analyses have been made where possible.

If hypervelocity systems can be successfully employed to perform simultaneous "drilling and blasting," no other large scale drilling equipment may be required. Drilling and turnaround time for drills could be eliminated. For practical applications at a working face a cross-face conveyor is visualized, which would feed a larger conveyor leading away from the face. Ideally, sequences should be arranged so that the broken material will be loaded on the cross conveyor by the excavating process. With proper design of a loading-hauling system (conveyors) at the face, mucking and haulage would proceed simultaneously. Such methods should be applicable to all types of rock, strong and weak, wet or dry, and largely independent of the composition and structure of the rock.

Other proposed systems do not enjoy this advantage. Flame jet piercing is markedly dependent on the quartz content and composition of the rock.

Boring methods of tunneling are only applicable to soft rocks. Laser and chemical methods are sensitive to rock composition and structure and probably will only supplement primary excavation methods if they are technically and economically applicable.

The theory of shock waves and necessary equations of state are presented to lay a groundwork for understanding some of the physical processes of hypervelocity phenomena. The theory of water jet stability has been developed in the literature for only low order shocks and small pressure differences between reservoir and atmospheric pressure. The low pressure theory indicates some of the basic stability phenomena, however, and shock waves undoubtedly play a dominant role in stability of hypervelocity water jets.

Useful measurements have been made on velocity and momentum distribution in water jets at moderate velocities. Compressors and water cannons have been employed to produce high velocity jets.

The accepted two-dimensional theory of shaped charge and augmented water jet formation is presented, together with the inertial theory of penetration. Hypervelocity projectile generation and terminal ballistics have been described and their effects on rock analyzed. The theory of light gas guns and water cannons is given in appendices.

The compiled information furnishes a reasonably good basis for conclusions on the state of the art and recommendations for future consideration in developing rapid excavation processes.

CHAPTER II
EQUATIONS OF STATE

Appropriate equations of state cover a wide range of pressures for gases, liquids and solids. For gases the ideal equation is used at low pressures, and Van der Waals' at intermediate pressures.

For very high pressures (detonations) virial equations either in terms of gas pressure or specific volume, the Kistiakowski-Wilson-Brinkley, or modified Abel equations, which attempt to account for covolume and other effects, may be used.

The pressure virial equation of state was derived from the kinetic theory of gases considering the molecules as hard spheres (Ref. 1), and has been modified for high temperatures:

$$pV_g/RT = 1 + x + .625 x^2 + .2869 x^3 + .1928 x^4 \quad (2-1)$$

where

$$x = b/V \quad b = \sum x_i b_i$$

b_i = molar covolume, ith specie

x_i = mole fraction, ith specie

V_g = molar volume of gas mixture

p = pressure

T = temperature

R = gas constant

The b_i are taken as being equal to four times the molecular volume multiplied by Avogadro's number. However, the equation has been found

to be somewhat inaccurate for calculation of detonation properties.

The virial expansion in terms of pressure is of similar form:

$$pV_g = RT + bp + cp^2 + dp^3 \quad (2-2)$$

where the constants a, b, c and d were found empirically by use of measured detonation velocities for TNT. The equation has not been widely used because TNT does not have thermodynamic properties representative of all condensed explosives.

Ficket and Cowan (Ref. 2) proposed a modification of the well-known K-W-B equation to set it in the form:

$$pV_g/RT = 1 + xe^{\beta x} \quad (2-3)$$

where

$$x = \kappa \sum x_i k_i / V_g (T + \theta)^\alpha \quad (2-4)$$

and where α, β and κ are adjustable constants determined from detonation data and θ is a constant temperature.

This equation has been used extensively and is the basis of several computer codes. However, no single set of constants has been found to fit all C-H-N-O condensed explosives.

A modified Abel equation of state was used by Cook (Ref. 3):

$$p(v-\alpha) = RT \quad (2-5)$$

where α is an effective covolume and the other letters have their usual meaning. The values of α are determined from measurements of detonation velocities through the hydrodynamic conservation equations and appropriate thermodynamic equations. It appears to give reasonable approximations for most explosives.

For liquids, p - V - T data from Bridgman or other sources is often employed, or formulas taking viscosity into consideration. Solids may behave in an elastic, viscoelastic, plastic or rheological manner, and at high pressures as fluids. Under shock conditions pressure-density-velocity data serve to define behavior, in conjunction with the hydrodynamic (shock) equations and Chapman-Hugoniot conditions.

Shock Waves

Because of the high velocities and pressures encountered in hyper-velocity processes, shock waves are generated in almost all of the media associated with an experiment. In light gas guns non-reactive shock waves are generated in the piston, the gun, the driving gas, and the projectile. Impact on the target produces shocks in the projectile and the target. Reactive shocks occur in most cases when high explosives are employed. Shock waves also occur in compressors, water cannons and other types of devices for producing water jets. None of these shocks assumes a steady state condition, except perhaps for a short time in explosives.

Analysis of the equations of flow must take shock conditions into account, with appropriate equations of state of the materials involved, including gases, liquids and solids. Chapman-Hugoniot conditions provide one of the bases of most analysis for both flow and energy partitioning.

Solutions of flow in light gas guns, compressors and water cannons usually require the use of (1) a continuity equation, (2) a momentum equation, and (3) an equation of state. These are combined into characteristic equations which are solved by the method of nets or similar numerical processes.

In light gas guns the ideal equation of state is often employed. For water a pressure-density relationship from Bridgman data has been used.

This study and a number of related investigations indicate that a great deal of research will yet be required in the unsteady flow of hypervelocity processes before they will be susceptible to successful engineering applications.

Much of the initial explanation of shock wave phenomena was developed individually by Chapman (Ref. 4), Jouget (Ref. 5), and Becker (Ref. 6) in conjunction with observed explosion phenomena of gases.

A shock wave may be either non-reactive or reactive. If a shock is initiated in an inert material, such as air, the energy is soon dissipated by dispersion, friction and other mechanisms. When such a shock is accompanied and supported by a chemical reaction, such as occurs in certain explosive gases, liquids or solids, it is a reactive shock or a detonation, and will propagate indefinitely under stable conditions.

The physical-mathematical treatment is identical for both types of shock waves, except for the energy equation, and is restricted largely to plane waves in most analyses.

A plane shock wave represents unsteady flow if it is non-reactive because of its decay. A stable detonation, on the other hand, is unsteady with respect to a fixed observer, but constitutes steady flow with respect to an observer traveling with the same speed as the detonation.

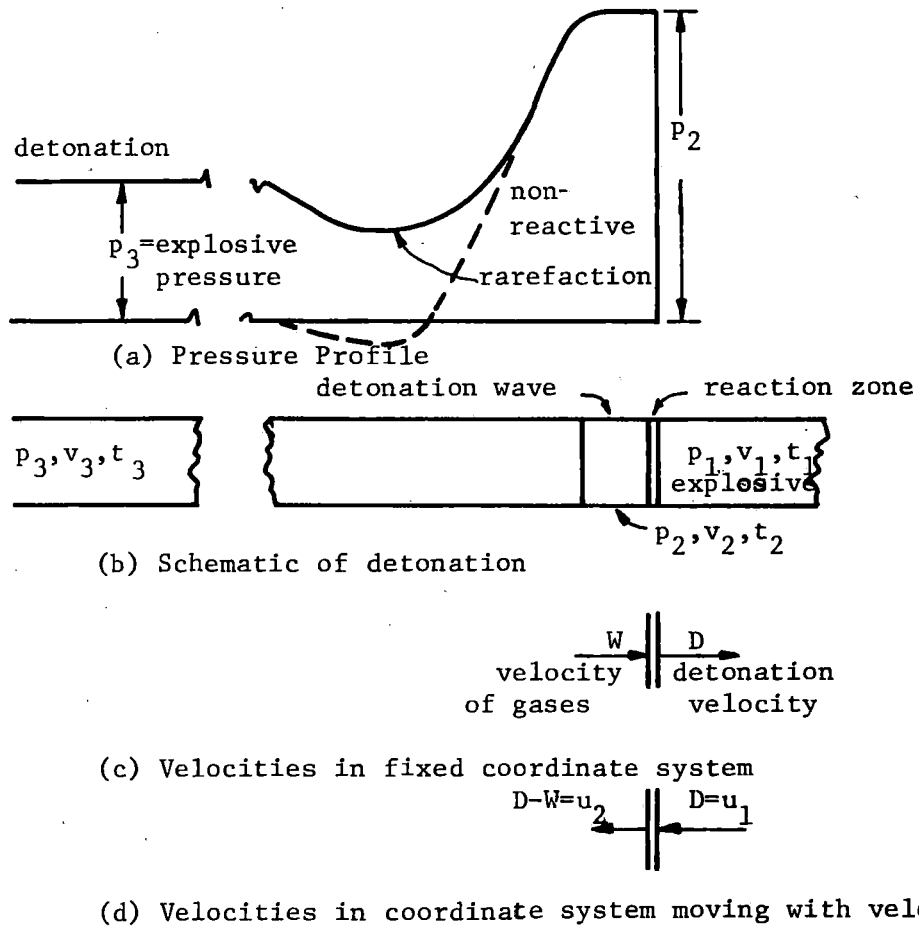


Fig. 2-1. Shock wave nomenclature for non-reactive or reactive shock wave.

If a shock wave is moving to the right with a velocity D , (Fig. 2-1) an observer moving with the wave would note that

(1) from the conservation of mass

$$u_1 \rho_1 = u_2 \rho_2 \text{ or } \frac{u_1}{v_1} = \frac{u_2}{v_2} \quad (2-6)$$

where

u_1 = velocity of material moving into wave front

u_2 = velocity of material moving out of wave front

v_1 = specific volume = $1/\rho_1$

v_2 = specific volume = $1/\rho_2$

(2) the conservation of momentum yields

$$\frac{u_1^2}{v_1} + p_1 = \frac{u_2^2}{v_2} + p_2 \quad (2-7)$$

and finally

(3) the energy balance gives for a non-reactive shock

$$E_1 + \frac{u_1^2}{2} + p_1 v_1 = E_2 + \frac{u_2^2}{2} + p_2 v_2 \quad (2-8)$$

From these equations there follows

$$u_1 = D = v_1 \sqrt{\frac{p_2 - p_1}{v_1 - v_2}} \quad (2-9)$$

$$E_2 - E_1 = 1/2(p_1 + p_2) (v_1 - v_2) \quad (2-10)$$

The last expression is often known as the Hugoniot equation.

If the development is for a detonation, then the heat of reaction Q of the exploding materials must be added to the right side of equation (2-10).

Also, if it is noted that for assumed adiabatic conditions

$$\text{or } E_2 - E_1 = \int_{T_1}^{T_2} C_V dT = \bar{C}_V(T_2 - T_1) \quad (2-11)$$

$$E_2 - E_1 = \bar{C}_V(T_2 - T_1) - Q_2$$

then equation (2-10) becomes

$$\bar{C}_V(T_2 - T_1) = 1/2(p_1 + p_2)(v_1 - v_2) + Q \quad (2-12)$$

For weak shocks in gases the ideal equation of state is usually employed for calculations of shock parameters. For detonations an equation of state must be employed which will take into account the imperfections of gases at high temperatures and pressures.

The equation of state for shock conditions can take various forms. Rinehart (Ref. 7) points out that most of the empirical data used for establishing Hugoniot curves for various materials is obtained from velocity measurements. In early research shock and particle velocities were measured simultaneously and the basic hydrodynamic conservation equations were employed to compute pressure, volume and thermodynamic relationships. Later an impedance match method became more popular because only the shock velocity must be measured. Measurement of density changes are made using x-ray, and piezoelectric measurements can be made to 40 kilobars. Shocks are generated with explosives, impactor plates and gun impactor devices. Several techniques are used to measure shock velocities.

It has been found for a large number of substances that shock velocity and particle velocity are linearly related:

$$v = a + bu \quad (2-13)$$

where v is the shock velocity and u the particle velocity, and a and b are constants for a given material.

Rinehart (Ref. 7) states it holds for ionic, molecular, and metallic crystals and includes liquids, solids and alloys. (Sand has been found to be an exception.) The slope changes with a phase change.

The basic shock equations may be written:

$$\text{Conservation of mass} \quad (v-u)\rho = \rho_0 u \quad (2-14)$$

$$\text{Conservation of momentum} \quad p - p_0 = \rho_0 u v \quad (2-15)$$

$$\text{Conservation of energy} \quad p u = \rho_0 v (E - E_0 + u^2/2) \quad (2-16)$$

where ρ and ρ_0 are the densities behind and in front of the shock, and E_0 and E are the energies of the material before and in the shock front. Combination of equations gives the well-known Rankine-Hugoniot relation:

$$(E - E_0) = 1/2(p + p_0) \left(\frac{1}{\rho_0} - \frac{1}{\rho} \right) \quad (2-17)$$

These equations may also be solved for shock and particle velocities:

$$v = \left[\left(\frac{\rho}{\rho_0} \right) (p - p_0) / (\rho - \rho_0) \right]^{1/2} \quad (2-18)$$

and

$$u = [(\rho - \rho_0)/\rho] v \quad (2-19)$$

For atmospheric pressures ($p_0 = 0$) the expressions for \underline{v} and \underline{p} are combined to give:

$$p = \rho_0 u(a + bu) \quad (2-20)$$

Equation (2-18) may also be written:

$$\rho_0/\rho = [a + (b-1)u]/(a+bu) \quad (2-21)$$

Elimination of u gives

$$p = \rho_0 a^2 \eta / (1 - b\eta)^2 \quad (2-22)$$

where

$$\eta = 1 - \rho_0/\rho \quad (2-23)$$

Equation (2-21) may be utilized as an equation of state and holds only for the linear relationship of equation (2-13). Non-linear equations have been employed by some investigators.

The impedance match method consists essentially of generating a shock of known strength in a material of known Hugoniot properties, and allowing the shock to reflect into an unknown medium, and measuring the transmitted shock. This is repeated for shocks of several different strengths to obtain several points for a curve.

CHAPTER III

WATER JETS

JET STABILITY - THEORY

Stability of jets of water is a prime factor in their effect on rock targets, although probable causes of instability of hypervelocity jets are not all clearly defined. Pai (Ref. 8) has assembled theoretical analyses of several types of jets and their stability, including: (1) ideal inviscid, noncompressible subsonic flow, (2) inviscid compressible subsonic flow, (3) laminar, incompressible, viscous flow, (4) turbulent, incompressible flow, (5) turbulent, compressible flow, and (6) supersonic, compressible, inviscid flow, including shock waves and neglecting heat conduction. All of these have possible elements of application.

For an ideal (incompressible) fluid Rayleigh (Ref. 9) assumed a slight disturbance of an axisymmetrical liquid body, surface tension being the stability force:

$$r = r_0 + b_n \cos n\theta \cos mz \quad (3-1)$$

where r_0 is the radius defining invariant volume, b_n are variable coefficients and θ and z are cylindrical coordinates.

For constant volume

$$r_0 = r_c \left(1 - \frac{1}{8} \frac{b_n^2}{r_c^2} \right) \quad (3-2)$$

where r_c is the radius of the undisturbed cylinder, and $n = 1, 2, 3, \dots$,

and,

$$r_o = r_c \left(1 - \frac{1}{4} \frac{b_o^2}{r_c^2} \right) \quad (3-3)$$

for $n = 0$.

The expression for potential energy due to capillarity is found to be

$$PE = T_s \frac{\pi}{4} (m^2 r_c^2 + n^2 - 1) \frac{b_o^2}{r_c} \quad (3-4)$$

where T_s is the surface tension.

If $m = 0$, PE has twice this value, and if $n = 0$

$$PE = T_s \frac{\pi}{2} (m^2 r_c^2 - 1) \frac{b_o^2}{r_c} \quad (3-5)$$

The solution of Laplace's equation for velocity potential gives the kinetic energy in terms of Bessel functions, and the equation of motion for $b_n = \cos(\omega t - \epsilon)$

is

$$\omega^2 = \frac{T_s}{\rho r_c^3} \frac{imr_c J_n'(imr_c)}{J_n(imr_c)} (n^2 + m^2 r_c^2 - 1) \quad (3-6)$$

for stable vibrations. For $b_n = e^{\pm\sigma t}$, the expression is

$$\sigma^2 = \frac{T_s}{\rho r_c^3} \frac{imr_c J_n'(imr_c)}{J_n(imr_c)} (1 - m^2 r_c^2) \quad (3-7)$$

or vibration is unstable. Addition of detergents (Ref. 10) was actually found to increase the effectiveness of jets at 600 atm pressure.

For high velocity inviscid gases compressibility is not negligible, and may affect high velocity water jets. A solution (Ref. 8) for the case where the jet pressure is equal to that of the surrounding medium is of interest. The flow equation in terms of velocity potential and Mach number (less than one) is solved in terms of a Bessel function of zeroeth order. The increment of velocity decreases exponentially with distance. The gradient increases with jet velocity and lines of constant velocity are closer together. When the jet velocity equals the velocity of sound in the medium, the total velocity change takes place at the nozzle. Thus, a subsonic compressible jet shortens as the reservoir pressure increases.

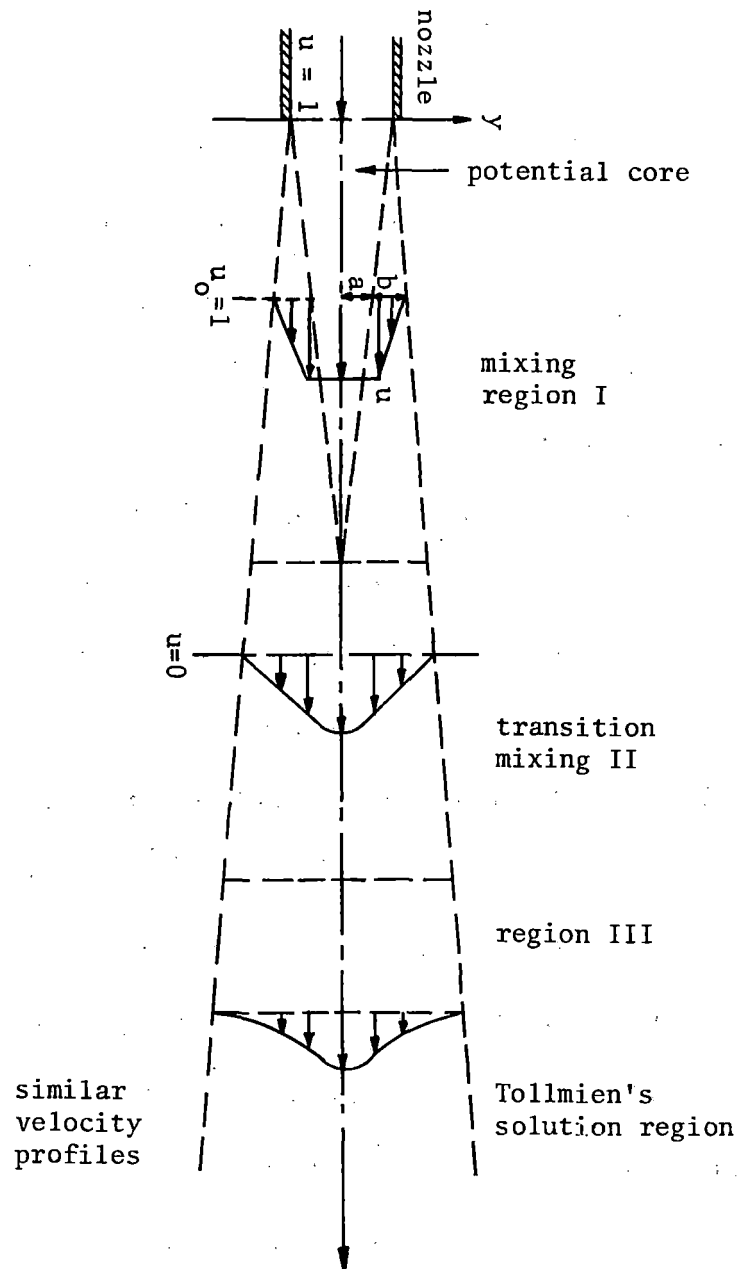
Pai indicates that the jet structure for laminar, viscous, incompressible flow may be divided into (1) a mixing region, and (2) a potential core, the latter being the continuous center of the jet near the nozzle. The mixing region begins on the boundary of the jet and widens downstream (Fig. 3-1). Russian scientists utilize three similar zones (Ref. 11). If viscosity is important, discontinuous surfaces do not occur and transfer phenomena of the mixing region becomes important. For special cases the coefficient of viscosity may be assumed to be constant, Prandtl's number equal to one and the relationship of velocity to temperature may be determined.

For given boundary conditions a solution is

$$\frac{u_1}{u_{10}} = r_0 \int_0^\alpha e^{-\lambda^2 a^2 x} J_0(\lambda r) J_1(\lambda r_0) d\lambda \quad (3-8)$$

where u_1 is the actual velocity and u_{10} is the exit velocity. Velocity distributions (Fig. 3-2) are similar to those observed for high velocity water jets (see below).

Fig. 3-1. Schematic for an axially symmetric jet into a medium at rest, turbulent incompressible flow. (Pai).



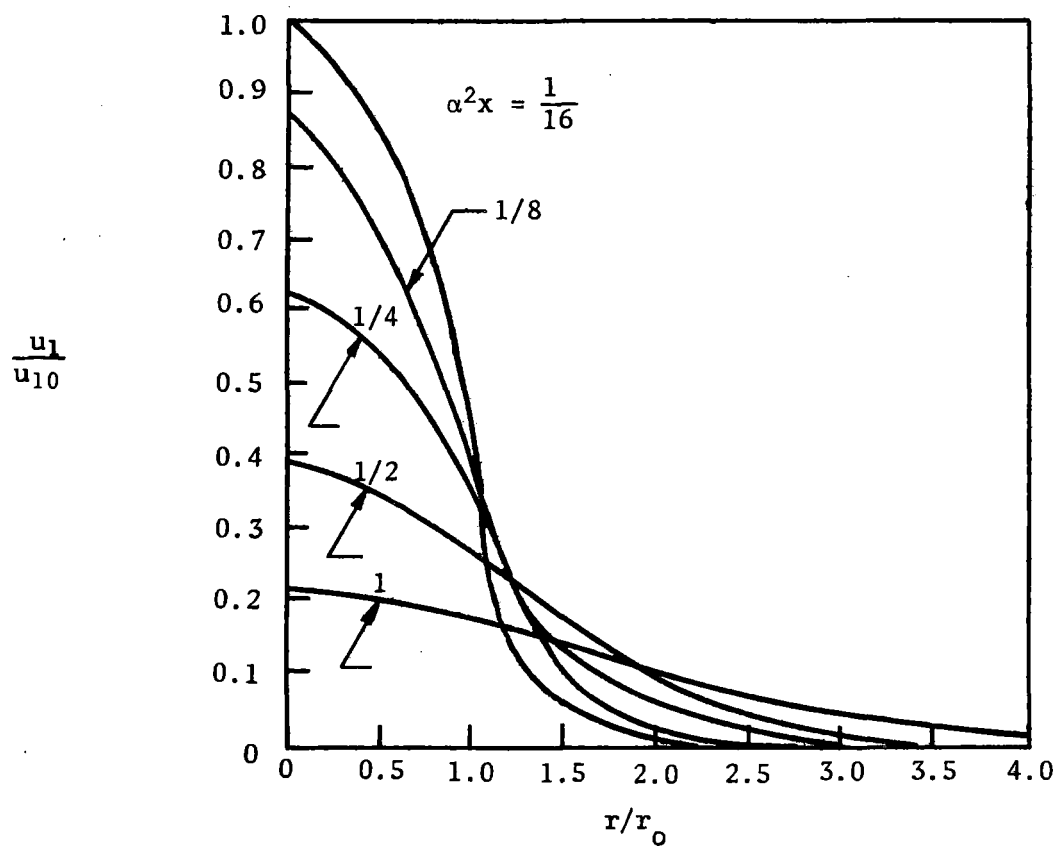


Fig. 3-2. Velocity distribution in jet with laminar viscous flow, solution by means of small perturbations. (Pai).

For turbulent compressible flow the effect of density cannot be neglected, and correlations must be made between velocity, pressure and density. Velocity and temperature fields must both be considered. In 1954 there were no means of measuring fluctuations in supersonic turbulent flow (Ref. 8). Under certain conditions the solutions for turbulent jet mixing are similar to laminar jet mixing. Theory has been found to be in agreement for observations in the turbulent mixing region.

Turbulent incompressible flows are characterized by high Reynolds numbers. Motion is steady only in terms of mean values of velocities and pressures, fluctuation being random in nature.

The problem of a small axisymmetric jet in a medium at rest was solved by Tollmien (Ref. 12) for the mixed low velocity region. The pressure in the jet is assumed constant and a differential equation obtained from the conservation of momentum. A series solution may be utilized for certain boundary conditions. The resultant normalized velocity distribution is shown in Fig. 3-3, where

\bar{u} = Mean velocity in x direction

\bar{v} = Mean velocity in y direction

$\xi = y/x \sqrt[3]{c^2}$

y = Radial distance

x = Distance along axis of jet

c = Constant

The mixing length for this particular case was found to be

$$l = cx = 0.0158x = 0.729y_r \quad (3-9)$$

where y_r is the value of y equal to the radius of the jet. However, the above solutions are held to be valid only for Region III (Fig. 3-1). In Region I the

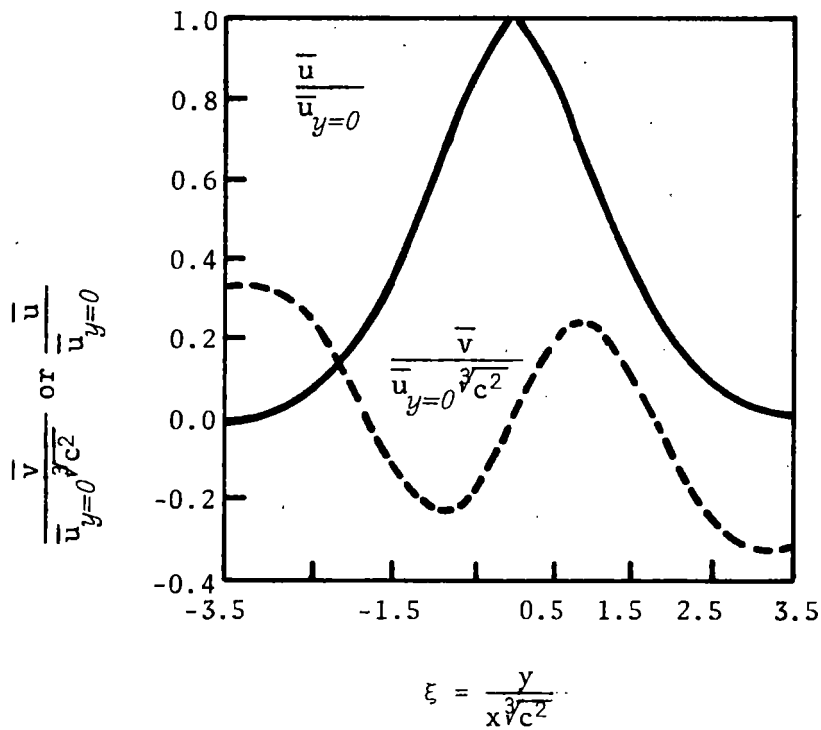


Fig. 3-3. Distribution of mean velocity components for turbulent incompressible flow, \bar{u} being axial flow and \bar{v} being radial flow. (Pai).

cone-shaped central core lies in the center with the mixing region between the core and the surrounding medium. In Region II, the velocity profile changes until similarity is established in Region III where mixing is complete. At velocities of 340 m/sec cores were found to be persistent but not continuous for distances up to 100 diameters (Ref. 10, see below).

It is pointed out (Ref. 8) that the work of Rayleigh and Tollmien described above furnishes the necessary and sufficient conditions for the existence of a disturbance of an inviscid incompressible fluid jet, self-excited, neutral or damped. The necessary condition for the occurrence of a self-excited or neutral disturbance of finite wavelength is the existence of a point of inflection in the velocity profile. For the case of a neutral disturbance, the phase velocity must be $c = w(y_s)$, where y_s is the point of inflection.

Supersonic (inviscid compressible) flow occurs when the medium/reservoir pressure is lower than a critical value, and the expansion and compression waves are accompanied by shock waves. This type of flow is of greatest interest in high velocity jets.

Sauer (Ref. 13) notes that when jet velocities become large and there is an increase in the ratio of the stream velocity to the velocity of sound, the influence of the compressibility on the stream lines becomes stronger. When the jet velocity exceeds the velocity of sound new phenomena appear. Disturbances no longer propagate through the whole field of flow, but only in the downstream region. There are continuous velocity and pressure changes, as well as continuous changes of state characterized by "compression shocks". A mathematical difference lies in the fact that while the potential equation for

subsonic flow is elliptic (for incompressible media) that for supersonic flow is hyperbolic.

Pai (Ref. 8) treats the case of a supersonic axisymmetric circular jet.

The flow equation takes the following form:

$$\beta^2 \frac{\partial^2 \phi}{\partial r^2} = \frac{\partial^2 \phi}{\partial x^2} + \frac{1}{r} \frac{\partial \phi}{\partial r} \quad (3-10)$$

in which $\beta^2 = M^2 - 1$ (M = Mach number) and r is the radial distance from the axis of the jet. Its solution is

$$\phi = A J_0(\lambda \beta r) \sin \lambda x \quad (3-11)$$

where J_0 is a zeroth order Bessel function of the first kind. The boundary condition is that the pressure at the boundary of the jet $r = r_j$ is equal to that of the surrounding medium. This requires that $\frac{\partial \phi}{\partial r} = 0$ for all x at $r = r_j$.

Hence, the solution becomes

$$J_0(\lambda \beta r_j) = 0 \quad (3-12)$$

Its first root is $z = 2.405$ and hence

$$\lambda_1 = 2.405 / \beta r_j \quad (3-13)$$

and the approximate wavelength of the jet is

$$L = \frac{2\pi}{\lambda_1} = 2.613 r_j \sqrt{M^2 - 1} \quad (3-14)$$

A general solution of the problem is given by

$$\phi = \sum_{n=1}^{\infty} A_n J_0(\lambda_n \beta r_j) \sin \lambda_n x \quad (3-15)$$

where the values of A_n are determined by the nozzle condition. Pai notes that Lord Rayleigh (Ref. 9) showed that the greatest swelling of the jet occurs

where the pressure at the axis is least:

Take

$$\Phi = AJ_0(\lambda_1 \beta r) \sin \lambda_1 x \quad (3-16)$$

hence,

$$\frac{\partial \Phi}{\partial r} = A \lambda_1 \beta J_0'(\lambda_1 \beta r) \sin \lambda_1 x \quad (3-17)$$

and

$$J_0'(z) = \frac{dJ_0(z)}{dz} \quad (3-18)$$

The radius of the jet varies from its mean value \underline{r} by

$$\delta r_j = \int_{r=r_j}^x \frac{1}{U} \left(\frac{\partial \Phi}{\partial r} \right) dx = - \frac{A \beta J_0'(\lambda_1 \beta r_j)}{U} \cos \lambda_1 x \quad (3-19)$$

where $J_0'(2.405) = -0.5191$.

Hence, the variation in the pressure at the axis is approximately

$$\frac{\delta p}{\rho_{av}} = \text{constant} - \frac{u^2}{2} = U \delta u = - U A \lambda_1 \cos \lambda_1 x \quad (3-20)$$

where $J_0(0) = 1$ and ρ_{av} is the average density. δu is the variation in the velocity component parallel to the axis. The ratio of 3.18 to 3.19 yields

$$\frac{\delta r_j}{(\delta p / \rho_{av})} = - 0.2158 r_j \frac{\beta^2}{U^2} \quad (3-21)$$

Thus, the parameters δr_j and $\delta p / \rho_{av}$ are of opposite sign and the greatest swelling is accompanied by the lowest axial pressure.

For a large pressure difference between the jet and the medium an increasing number of shock waves occur in the jet. As the pressure difference increases a shock pattern is set up in the jet. That shown (Ref. 13, Fig. 3-4)

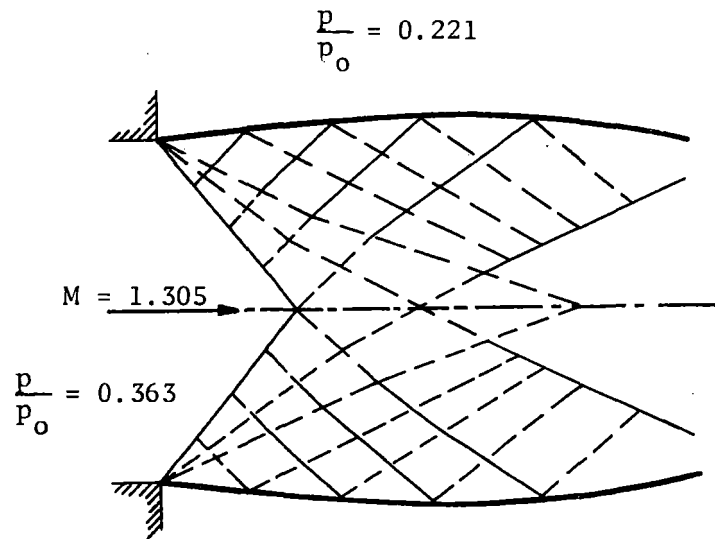


Fig. 3-4. Supersonic parallel axisymmetric jet into medium at lower pressure at Mach 1.305 showing generated and reflected shock waves. (Sauer).

is for a pressure ratio of 0.363. For the much smaller pressure ratios in the range of 10^{-3} or 10^{-4} the shock pattern is very complex. No experimental observations have been found in the literature, but the shocks undoubtedly contribute to jet instability.

Summary

For low velocities a small disturbance causes an oscillation of the jet which may be held in balance by surface tension. At moderately high velocities shock waves are generated in the portion of a jet downstream from the nozzle. Turbulence also appears to affect stability on both the upstream and downstream sides of the nozzle. No complete theory has been developed for large Mach numbers, but it appears that (1) turbulence, (2) air friction, and (3) shock waves in the jet are critical factors in jet stability. Also, there was no theory found for water jets where the jet approaches the speed of sound in water.

JET STABILITY - EXPERIMENTATION

Considerable experimentation has been performed on the stability of high speed water jets and mechanisms which cause instability, breakup, mixing and dispersion. However, no meaningful correlations have been made with the theories which have been presented above except in limited ranges.

The results of experimentation are described under the principal investigator's name. Projects which have been performed are somewhat diversified in research aims, approach and the empirical formulas and data developed.

Vereshchagin, et al.

By means of a suitable device to measure conductivity of jets from a 1 mm nozzle, Vereshchagin, et al., (Ref. 14) measured jet continuity for pressures varying from 9 to 1000 atm. The number of pulses in the closed circuit - ry (by the jet) was measured and the probability w of its length being continuous plotted against jet length for various pressures (Fig. 3-5). The results of tests in terms of pressure and length are given in Fig. 3-6, and the maximum length of jet versus pressure shows a first peak at about 7 atm and a second peak at 200 atm. The initial part of this curve agrees well with results obtained at low pressures by other investigators. No theory is employed to explain the observed phenomena.

Khamyak

This theoretical paper (Ref. 15) discusses a previously written article by Vivdenko and Chabalin, maintaining an opposing view that the breakup of jets is not due to a new mechanism but to vibrations of the jet, and that disturbances originating at the front end of the jet are not responsible for the disintegration. The work of Rayleigh is used to show that disturbances of various lengths may grow with different velocities. He showed that a disturbance may grow as

$$\epsilon = \epsilon_0 \exp qt \quad (3-22)$$

where ϵ_0 is an initial disturbance.

Kuklin and Shtukaturov

The methods employed by Kuklin, et al., (Ref. 16) involved measurement of the electrical resistance of the jet, its velocity, density, dynamic pressure and losses to determine in turn a quality coefficient of structure of

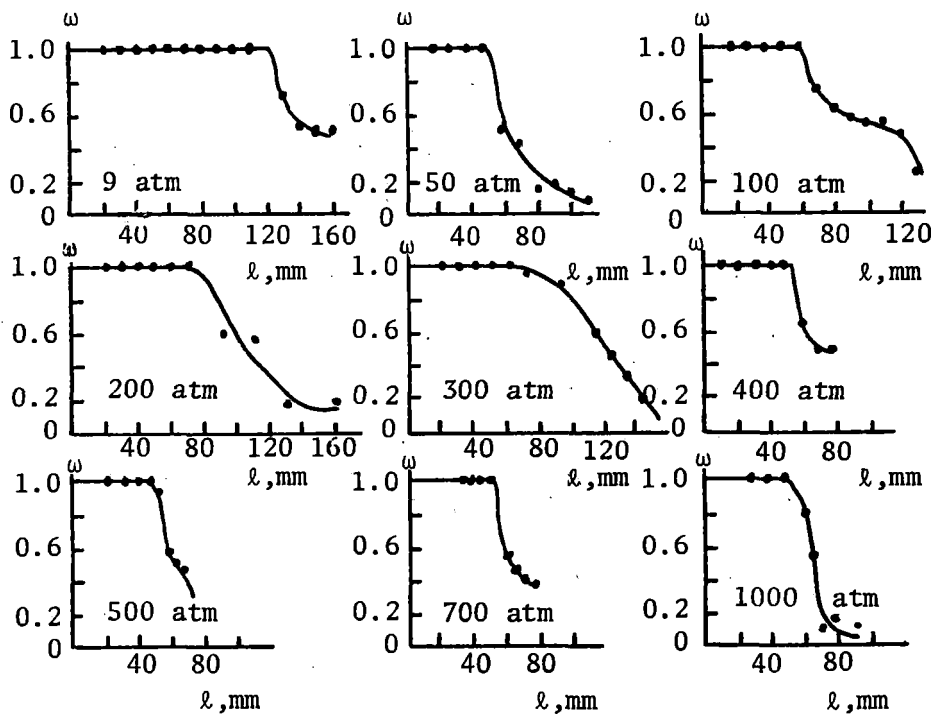


Fig. 3-5. Curves of probability of continuity of the jet for various pressures. (Vereshchagin).

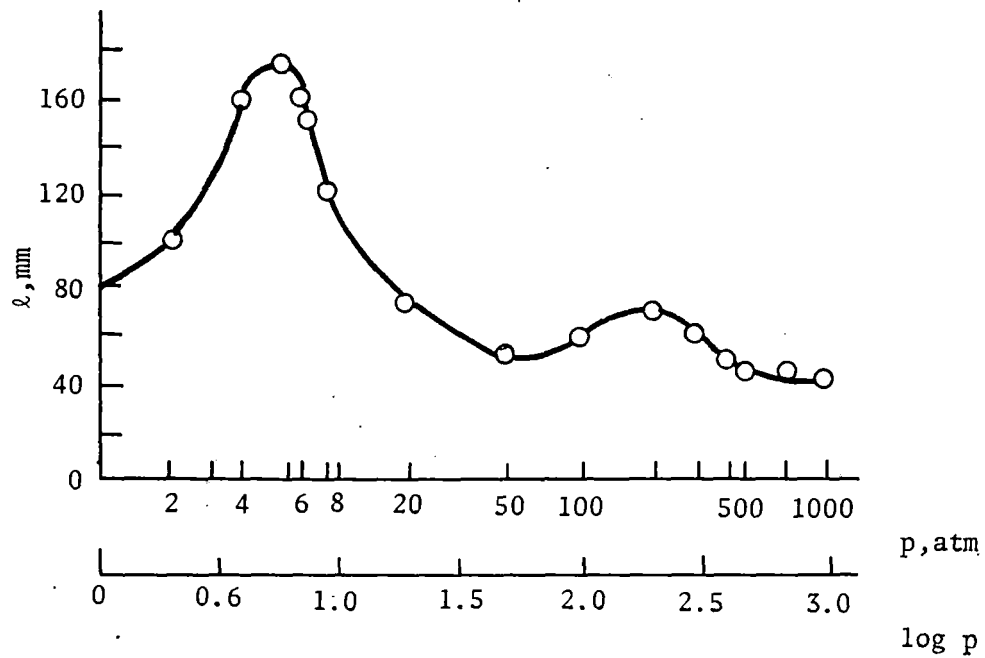


Fig. 3-6. Curve of the dependence of the length l of the continuous part of a jet of water on the pressure. (Vereshchagin).

the jet and nozzle.

The jet nozzle and a movable net of steel wire in the jet (Figs. 3-7 and 3-8) were used as electrodes. Jets varied in diameter from 1 to 25 mm with pressures of 0.5 to 30 atm. Resistance along the jet for fluids with and without surface tension indicate that the one with surface tension breaks up more rapidly:

The ideal velocity-pressure relationship of a jet for constant density is

$$v = (2P/\rho)^{1/2} \quad (3-23)$$

However, this gives a "fictional" velocity. The "partial expenditure" q and pressure p were measured at a given point (Fig. 3-9).

They are related by

$$q = Avg\rho \quad (3-24)$$

where A is the cross-sectional area. Other parameters are related by

$$v = \frac{2gHA}{q} \quad (3-25)$$

$$\frac{v}{v_o} = \frac{H \cdot q_o}{H_o \cdot q} \quad (3-26)$$

$$\rho = \frac{q^2}{2g^2pA^2} \quad (3-27)$$

$$\frac{\rho}{\rho_o} = \frac{q^2 H_o}{q_o^2 \cdot H} \quad (3-28)$$

where p_o , H_o , v_o , q_o and ρ_o are the pressure, dynamic pressure, velocity, partial expenditure and density of the jet at the nozzle exit.

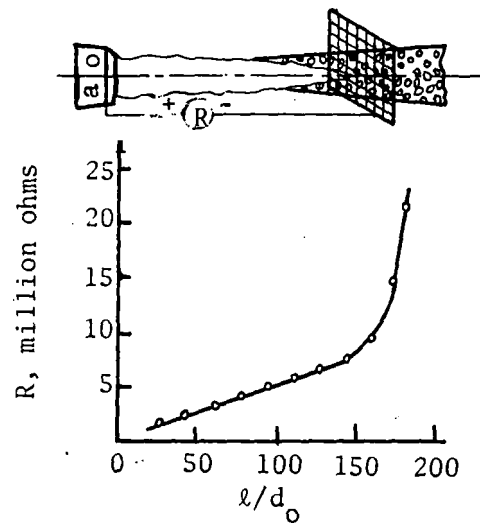


Fig. 3-7. The electrical resistance of a jet with a film of surface tension. (Kuklin and Shtukaturv).

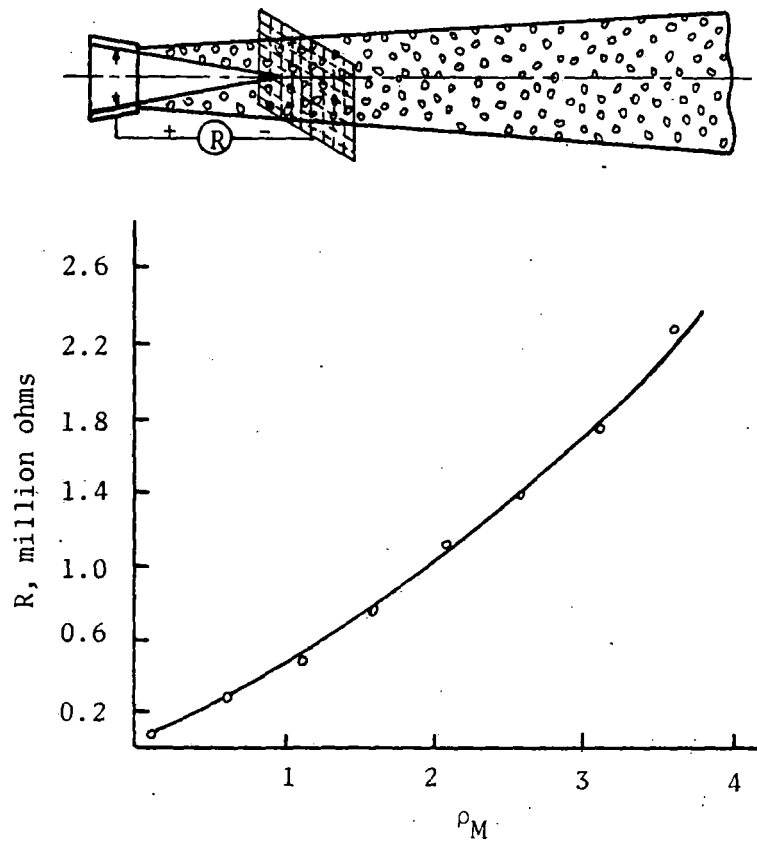


Fig. 3-8. The electrical resistance of a jet without a film surface tension. (Kuklin and Shtukaturv).

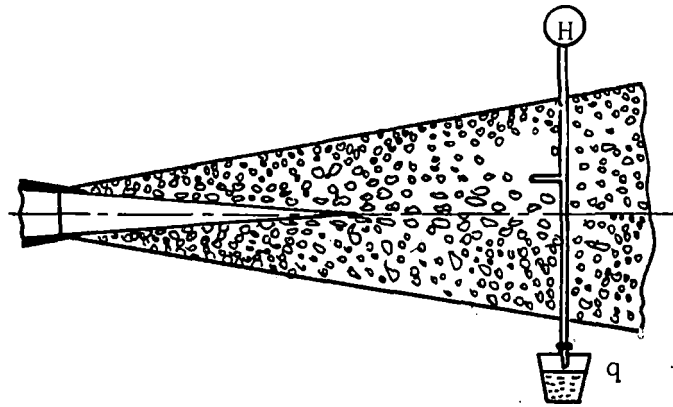


Fig. 3-9. The scheme of the experiments on measuring the pressure and partial pressure loss expenditure in a jet. (Kuklin and Shtukaturov).

The coefficient of structure of a jet is given by

$$a = C_1\alpha_1 + C_2\alpha_2R_e \quad (3-29)$$

where C_1 and C_2 are constant coefficients, α_1 is the quality coefficient of the nozzle, α_2 is quality coefficient of the hydromonitor and R_e is Reynolds number of the water in the pipe in front of the monitor. The coefficient \underline{a} is also related to the length of primary section ℓ_H and the jet diameter d_c in the compressed section by

$$a = d_c/\ell_H \quad (3-30)$$

These quantities are measured experimentally and \underline{a} calculated. The unknowns in equation (3-29) are then determined as follows: The nozzle is placed in a pipe equivalent to the monitor pipe. If the nozzle entrance is smooth, then

$$a_1 = C_1\alpha_1 \quad (3-31)$$

if turbulence is negligible. For turbulent entrance α_2 is taken equal to one and

$$a_2 = C_1\alpha_1 + C_2R_e \quad (3-32)$$

For the nozzle in the monitor a third equation is obtained

$$a_3 = C_1\alpha_1 + C_2\alpha_2R_e \quad (3-33)$$

The case for $\alpha_2 = 1$ is for an aperture in a thin membrane, and if experiments are repeated for this condition, the equations in Table 3-1 are obtained.

The first four equations are solved, and the last two used for verification to give $C_1 = 0.025$, $C_2 = 1.2 \times 10^{-8}$, $\alpha_1 = 0.4$ and $\alpha_2 = 9$. This value of α_2 for a hydromonitor (GMDTS-2) indicates that its design makes the quality of the jet worse. The smaller the value of \underline{a} , the greater the length of the primary section of the jet.

The above method may be used to determine the quality of hydromonitors and nozzles and to predict jet structures.

TABLE 3-1

Determining the coefficient of the structure of a jet

Condition of the experiment	Coefficients		l_H mm	α	Equations
	α_1	α_2			
A nozzle in a pipe with a smooth contraction	?	0	1500	0010	$a_1 = C_1\alpha_1$
A nozzle in an ordinary pipe	?	1	1250	0012	$a_2 = C_1\alpha_1 + C_2R_e$
A nozzle with hydromonitor GMDTs-2	?	?	540	0028	$a_3 = C_1\alpha_1 + C_2\alpha_2R_e$
An aperture in a thin membrane, placed in a smooth contraction	1	0	600	0025	$a_4 = C_1$
The same, in an ordinary pipe	1	1	560	0027	$a_5 = C_1 + C_2R_e$
The same, in an hydromonitor GMDTs-2	1	?	350	0043	$a_6 = C_1 + C_2\alpha_2R_e$

Semerchan, et al.

A liquid jet of supersonic velocity is described (Ref. 17) as a liquid "rod" as it leaves the nozzle, quickly becomes a rod surrounded by a mixture of air and droplets and at a certain distance the continuous liquid disappears, the jet becoming a cone of droplets and air. The velocity decreases both along the axis from the nozzle and away from the axis in the cross section, with a corresponding distribution in momentum and energy.

The method of investigating these distributions was to record the momentum by means of a pendulum (sand behind screen for target) which would completely absorb the momentum of the jet. Measurements were made of portions of the jet passing through circular orifices of 30 to 100 mm diameter at varying distances from the nozzle, screening out part of the jet.

Experiments were carried out using the nozzle in Fig. 3-10 utilizing water, glycerin, and 10%, 20% and 40% mixtures of glycerin with water.

The momentum of the jet is given by

$$mv = \rho v^2 \quad (3-34)$$

and

$$v^2 = 2 p/\rho \quad (3-35)$$

where

m = mass flow rate

v = velocity of efflux

ρ = density of liquid

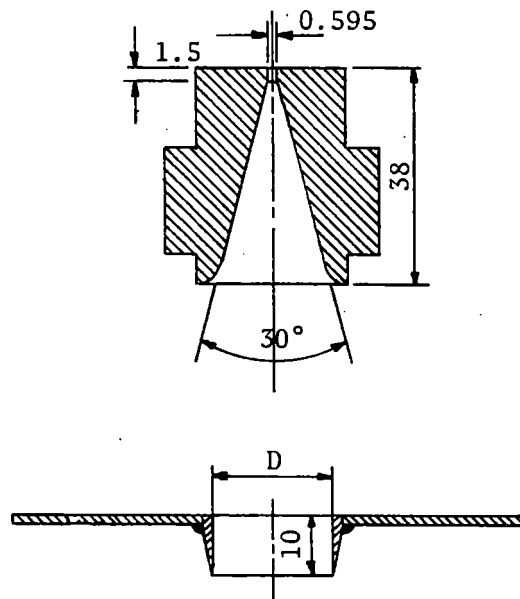


Fig. 3-10. Nozzle and Diaphragm. Systematic measurements were carried out with $D = 30, 40, 50, 70$ and 100mm . Separate measurements close to the nozzle were made with $D = 10$ and 20 mm . (Semerchan).

From equations(3-34) and (3-35)

$$mv = 2 p_0 \quad (3-36)$$

that is, the momentum per unit time is directly proportional to the nozzle pressure.

Subsonic to supersonic velocities (340 to 540 m/sec) were utilized in experiments and good reproducibility was obtained. For water the theoretical curve (Fig. 3-11) for force versus pressure is shown as a dashed line, and the other force curves for $F = mv$ for five screening orifices for distances varying from 100 to 1000 mm. Force decreases rapidly with travel distance (Figs. 3-12 and 13) and approaches a maximum with increase in orifice size (Fig. 3-14). The distribution of momentum is shown in Fig. 3-15.

There is a less rapid decrease in force versus distance for mixtures of glycerin and water and for glycerin. This is believed due to a decrease in "conicity" of the jet with increase in viscosity.

Leach and Walker

Leach and Walker (Ref. 10) studied the stability of jets from a 1 mm nozzle at pressures of 130 and 600 atm. Flash tube and spark photography showed a dispersing jet. X-ray photos, however, indicated a continuous central core which contained most of the mass of the water.

The pressure distribution of the cross section of the jet was found to be

$$p = p_0 + 1/2 \rho u^2 \left[1 - 3 \left(\frac{r}{R} \right)^2 + 2 \left(\frac{r}{R} \right)^3 \right] \quad (3-37)$$

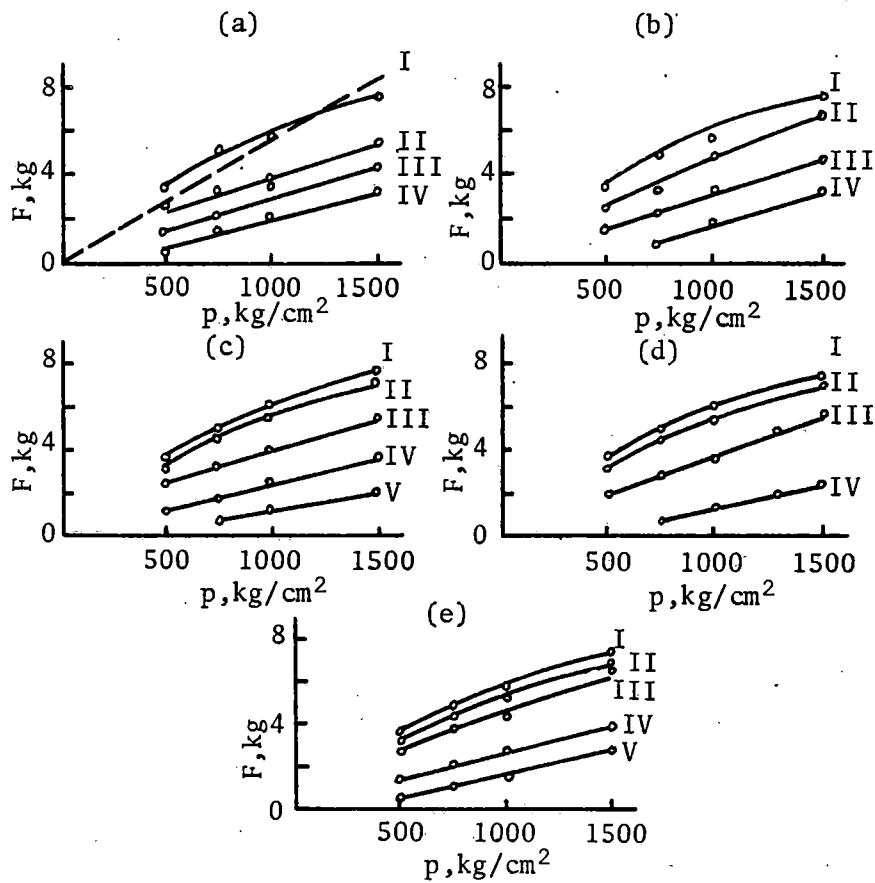


Fig. 3-11. Dependence of F - the force of reaction of the jet on an obstacle - on the pressure p ahead of the nozzle. a: I) $\ell = 100$ mm, II) $\ell = 300$ mm, III) $\ell = 400$ mm, IV) $\ell = 500$ mm, $D = 30$ mm. b: I) $\ell = 100$ mm, II) $\ell = 300$ mm, III) $\ell = 500$ mm, IV) $\ell = 600$ mm, $D = 40$ mm. c: I) $\ell = 100$ mm, II) $\ell = 300$ mm, III) $\ell = 500$ mm, IV) $\ell = 700$ mm, V) $\ell = 800$ mm, $D = 50$ mm. d: I) $\ell = 100$ mm, II) $\ell = 500$ mm, III) $\ell = 700$ mm, IV) $\ell = 900$ mm, $D = 70$ mm. e: I) $\ell = 100$ mm, II) $\ell = 500$ mm, III) $\ell = 700$ mm, IV) $\ell = 800$ mm, V) $\ell = 1000$ mm, $D = 100$ mm. (Semerchan).

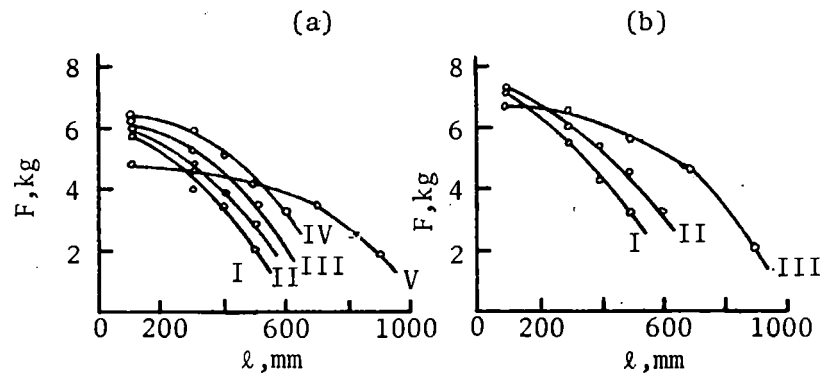


Fig. 3-12. Dependence of F - the force of reaction of the jet on an obstacle - on the distance l between the obstacle and the nozzle for jets of different liquids, a) $p = 1000 \text{ kg/cm}^2$, $D = 30 \text{ mm}$; b) $p = 1500 \text{ dg/mm}^2$, $D = 30 \text{ mm}$. I) water; II) 10% solution of glycerin in water; III) 20% solution of glycerin in water; IV) 40% solution of glycerin in water; V) glycerin. (Semerchan).

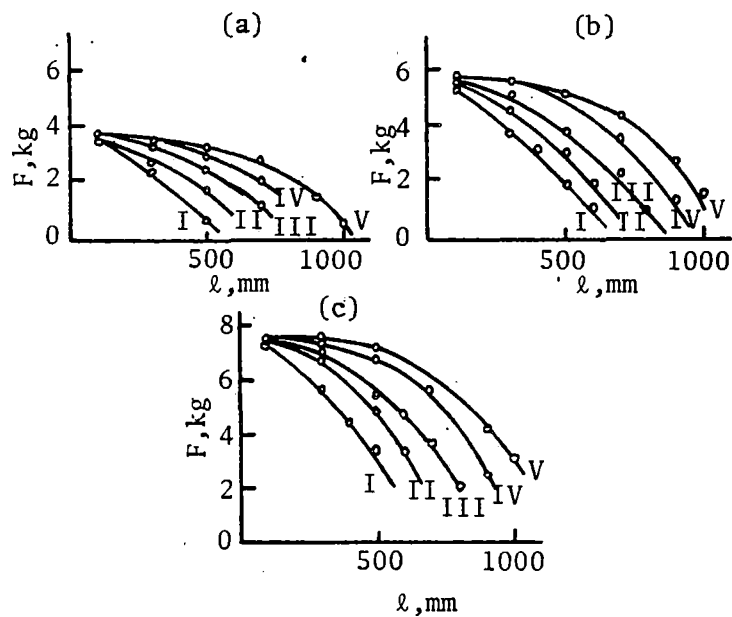


Fig. 3-13. Dependence of F - the force of reaction of the jet on an obstacle - on the distance l between the obstacle and the nozzle. a) $p = 50 \text{ kg/cm}^2$; b) $p = 1000 \text{ kg/cm}^2$; c) $p = 1500 \text{ kg/cm}^2$. For a, b, c, : I) $D = 30$, II) $D = 40$, III) $D = 50$, IV) $D = 70$, V) $D = 100 \text{ mm}$. (Semerchan).

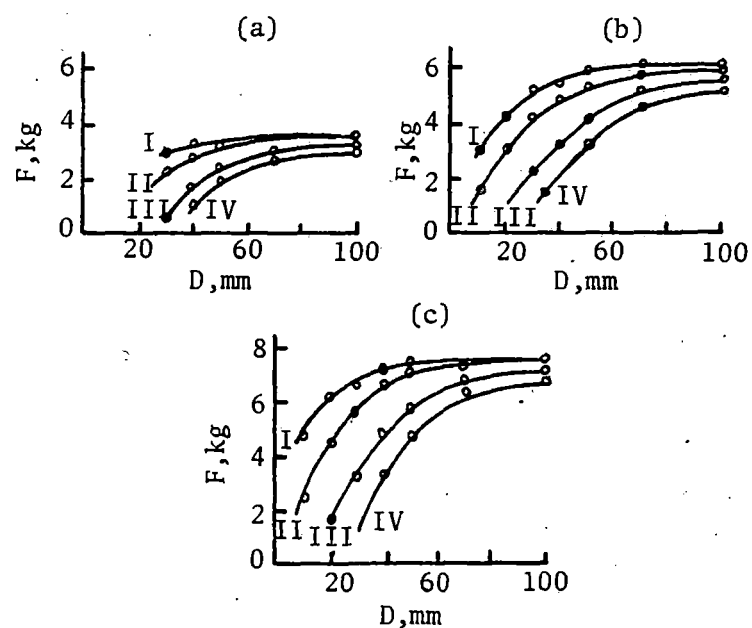


Fig. 3-14. Dependence of F - the force of reaction of the jet on an obstacle - on the diameter of the diaphragm D . a) $p = 500$ kg/cm²; b) $p = 1000$ kg/cm²; c) $p = 1500$ kg/cm². For a, b, c: I) $\ell = 200$, II) $\ell = 300$, III) $\ell = 500$, IV) $\ell = 600$ mm. (Semerchan).

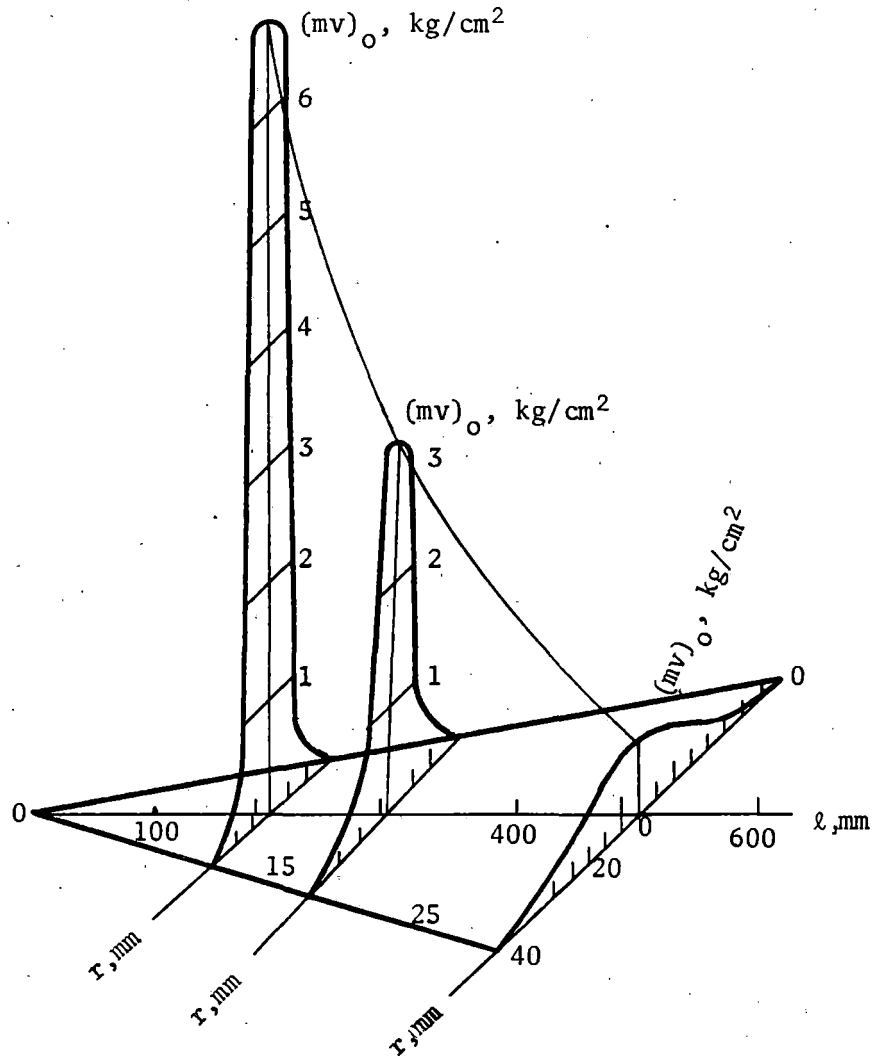


Fig. 3-15. Distribution of momentum in a jet of water flowing continuously from a circular opening of diameter $d = 0.595$ mm under a pressure $p = 1500$ atmos. (Semerchan).

where

ρ = water density

p = pressure at target

p_0 = ambient pressure

r = radial distance

u = mean jet velocity

R = distance from where $p = p_0$

which was in substantial agreement with measured values and in qualitative agreement with theories for low velocity jets.

Dunne and Cassen

Dunne and Cassen (Refs. 18 and 19) utilized an injector with nozzles of 0.13 and 0.20 mm diameters to produce jets of various liquids of velocities up to 460 m/sec. By imposing a step function impulse on an existing jet, the effect of a faster jet impinging on a slower one was found to produce discs or nodules of fluid in the jet stream. The assumptions were made that surface and viscous forces were negligible compared to inertial forces. The downstream impingement of a higher velocity jet on a lower velocity stream represents one special type or source of instability.

Zelenin, et al.

In spite of dispersion and mixing, total impact pressure of jets was found to be practically constant with increased distance by Zelenin (Ref. 20) for receiver pressures up to 1000 atm (Table 3-2). Thus, while there is considerable dispersion of jets over relatively short distances, the length of continuous jet depends upon the nozzle pressure, but the total pressure is

not seriously decreased. However, for jets from a nozzle of 0.595 mm and a pressure of 1500 atm, Semerchan, et al., (Ref. 17) found that the momentum and unit pressure decreased rapidly with distance (Fig. 3-15) in general agreement with theory, although no specific comparisons appear to have been made.

TABLE 3-2

Total Pressure of Jet

Receiver Pressure, Atm	$l = 3$ cm	5 cm	12 cm	25 cm	45 cm
300	4.0	7.0	3.5	3.4	3.5
500	9.0	7.0	7.0	7.5	10.0
700	10.0	11.0	11.5	11.0	12.0
1,000	15.0	14.0	14.0	15.5	15.0

PULSED JETS - THEORY AND EXPERIMENT.

Aside from the report of results of breakage of rock by pulsed jets by Zelenin (Ref. 20) and a very brief report on their use by Cooley (Ref. 31), there is no detailed description of the mechanics of their production or their underlying theory published in available literature. As indicated above, they are reported to require less power than steady jets and to be more effective in breaking of certain types of friable rock. At very high velocities their terminal ballistic effects are probably similar to those of low density hypervelocity projectiles.

NOZZLES

Nozzle design is a critical factor in minimizing turbulence in high velocity jets. Nozzle tests for fire fighting with water at relatively low velocities indicate that the best design for large scale flow at low velocities is somewhat similar to that for capillary jets (Ref. 21). An internal channel designed for streamline flow would be most desirable. However, the difficulties in machining curved interiors in small nozzles do not appear to justify improvements in results. Most of the research on small nozzles has been performed in England and the USSR.

Leach and Walker

In their tests on rock Leach and Walker (Ref. 10) investigated a series of 1 mm nozzles whose internal openings (longitudinal) were in the form of a contraction followed by a 3 mm length of 1 mm diameter section. The simplest nozzle was found to be one with a small angle cone (6 to 20°) followed by a straight section of 2 to 4 nozzle diameters in length. Pressures to 80% of the initial pressure exist at distances up to 100 nozzle diameters.

Although the research of Leach and Walker (Ref. 10) was performed at relatively low pressures, their results are the most complete described in English. They measured pressures on target plates, observing fluctuations at distance, probably due to impact of drops, indicating a discontinuous core. Water hammer pressures were not measured.

The best results from five different nozzles (Fig. 3-16) were (a) with a 13° conical section followed by 2.5 diameters of straight section. Fourteen other shapes were tested (Fig. 3-17). Several gave good results, large

NOZZLE SHAPES

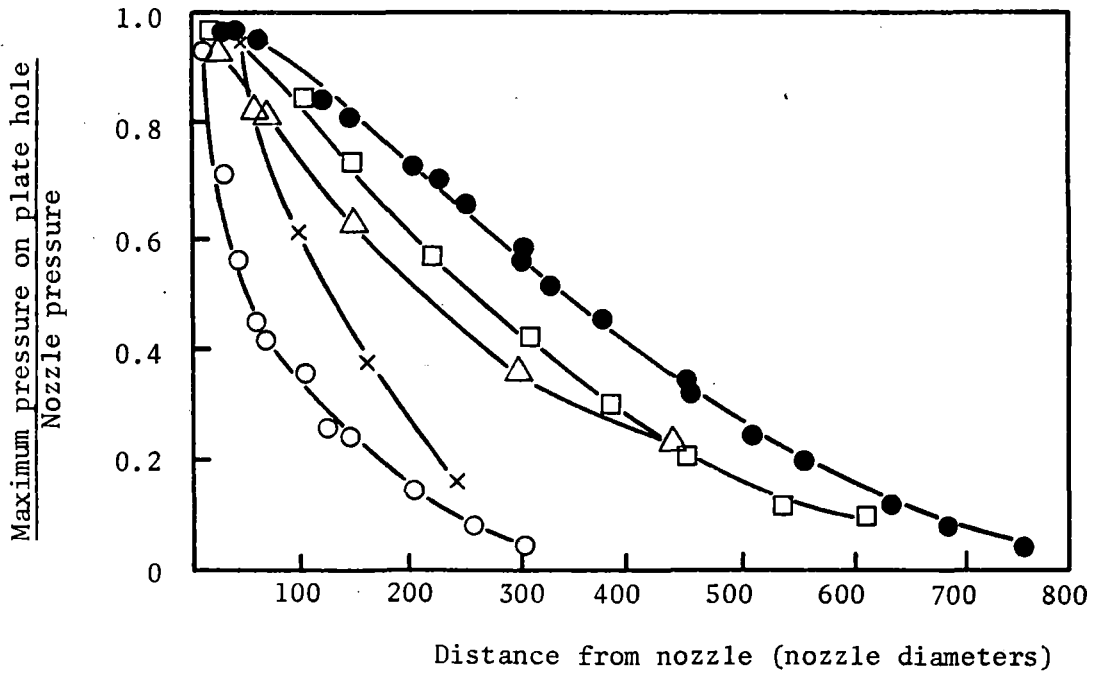
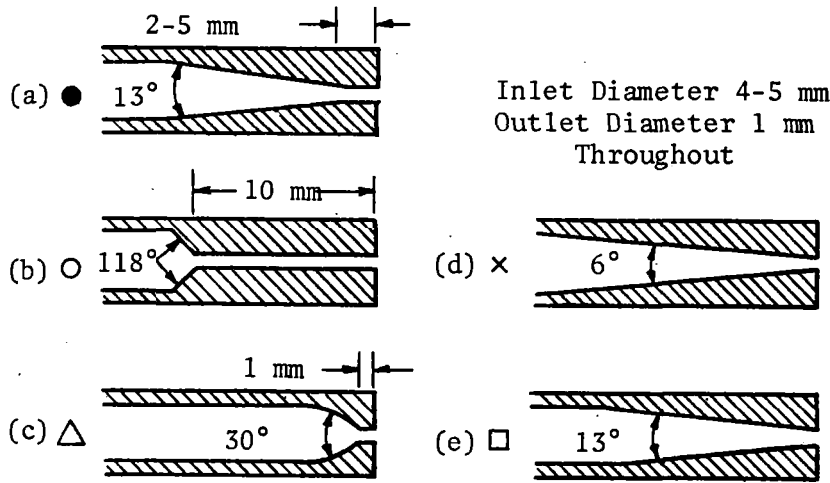


Fig. 3-16. Effect of nozzle shape on performance. (Leach and Walker)

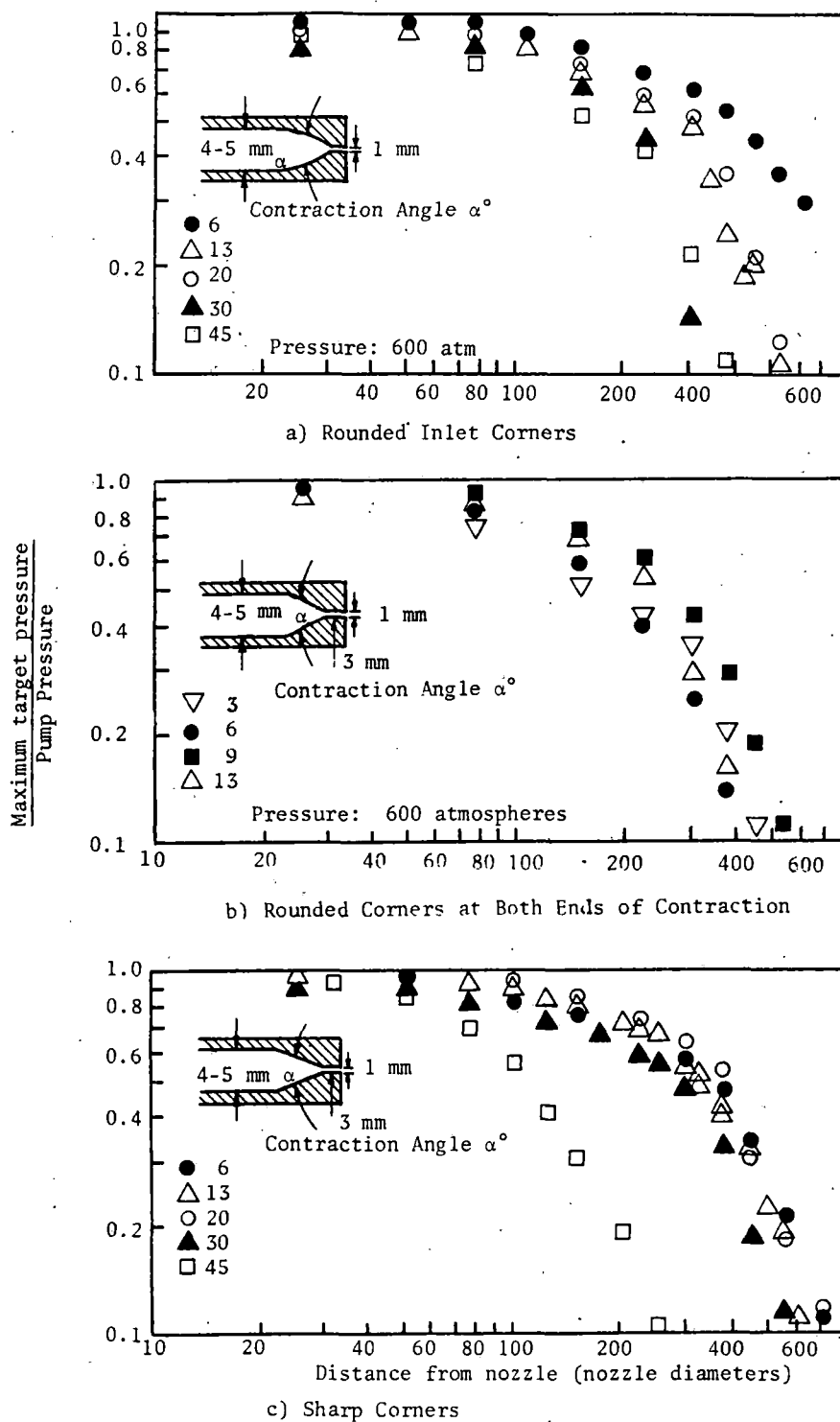


Fig. 3-17. The effect of contraction angle on nozzle performance. (Leach and Walker).

contraction angles giving the poorest and sharp internal corners are better than rounded. The effect of length of straight section (Fig. 3-18) indicates that the best results are obtained with a straight section of about three mm for a one mm opening.

A change in the driving pressure changes Reynolds, Weber and Mach numbers, the difference in jet pressure for two driving pressures being shown in Fig. 3-19. Surface tension was changed with a detergent and viscosity with sodium carboxymethyl cellulose, both of which improved performance, indicating that surface tension has a minor effect in jets of the velocity range tested (340 m/sec, Fig. 3-20).

Data for pressure distribution across the jet at two distances from the nozzle at two different driving pressures shows a variation which is similar to the theoretical values represented by the curve (Fig. 3-21).

Farmer

In his early work, Farmer (Ref. 22) employed a nozzle with a 45° entrance angle (Fig. 3-22) and a cylindrical portion $1/16$ inch diameter and about one inch long. He found that this induced turbulence, and that for nozzles below $1/16$ inch diameter the jet tended to break up close to the nozzle.

In later work Farmer (Ref. 23) measured jet core continuity by means of an electrical device and tested the continuous jet length for the seven nozzle profiles in Fig. 3-23, all with outlet diameters of $1/16$ inches (1.59 mm). The best results were obtained with an entrance angle of 40° , and a smooth nozzle profile (Table 3-3 and Fig. 3-23).

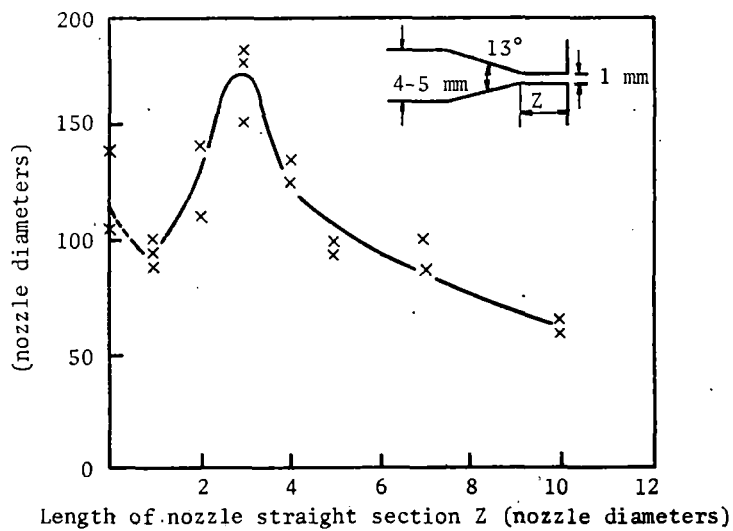


Fig. 3-18. The effect of length of nozzle straight section on performance. (Leach and Walker).

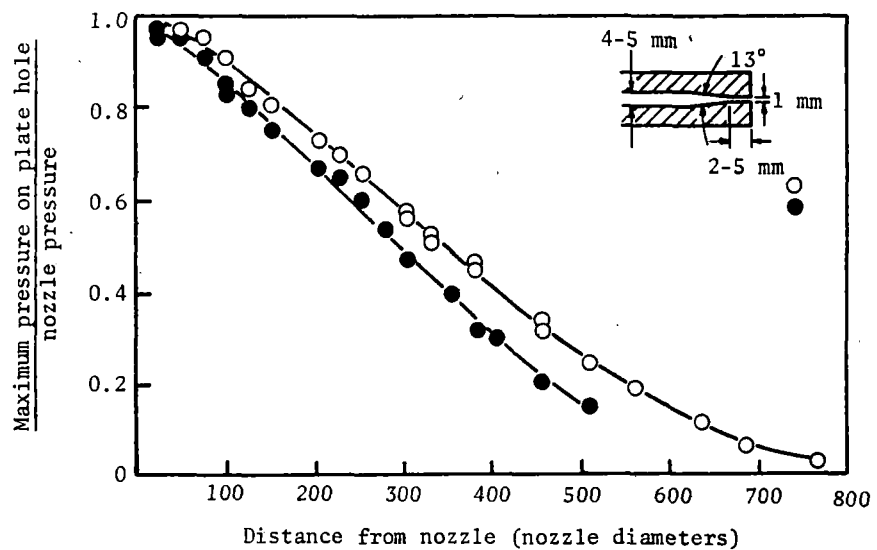


Fig. 3-19. Variation of maximum pressure on plate hole with distance from nozzle, for pump pressure of 600 and 130 atmospheres. (Leach and Walker).

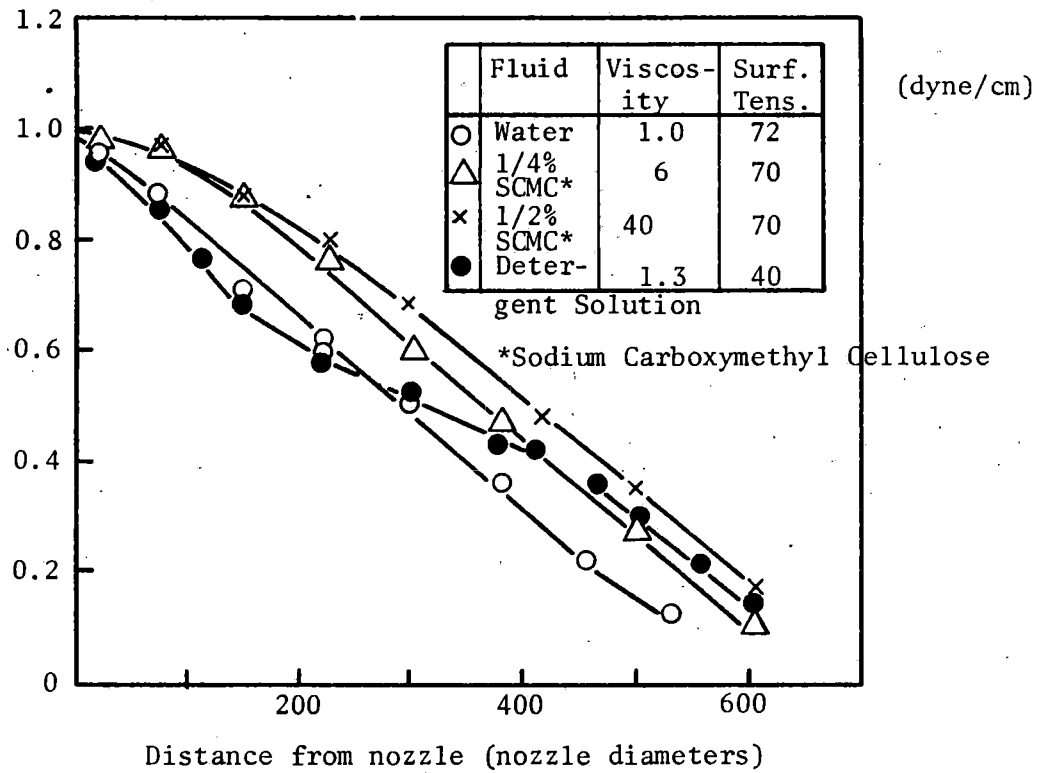


Fig. 3-20. Effect of changes in viscosity and surface tension. (Leach and Walker).

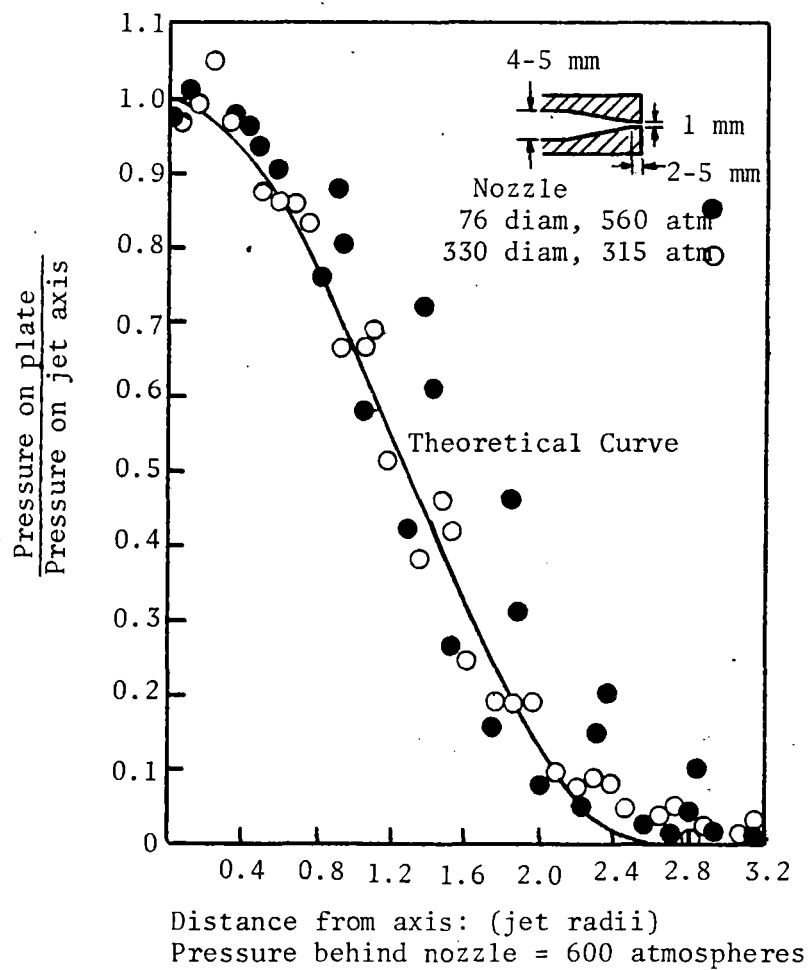


Fig. 3-21. Pressure distribution on a plate at right angles to the jet at 76 nozzle diameters and 560 atm, and 330 nozzle diameters and 315 atm. (Leach and Walker).

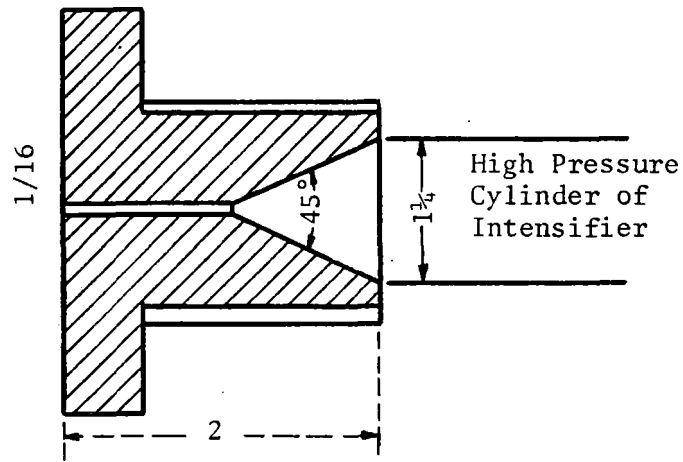


Fig. 3-22. Early design of nozzle. (Farmer).

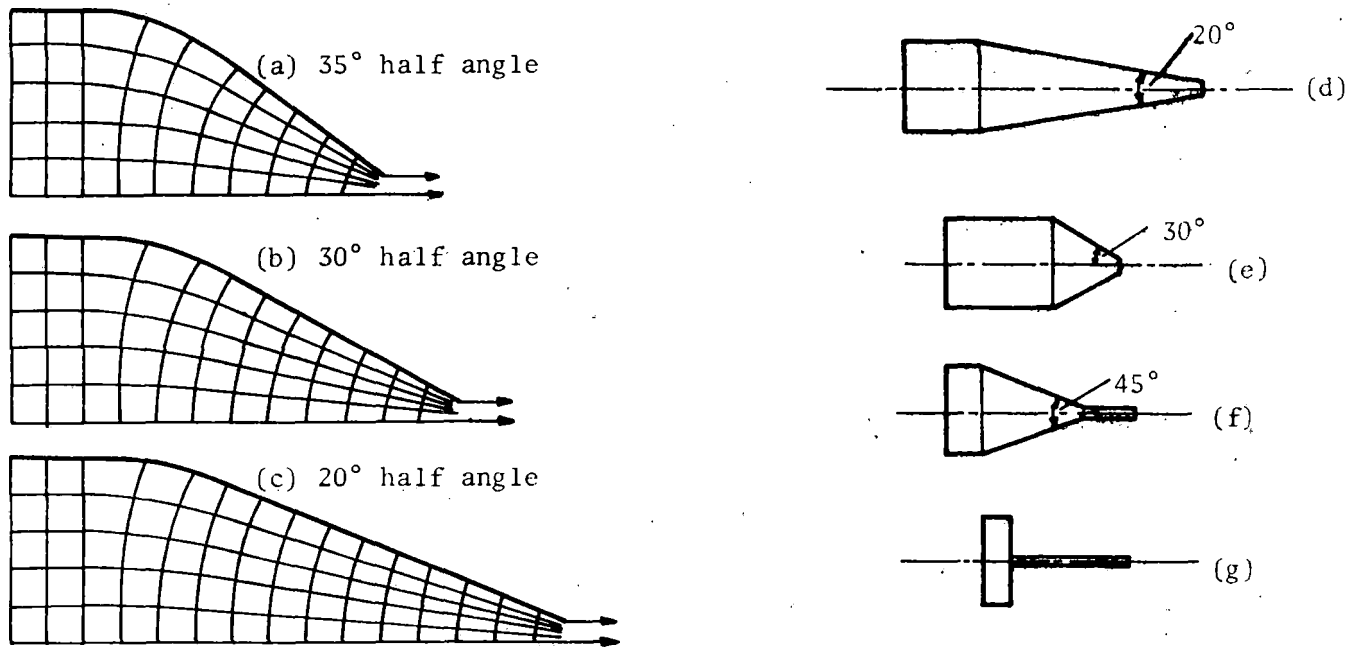


Fig. 3-23. Nozzle designs. (a) to (c) streamline nozzle designs, (d) unstreamlined nozzle design, (e) to (g) experimental profiles. (Farmer).

TABLE 3-3

Nozzle Device	Max. Jet Length (m)
a	0.60
b	0.55
c	0.65
d	0.60
e	0.40
f	0.25
g	0.20

Zelenin

Investigators in the USSR (Ref. 20) used smaller entrance angles in their nozzles, i.e., from 9° to 13°, with the cylindrical section at the exit about two diameters in length (Fig. 3-24). Nozzles of the diameters shown in Table 3-4 were tested for effect on slotting of rock. (See also Fig. 4-11).

TABLE 3-4

Orifice diameter mm	Cone angle degrees	Orifice Area mm ²
0.48	13	0.180
0.73	13	0.416
0.95	12	0.706
0.98	12	0.832
1.08	9	0.915
1.19	9	1.107

Voytsekhovskiy, et al.

One Russian group of researchers (Ref. 24) comments (without substantiating theory) that nozzles can be designed in accordance with the relation

$$p = \frac{k}{d^4} \quad (3-38)$$

where

p = pressure

k = a design constant

d = diameter

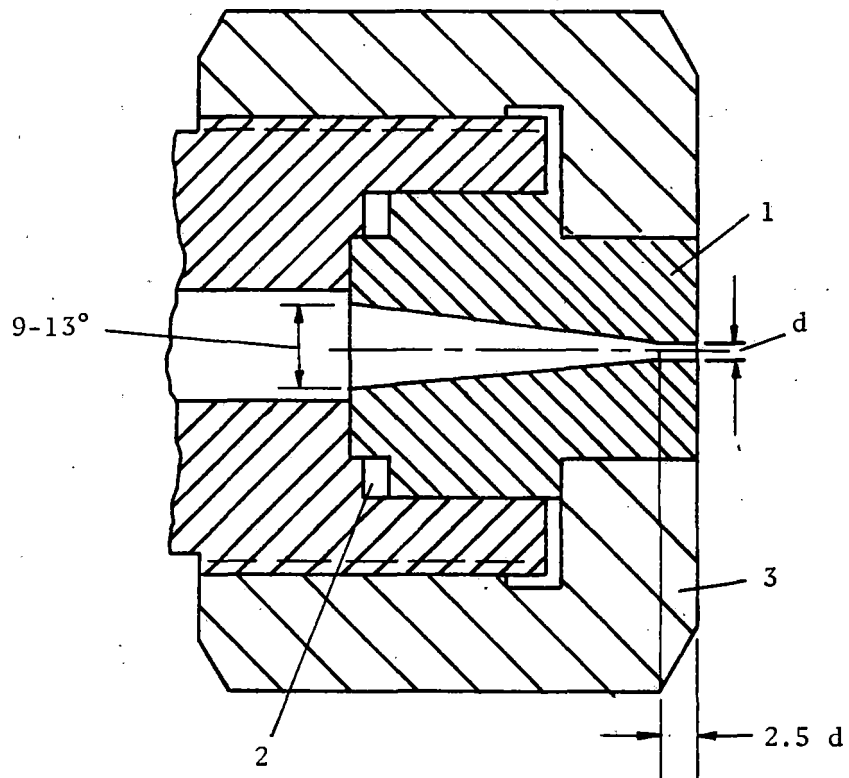


Fig. 3-24. Nozzle for single slots and method for packing. (Zelenin).

1. Orifice
2. Packing washer (Cu, Al)
3. Nozzle housing

Vereshchagin, et al., (Ref. 25)

To approximate the effects of friction in small nozzles water was collected and its temperature measured after flow through four sizes of nozzles at varying pressures to 2000 atm. Nozzle effects are small below 700 atm (Figs. 3-25 and 3-26). It was concluded that nozzle friction may be neglected for diameters larger than 1.25 mm or below 700 atm pressure. Friction loss is dependent upon diameter and pressure.

Schweitzer

In a study of sprays Schweitzer (Ref. 26) states that laminar flow through nozzles is not likely to occur in nonviscous fluids, and consequently the Rayleigh theory is not applicable. He also concluded that, in high pressure sprays (up to 4000 psi) into atmospheres to 200 psi, viscosity is recognized as having a decisive influence on jet disintegration. For the sprays tested the surface tension had a minor effect.

Summary - Nozzles

A variety of nozzles has been tested by British and Soviet investigators. The latest tests by both groups indicate that for capillary jets the entrance angle should be about 13° followed by a cylindrical section about two diameters in length. Some tests were conducted using streamline profiles, but these are too difficult to machine in such small nozzles. American designs of nozzles have not been published.

COMPRESSORS

Konyashin gives detailed descriptions of two types of hydrocompressors which have been used in Russia for research in cutting rocks, the first

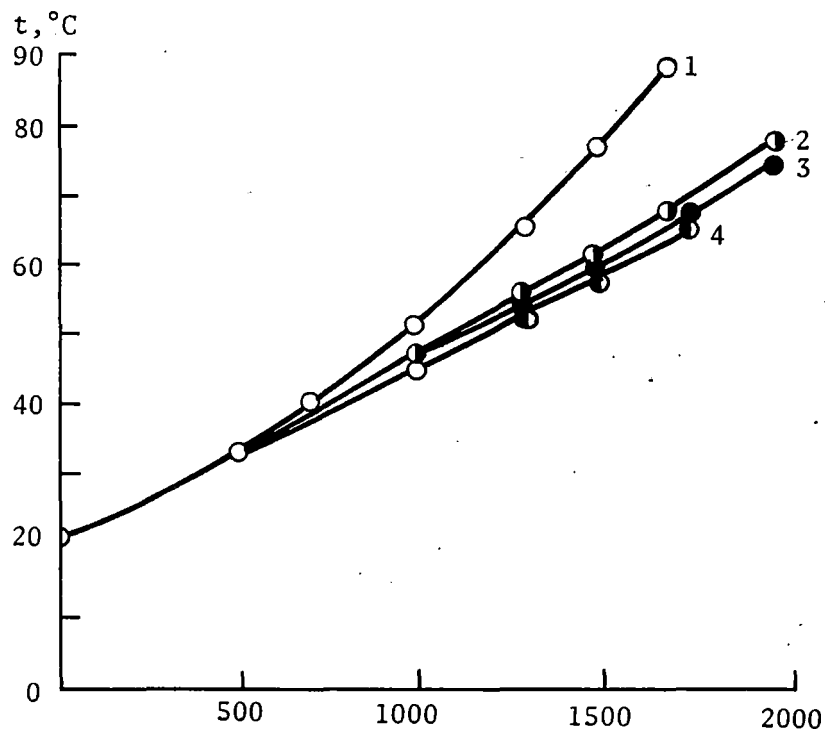


Fig. 3-25. Temperature of water vs. reservoir pressure for nozzle sizes: 1) $d = 0.47$ mm; 2) 0.8 mm; 3) 1.0 mm; 4) 1.25 mm. (Vereshchagin).

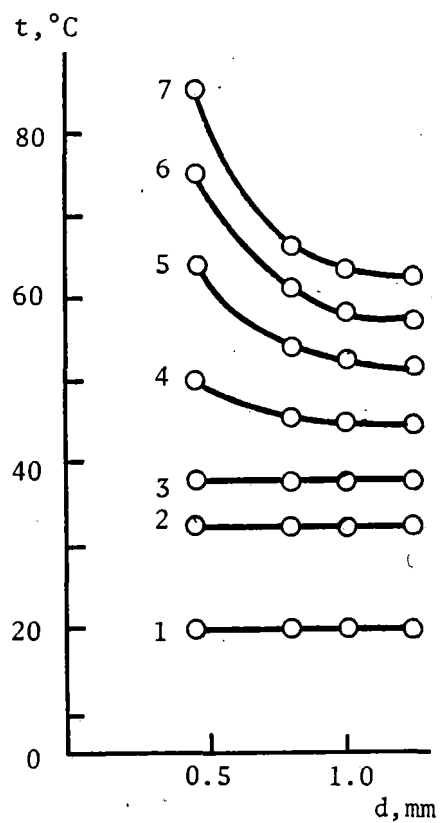


Fig. 3-26. Temperature of water versus nozzle diameter for seven pressures: 1) $p = 1$ atmos; 2) 500 atmos; 3) 700 atmos; 4) 1000 atmos; 5) 1300 atmos; 6) 1500 atmos; 7) 1700 atmos. (Vereshchagin).

being type K-17, a single cylinder, 1000 atm, 1000 liter/hr machine. The type GK 2/2 is a one-step, three cylinder machine of twice the capacity and pressure (see Table 3-5). A pressure multiplier was also employed in some experiments (Ref. 27).

The K-33 hydraulic compressor was used by Vereshchagin (Ref. 14) and is described as a one cylinder piston machine of 980 strokes per minute, diameter 33 mm and length of stroke 20 mm. The whole is powered by a 240 kw motor.

Leach and Walker (Ref. 10) used a 90 hp motor to drive a pump of 45 l/min capacity at a pressure of 600 atm. For pressures to 5000 atm a pressure multiplier was used.

WATER JET PRODUCTION

In addition to the compressors described above, which operate in conjunction with a reservoir or receiver, several types of mechanisms are employed to create high velocity water jets. These include pressure multipliers, "ballistic stand" water cannons, hydraulic rams and other devices. Most large scale tests have been conducted in the USSR.

Ostrovskii

Ostrovskii (Ref. 28) summarized much of the Russian research that had been done to 1960. The first Russian experiments in breaking rock with liquid jets (2 mm diameter) indicated that pressures as high as 4000 kg/cm^2 with energy requirements of 1500 horsepower for continuous jets were needed. This figure was considerably reduced for intermittent jets.

TABLE 3-5

Specifications of the Hydrocompressor KG-2/2

Number of cylinders	3
Bore diameter in mm	22
Stroke in mm	60
Crankshaft, rpm	735
Capacity of hydrocompressor in ℓ /hr	2000
Pressure maximum in atm	2000
Electromotor, asynchronous, type AM6-138-8: Power in kilowatt	245
Pressure at the inlet pipe branch, guaranteed by auxiliary pump in atm	3-10
Pumping liquid - filtered water with the $t^\circ = 20^\circ$ Weight, in kg:	
Hydrocompressor	1500
Electric motor	2100
Whole aggregate	4500

Specifications of Hydrocompressor K-17

Number of cylinders	1
Bore diameter in mm	22
Stroke in mm	70
Crankshaft, rpm	975
Capacity of hydrocompressor in ℓ /hr	1000
Pressure, maximum in atm	1000
Electromotor power, kilowatt	95
Electromotor, rpm	975

The latter type of flow was also generated by means of a "ballistic" stand. Combustion of burning powder or liquids developed pressures (Fig. 3-27) from 3000 to 8000 kg/cm² which in turn created a 2 mm diameter jet (100 ml) which cut a hole through several millimeters of metal. Typical pressure time records indicate chamber pressure of 6350 kg/cm² and impact pressure of 3420 kg/cm² (Fig. 3-28). The liquid fuel, oxidizing agent and water are pressure fed into the chamber by pistons measuring predetermined amounts of each. Frequency stated to be in tens of cycles per minute.

A mechanical pressure multiplier has also been employed. It consists primarily of a hydraulic pump with a pneumatic drive (Fig. 3-29) using a standard pressure multiplier design. It creates a jet at 5000 kg/cm², two cycles per minute, or 1000 kg/cm² at 75 cycles per minute. Arrangements are suggested for using both types of devices in the bottoms of deep drill holes.

Vereshchagin, et al.

Jet experiments were carried out assuming that the water pressure from a compressor was constant (Ref. 29). Actual pulsations of the compressor stroke and the damping effect of the reservoir and compressibility of the water were desired.

Notations are:

p = pressure

t = time

d_n = diameter of nozzle

v = velocity through nozzle

d_p = diameter of piston

l = length of stroke of piston

w = speed of motion of piston

τ = time of single stroke

V = volume of reservoir

α = coefficient of compressibility of water

ρ = density of water

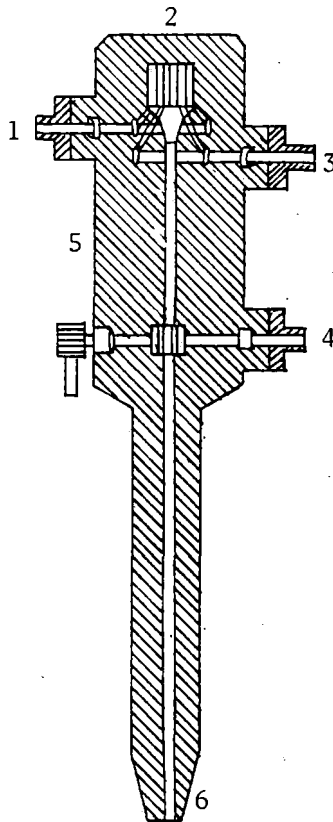


Fig. 3-27. Combustion chamber of the jet device. 1) Entrance for oxidizing agent; 2) combustion chamber; 3) entrance for fuel; 4) supply of water; 5) pressure transmitter; 6) nozzle. (Ostrovskii).

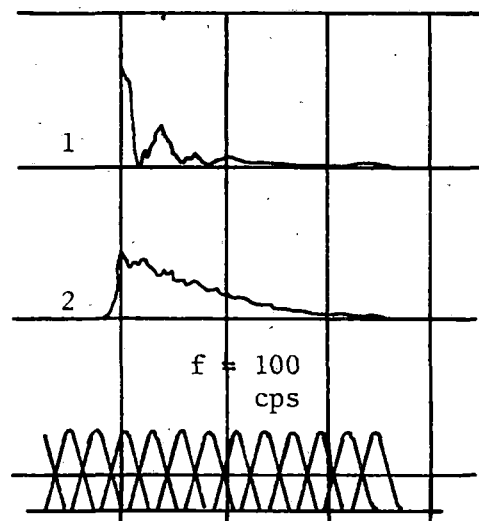


Fig. 3-28. Oscillograms of pressure. 1) In the combustion chamber of the ballistic stand ($P_{\max} = 6350 \text{ kg/cm}^2$); 2) in the high pressure liquid jet where it encountered the bar ($P_{\max} = 3420 \text{ kg/cm}^2$). (Ostrovskii).

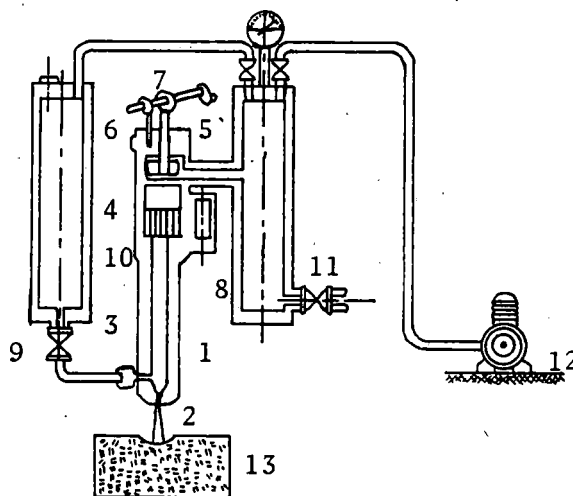


Fig. 3-29. Stand with mechanical pressure multiplier.. 1) High-pressure piston; 2) nozzle; 3) check valve; 4) low-pressure piston; 5) main valve; 6) escape valve; 7) cam shaft; 8) hydraulic shock absorber; 9) globe valve; 10) lubricator; 11) receiver; 12) compressor; 13) block of rock. (Ostrovskii).

The following equation may be written for the half-period of compression:

$$\frac{\pi d_p^2}{4} w dt = \frac{\pi d_n^2}{4} v dt + \alpha V dp \quad (3-39)$$

For the suction period the left side of the equation is zero.

The following simplifying approximations are made: The nozzle velocity is assumed to be constant across the cross-sectional area, and equal to $14\sqrt{p}$. The speed of the piston is assumed constant and $w = 2\ell/r$. Finally,

$\alpha = \frac{1}{c} \left(\frac{\partial p}{\partial \rho} \right) \tau$ is taken as 0.035×10^{-3} . For 1000 rpm equation (3-39) takes the following form:

$$100 \pi d_n^2 dt + \frac{V dp}{\sqrt{p} - 0.16 d_p^2/d_n^2} = 0 \quad 0 \leq t \leq \frac{1}{32} \quad (3-40)$$

$$100 \pi d_n^2 dt + \frac{V dp}{\sqrt{p}} = 0 \quad \frac{1}{32} \leq t \leq \frac{1}{16} \quad (3-41)$$

and the solutions are:

$$50\pi d_n^2 t + V\sqrt{p} = 0.16 \frac{D^2}{d^2} V \ln \left| \sqrt{p} - 0.16 \frac{D^2}{d^2} \right| = c_1 \quad (3-42)$$

$$50\pi d_n^2 t + V\sqrt{p} = c_2 \quad (3-43)$$

Results of calculations for various parameters are given in Tables 3-6 and 3-7. For a given reservoir pulsations increase with both d_p and output. Percentage variations of pressure decreased with the magnitude of the total pressure. On the other hand pulsations decrease markedly with increase of reservoir volume. Experimental results are given in Figs. 3-30 and 3-31

TABLE 3-6

P_{\max}	P_{\min}	$\frac{P_{\min}}{P_{\max}}$	P_{av}	Δ_p	$\frac{\Delta p}{P_{\text{av}}}, \%$
D = 22 mm					
1690	1310	0.775	1550	± 190	± 12.7
2475	2095	0.848	2285	± 190	± 8.1
D = 27 mm					
1925	1355	0.705	1640	± 285	± 17.4
D = 30 mm					
2160	1460	0.675	1810	± 350	± 19.3
D = 33 mm					
1925	1075	0.558	1500	± 425	± 28.3
3095	2245	0.726	2670	± 425	± 15.9
D = 38 mm					
2570	1430	0.556	2000	± 570	± 28.5
3570	2430	0.681	3000	± 570	± 19.0

TABLE 3-7

 $d_p = 38 \text{ mm}$ $p_{\max} = 2000 \text{ kg/cm}^2$

V	P_{\min}	$\frac{P_{\min}}{P_{\max}}$	P_{av}	Δ_p	$\frac{\Delta p}{P_{\text{av}}}, \%$
1	870	0.43	1430	± 570	± 0.28
2	1430	0.71	1710	± 290	± 0.14
4	1720	0.86	1860	± 140	± 0.07
6	1810	0.90	1900	± 100	± 0.05
10	1890	0.94	1940	± 60	± 0.03

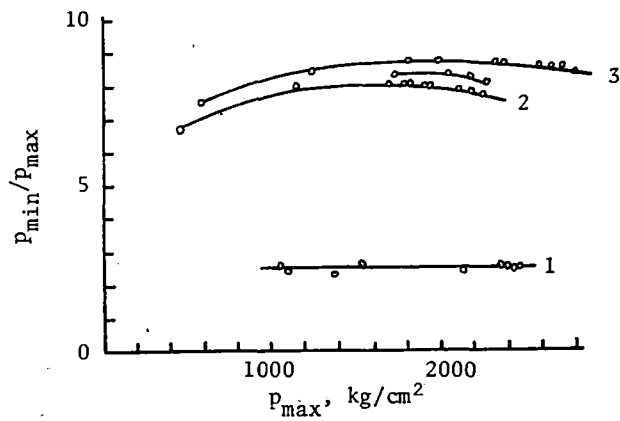


Fig. 3-30. Dependence of $\frac{P_{min}}{P_{max}}$ on the pressure for various reservoir volumes. 1) 1 l; 2) 3.3 l; 3) 4 l; 4) 5.85 l. (Bowles Eng. Corp.).

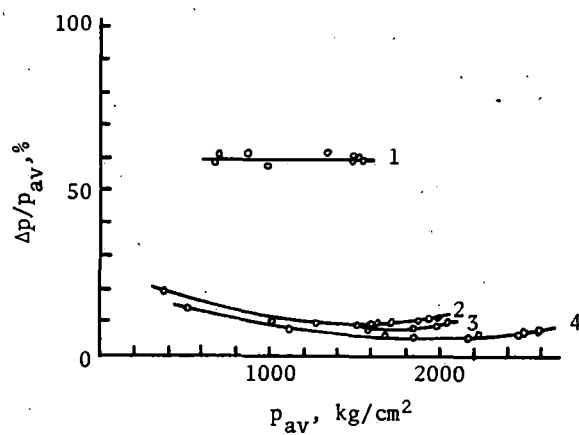


Fig. 3-31. Dependence of $\frac{\Delta p}{P_{av}}$ % on the pressure for various reservoir volumes. 1) 1 l; 2) 3.3 l; 3) 4 l; 4) 5.85 l. (Bowles Eng. Corp.).

and a comparison with theoretical calculations shows a fair agreement for pressure and volume relationships (Figs. 3-32 and 3-33). Some of the difference is probably due to the simplifying assumptions made in the solution of the equation.

Semerchan and Plotnikov

These investigators (Ref. 30) describe an apparatus which has a free liquid (oil) jet blow-out at a velocity of 2000 m/sec and higher. It consists essentially of a pressure multiplier with two coaxial cylinders with a multiplication coefficient of 25, a useful volume of the high pressure chamber of 1.57 cm³ and a burst diaphragm for oil release in the low pressure cylinder.

After the diaphragm bursts, the piston moves irregularly for 0.01 sec, compressing the oil to a given pressure and density, 5 percent of the oil leaking through the nozzle. A period (0.05 to 0.14 sec) of uniform piston movement and fluid flow follows. The true values lie between those calculated from Bernoulli's equation and a flow calculated on the basis of constant preflow density, i.e., $p = c \exp B \rho_o$, where p is pressure, B and c are constants determined from Bridgman's high pressure data and ρ_o is the preflow oil density. The microcanal of the nozzle has a length to diameter ratio of one.

Cooley

Perhaps the most complete description of jet producing mechanisms has been published by Cooley (Ref. 31). Several methods of producing jets of water, semi-solids such as wax, and metallic particles have been studied for various purposes.

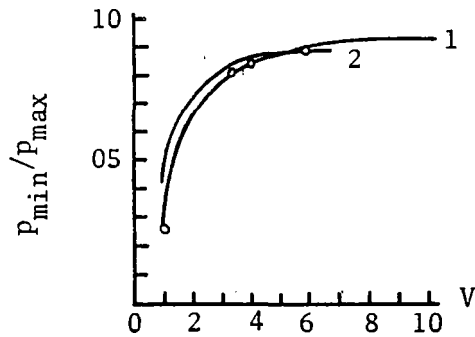


Fig. 3-32. Dependence of $\frac{P_{\min}}{P_{\max}}$ on the volume of the reservoir.
 1) theoretical; 2) experimental. P_{\max} 2000 kg/cm².

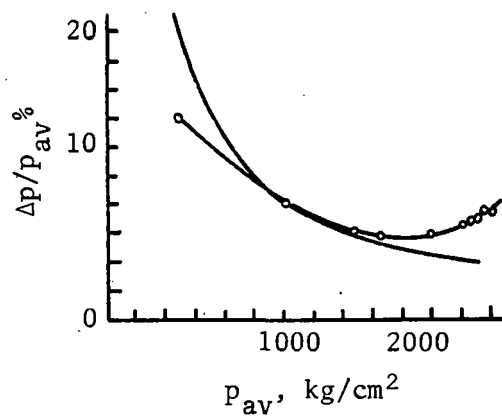


Fig. 3-33. Dependence of $\frac{\Delta p}{P_{av}}$ % on the working pressure. 1) theoretical; 2) experimental. $V = 5.85$ liters.

Water jets are produced by means of compressors, water cannons, and hydraulic ram jets. Jets of wax are produced by impacting a semi-hollow, confined cylinder by a piston, causing the cylinder to collapse and form a jet from the "lining" of the cavity, by means of cumulation. Cooley, et al., classify the methods of producing liquids jets as:

- (a) Piston impact extrusion - water cannon
- (b) Cumulation - jets from cavities (see Chapter VI)
- (c) Water hammer (hydraulic ram)

One form of water cannon has a large piston in a heavy cylinder, with or without a small diameter plunger on the downstream side of the piston, (Fig. 3-34). The piston is accelerated by an explosive charge or pneumatic force, and when it impacts the water a shock wave is produced both in the piston and the water, the latter being reflected back and forth in the water until extrusion is complete, and the piston has stopped or rebounded.

The extrusion process can be analyzed by means of four different models, (1) full crush, (2) half crush, (3) piston impact with no air and (4) piston impact with air.

In the full crush case shock waves, negligible water escape is assumed, and after impact a shock is initiated and multiply reflected. At peak pressure the piston stops, and the pressure is assumed to be the same as in steel impact on a rigid target:

$$P_R = \rho_s v_o^2 D_s \approx \rho_s v_o^2 c_s \quad (3-44)$$

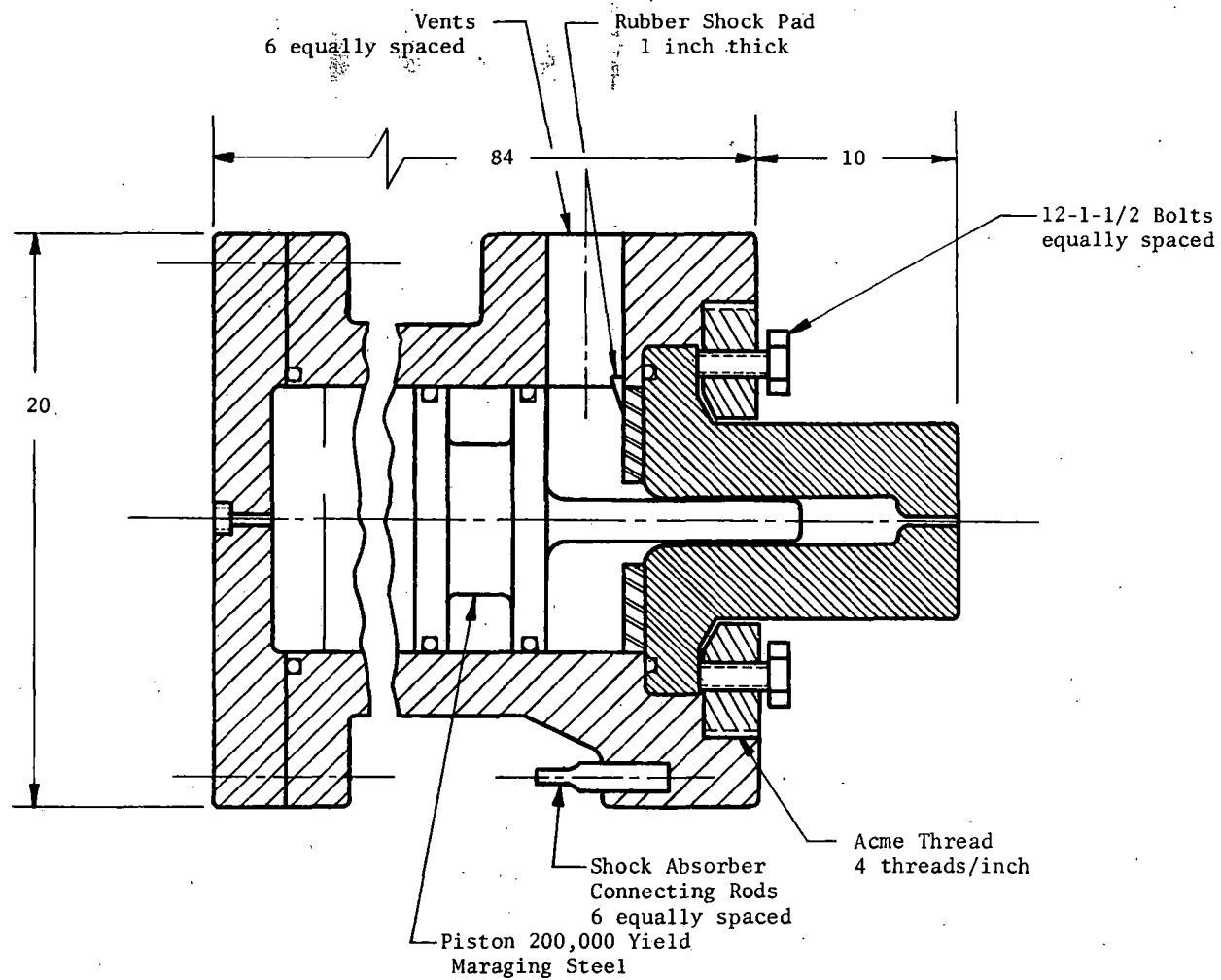


Fig. 3-34. Exotech Incorporated Hydraulic Cannon. (Cooley).

where

ρ_s = density of steel

v_o = impact velocity

D_s = shock velocity in steel

c_s = speed of sound in steel

Steady flow from the nozzle is found in terms of enthalpy:

$$\frac{u_o^2}{2} + h_o = h_r \quad (3-45)$$

where

h_o = enthalpy at 1 atm pressure

h_r = enthalpy at reservoir pressure

The equation of state for water is of the form

$$\frac{p + 3000}{3000} = \left(\frac{\rho}{\rho_o} \right)^7 \quad (3-46)$$

which gives

$$\frac{u_o^2}{c_o^2} = \frac{1}{3} \left[\left(\frac{p_r + 3000}{3000} \right)^{6/7} - 1 \right] \quad (3-47)$$

where

c_o = velocity of sound in H_2O at one atm.

For the half crush case the pressure is assumed to be that of steel on steel

$$p_r = \rho_s \frac{v_o}{2} D_s \approx \rho_s \frac{v_o}{2} c_s \quad (3-48)$$

The reservoir has a residual velocity of $v_0/2$ after piston impact and the velocity of the jet is given by

$$v_j = u_0 + \frac{v}{2} \quad (3-49)$$

where u_0 is defined in equation (3-47). For piston velocities up to 300 ft/sec jet velocities for full crush conditions are greater than half crush, but less than the velocity of cumulation jets for the same piston velocity (Fig. 3-35). The relationships between pressures and velocities also appear to favor cumulation. (Figs. 3-36 and 3-37).

For analysis of the more practical case of piston water impact with no air in the cylinder the hydrodynamic theory for the full and half crush cases is extended. Here the relative volume of water and areas of the nozzle are larger, and the piston may have some residual velocity. (See Appendix C).

The Exotech water cannon (Ref. 31) consists of a heavy cylinder 84 inches long with a piston of 200,000 psi yield maraging steel (Fig. 3-34). It is powered by water at pressure of 200 to 2000 psi. The water cocks a pneumatic gun and compresses enclosed gas. At the desired pressure the nozzle and vent valves are opened, the moving piston entraps a small quantity of water ahead of the plunger and extrudes it through the nozzle. Losses occur due to throttling of inlet water and escape of water when the piston is accelerated. Efficiencies are not reported, although they are said to be relatively high if the residual velocity of the piston approaches zero.

An approximate work analysis is made neglecting the loss due to water throttling. However, it was assumed that most compression processes are linear and that average pressures and velocities can be employed as first approximations. This ignores the necessity of assuming an equation of state

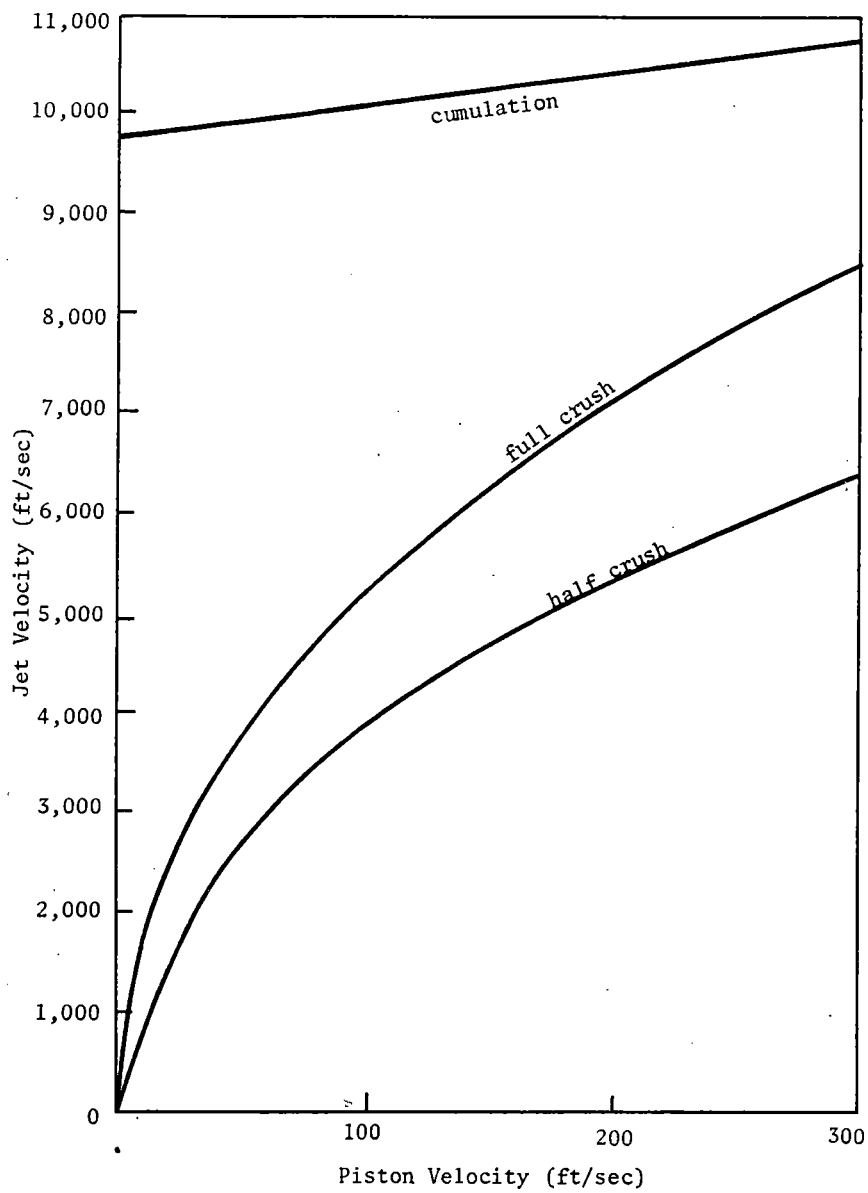


Fig. 3-35. Jet velocities attainable. (Cooley).

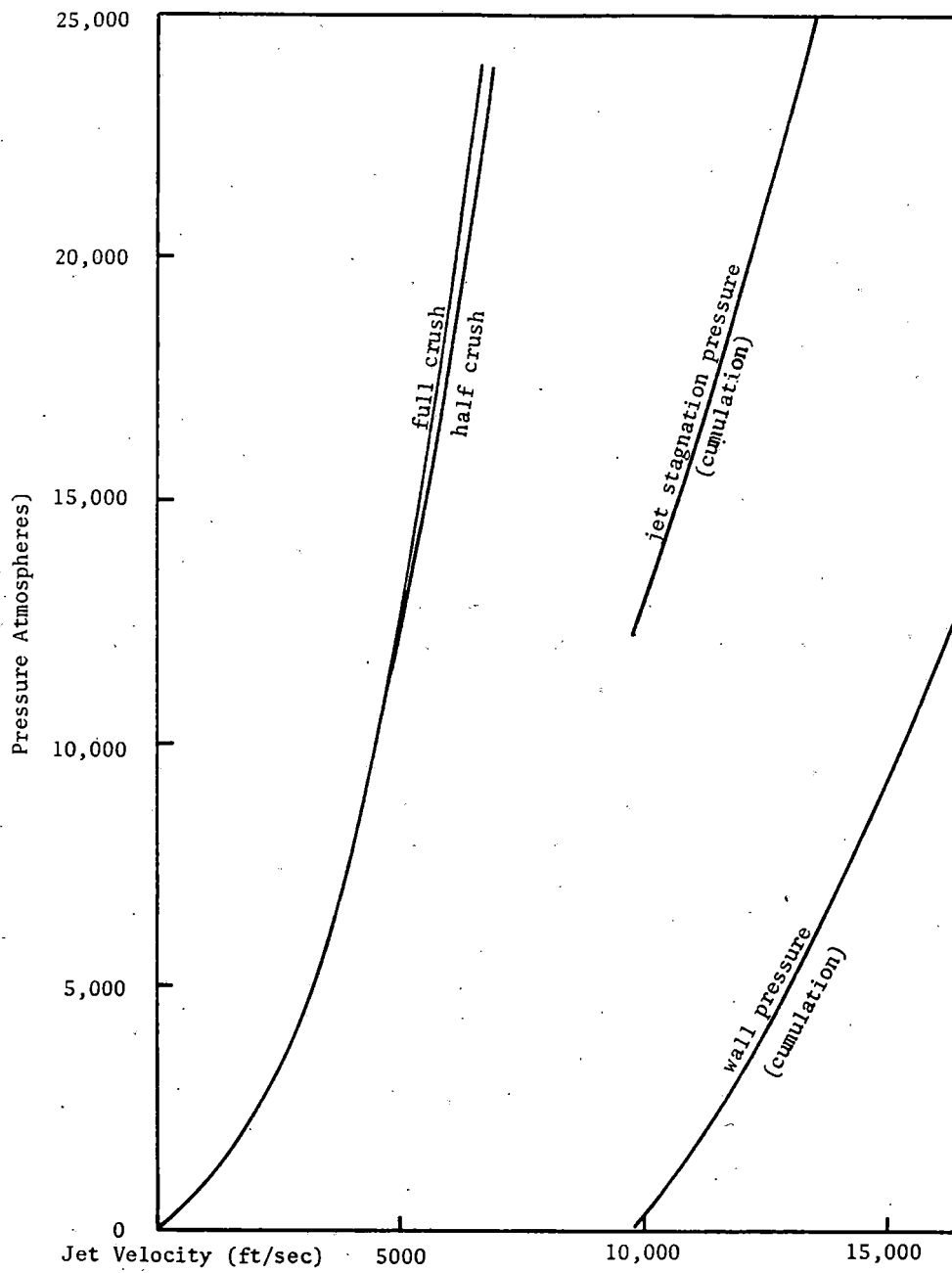


Fig. 3-36. Pressures attainable versus jet velocity. (Cooley).

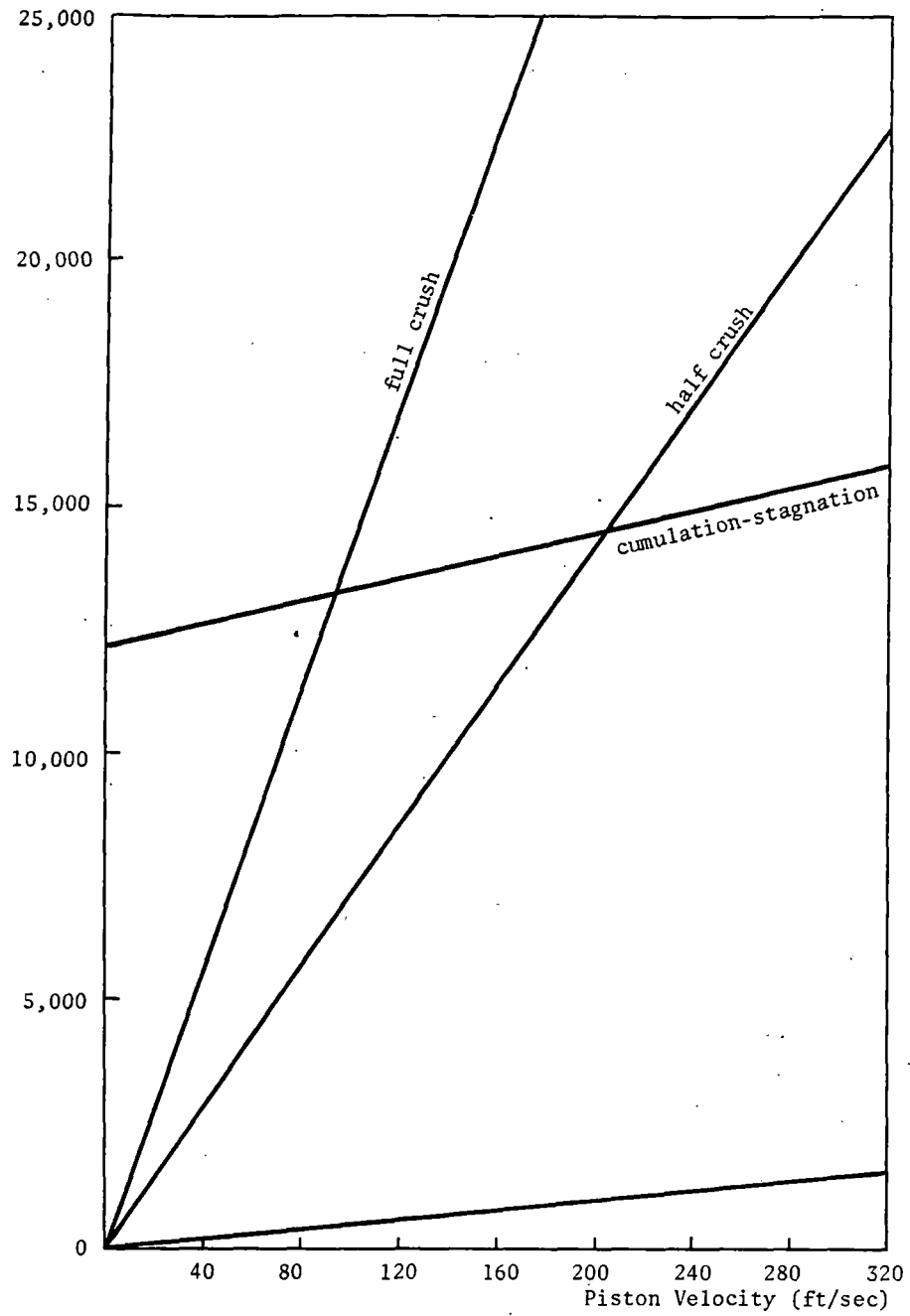


Fig. 3-37. Pressures attainable versus piston velocity. (Cooley).

for both gas and water, and does not take heat losses into account. An average velocity is assumed for the jet, which is a possible source of large error. Inasmuch as kinetic energy varies as the velocity squared, an average velocity concept appears subject to considerable error. Average pressures likewise have little significance unless the compression process is linear in the necessary parameters. Efficiencies in the processes indicated never approach high percentages. Hence, the final estimate that 200 horsepower stored in compression could yield 100,000 horsepower in a jet is also subject to some question.

The Exotech Hydro-Ram (Ref. 31) consists of a thick rigid cylinder with a nozzle at one end which has a spring-loaded valve that oscillates during operation. It opens large ports, closes them, opening a small port through which water passes under the water hammer pressure. A model built by Exotech with an inlet pressure of 70 psi delivered 5 to 10 pulses per second at 600 psi through a 1/16 nozzle. It is claimed that the supply pressure may be scaled up to 30,000 psi and the jet pressure 145,000 psi for the Hydro-Ram, in which five times more water is pumped than expelled.

The repetition rate theoretically depends on the time to establish flow at 1255 ft/sec in a pipe 0.07 inches in diameter and 10 feet long. A 6 gpm pump would be required at 30,000 psi and 125 hp.

A water hammer extrusion is also described which involves firing a slug of water at high velocity against a constriction with a nozzle escape. According to calculations a slug water pressure of 53,000 atm with a slug velocity of 4,000 fps would result in a jet velocity of 9300 ft/sec.

Cooley, et al. (Ref. 31) conducted (piston-impact) experiments with a 20 mm gun to fire pistons of 4.41 and 9.42 inch lengths on an enclosed volume of water (Fig. 3-38) at velocities to 490 ft/sec. Measured peak water chamber pressures were as high as 50,000 to 100,000 psi and durations of 0.56 to 0.7 ms. Wood, rock and concrete targets were used and small craters were made in brittle materials with tensile fractures and spallation around the craters.

An approximate method of calculating expulsion efficiency is also presented (Ref. 31). Given area ratios, jet pressure, pulse and piston velocity, the period of the pulse above the critical (crushing) pressure is calculated. The pulse is then approximated by a parabola and the energy of the piston and the jet calculated. For assumed experimental conditions it was found that the propulsion efficiency varied between approximately 47-59 percent.

Jet pressure and power are calculated as follows (Ref. 31). For high pressures the relationship between reservoir pressure p_0 and jet velocity is to a very close approximation:

$$p_0 = \frac{\rho v_j^2}{2g} = q \quad (3-50)$$

where q is the dynamic flow pressure. It is approximately equal to the stagnation pressure except for rapid rates of penetration.

The rate of mass flow is the velocity times the effective cross sectional area of the nozzle or

$$m = \rho \pi \frac{d^2}{4} v \quad (3-51)$$

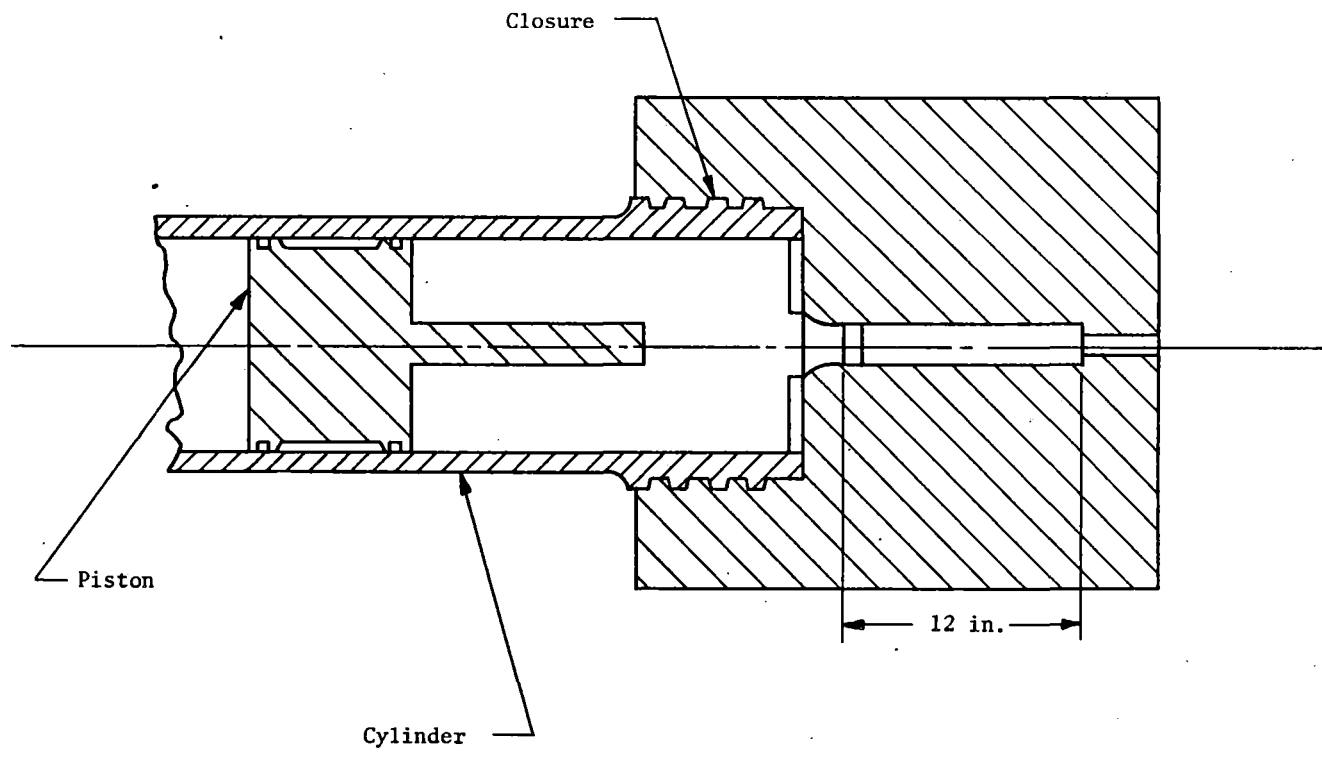


Fig. 3-38. Sketch of two diameter piston impact extrusion section for large water cannon. (Cooley).

The rate of kinetic energy or power becomes

$$N_j = \frac{mv^2}{2g} = \frac{\rho \pi d^2 v^3}{8g} = \frac{\pi \sqrt{2}}{4} \left(\frac{g}{p}\right)^{\frac{1}{2}} d^2 \rho_o^{3/2} \quad (3-52)$$

Thus, for a 2 mm jet at 70,000 psi requirements are in excess of 2000 hp for continuous operation.

FLUID JET AUGMENTATION

The Bowles Corporation (Ref. 32) has conducted research on external augmentation of jets of water by shaping and fixing the relative directions of two water "slugs" of square cross-sections and plane fronts. (Fig. 3-39).

Application of Bernoulli's theorem gives:

$$v_j = v_a + v_r \quad (3-53)$$

and

$$v_a = \frac{v_o}{\sin \alpha} \quad (3-53a)$$

$$v_r = \frac{v_o}{\tan \alpha} \quad (3-53b)$$

Substituting in equation (3-53) the following is obtained:

$$\frac{v_j}{v_o} = \frac{1 + \cos \alpha}{\sin \alpha} \quad (3-54)$$

where

v_o = velocity of slug

v_r = velocity of slug relative to moving intersection

v_a = velocity of intersection

v_s = velocity of fast jet

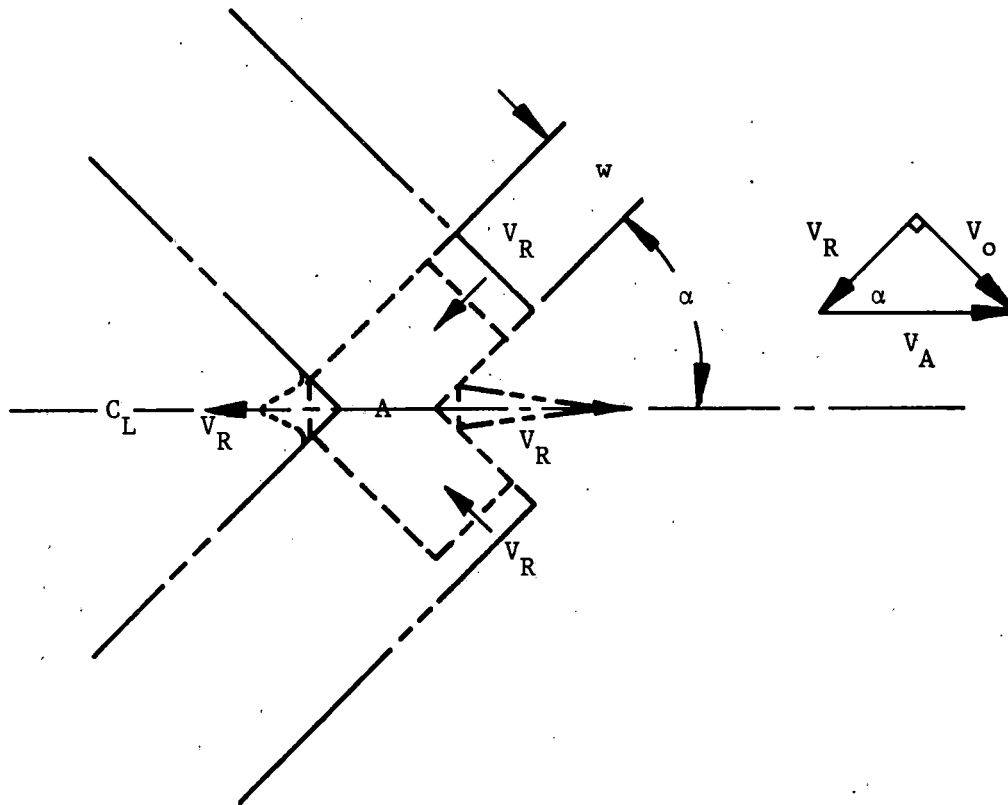


Fig. 3-39. Control volume - early stage of impact. (Bowles Eng. Corp.).

The ratio of the two velocities is called the velocity augmentation and is plotted as a function of the angle α in Fig. 3-40. The resulting jet is wedge-shaped and for complete jet formation the slug velocity must be inward almost linearly with the impact angle. (Fig. 3-41). The mass of the jet is given by

$$m_j = \frac{\rho h b^2}{2} \tan \alpha (1 - \cos \alpha) \quad (3-55)$$

where

m_j = fast jet velocity

ρ = density

h = depth of the jet wedge

b = width of the jet wedge

The length of the slug needed is that required to permit formation of the wedge. A flat or only a slightly curved face of the slug is necessary for fast jet formation.

By simple calculations it can be shown that the ratio of the kinetic energies of the fast jet and the minimum required slug is given by:

$$\frac{KE_f}{KE_s} = \frac{1 + \cos \alpha}{4} \quad (3-56)$$

where

KE_f = kinetic energy of jet

KE_s = kinetic energy of slugs

The maximum value of this ratio is theoretically 0.5 at 0° impact and it decreases to 0.25 at 90° impact (Fig. 3-42). No fast jet is formed at 0° and 90° , however, so the graph is of interest between 5° and 60° . Thus, the maximum energy to be obtained from such a jet is only 50% under optimum

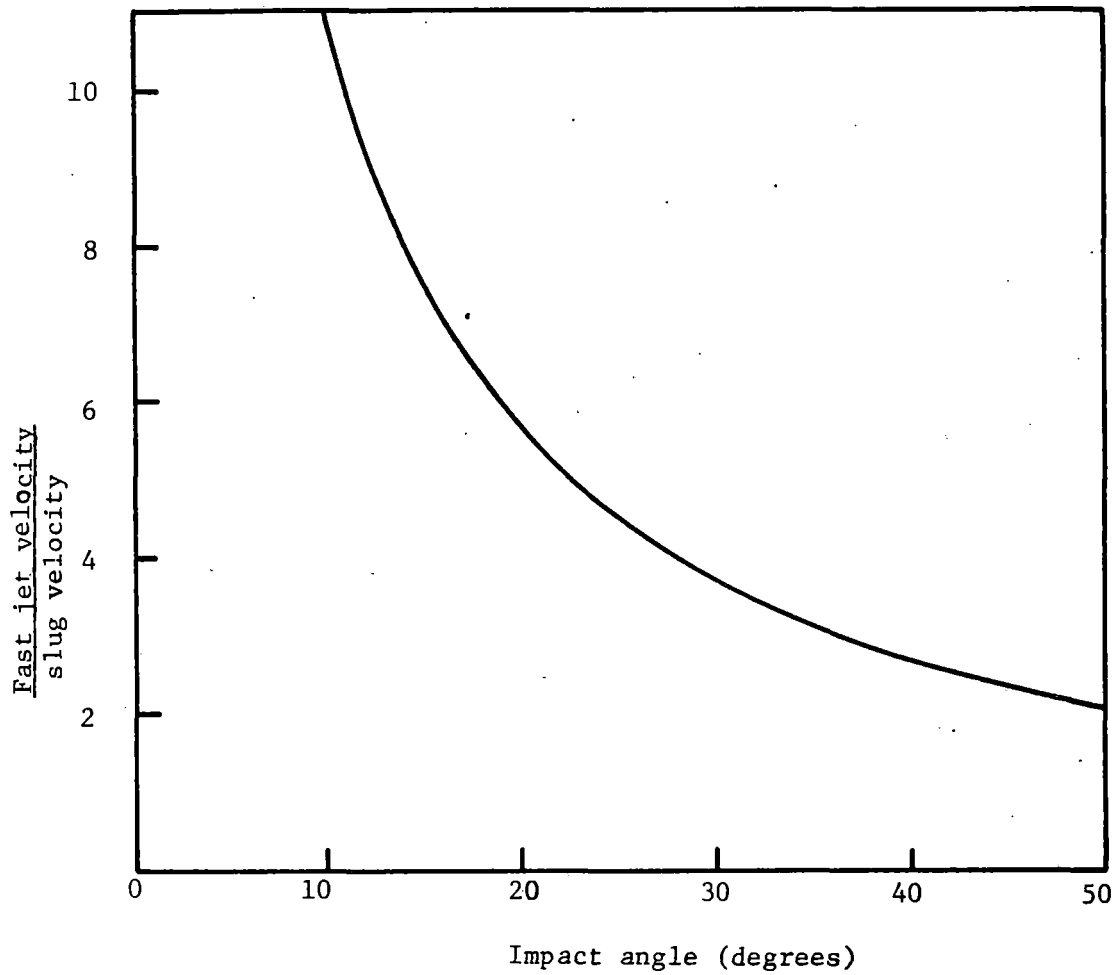


Fig. 3-40. Jet velocity augmentation vs. impact angle.
(Bowles Eng. Corp.).

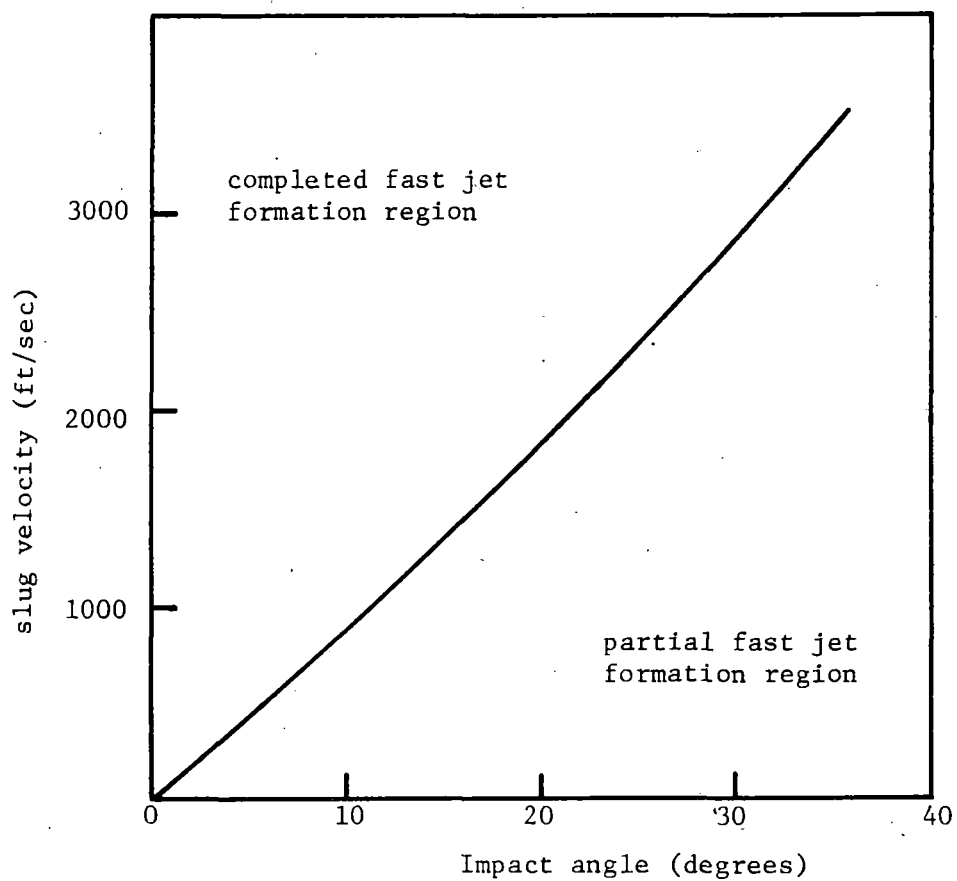


Fig. 3-41. Fast jet prediction for water. (Bowles Eng. Corp.).

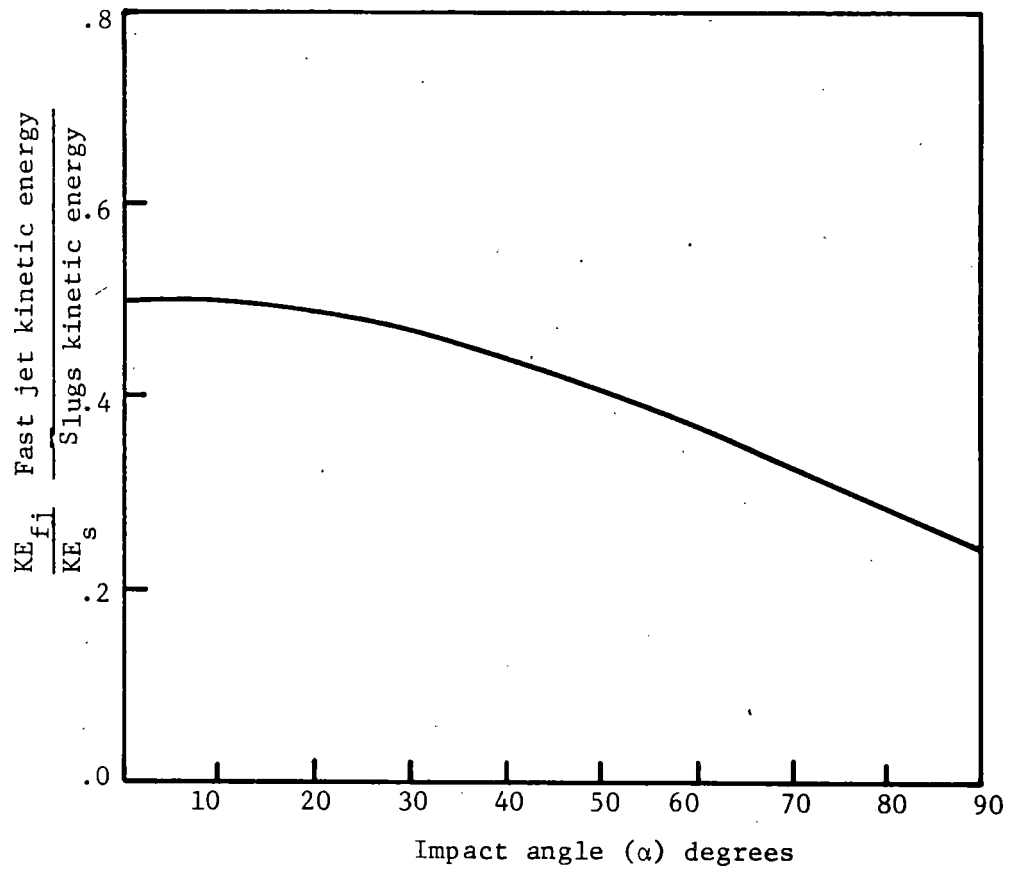


Fig. 3-42. Effect of impact α on the efficiency of delivery of kinetic energy to target. (Bowles Eng. Corp.).

conditions and it would be considerably smaller unless the slug producing mechanism could furnish slugs of just the right length. A special nozzle is required to produce slugs with flat faces. Driving pressures of 750 psi are reported giving augmentation ratios as high as 13.5. A ten degree nozzle was found to produce a velocity augmentation of 11.6 and the jet penetrated 3/4 inches of paraffin. Driving pressures or energy requirements were not reported.

HIGH PRESSURE FREEZING OF WATER

Although some investigators have proposed that water will freeze when shocked at high pressures, a study of p-V data and shock Hugoniot indicate that freezing will not take place under some conditions (Ref. 31).

Results of Bridgman's high pressure p-V-T measurements on water (Ref. 33) were plotted in the p-V and p-T planes with the Hugoniot from Walsh and Rice (Ref. 34).

The Hugoniot approaches the phase boundary of ice VII at about 30 kbars but does not intersect. Hence, it is concluded that ice will not form. In the p-T plane two isentropes are drawn from about 20°C and 38°C. These intersect the ice VI phase line at 16 and 27 kilobars. The actual path of non-shock compression is between the isentrope and the Hugoniot. Freezing may occur, therefore, at 16 kilobars or above. Preheating the water or addition of antifreeze would raise the freezing pressure. The heat of compression would also be of some assistance in reducing freezing.

Snay and Rosenbaum

Snay and Rosenbaum (Ref. 35) have made an analysis of shock wave parameters in fresh water up to 95 kilobars in connection studies of detonation of high explosives under water.

It is noted that for the Rankine-Hugoniot relations to be evaluated the equation of state must be known. Equations of state proposed by several investigators for different ranges of pressure are discussed. Some considered the possibility of the formation of ice at high pressures. The following has been abstracted in detail from Snay and Rosenbaum.

Calculation of Shock Front Parameters

The hydrodynamic conservation equations are written in the following form:

$$D = v_o \left[(p-p_o) / (v_o - v) \right]^{1/2} \quad (3-57)$$

$$u = D(v_o - v) / v_o \quad (3-58)$$

$$H - H_o = 1/2(p - p_o)(v_o + v) \quad (3-59)$$

where

D = wave velocity

v = specific volume

p = pressure

H = enthalpy

and the subscript o refers to the undisturbed liquid. The enthalpy is a function of the final state only. For final temperatures above and below 100°C enthalpy differences can be found in steam tables. The remaining enthalpy is calculated from

$$H(p,T) - H(p_1,T) = \int_{p_1}^p \left[v - T \left(\frac{\partial v}{\partial T} \right)_p \right] dp \quad (3-60)$$

where p_1 is the pressure corresponding to a final temperature above 100°C. The above integral can be evaluated if the equation of state is known and if no phase change takes place. However, if a phase change takes place and ice VII is formed, i.e., the pressure and temperature p_3 and T_3 are on the phase line, then all the water is converted to ice. For partial formation of ice

$$H(p,T) - H(p_1,T) = \int_{p_1}^p \left[v - T \left(\frac{\partial v}{\partial T} \right)_p \right] dp - q\Delta H_f \quad (3-61)$$

where

q = fraction solidified

ΔH_f = specific enthalpy of fusion of ice VII at (p_3, T)

and the subscript 3 refers to the liquid-ice VII phase line.

The solution of equation (3-57) to (3-61) for no phase change requires a knowledge of thermal data for saturation at 1 atm and the equation of state of the liquid up to the final temperature and pressure. For two phases, liquid water and ice VII, the solution of equations (3-57, 3-58, 3-59, 3-60) requires the use of the phase line, the enthalpy of fusion, the specific volume change

(ΔV_f) accompanying the transition which is necessary in evaluating \underline{v} :

$$v = (1-q)v_\lambda + v_\Sigma \quad (3-62)$$

$$v_\Sigma = v_\lambda - \Delta v_f \quad (3-63)$$

where λ refers to the liquid state and Σ the solid state (ice VII).

For a single liquid phase equations (3-59 and 3-60) are solved for \underline{p} by iteration. For two phases both \underline{T} and \underline{p} must lay on the phase line, and equations (3-59 and 3-61) can be solved directly for \underline{q} . The specific volume \underline{v} is obtained from the equation of state and \underline{D} and \underline{u} from equations (3-57 and 3-58).

The compressibility or sound velocity behind the front can then be evaluated from the Rankine-Hugoniot conditions. For a liquid only

$$c = v \left[- \left(\frac{\partial p}{\partial v} \right)_s \right]^{1/2} = v \left[\frac{T \left(\frac{\partial p}{\partial T} \right)_v^2}{C_v} - \left(\frac{\partial p}{\partial v} \right)_T \right]^{1/2} \quad (3-64)$$

where the subscripts have their usual meaning.

The values of \underline{v} , \underline{T} , $(\partial p/\partial T)_v$ and $(\partial p/\partial v)_T$ are obtained from the equation of state, while C_v is obtained from

$$C_v = C_p - T \left(\frac{\partial v}{\partial T} \right)_p \left(\frac{\partial v}{\partial T} \right)_v \quad (3-65)$$

where

$$c_p \approx \left(\frac{\Delta H}{\Delta T} \right)_p \quad (3-66)$$

Thus, the values for $(H-H_0)$ are evaluated at the final pressure and different temperatures, and C_p is the slope of $(H-H_0)$ against \underline{T} .

For two phases the derivation of sound velocity is more complex and is not given here.

Extrapolation of p-V-T Data

The p-V-T data of Bridgman (Refs. 33, 36, 37, 38, 39) cover the range of 0-95°C up to 5000 kg/cm² and 25-175°C from 5000 to 50,000 kg/cm². Values for the liquid state above 200°C and to 2500 bars is given by Kennedy (Ref. 40) and that at the saturation line by Keenan and Keyes (Ref. 41).

The liquid-ice VII phase line may be extrapolated and equations for relationships between Δv_f and T_3 in terms of p_3 (Fig. 3-43). This does not account for the possibility of a new type of ice at higher pressures. The equations of state in p-V are projected from experimental data. The procedure to determine the curves is as follows:

The value of $(\partial v / \partial t)_p$ at 5000 kg/cm² is taken as being constant, 4.0×10^{-4} cc/g°C. This comes from Bridgman's data and is used to fix the lower ends of the 175°C and other isotherms. The extrapolations from Fig. 3-43 are used to obtain the points on the liquid phase line up through the pressure range to 50,000 kg/cm², the phase line for ice VII being determined from experimental data. The thermal expansion of ice is $\sim 1.07 \times 10^{-4}$ cc/g°C at 45,000 kg/cm² and the phase line temperature as shown. The specific volume of fusion is taken from Fig. 3-43 and this procedure establishes the phase line to 50,000 kg/cm² with reasonable accuracy.

Experimental values of specific thermal expansion (Fig. 3-44) are extrapolated assuming that at higher pressures it will decrease but remain positive. The change $(\partial^2 v / \partial T^2)_p$ becomes smaller, is assumed to be constant at 15,000

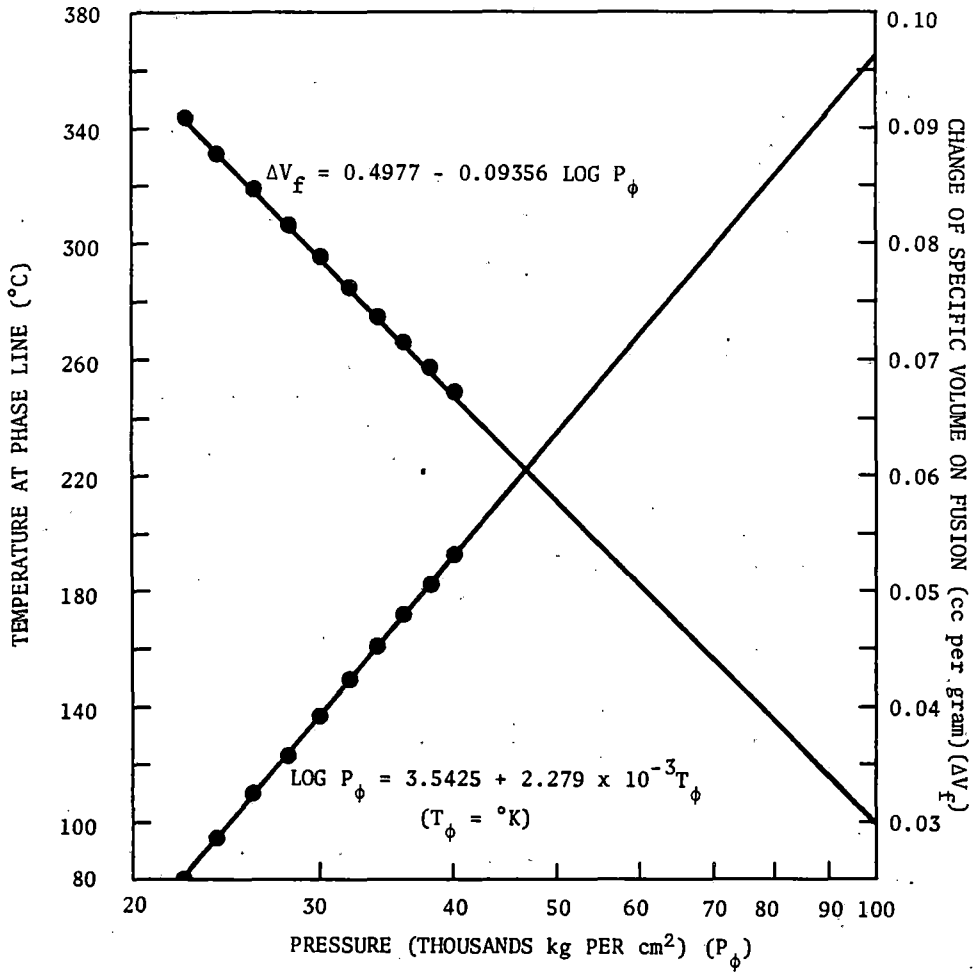


Fig. 3-43. Extrapolation of the temperature and the specific volume change of fusion at the liquid-ice VII phase line. Based on data from Ref. 30. (Snay and Rosenbaum).

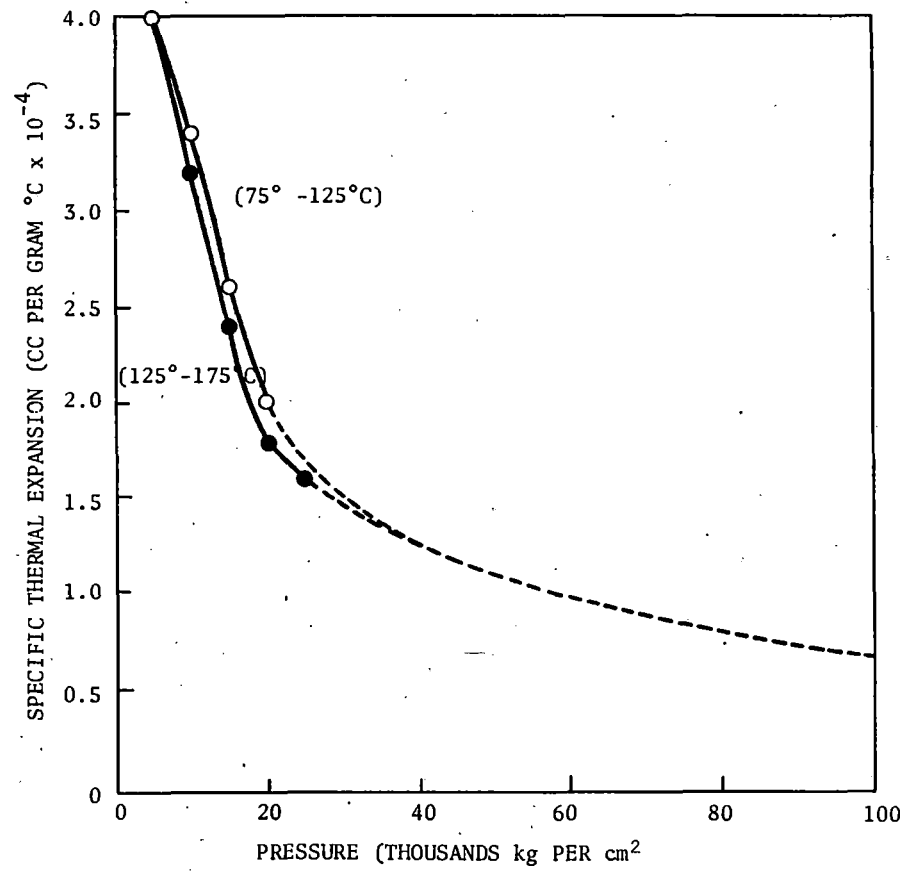


Fig. 3-44. Extrapolation of the specific thermal expansion (75-125°C and 125-175°C) as a result of the extrapolations of Figure 3-43.

kg/cm² and to become negligible above 40,000 kg/cm². These assumptions permit extrapolation of curves in Figures 3-44 and 3-45 to 40,000 kg/cm².

Further extrapolation is accomplished by projecting the isotherms as straight lines on a semi-log plot. The specific thermal expansion is expected to decrease, but to remain positive and independent of temperature. The extrapolation in Fig. 3-43 also gives the intersection of the isotherm and the phase line.

The following equations are used for the pressure ranges indicated:

- (1) From liquid at saturation pressure to 5000 kg/cm²

$$(v_2 - v) = \frac{2.303}{n} \log_{10} \frac{p+B}{p_2+B} \quad (3-63)$$

where B and n are functions of temperature only:

T(°C)	25	75	125	175	225	275
B	2,940	2,660	1,970	1,570	1,150	650
n	7.652	7.962	8.280	7.584	6.700	6.020
v ₂	1.0029	1.0258	1.0655	1.121	1.200	1.3175

- (2) Liquid between 5000 to 40,000 kg/cm²

$$(v_3 - v) = \frac{2.303}{n} \log_{10} \left(\frac{p+B}{p_3+B} \right) \quad (3-64)$$

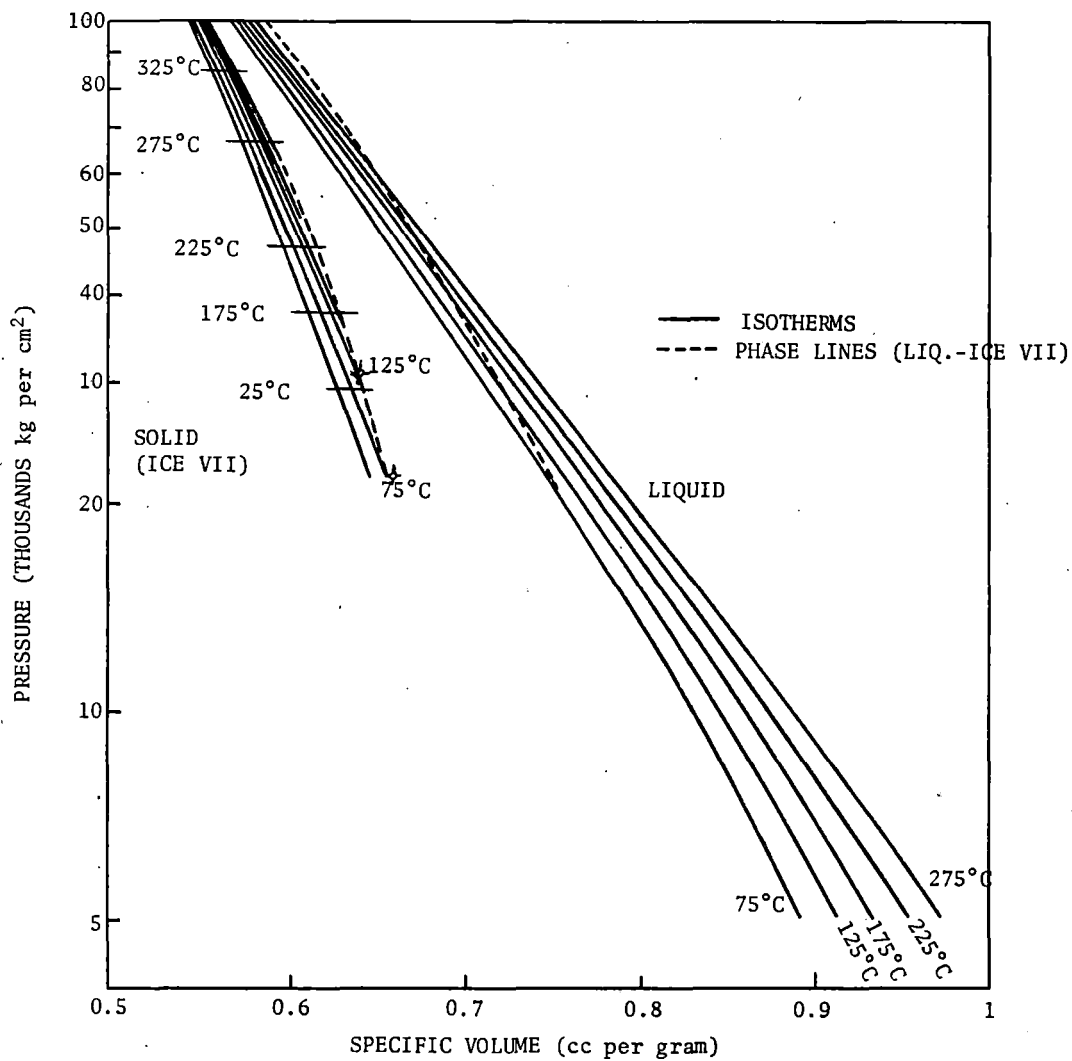


Fig. 3-45. The equation of state as fitted to the experimental data and extrapolated to 100,000 kg per cm². (Snay and Rosenbaum).

where B and n are again functions of temperature only:

T(°C)	75	125	175	225	275
B	2,560	2,470	2,090	1,510	790
n	8.022	7.581	7.327	7.220	7.220
v_p	.893	.913	.933	.953	.973

(3) Liquid above 40,000 kg/cm²

$$\log_{10} p = mv + b \quad (3-65)$$

where

$$m = -3.8337 + 2.100 \times 10^{-3} T - 9.05 \times 10^{-7} T^2$$

$$b = 7.1648 - 9.4175 \times 10^{-4} T + 4.15 \times 10^{-7} T^2$$

(4) For ice VII

$$\log_{10} p' = m'v' + b' \quad (3-66)$$

where m' and b' are functions of temperature only:

T(°C)	25	75	125	175	225	275	325
m'	-6.460	-6.066	-5.742	-5.431	-5.206	-5.000	-4.773
b'	8.5226	8.3193	8.1524	7.9919	7.8774	7.730	7.657

For numerical compilations the equations and graphs are adequate to solve for shock wave parameters. Values for enthalpy changes are given in

Table 3-8:

DEPENDENCE OF THE ISOTHERMAL SPECIFIC ENTHALPY CHANGE BETWEEN SATURATION PRESSURE (p_2) and 40,000 kg/cm² ON THE TEMPERATURE

$$\Delta H = H(T, 40,000 \text{ kg/cm}^2) - H(T, p_3)$$

T°C	100	150	300	250	275
ΔH	27,620	27,563	27,440	27,943	27,665

AVERAGE $\Delta H = 27,646 \text{ kg/cm per gram}$

TABLE 3-9

SHOCK WAVE PARAMETERS IN FRESH WATER INITIALLY AT 20°C AND 1 ATMOSPHERE

P kb	T		V		U		u		c		H-H ₀		q fraction
	Liq °C	P.fr.	Liq cc/g	P.fr.	Liq m/sec	P.fr.	Liq m/sec	P.fr.	Liq M/sec	P.fr.	Liq kg-cm/g	P.fr.	
0	20.0	--	1.0018	--	1,483	--	0	--	1,483	--	0	--	--
10	56.4	--	.8253	--	2,350	--	410	--	2,683	--	9,250	--	--
15	75.3	--	.7862	--	2,643	--	568	--	3,050	--	13,700	--	--
20	94.2	--	.7580	--	2,880	--	700	--	3,313	--	18,150	--	--
25	112.4	--	.7358	--	3,092	--	823	--	3,501	--	22,120	--	--
26.7	118.8	118.8	.7290	.7290	3,158	3,158	861	861	3,560	2,717	23,500	23,500	0
30	130.9	140.3	.7172	.7100	3,281	3,200	934	937	3,672	2,941	26,300	26,200	.1025
35	150.0	170.1	.7012	.6921	3,446	3,367	1,036	1,040	3,833	3,223	30,330	30,230	.1600
40	169.3	195.8	.6870	.6781	3,597	3,520	1,130	1,138	3,996	3,460	34,400	34,270	.1872
45	188.9	218.0	.6747	.6657	3,728	3,663	1,217	1,229	4,152	3,658	38,400	38,270	.2016
50	208.2	238.0	.6639	.6552	3,860	3,802	1,302	1,315	4,298	3,823	42,500	42,250	.2074
55	226.6	256.1	.6538	.6457	3,986	3,935	1,386	1,400	4,424	3,966	46,450	46,200	.2066
60	244.5	272.5	.6442	.6368	4,107	4,060	1,466	1,481	4,530	4,090	50,300	50,100	.1999
65	260.4	287.9	.6352	.6287	4,221	4,181	1,542	1,559	4,624	4,211	54,240	54,000	.1890
70	276.2	302.2	.6269	.6212	4,332	4,297	1,620	1,633	4,710	4,328	58,120	57,880	.1752
75	292.0	315.2	.6197	.6146	4,438	4,410	1,693	1,705	4,788	4,442	62,000	61,780	.1591
80	307.6	327.7	.6120	.6086	4,541	4,518	1,766	1,772	4,859	4,553	65,830	65,720	.1410
85	323.5	339.6	.6051	.6026	4,642	4,622	1,836	1,840	4,922	4,661	69,640	69,600	.1208
90	339.7	350.4	.5985	.5970	4,742	4,724	1,904	1,908	4,981	4,763	73,470	73,420	.0962
95	355.5	361.0	.5921	.5916	4,842	4,820	1,972	1,972	5,038	4,863	77,300	77,250	.0637

Discussion

Numerical values (Table 3-9) show from 26.7 kilobars up values for both supercooled liquid and partial freezing. From the position of the Rankine-Hugoniot curve (Fig. 3-46) it is seen that at 26.7 kilobars this curve crosses the phase line and above this point supercooling or partial instantaneous freezing may occur at the shock front.

Snay and Rosenbaum do not discuss whether actual freezing occurs. (Freezing does take place in carbontetrachloride). However, the cases of partial freezing and supercooling are presented as possible extremes. The R-H curve and the water-ice VII phase line are never far apart, and at 100 kilobars the R-H curve again enters the liquid region. Thus, it is reasoned that the question of freezing cannot be settled by observation of shock wave propagation.

Particle velocity calculations (Fig. 3-47) are in good agreement with other investigators, but disagreement occurs in values of propagation velocities. Sound velocity is changed by freezing with a distinct discontinuity at 26.7 kbars (Fig. 3-48).

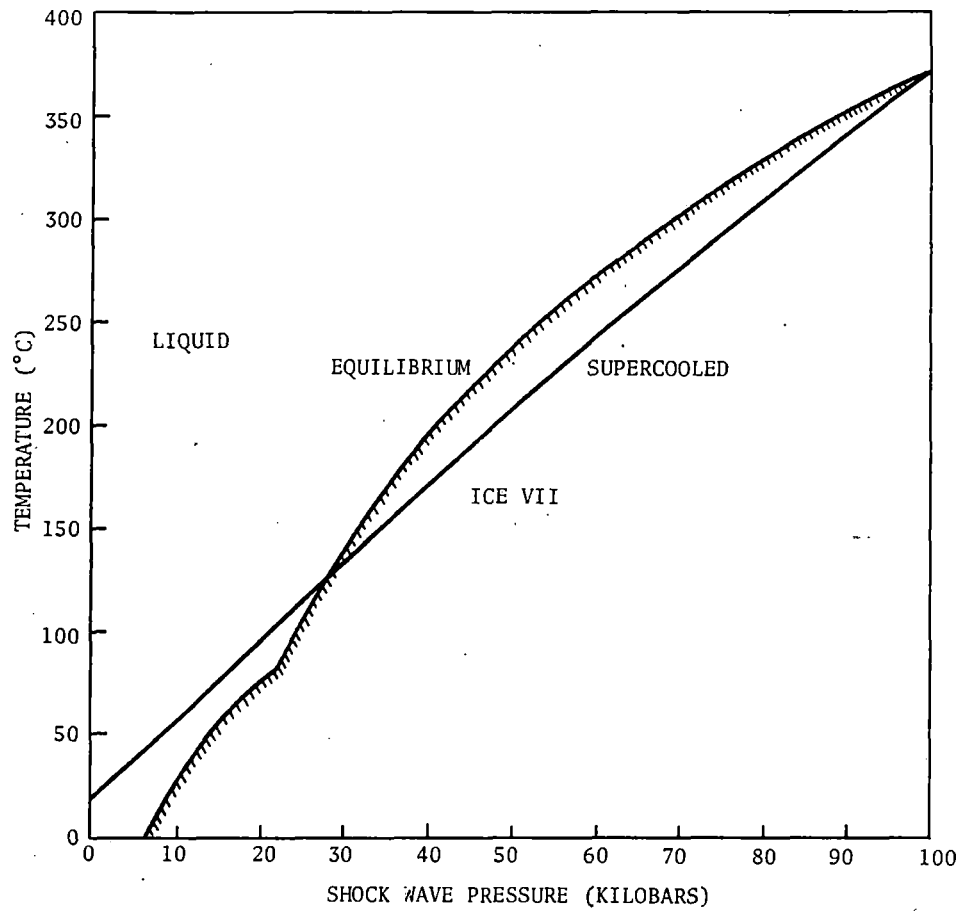


Fig. 3-46. Temperature at the shock front as a function of pressure. (Snay and Rosenbaum).

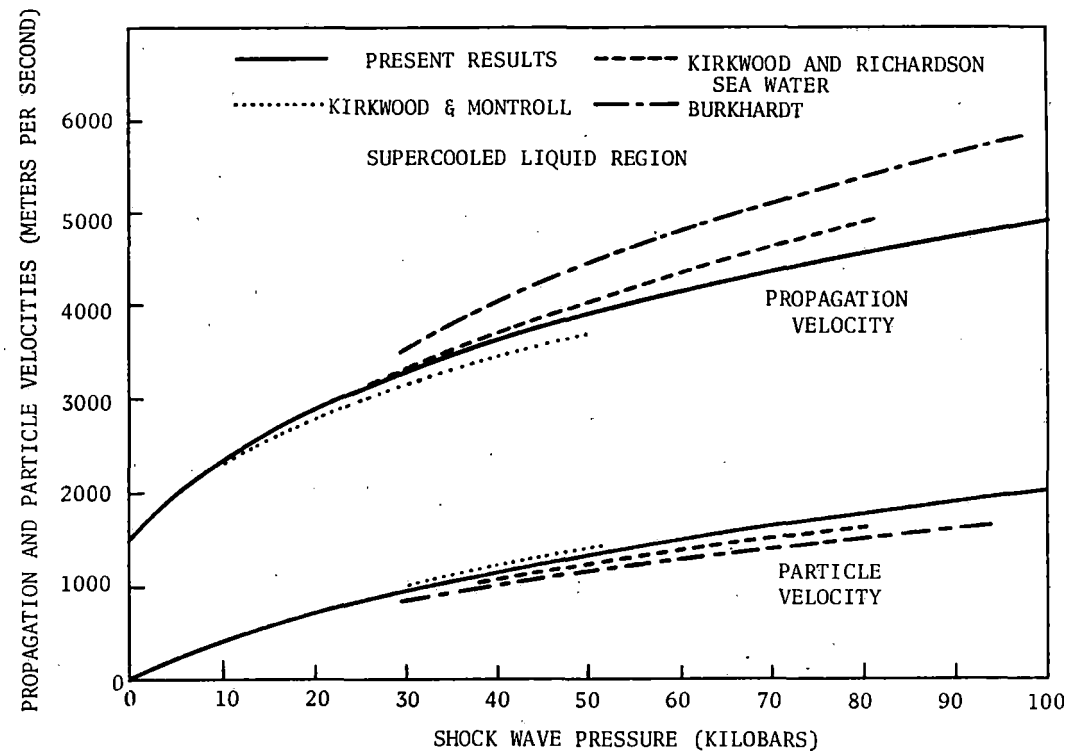


Fig. 3-47. Propagation velocity of the shock wave and particle velocity at the shock front as a function of pressure. (Snay and Rosenbaum).

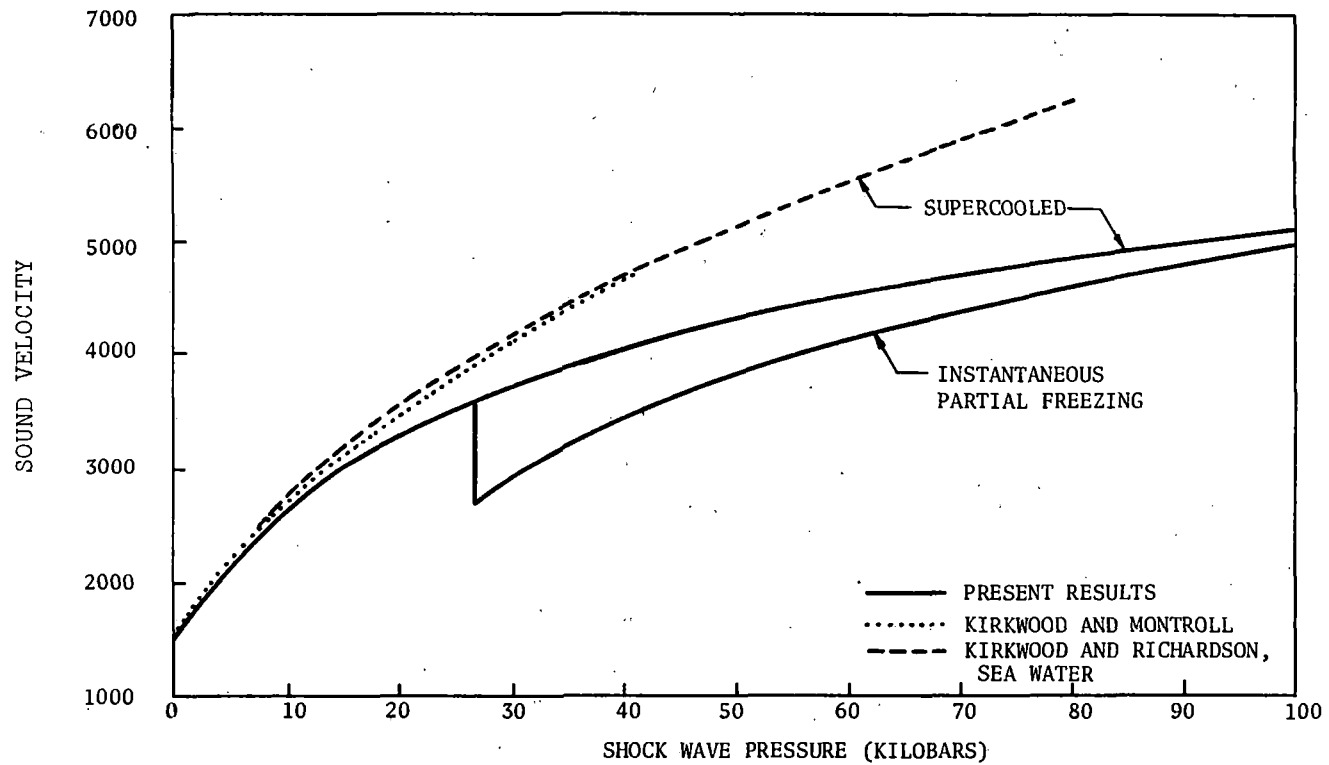


Fig. 3-48. Sound velocity at the shock front as a function of pressure. (Snay and Rosenbaum).

CHAPTER IV

WATER JET IMPACT ON ROCK

There is a rich fund of information concerning hypervelocity impact on metals, by water, by projectiles and by jets from shaped charges. However, the theory and data for water impact is for relatively low velocities, i.e., maximum velocities are near 1200 km/sec. Numerous projectile studies have been made in efforts to determine the effects of micrometeorites on space vehicles outside of the earth's atmosphere. Shaped charge data is concerned largely with effects on metals, but provides some informative comparisons.

Many of the phenomena for various materials used for impacting agents and for targets are similar, but there are important differences between water jets and metal jets or projectiles, and between the behavior of ductile metals and brittle rock targets. While a fair number of tests have been performed utilizing water jets and rock targets, little basic theory has been derived to describe the mechanics of impact. Valuable data and empirical ideas are available, however, and these are described below. There is not enough information in particular areas to lead to complete analyses, so results are described under the names of particular investigators whose work is pertinent.

Ostrovskii

In his report (1960) Ostrovskii (Ref. 28) made a summary of some of the latest developments in Russian methods of drilling, with fragmentary but useful information on use of high velocity jets. He reports that tests had been made on limestone and dolomite with pressures of 5000 kg/cm² and velocities

to 1000 m/sec. These experiments showed that breaking of rocks by high velocity jets depends upon the physical-mechanical properties, mineral composition, and small scale structural features. Strong rocks such as granites (Fig. 4-1), limestones and dolomites, are slabbed off in large fragments, resulting in the formation of conical craters of apex angle greater than 90° . Inhomogeneous rocks such as sandstone are shattered without appreciable spalling, resulting in a cylindrical crater. The effects in clays are similar to those in sandstone. When blocks of hard rock (1 x 1.5 x 1 m) were impacted by pulsed jet the blocks were fractured as well as cratered.

The effect of standoff on penetration of jets in air and in water for a granite with a uniaxial compressive strength of 2000 kg/cm^2 (Fig. 4-2) indicates that the peak penetration is obtained at about 55 mm standoff for a combustion chamber pressure of 3500 kg/cm^2 , jet diameter 3.15 mm in air and 3.10 in a layer of water.

According to Ostrovskii, the Russian experiments indicate that the optimum diameter of jets is 0.8 to 1.0 mm at a standoff of 4 to 5 cm for the range of pressures and velocities investigated, i.e., to 5000 kg/cm^2 . The width of cut varies from 3 to 5 mm and depth increases as a linear function of pressure in strong rock such as granite. At a nozzle pressure of 2000 kg/cm^2 , a transverse cutting rate of 1.4 cm/sec, the depth of cut for granite (compressive strength 1300-1500 kg/cm^2) was 30 mm, for marble (800 kg/cm^2) it was 74 mm and for limestone (600 kg/cm^2) 97 mm. As indicated elsewhere, cutting depths vary widely with type of jet, nozzle pressure, standoff, nozzle

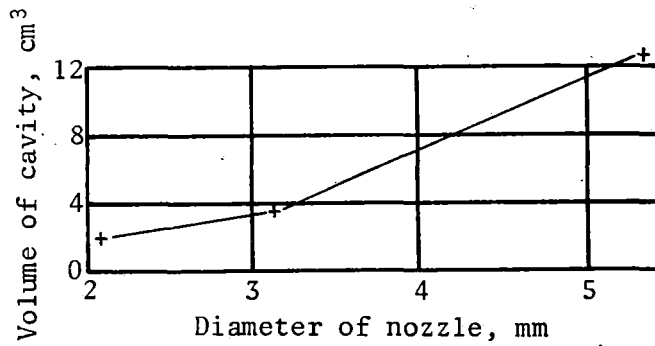


Fig. 4-1. Relation of volume of excavated cavity in granite to diameter of nozzle (movement of liquid jets through a layer of water). (Ostrovskii).

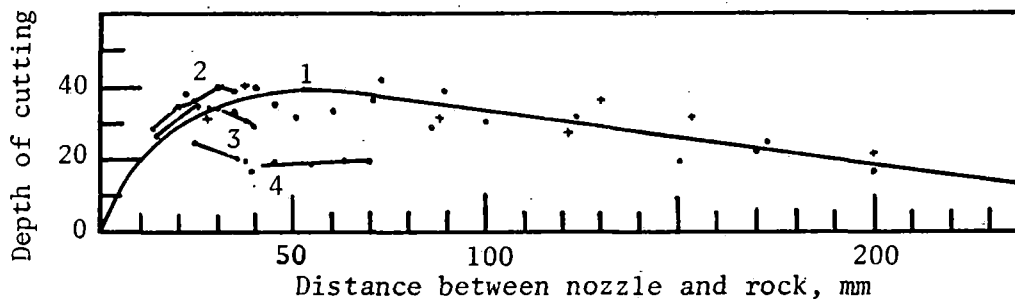


Fig. 4-2. Relation of depth of cutting granite to the distance between nozzle and rock. 1) With the liquid (water) jets traveling in air and through a layer of water (diameter of nozzle, 3.15mm); 2) with the liquid jets moving through a layer of water (diameter of nozzle, 3.10mm); 3) same as last with a nozzle diameter of 2.25mm. ·) Movement of jets through a layer of water; +) movement of jets in air. (Ostrovskii).

diameter, jet velocity, cutting speed, as well as other variables. For example, some types of shales are not susceptible to cutting with nozzle pressures of 2000 kg/cm^2 .

Farmer and Attewell

Farmer and Attewell (Ref. 22) postulate that in low velocity water impact a two wave structure is set up, a leading dilatation wave and a following shear wave (Fig. 4-3). Also, a small area subject to a high pressure jet causes erosion because of the instantaneous compression. Rock under impulsive load is said to gain in strength under high rates of loading. For sustained jets the compressive force exceeds the dynamic strength of the rock, which is degraded and the particles flushed out by the water. Fracturing by jets is related to Griffith's theory, and the fact that adsorption of a gas or liquid on the surface of a rock decreases its surface energy.

Farmer, et al., used a pressure intensifier of volume ratio of 2.5:1, (Fig. 4-4) with an input pressure of 10,000 psi and a volume of 5.6 in.^3 of water was delivered at 25,000 psi. The nozzle was composed of a 30° and 45° cone leading down to a cylindrical opening of $1/10$ inch diameter. Reduction in diameter is less for larger nozzles, and smaller jets than $1/10$ inch were found to break up.

The greatest penetration was achieved at zero standoff (Fig. 4-5), while crater diameters increased with an increase in standoff (Fig. 4-6). At low velocities there is also a marked dependence of penetration on compressive strength (Fig. 4-7). Water velocities were found to have a mean value of 2,800 ft/sec, and the impact pressure, calculated from $p = \rho cv$ was found to be 14 kilobars.

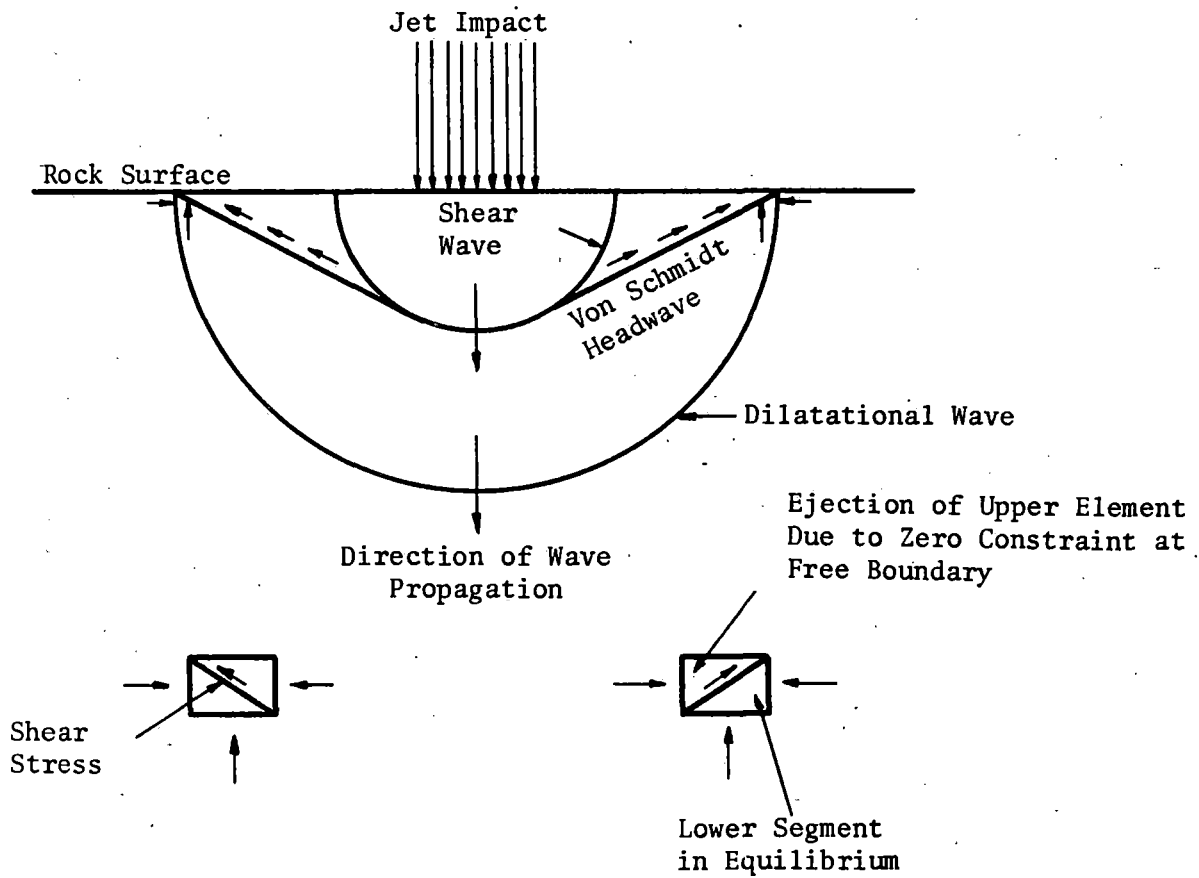


Fig. 4-3. Propagation of spherical wave structure in a semi-infinite medium, showing contribution of shearing effects to crater formation. Thickening of wave boundary denotes relative intensity of particle displacement. (Farmer) .

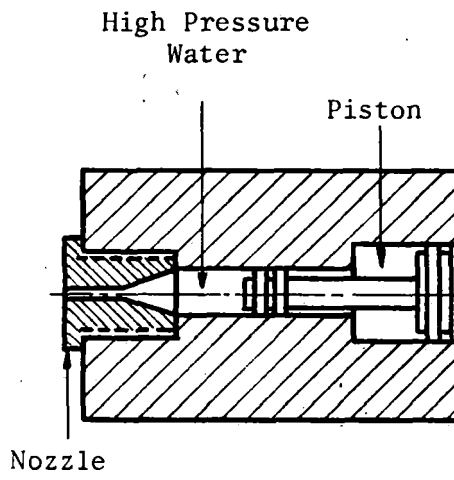
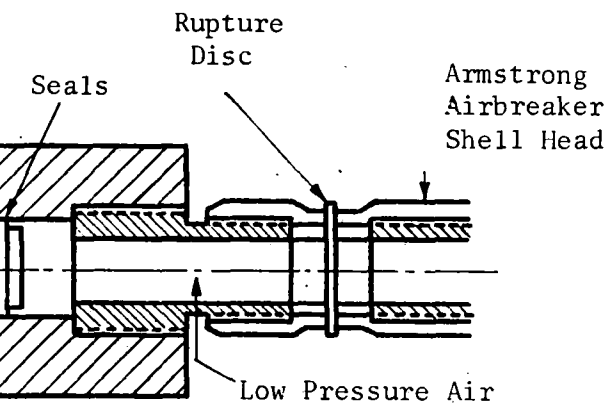


Fig. 4-4. Pressure Intensifier. (Farmer).



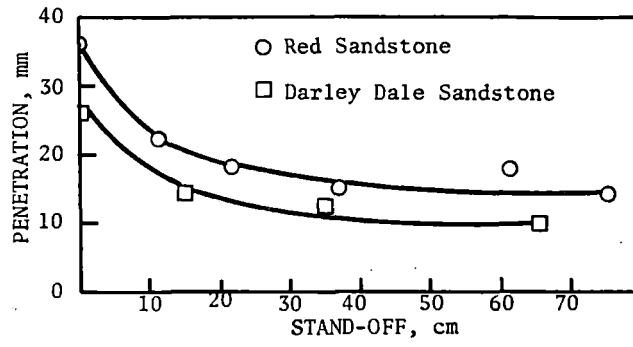


Fig. 4-5. Loss of penetration at increased stand-off. (Farmer)

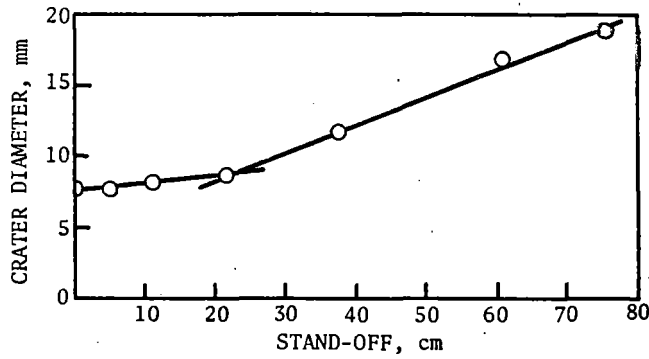


Fig. 4-6. Graph showing abrupt increase in crater diameter. (Farmer).

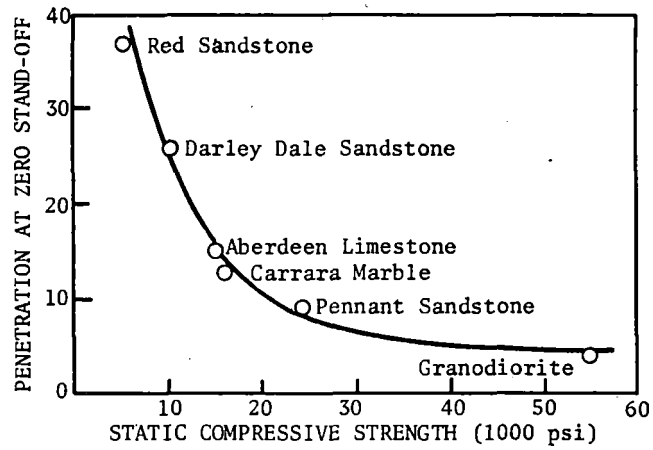


Fig. 4-7. Relationship between penetration and "static" compressive strength at zero stand-off. (Farmer).

Tests were also made on three relatively soft rocks for velocities between 200 and 500 m/sec (Fig. 4-8). The transition velocity between 250 and 300 m/sec is believed to be due to turbulence in the crater. Maximum penetration is not necessarily obtained with smaller jets, indicating that kinetic energy of the jet is important (Ref. 42).

In a comparison of jets and projectiles, for low velocity projectiles Farmer, et al., (Ref. 23) suggests that the penetration is proportional to the momentum:

$$h = \frac{k}{a} mv_o \quad (4-1)$$

where

m = mass of projectile

v_o = impact velocity

a = cross section of projectile

k = a constant dependent on projectile and target projectiles

Equation (4-1) may also be written:

$$h = \frac{k}{a} m(v_o - v_e) \quad (4-2)$$

where

v_e = critical (minimum) velocity for penetration.

The static compressive strength of the rocks tested by Farmer and Atte-well is given in Table 4-1.

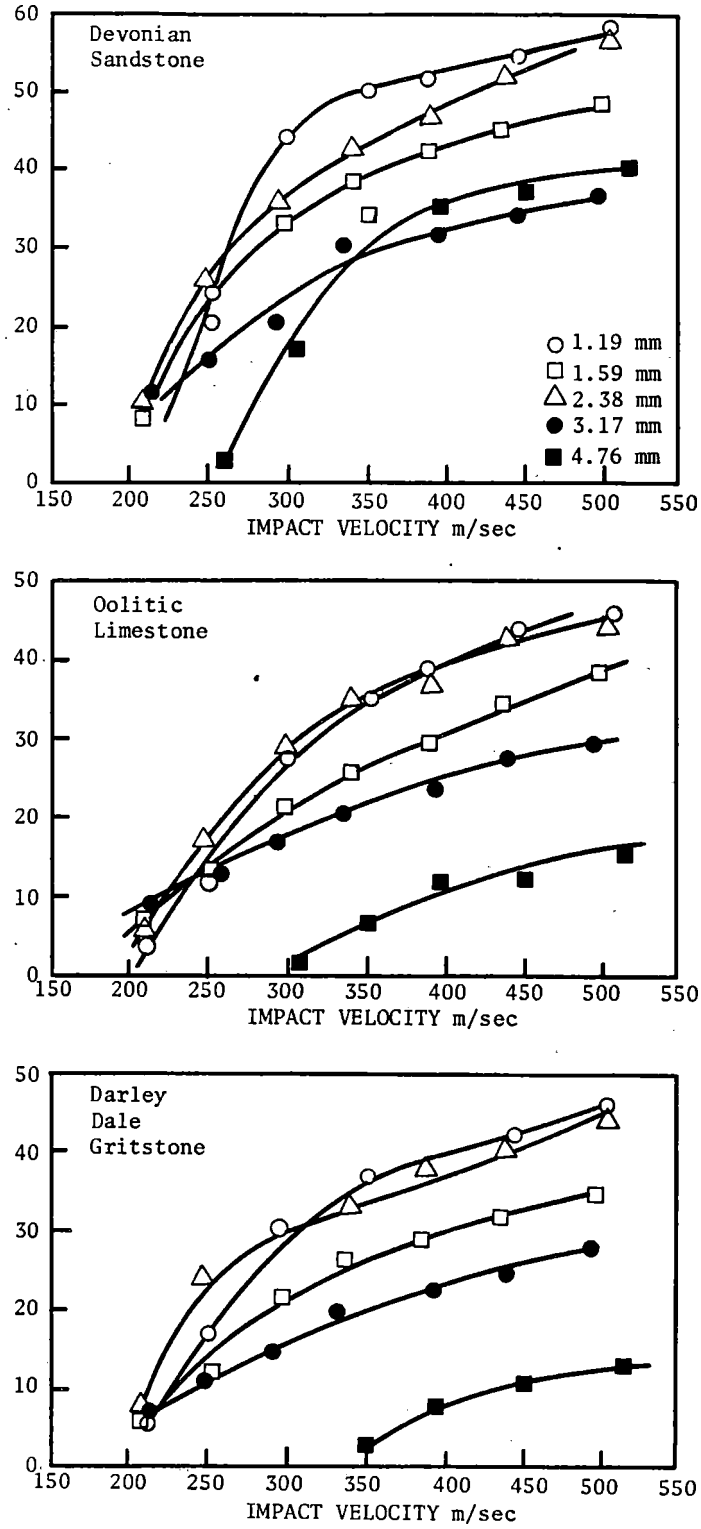


Fig. 4-8. Rock penetration by water jet impact. (Farmer).

TABLE 4-1

Rock	Static Compressive Strength kg/cm ²	Wave Velocity c, m/sec
Ferruginous sandstone	270	2400
Darley Dale sandstone	580	2400
Oolitic limestone	540	3900
Carrara marble	1090	4900
Anhydrite	1200	4600

With the pressures and velocities available it was found that larger diameter jets would not penetrate the two strongest rocks.

It was found that above a certain critical velocity the rate of penetration was less for higher velocities. The penetration equation for the region above 300 km/sec was found to be

$$h = kdc(v_0/c)^{2/3} \quad (4-3)$$

Jet instability (Ref. 23) is stated to be due to surface waves and a turbulent mixing zone. Some behavior is varicose, but at higher velocities is sinuous or helical.

Konyashin and Veselev

Konyashin (Ref. 27) used two types of hydrocompressors and a pressure multiplier for research in cutting rocks; type K-17 with a single cylinder, 1000 atm, 1000 liter/hr capacity, and a type GK 2/2, a one-step three cylinder machine with twice the volume and pressure.

Continuous jets were obtained with the multiplier at 500 atm with nozzles of 1 mm. Without a multiplier pressures of 150 to 200 atm were obtained

with a 3 mm nozzle. The latter was also employed with abrasive material in the jet, but it caused too much wear in the nozzle. The primary purpose of the multiplier was for obtaining preliminary data.

In comparative experiments, specimens were mounted on a lathe so that they could be moved with a transverse velocity v_n . All three types of equipment were employed, i. e., pressure multiplier, K-17 and GK 2/2 compressors, to determine cutting ability on two types of limestone. (Table 4-2).

The K-17 pulsating jets gave better results than the constant jets from the multiplier, and pulsating jets from the GK 2/2 were poorer than both the others.

Further tests were conducted with the K-17 without a receiver (last line Table 4-2). The nozzle pressure was measured, as well as the power consumption of the motor (1516 kw). Both the K-17 and GK 2/2 were constructed so that part of the water only went through the nozzle. That flowing through the nozzle is given by:

$$Q = av \quad (4-4)$$

and

$$v = \phi\sqrt{2gp} \quad (4-5)$$

where

Q = quantity of water m^3/sec

v = velocity of flow, m/sec

ϕ = coefficient of velocity, 0.9

g = gravity

p = pressure, meters water

TABLE 4-2

Results of Cutting Tests

Equip.	Standoff cm	Jet Type	Jet Dia.	Rock	Depth mm	Width mm	% Increase (c-P)/c	Vn cm/sec	Press atm	Pulses/ sec
M	5.0	C	0.98	I	65	-	-	1.0	400	-
K-17	5.0	P	0.98	I	90	-	38.5	1.0	400	16
M	5.0	C	0.98	I	35	1.5	-	10.0	500	-
K-17	5.0	P	0.98	I	43	1.5	22.8	10.0	500	16
M	5.0	C	0.98	I	26	2.5	-	19.0	500	-
K-17	5.0	P	0.98	I	38	2.5	46.0	19.0	500	16
M	1.0	C	0.73	I	48.7	-	-	1.0	550	-
K-17	1.0	P	0.73	I	49.3	-	+ 1.2	1.0	550	16
GK 2/2	1.0	P	0.73	I	40.5	-	-16.8	1.0	550	12
M	1.0	C	0.73	K	11.8	-	-	1.0	550	-
K-17	1.0	P	0.73	K	13.0	-	+10.2	1.0	550	16
GK 2/2	1.0	P	0.73	K	8.4	-	-28.8	1.0	550	12
GK 2/2	1.0	P	1.08	K	37.0	-	-	1.4	1000	12
K-17	1.0	P	1.08	K	44.8	-	(K17-GK)/GK	1.4	1000	16
(K-17 {w/o rec.	1.0	P	0.78	K	28.0	-	+21.1	1.4	1000	16

The magnitude of pressure is limited. For the K-17 of $Q=1000$ liters/hr, high pressures are not obtainable with nozzles greater than 1.1 mm. From the above equations

$$p = \frac{Q^2}{a^2 \phi^2 2g} \quad (4-6)$$

and for a nozzle 1.3 mm diameter the corresponding pressure is 277 atm. Due to the loss through release valves the actual relative power in the jet could not be obtained.

The power in the jet is

$$N_n = \frac{Q_n p}{367.2} \quad (4-7)$$

where

N_n = power in jet, kw

Q_n = liquid through nozzle m^3/hr

The Sharymov method of calculating useful work by multiplying $v_n \times h$ was used, or multiplying the lateral velocity of cutting by the depth of cut. On this basis the relative energy capacity of the K-17 without and with a receiver was found to be 40 percent.

The magnitude of the useful power was determined by

$$N_n = N_o \frac{Q_n}{Q_o} \quad (4-8)$$

where

N_o = power consumption of motor

Q_o = production capacity of compressor, m^3/hr

The power in the jet was determined by calculation and verified by an especially designed experiment.

The cutting capacity of the K-17 (1) with and (2) without a receiver was found by determining the pressures necessary to produce the same depth of cut for both conditions at the same value of v_n . The same depth of cut (Table 4-3) was obtained for approximately the same maximum pressure, but the energy capacity and minimum pressure were greater for the compressor with a receiver. It is recommended, therefore, that for pulsating jets greater fluctuations in the nozzle pressure are desirable for velocities v_n up to 1.4 cm/sec.

TABLE 4-3

Pressure Required for Same Depth of Cut

Equipment	Gage	Pressure, atm		
		Max.	Min.	Ave.
K-17 with receiver	1000	1310	932	1130
K-17 without receiver	----	1365	0.75	754

In experiments conducted with v_n up to about 20 cm/sec only conical holes were formed with pulsating jets. For such high transverse speeds higher jet velocities are recommended. It is also concluded that pulsed jets may be inadequate for cutting rock, but may be better for rock breakage.

The production of pulsed jets also was found to increase the breakage of machinery parts. The final recommendation (1963) was therefore that hydrocompressors be constructed with small receivers.

Zelenin, et al. (Ref. 20)

Maximum slotting is obtained at 90° incidence of impact with $9-13^{\circ}$ nozzle (Fig. 4-9). Rocks tested are:

Type of Rock	Protodyakonov hardness, f
Limestone	5 to 6
Marble	8 to 10
Granite	12 to 14

Jet cutting effects were recorded in terms of slot depth h in mm in ten completed cuts. Maximum slot depth was obtained with minimum standoff, (Fig. 4-9). Increase in depth with receiver pressure (Fig. 4-10) was greatest for the softest rock, while depth of cut approached a maximum for increase of nozzle opening (Fig. 4-11) as well as with the number of passes by the jet (Fig. 4-12). The initial percentage increase is greatest for harder rock. The feed speed (traverse speed of the nozzle parallel to the rock surface) increases the cutting effectiveness in soft rock up to 180 cm/sec. In very hard rock the optimum feed speed is between 4 and 8 cm/sec. The relationship between hardness and slot depth for selected rocks (Fig. 4-13) shows a rapid decrease in cutting power with increased hardness.

The breaking power of jets was also investigated with nozzles of 1.11 and 0.98 mm at 1,000 atm pressure and a standoff of 5 cm. Tough limestones were not broken, but holes were drilled. Granite and sandstone blocks 5 x 30 x 10 cm were broken by a jet impacting at the center of the larger face. Marble blocks 40 x 30 x 30 cm were likewise broken. However, some hard

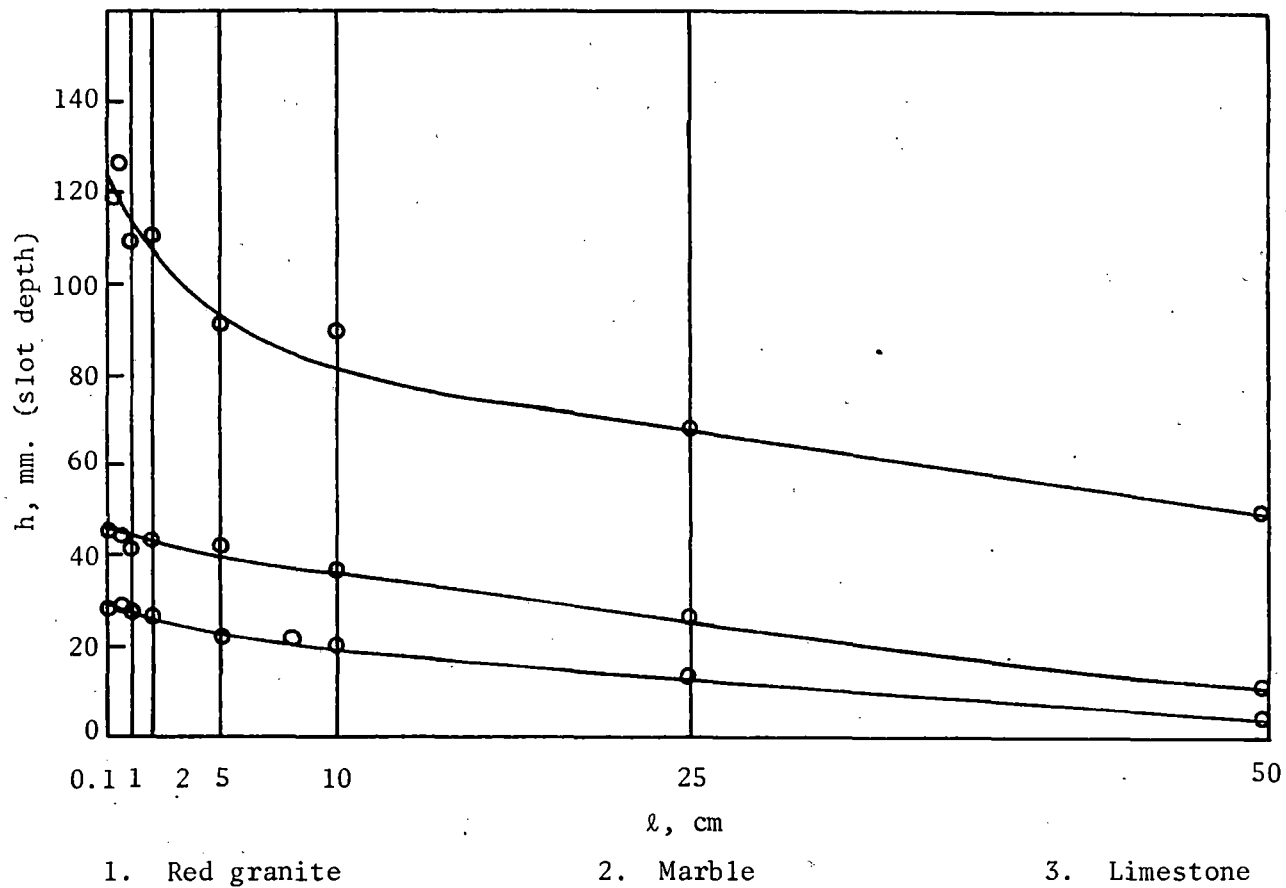


Fig. 4-9. Relationship between the slot depth - h and the distance between nozzle and specimen - l . ($P_p = 2,00$ atm.; $d = 1.08$ mm.; $v_n = 1.4$ cm/sec). (Zelenin).

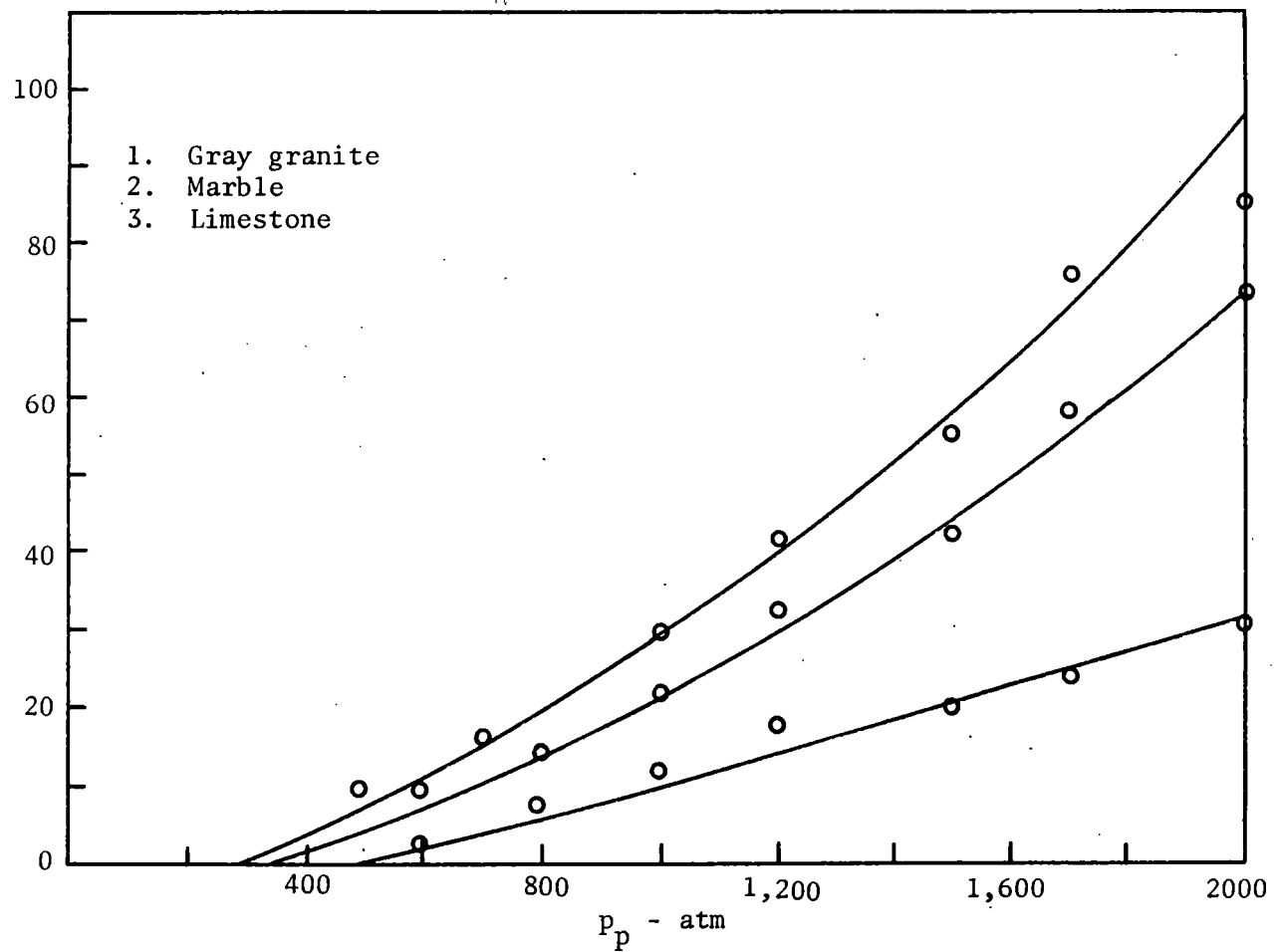


Fig. 4-10. Relationship between the slot depth - h and water pressure p_p at the receiver. (Nozzle d - 1.08 mm.; v_n - 1.4 cm/sec; l - 1 cm). (Zelenin)^P

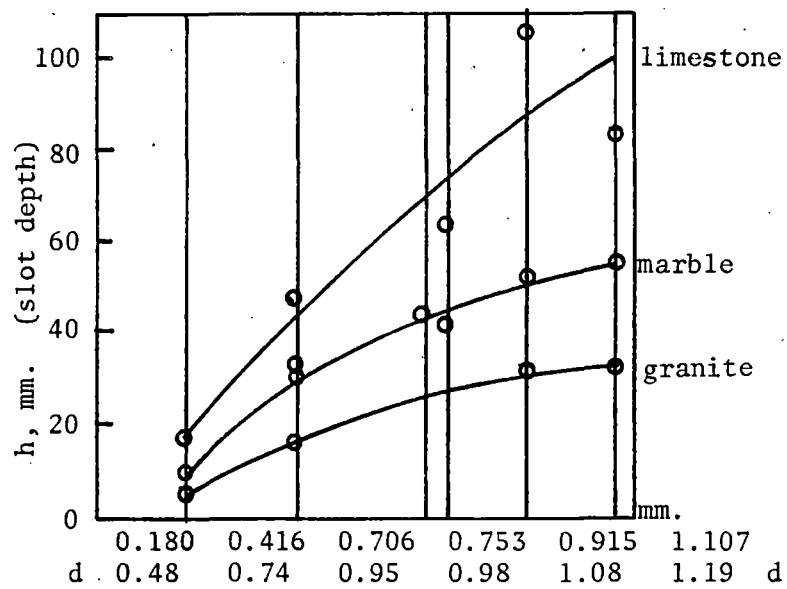


Fig. 4-11. Dependence of slot depth - h on the area of the nozzle openings - ω (p_n - 2,000 atm; nozzle d - 1.03 mm; v_n - 1.4 cm/sec, λ - 10^{-4} cm). (Zelenin).

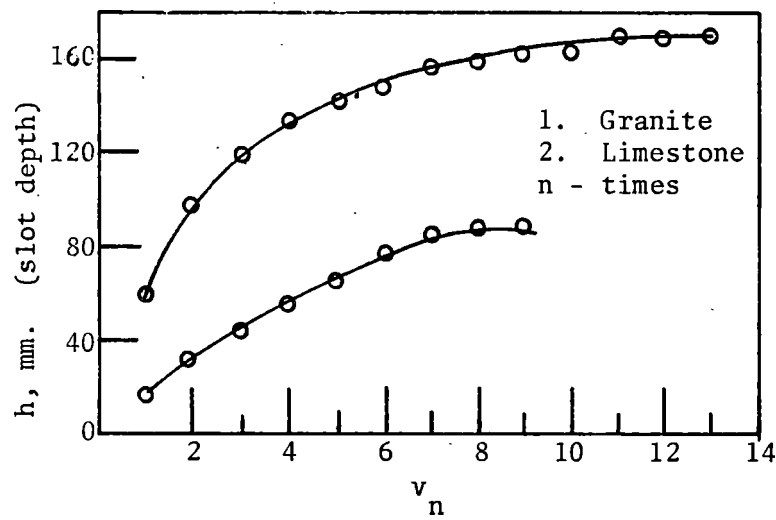


Fig. 4-12. Dependence of slot depth - h on the number of passages by water stream in the same slot - n .
 (p_p - 1.500 cm; nozzle d - 1.03 mm; v_n - cm/sec, l - cm). (Zelenin).

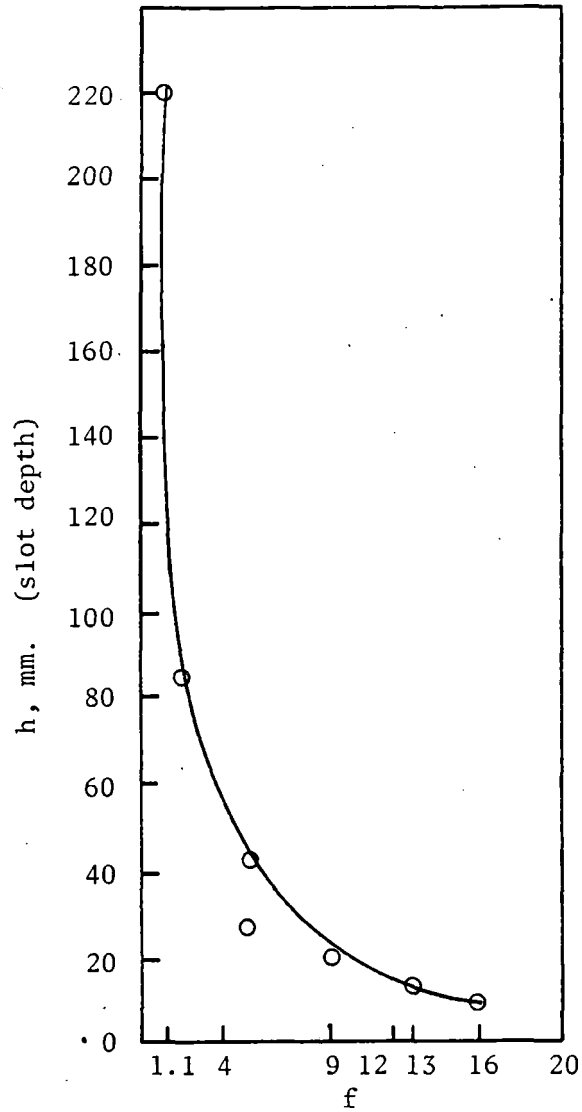


Fig. 4-13. Relationship between the slot depth cut by water jet - h and the coefficient of rock hardness - f , ($p_n = 1,000$ atm; nozzle $d = 1$ mm. $v_n = 1$ cm/sec; $l = 5$ cm). (Zelenin).

and brittle rocks were not broken by jets impacting from 30 to 60 seconds.

The formula for jet energy is given by

$$E = \frac{Q p_r t}{367.2 \times 3600} \text{ kw-hr} \quad (4-9)$$

where

Q = quantity of water, m^3/hr

p_r = receiver pressure, meters

t = time of jet action, sec.

However, a comparison of crushing energy of the rock with calculated energy gave too wide a scatter of data to establish any useful relationships. (This method of test was discontinued.)

A device was designed to measure the total force of a water jet at varying standoff distances. Results (Table 4-4) show that the force is approximately constant, probably due to little loss in jet velocity in distances to 45 cm. The decrease in slot depth h with increase of standoff is due to the growth of jet cross-section with distance traveled. It is concluded that the slot depth is proportional to the water jet pressure.

TABLE 4-4

Pressure in receiver p , atm.	Acting force of water stream p , kg				
	$\ell = 3$ cm	$\ell = 5$ cm	$\ell = 12$ cm	$\ell = 25$ cm	$\ell = 45$ cm
300	4.0	4.0	3.5	3.9	3.5
500	9.0	7.0	7.0	7.5	10.0
700	10.0	11.0	11.5	11.0	12.0
1000	15.0	14.0	16.0	15.5	15.0

It was found that for a given traversing speed there is a definite critical specific pressure for a given rock at which slot cutting is initiated. This value is directly proportional to the coefficient of hardness of the rock, i. e.,

$$p_{\min} = 13 f \quad (4-10)$$

and the critical receiver pressure is given by

$$p_c = 25 f \quad (4-11)$$

It was also found that the product of the working area of a jet, w_1 , and the cut depth h is constant for a given material and is independent of standoff. Also, $h \times w$, is inversely proportional to f . Thus, for $p=1000$ atm, $v_n = 1$ cm/sec and $d = 1$ mm, for rocks of $f = 5$ to 16,

$$h \cdot w \cdot f \approx 0.5 \quad (4-12)$$

For rocks where f varies from 5 to 20 the following range of operational values for rock cutting were recommended:

- (a) Pressure: 800 to 1500 atm
- (b) Nozzle dia.: 0.8 to 1.5 mm
- (c) Standoff: 1 to 5 cm
- (d) $v_n = 40$ to 170 cm/sec

For rock breakage standoff should be zero.

Lyschevskiy

Lyschevskiy (Ref. 11) notes that a theory for fracturing of rocks by water jets had not been established (1963), and therefore laws must be based on results of experimental research.

A method of dimensional analysis is therefore proposed. The pertinent parameters selected are:

- b = depth of cut
- ρ_1 = density of jet
- μ_1 = dynamic viscosity of jet
- σ = surface tension of jet
- ρ_2 = density of target material
- μ_2 = dynamic viscosity of target material
- u_c = nozzle velocity of jet
- ℓ = distance from nozzle
- v_t = transverse velocity of target
- f = Protodyakonov hardness
- θ = angle of incidence of jet

Thus,

$$h = F(\rho_1; \mu_1; \sigma; \rho_2; \mu_2; u_c; d_c; \ell; v; \theta; f) \quad (4-13)$$

To obtain dimensionless quantities, the units of L, G and T are used for length, time and gravity in the cgs system, and

$$hL = F_1 \left(\rho_1 \frac{GT^3}{L^4}; \mu_1 \frac{GT}{L^2}; \sigma \frac{G}{L}; \rho_2 \frac{GT^2}{L^4}; \mu_2 \frac{GT}{L^2}; \right. \\ \left. u_c \frac{L}{T}; d_c L; \ell L; v \frac{L}{T}; \theta; f 10^5 \frac{G}{L^2} \right) \quad (4-14)$$

One set of dimensionless quantities is given by

$$\frac{h}{d_c} = F_2 \left(\frac{\mu_1}{\sqrt{\rho_1 d_c \sigma}} ; \frac{\rho_2}{\rho_1} ; \frac{\mu_2}{\sqrt{\rho_1 d_c \sigma}} ; u_c \sqrt{\frac{\rho_1 d_c}{\sigma}} ; \frac{\ell}{d_c} ; \right. \\ \left. v \sqrt{\frac{\rho_1 d_c}{\sigma}} ; \theta ; 10^5 f \frac{d_c}{\sigma} \right) \quad (4-15)$$

However, μ_1 and μ_2 are analogous, and the following expressions are utilized:

$$W = u_c^2 \frac{\rho_1 d_c}{\sigma} ; W_v = v \sqrt{\frac{\rho_1 d_c}{\sigma}} ; \phi = 10^5 f \frac{d_c}{\sigma} ; M = \frac{\mu_1^2}{\rho_1 d_c \sigma} \quad (4-16)$$

which gives

$$\frac{h}{d_c} = F_3 \left(M ; \frac{\rho_2}{\rho_1} ; \frac{\mu_2}{\mu_1} ; W ; \frac{\ell}{d_c} ; W_v ; \theta ; \phi \right) \quad (4-17)$$

The sections of the jet are (1) the initial undispersed jet ℓ_1 ,
(2) the transition section ℓ_2 , and (3) the final or dispersed section ℓ_3 .

The following empirical equation has been obtained from data for the
length $\frac{\ell_1}{d_c}$

$$\frac{\ell_1}{d_c} = C \frac{M^{0.308}}{W^{0.71} \left(\frac{\rho_2}{\rho_1} \right)^{1.21}} \quad (4-18)$$

while the value of ℓ_2/d_c is given by

$$\frac{\ell_2}{d_c} = C_1 \frac{W^{0.25} M^{0.4}}{\left(\frac{\rho_2}{\rho_1} \right)^{0.24}} \quad (4-19)$$

for variation of the parameters W , M and ρ_1/ρ_2 :

$$(\rho_2/\rho_1) W = 60 \text{ to } 7000; M < 0.25; (\rho_2/\rho_1) = 0.014 \text{ to } 0.0095.$$

For nozzles designed with a conical entrance and cylindrical exit, $C = 1096$, and C_1 takes on different values. For water jets on a given rock (ρ_2/ρ_1) and (μ_2/μ_1) have constant values. Also $\mu_1^2/\rho_1 d_c$ varies in a minor way and it may be neglected. Equation (4-17) may then be written as

$$\frac{h}{d_c} = F_1 \left(W; \frac{\ell}{d_c}; W_0; \theta; \phi \right) \quad (4-20)$$

Utilizing $\rho_1 = 1.02 \times 10^{-3} \text{ g/sec}^2/\text{cm}^4$, $\mu_1 = 10.2 \times 10^{-6} \text{ sec/cm}^3$, and $\sigma = 0.072 \text{ g/cm}$, $\rho_2 = 1.25 \times 10^{-6} \text{ g/sec}^2/\text{cm}^4$ and considering that

$u_c = \sqrt{2\mu_c^2 p/\rho_1}$ where p is the pressure of the liquid in kg/cm^2 and μ_c is the loss coefficient

$$\ell_1 \cong 39.5 (\mu_c^2 p)^{-0.71} \quad (4-21)$$

and

$$\ell_2 = 14.1 \mu_c^{1/2} p^{1/4} d_c^{0.85} \quad (4-22)$$

Research results of Zelenin, et al., (Ref. 20) were obtained with nozzles of 0.4 to 1.2 mm diameter, p varying from 400 to 2000 atm and transverse velocities of 1 to 20 cm/sec on limestone, marble, granite, labradorite and other rocks with f varying from 0.00 to 16. The criterion W_p is employed because of the importance of p , and is obtained by substituting W for μ_c , i.e., $W_p = \mu_c^2 p d_c / \sigma$. For a range of values of W_p from 5×10^5 to 26×10^5 the data may be represented by (Fig. 4-14)

$$\frac{h}{d_c} = \text{const } W_p^{1.6} \quad (4-23)$$

A log-log plot of h/d_c against ϕ (Fig. 4-15) also gives the relationship

$$\frac{h}{d_c} \phi = \text{const} \quad (4-24)$$

for a range of values of ϕ from 9.9×10^2 to 224×10^2 .

The plot of the effect of angle of incidence (Fig. 4-16) gives the following for limestone and marble

$$\frac{h}{d_c} = \text{const } W_p^{1.6} (\sin\theta)^{1.6} = \left(\frac{h}{d_c} \right)_{\text{max}} (\sin\theta)^{1.6} \quad (4-25)$$

Likewise, the influence of W_v on the dimensionless depth of the cut (Fig. 4-17) is expressed as:

$$\frac{h}{d_c} = \frac{\text{const}}{W_v^{0.31}} \quad (4-26)$$

The effect of the distance from the nozzle to the rock is different for the three characteristic sections of the jet (Fig. 4-18). For the solid core section the force is virtually unchanged, i.e., there is little attenuation or dispersion. Because of dispersion and other processes there is a decrease in pressure and cutting effectiveness (Fig. 4-19). The rate of decrease in the last section is even greater. The boundaries between the sections are indicated by equations (4-21 and 4-22). The empirical expressions applicable to the sections are

Transfer section

$$\frac{h}{d_c} = \frac{\text{const}}{\left(\frac{l}{d_c} \right)^{0.12}} \quad (4-27)$$

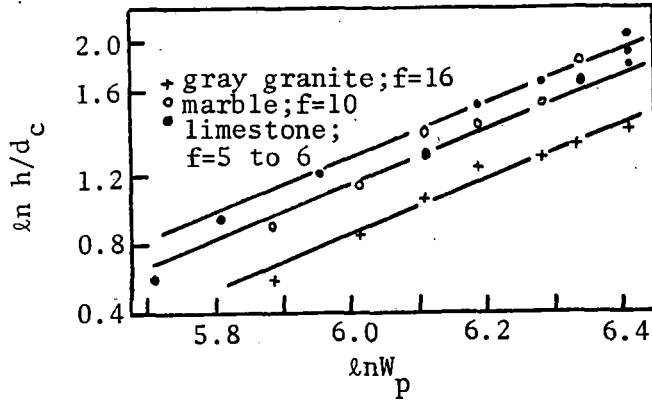


Fig. 4-14. The relationship of $h/d_c = f(W_p)$ for different rocks. $d = 0$ fcm; $\ell = 1$ cm; $v_n = 1.4$ cm/sec; $\theta = 90^\circ$. (Lyschevskiy).

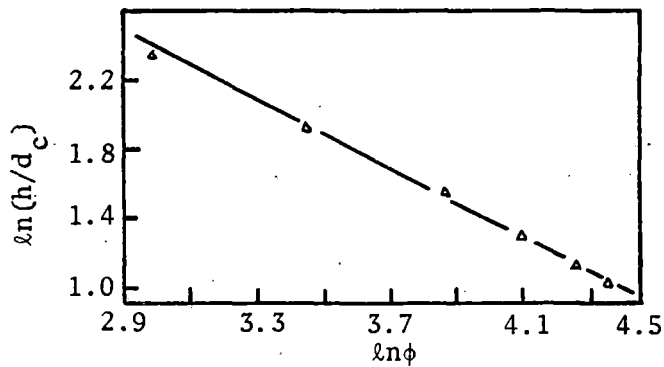


Fig. 4-15. The relationship $h/d_c = f(\phi)$. $p_o = 1000$ atm; $d_c = .1$ cm/set; $\ell = 5$ cm; $\theta = 90^\circ$. (Lyschevskiy).

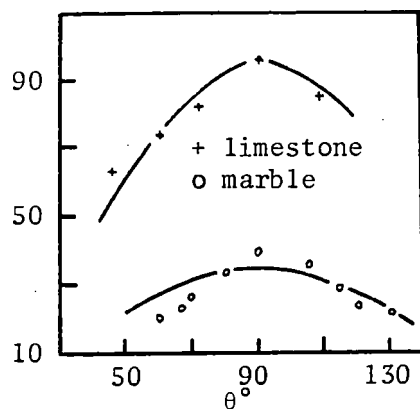


Fig. 4-16. The relationship of $h/d_c = f(\theta)$ for limestone and marble, limestone $f = 7$, $p_o = 1000$ atm, $\ell = 10$ cm, $d = 0.1$ cm, $v = 20$ cm/sec, - marble $f = 10$, $p_o = 800$ atm, $d = 0.1$ cm, $v = 1$ cm/sec; $h/d_c = (\sin \theta)^{1.6}$ for both rocks. (Lyschevskiy).

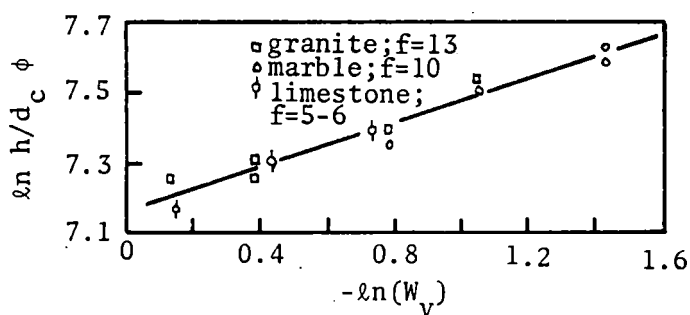


Fig. 4-17. The relationship of $h/d_c \phi = f(W_v)$; $d_c = 0.1$ cm; $p_o = 1000$ atm. (Lyschevskiy).

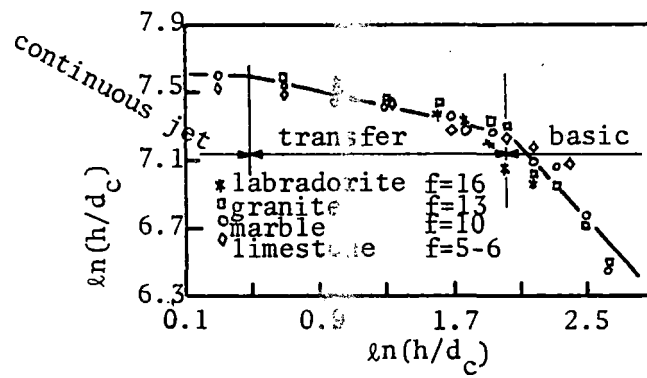


Fig. 4-18. The relationship of $h/d_c \phi = f(\lambda/d_c)$. $d = 0.1$ cm; $p = 1000$ atm. (Lyschevskiy).

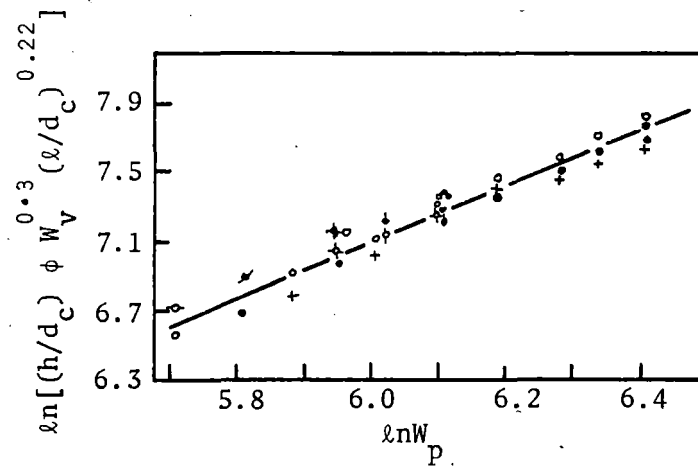


Fig. 4-19. The general relationship for the transfer section of the jet. (Lyschevskiy).

Data for Figure 4-19

	f	l cm	v cm/sec	d _c cm	
marble	10	5.0	1.0	0.072	o
limestone	5	5.0	1.0	0.072	φ
marble	10	5.0	1.0	0.04	-o-
limestone	0.7	10	20	0.1	
marble	10	5.0	1.0	0.118	o
				0.099	-o-
limestone	5	5.0	1.0	0.099	-φ-
				0.118	φ
granite	16	1.0	1.4	0.1	+
marble	10				o
limestone	5-6				●

and dispersed section

$$\frac{h}{d_c} = \frac{\text{const}}{\left(\frac{\ell}{d_c}\right)^{1.14}} \quad (4-28)$$

Cutting should therefore be performed by the jet at distances less than the end of the transfer section.

Also, the expressions for cutting for a given angle of incidence is for

(a) the transfer section

$$\frac{h}{d_c} = 0.305 \times 10^{-2} \frac{(Wp \sin \theta)^{1.6}}{\phi W_v^{0.31} \left(\frac{\ell}{d_c}\right)^{0.22}} \quad (4-29)$$

(b) the non-dispersed section

$$\frac{h}{d_c} = 0.23 \times 10^{-2} \frac{(Wp \sin \theta)^{1.6}}{\phi W_v^{0.31}} \quad (4-30)$$

(c) the dispersed section

$$\frac{h}{d_c} = 21.5 \times 10^{-2} \frac{(Wp \sin \theta)^{1.6}}{\phi W_v^{0.31} \left(\frac{\ell}{d_c}\right)^{1.14}} \quad (4-31)$$

Inserting the parameters for cutting by capillary jets of water at normal incidence ($\theta = 90^\circ$) for depth of cut is

(a) for the non-dispersed section

$$h = 1.405 \times 10^{-2} \frac{(\mu_c^2 p)^{1.6} d_c^{1.445}}{f_v^{0.31}} \quad (4-32)$$

(b) for the transfer section

$$h = 1.865 \times 10^{-2} \frac{(\mu_c^2 p)^{1.6} d_c^{1.665}}{f_v^{0.31} \ell^{0.22}} \quad (4-33)$$

and

(c) for the dispersed section

$$h = 131 \times 10^{-2} \frac{(\mu_c^2 p)^{1.6} d_c^{2.585}}{fv^{0.31} \ell^{1.14}} \quad (4-34)$$

in which the linear measurements are in centimeters, the velocity in cm/sec, and the pressure p in atmospheres. Thus, standoff does not enter in for cutting at small values of ℓ and cutting is most efficient in this region.

Voytsekhovskiy, et al.

The IV-4 pulsed water jet was developed in 1961 (Ref. 24), the jet developing approximately 5000 kg/cm².

Hardness of blocks of sandstone 13 x 11 x 7 cm was determined and these were shot at distances of 85-90 cm from three coordinate directions. Normal to the stratification, small cracks and spalls occurred with the first 3 to 5 shots. Subsequent shots penetrate these cracks, form hydraulic wedges which break the rock to form cone-shaped craters with a compressed rock nucleus. The angle of fracture of the side of the cone varies from 26° to 30° for the sandstone tested.

For the full series of shots at one position small volumes up to 100 cc were broken out (Fig. 4-20) by 3 to 5 shots, and increased sharply thereafter. In shots parallel to stratification, the first shot broke 25 cc, and the presence of existing cracks enhanced the breakage. The 37th shot broke the block. A second group of tests was made on limestone of hardness $f = 7$ to 8. The first shot, at normal incidence and a standoff of 1.1 to 1.5 meters, made a hole of $h = 16$ to 18 cm and diameter 19 to 21 cm, and a second shot increased the depth to 19 to 21 cm. Shots at 82.5° incidence formed holes

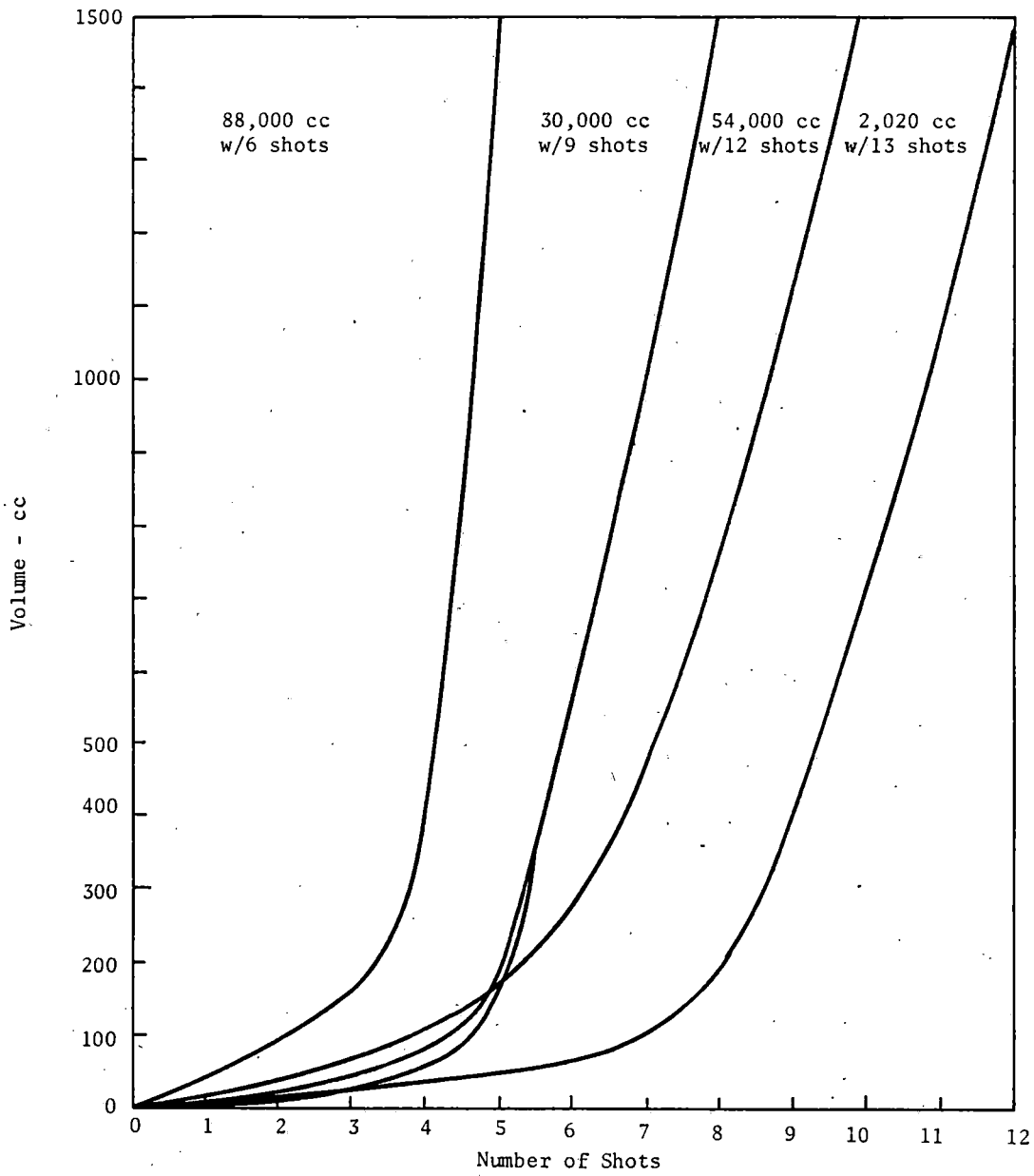


Fig. 4-20. Relationship between the volume of destroyed sandstone and the number of shots directed to one point. (Voytesekhovskiy).

\underline{h} = 13 cm and 4 to 5 cm diameter.

The average breakage per shot varied from 2 to 2.9 cm. The power required per shot is given by

$$A = vp \quad (4-35)$$

where

v = 30 liters, volume per shot

p = 65 atm = average pressure supplied to water jet

A = 1950 liter - atm or 0.054 kw-hr

This indicates a power consumption of 18 to 27 kw-hr/cu meter.

The conclusions were:

1. The IV-4 pulsed water jet developing 7000 kg/cm² dynamic pressure will successfully break rocks of \underline{f} = 5 to 6 containing cracks.
2. Effective breakage requires from 3 to 5 shots in the same position, or one shot where cracks are present.
3. Less unit power is required for higher pressure jets.

In these tests all rocks were made with blocks in the laboratory. Complete fracture of such blocks is not analogous to the type of fracture which would occur in a solid face.

Chastovitin and Cherkasov

In 1960 Chastovitin (Ref. 43) noted the possible use of high speed water jets in tunnels. Pressures varied from 1000 to 1500 atm forcing water through nozzles of 1 to 3 mm diameter with speeds of 300 to 450 meters/sec. Transverse cutting speeds varied from 5 to 30 cm/sec. Slots are cut in the

working face and the rock between split by "known means". Further studies on the productivity, energy and other factors were reported to be in progress.

Konyashin and Veselev

Konyashin and Veselev (Ref. 27) report results of rock cutting experiments with pulsed jets. Pressures were varied from 400 to 1000 atm, nozzle diameter from 0.73 to 1.08 mm and pulse rates were 12 to 16 per sec. Two types of limestone were used for targets and traversing speeds were varied from 1.0 to 19.0 cm/sec.

At traverse speeds of 20 cm/sec only conical holes were obtained. Also, producing pulsed jets increases machinery breakage. It was concluded that pulsed jets are adequate for rock breakage and not cutting.

This conclusion was borne out by Voytsekhovskiy (Ref. 24) who concluded that pulsed jets developing 7000 kg/cm^2 dynamic pressure will successfully break moderately hard rock. Little is given on the mechanics of breakage. However, the fractures produced by the first few shots provide a means for crack penetration and fracture by subsequent shots.

Kuklin

Kuklin (Ref. 16) states that the fracturing of rock by water jets depends upon the following factors:

1. The physical-mechanical properties of the rock and the in situ structure.
2. The technical processes and the method of hydraulic fracturing; and

3. The combination of the action of hydraulic fracturing with mechanical, blasting and other methods.

Four types of hydraulic fracturing are indicated:

1. The hydro-washing of slightly cemented materials, or grains or fragments, such as sands, broken coal or other granular material.
2. Washing off of laminated sandy-clay rocks, accompanied by filtration into the force, in materials such as are mined by open pit methods.
3. Hydrofracturing of cracked or fragile rocks due to cutting action and pressure, particularly by pulsed jets, characterized by large spalls or fragments.
4. The cutting of dense or lengthy fractional rocks by pulsed or continuous jets, characterized by formations of small fragments, utilizing pressures to 2500 atmospheres.

These categories may overlap considerably.

Kuklin stated in 1962 that the primary objective of further research should be the development of combined methods of fracturing. He recommended (a) the adoption of a unified terminology, (b) determination of energy and other parameters of the jet, and (c) production of research results of rock properties and methods of testing.

Leach and Walker

Leach and Walker (Ref. 10) studied the effect of 1 mm water jets at about 1000 m/sec (Mach number 3.5) on 30 cm cubes of three sandstones,

a marble and a granite. Compressive strength Rss-330 atm, DDss-670 atm, Pss-1460 atm, C marble 1100 atm, and A granite 1370 atm.

Jets usually produced a hole, with occasional large cracks or shallow craters. The holes for all rocks were 5 ± 1 mm diameter. For harder rocks penetration did not take place below a (suggested) critical pressure of 2000 atm. Hole diameter did not vary significantly with depth.

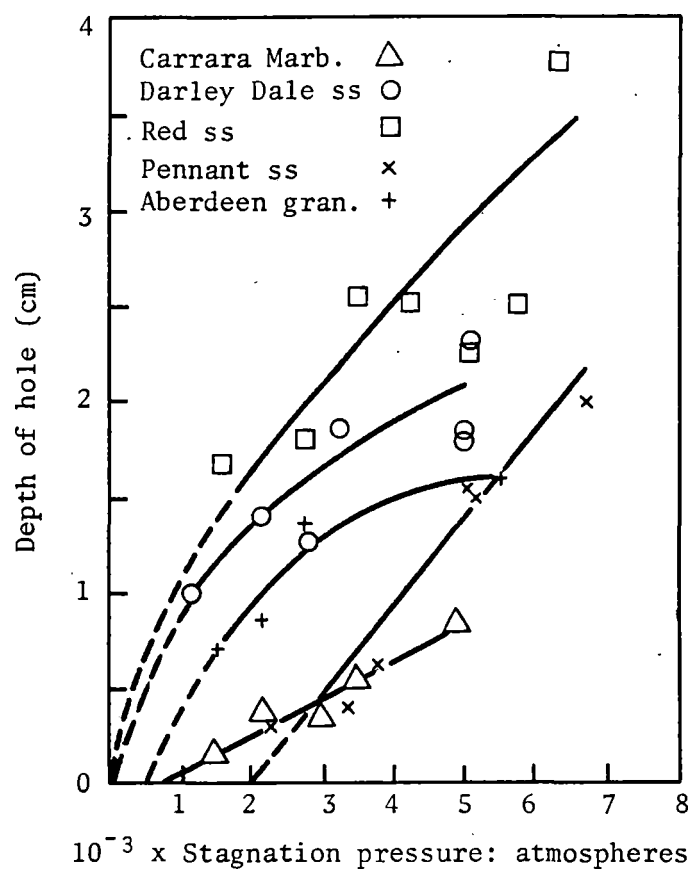
Rock strength effects hole depth, which increases with pressure (Fig. 4-21). Repeated shots at 5000 atm suggest a critical depth for DDss, (Fig. 4-22). Simulated pressures (Fig. 4-23) at the hole bottoms were measured for 130 and 600 atm nozzles with a special device and were found to decrease to a constant value of about one-tenth the pump pressure for hole depth greater than 10 hole diameters. A similar phenomenon is thought to occur for pressures of 2000 atm to account for limiting hole depths.

Assuming spaced geometrical water jet cutting normal and parallel to a face of rock, an estimate of 40 kg/min for Rss is estimated, which production is not as great as mechanical methods for the same horsepower (500) at the nozzle outlet.

Cooley, et al.

Cooley (Ref. 31) compares effectiveness of steady and pulsed jets on the basis of amount of rock broken for the same nozzle diameter, pressure and horsepower. The volume rate parameter is defined as the amount of rock broken per jet horsepower

$$\theta = \frac{V_r}{d^2 p_o^{3/2}} \quad (4-36)$$



30 cm cube of rock, 2.5 cm from nozzle, single shots of 10 cm^3

Fig. 4-21. Variation of hole depth with water pressure for different rocks. (Leach & Walker).

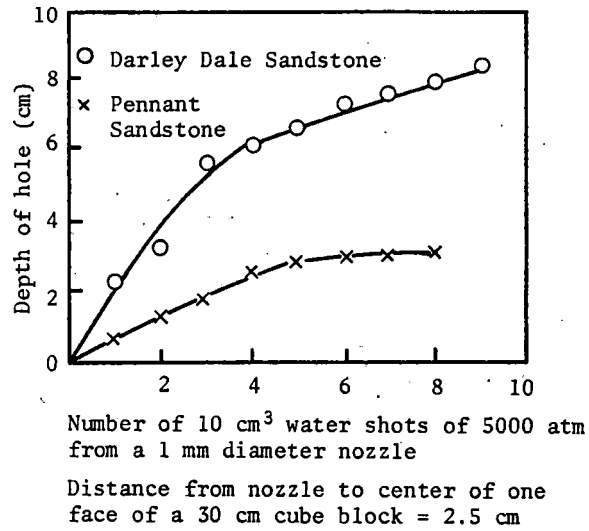


Fig. 4-22. Rock penetration by water jets. (Leach & Walker).

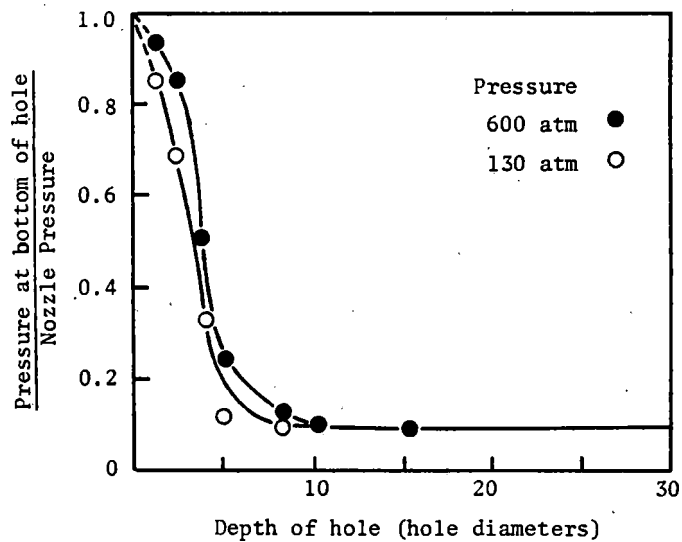


Fig. 4-23. Pressure at the bottom of a simulated hole. (Leach & Walker).

CHAPTER V

PROJECTILE ACCELERATION AND IMPACT

INTRODUCTION

Most of the research performed with hypervelocity projectiles has been for the purpose of simulation of meteorite impact. The maximum velocities obtainable for undeformed projectiles (1968) appears to be in the neighborhood of 40,000 fps for small, low density material. Several means have been explored and utilized for accelerating projectiles such as direct projection by explosives, electric arc guns, magnetic accelerators and others. Implosion techniques in the chamber of a gun are currently under experimentation. The most successful device to date, however, appears to be the light gas gun (see Appendix A for theory).

Experimental conditions often require that the projectile be undeformed and of its original mass when it reaches the target. This means that the acceleration forces cannot exceed the strength of the projectile. Likewise, the mass of the projectile must be small, and while there is no theoretical upper limit to attainable velocities, practical considerations in size, strength and pressures have placed an upper limit on projectile velocity.

Limitations - High Velocity Guns

In research and applications of high velocity guns to rock fracture problems it is necessary to know what the limitations are with respect to the mass and velocities of projectiles as related to their properties and the parameters of the gun. Curtis (Ref. 45) stated in 1964 that "no clearly defined theoretical upper limit to the velocity capability of a light gas gun exists."

where V_r is the volume of rock broken.

Repeated shots for sandstone have yielded 500 times the volume of rock broken by a steady jet (Russian tests - Ref. 24). However, the tests were made on unconfined blocks of rock. The added effectiveness was due to the porosity and fractures in the sandstone. The same was true of granite when a second shot broke 10 times more rock than a first shot. The cracks caused by the first shot permitted pressure to be exerted beyond the crater into the rock, resulting in direct tensile slabbing.

Bowden, et al.

Bowden and colleagues, (Ref. 44) discussed the effects of liquid impact on metals, particularly with reference to raindrop erosion. However, droplet velocities were limited to a maximum of 1200 m/sec. The principle mechanism of removal of material appears to be by means of a process of erosion. The research results in the paper by Leach and Walker, which is concerned with impact of water jets on rock, is presented elsewhere in this report.

The primary factor appears to be the ratio of the accelerating forces to the strength of the projectile. The following discussion is taken from Curtis (Ref. 45).

The velocity of the projectile is obtained by integrating Newton's equation of motion

$$m \frac{dv}{dt} = Ap(t) \quad (5-1)$$

where m is the mass of the projectile, u is velocity, A is the effective area of the projectile and $p(t)$ is the actual pressure on the projectile. The mass of the projectile should be small and also either the pressure and/or the time of application of pressure must be large. Thus, the gas pressure or the length of the gun barrel must be increased. The pressure can only be increased until the limit of strength of either the projectile or the gun is reached. To increase time of launch the length of the barrel must be increased, but the length is proportional to the square of the launch time. Hence, it is desirable to increase the pressure to a feasible maximum. However, even well designed projectiles will only sustain pressures which are an order of magnitude lower than operational pressures of guns.

Ideally, the propulsive pressure should be kept constant during the launch period for maximum velocity. Practically, this is not possible, and even undesirable to do, but the "ideal gun" may be used as a basis for comparison of performance with real guns. The performance factor is defined as the ratio of the maximum base pressure to the average base pressure. Early light gas guns had performance factors as high as five, while that built at General Motors Defense Research Laboratory (1964) has a factor of two or less.

Another main constraint is the strength of the projectile. Acceleration distance-relation (Fig. 5-1) shows that an acceleration on the order of 10^6 g is required to accelerate a projectile to 30,000 to 40,000 fps in a distance of 20 feet. The stresses in a right cylindrical projectile (Fig. 5-2) for 10^6 g exceed the computed ultimate strength of most materials at a distance of one inch from the front face. From the simple design nomograph (Fig. 5-3) an aerodynamic projectile approximated by a cylinder one inch long, velocity 40,000 fps, material Al of 60,000 psi compressive strength gives a permissible acceleration of 620,000 g. The average acceleration is equal to the maximum acceleration divided by the performance factor. For a performance factor of two, the average acceleration is 310,000 g, and the length of gun required (Fig. 5-4) is 82 ft. For a gun of 300 caliber length this would require a 3.3 inch diameter. Velocity-projectile length relations for aluminum projectiles (Fig. 5-3) indicate that extremely large guns would be required for one inch projectiles at 40,000 fps.

The curves used above were found by Curtis (Ref. 45) to be roughly valid for approximate estimates of performance at the Ballistics Range of the General Motors Defense Research Laboratory. From this analysis three rules were established:

1. For given size and properties of the projectile, the minimum linear gun dimensions required are proportional to the square of the launch velocity, and the mass of the gun is proportional to the sixth power of the launch velocity.

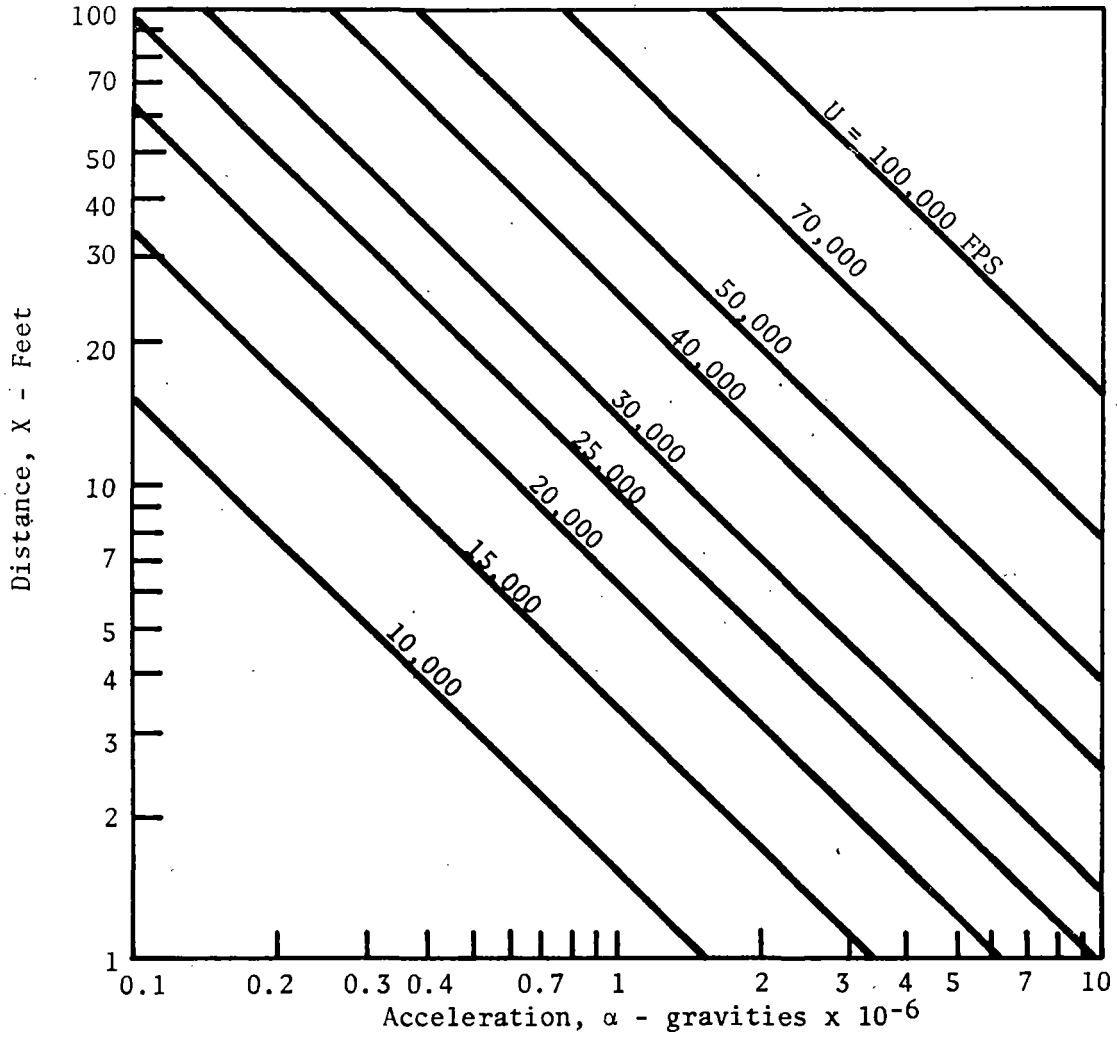


Fig. 5-1. Velocity - Distance relationship at constant acceleration.
(Curtis).

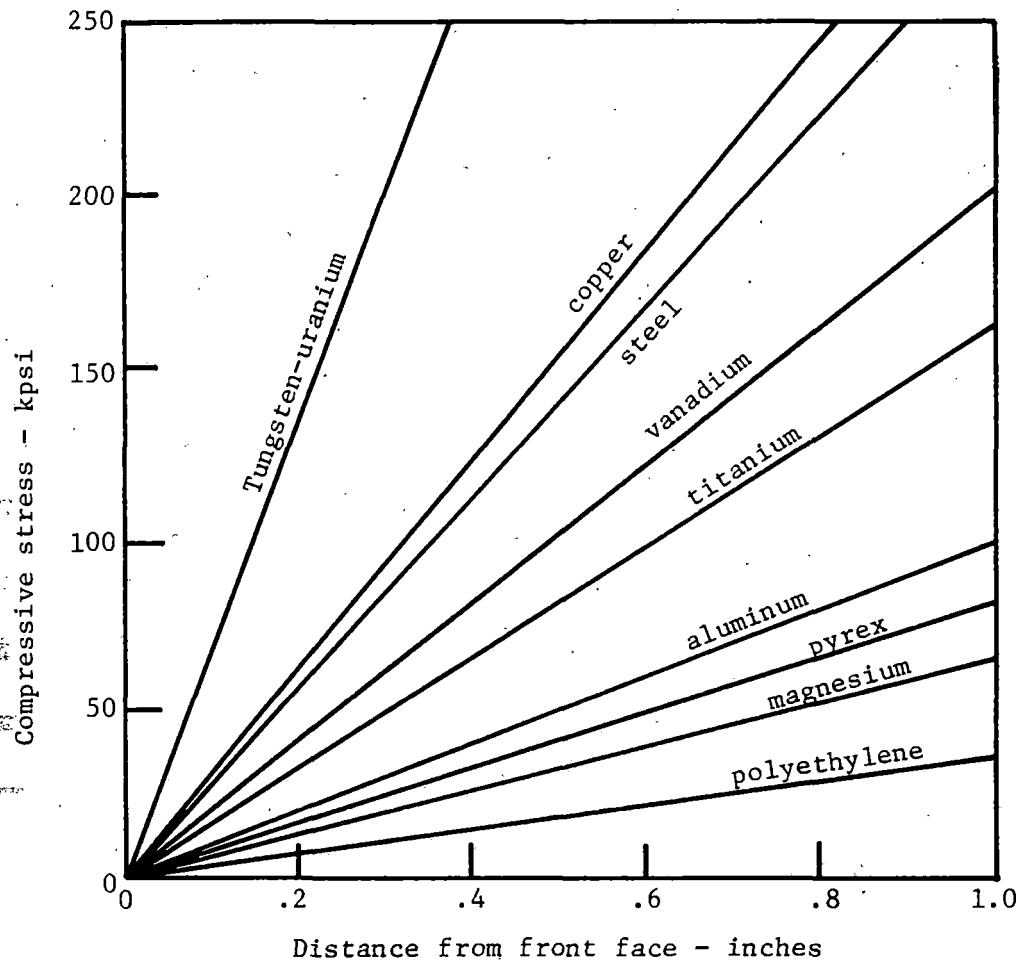


Fig. 5-2. Compressive stress as a function of distance from front of a cylindrical projectile accelerated by a force applied to one end, resulting in an acceleration of one million gravities. (Curtis).

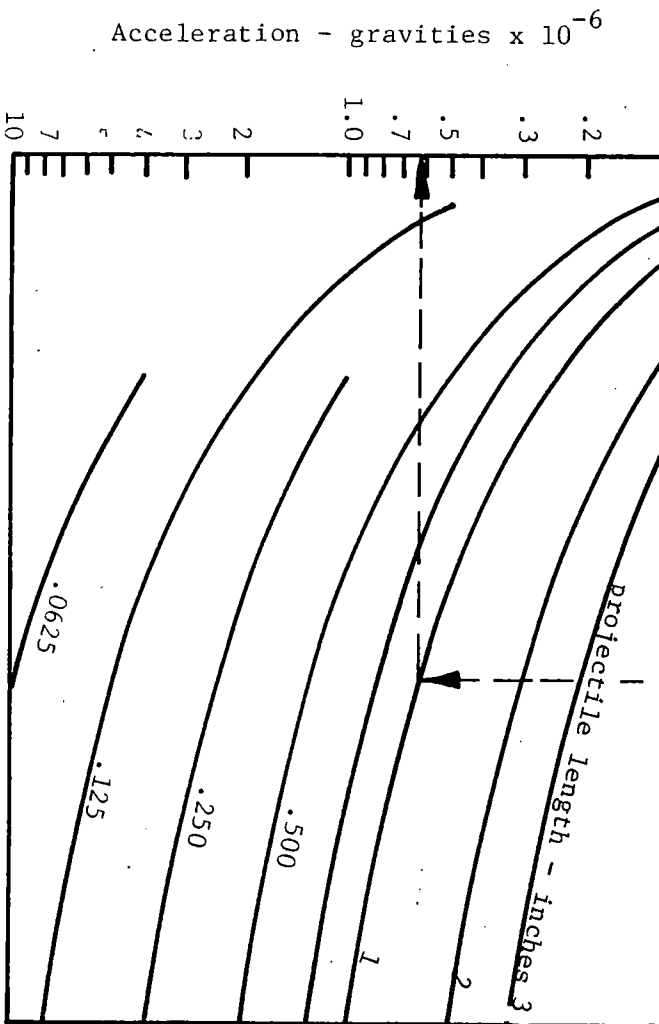
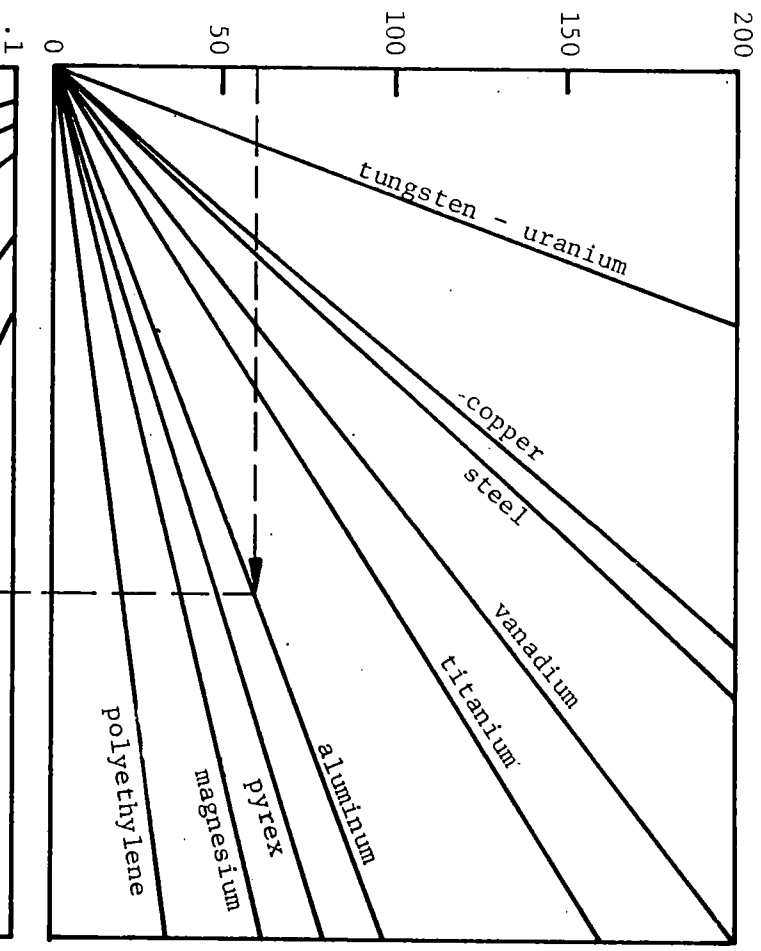


Fig. 5-3. Nomograph. (Curtis).

Compressive stress - kpsi



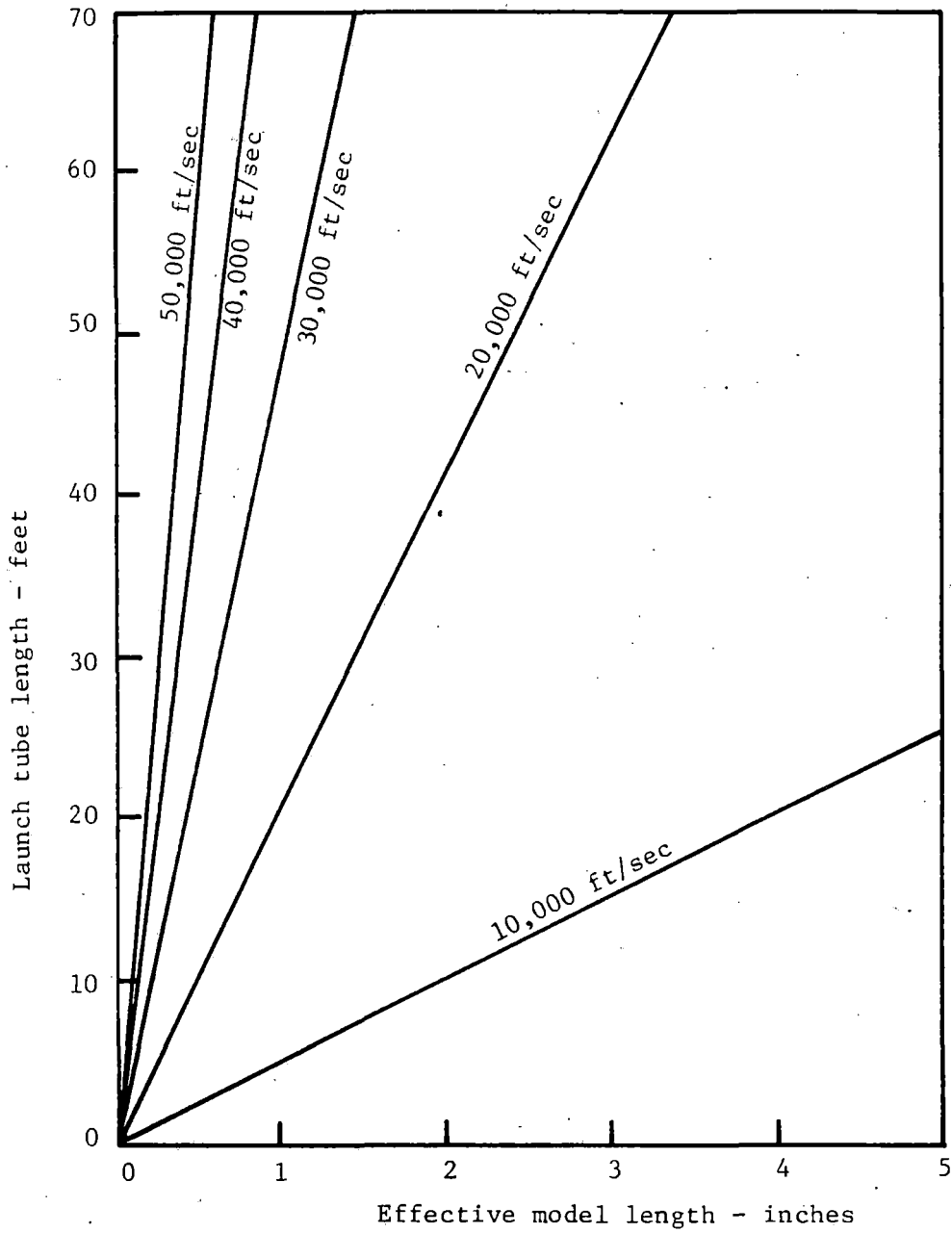


Fig. 5-4. Launch tube length required to launch aluminum models of various effective lengths. (Curtis).

2. For constant launch velocity the required linear gun dimensions are directly proportional to the length of projectile, and the gun mass is proportional to the projectile length.

3. For constant gun size the length of projectile for successful launch is inversely proportional to the square of the launch velocity.

The upper limit of velocities for discreet undeformed projectiles in March 1967 (Ref. 46) was about 35,000 fps for an 0.05 gm projectile. Jet spray velocities to 100 km/sec have been reported by Polish investigators (Ref. 47). The personnel at UTIAS (Ref. 48) have developed two types of explosion launchers.

The first has a driving chamber which is hemispherical in shape filled with an explosive mixture of gases such as diluted hydrogen and oxygen. The mixture is ignited at the center of the flat face of the hemisphere and the reflected shock waves from the walls of the container develop a high pressure at the ignition point, which is employed to accelerate a projectile.

A second method utilizes a high explosive liner inside the surface of the chamber, the whole being ignited simultaneously over its surface. The resulting explosion develops very high pressures at the center of the flat face of the hemisphere. The first mechanism (gaseous detonation) may be employed to initiate the second. The implosion of high explosives generated pressures an order of magnitude higher than those developed by reflected shocks. The more intense pressure is of short duration, however, and would place larger acceleration loads on the projectile causing deformation and fragmentation. Erosion may also cause serious problems.

CRATERING AND PENETRATION THEORIES

Herrmann and Jones (Ref. 49) published an excellent summary of data and theories on hypervelocity impact which had been developed to 1961. This was updated in 1963 (Ref. 50) but few new theoretical ideas were added. Much of the following is taken from these summaries, although in some cases the original sources were also reviewed.

The existing theoretical analyses were categorized by Herrmann and Jones into four groups based upon the simplifying assumptions involved:

I. Rigid projectile theory in which the projectile is assumed to be undeformed during penetration (low velocities).

II. Hydrodynamic theory, in which the projectile is assumed to have zero shear strength. The strength of the target is neglected or introduced as a correction factor.

III. Thermal penetration, in which the material is assumed to be removed by melting or vaporization.

IV. Explosive analogy, in which the crater formed is assumed to be identical to that formed by an equivalent mass of high explosive detonated at the surface of the target material.

I. Rigid Projectile

These theories were developed primarily for the penetration of thin targets and are not applicable to penetration of semi-infinite targets of either metals or rock. Qualitative information from them is of interest, however. Some propose that the projectile is slowed by fluid drag after which empirical armor penetration laws apply. Another assumed a similar drag force, with

an additional static force proportional to Brinell hardness. Still another suggested a model in which the projectile is separated from the rigid part of the target by a zone of incompressible fluid composed of both projectile and target material, which flows outward, eroding the target and forming a crater.

II. Hydrodynamic Theory

In conjunction with their studies of shaped charge jet penetration, Birkhoff, et al., (Ref. 51) proposed that since the pressures on the target are so much greater than target strength, shear forces can be neglected. The resistance to penetration is then due only to inertial forces required to accelerate the target material. Thus, the jet (projectile) and target are considered to be inviscid fluids, and, hence, theories based on this assumption are termed hydrodynamic (not to be confused with the hydrodynamic theory of shock waves).

It is noted (Ref. 49) that Bjork (Ref. 52) has offered one of the more complete solutions, in which he numerically integrated the two-dimensional equation of flow for a compressible inviscid fluid, utilizing an entropic equation of state for the material. Non-linear equations are involved, which could not be solved by analytical methods. Opik (Ref. 53) obtained a simplified solution, assuming that the projectile and target are incompressible, and are included as correction for target strength. For jets the theoretical development is more simple if a fluid jet or projectile-target condition is assumed and motion continues only while the jet impinges on the target. In this case lateral expansion of the crater after the jet stops is neglected. Such theories are only approximate, and apply only to jets or long slender rods, but are useful in estimating penetration by short projectiles.

Bjork's theory (Ref. 52) utilizes an entropic equation of state relating the internal energy, pressure and specific volume, but neglects the strength of the material. Conditions were for normal impact of a cylindrical projectile. Equations of motion for fluid flow, together with initial conditions of zero for all parameters except projectile velocity, were solved numerically using a space mesh for 25 x 25 cells (Figs. 5-5 and 5-6). Calculated results are approximately represented by

$$h/d = kv^{1/3} \quad (5-2)$$

where \underline{d} is taken as

$$d = (\pi r^2 L)^{1/3} \quad (5-3)$$

and

$k = \text{constant}$

$v = \text{projectile impact velocity}$

$p = \text{crater depth - penetration}$

$d = \text{projectile diameter}$

$L = \text{projectile length}$

The quantity \underline{d} is taken as the representative dimension of the projectile.

Opik's theory (Ref. 53) makes allowance for target strength, considers an incompressible projectile ($L/d=1$) of radius \underline{r} , density ρ_p , mass m_p and velocity \underline{v} impacting a target of density ρ_c . The projectile shape after time t_0 is defined by penetration \underline{h} and radius \underline{r} of the crater occupied by the projectile, where

$$2\pi r_p^3 \rho_p = 2\pi r_c^2 (h-\bar{h}) \bar{\rho}_p \quad (5-4)$$

Pressure Contours and Velocity Field

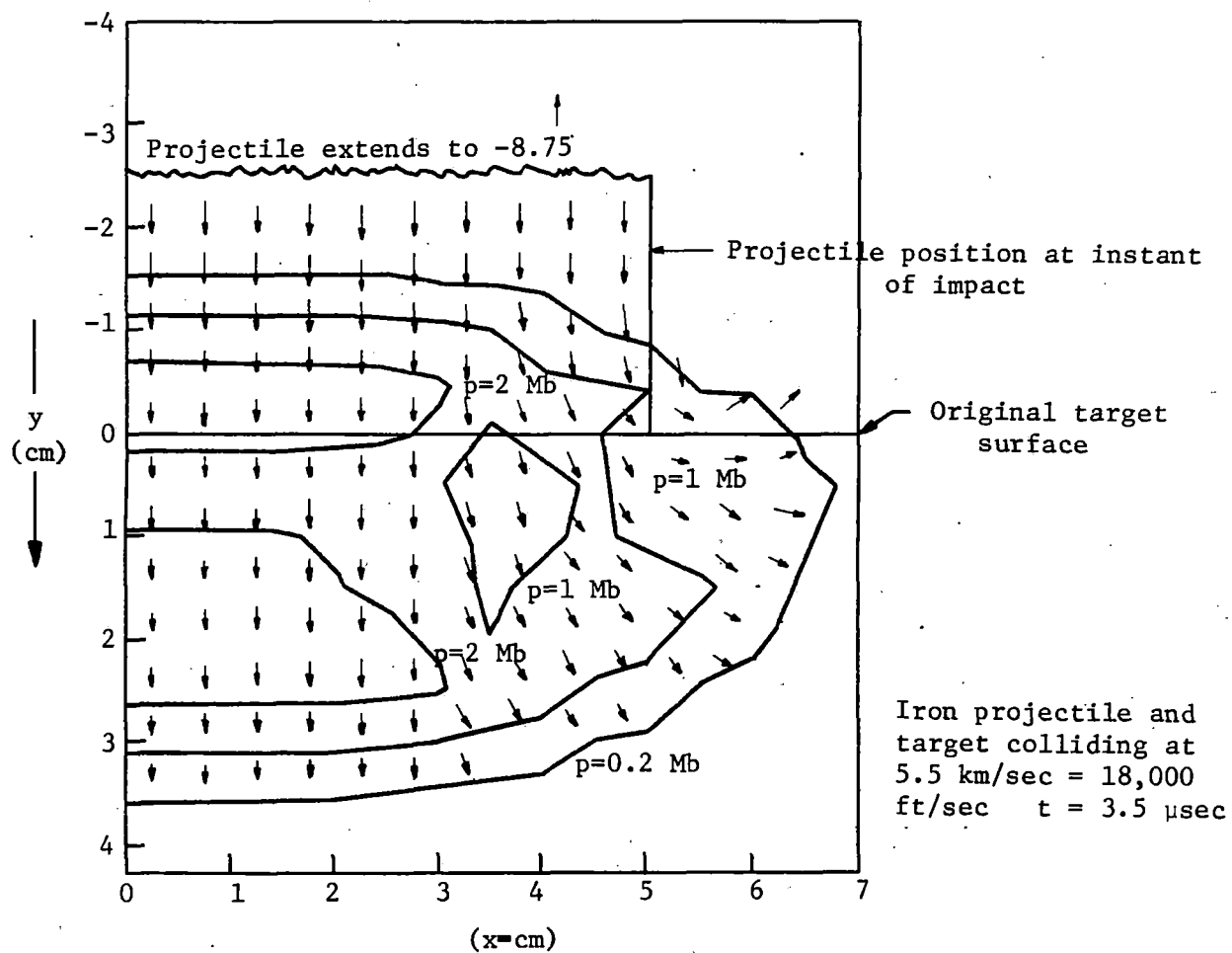


Fig. 5-5. Numerical solution of penetration of an iron projectile into an iron target, neglecting material strength. (Bjork).

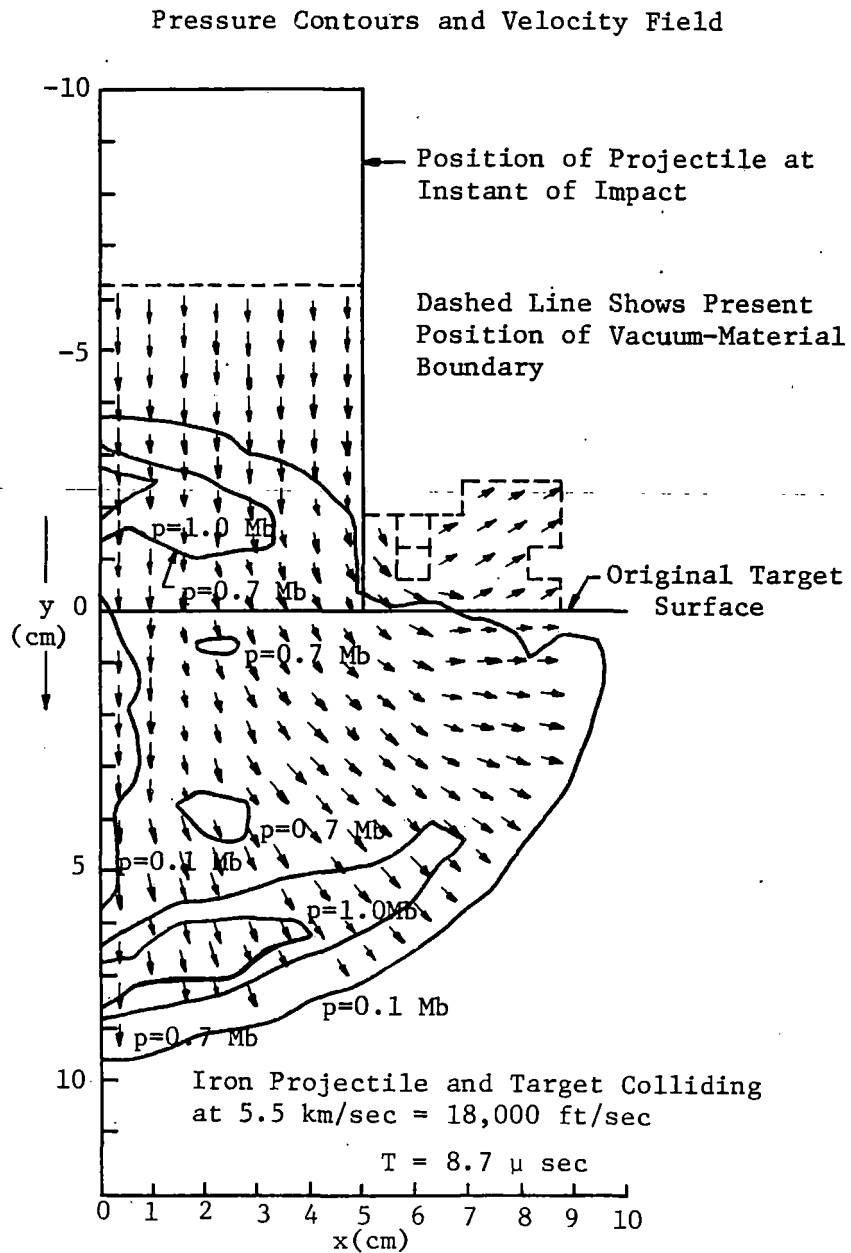


Fig. 5-6. (Fig. 5-5 continued). (Bjork).

where \bar{h} is the depth of the center of gravity of deformed projectile below the original target surface. The equation for momentum is then

$$m\ddot{h} = -\pi r_c^2 p_c \quad (5-5)$$

where p_c is the pressure at the bottom of the crater which resists penetration.

Application of Bernoulli's theorem results in

$$p_c = 1/2 \rho_t \dot{h}^2 + k \quad (5-6)$$

where k is the minimum pressure at which penetration will occur. Likewise, for radial expansion

$$p'_c = 1/2 \rho_t \dot{r}^2 + k \quad (5-7)$$

\underline{p} and \underline{p}' are related by use of Bernoulli's equation in the coordinate system moving at a velocity \underline{u} :

$$p_c = p'_c + 1/2 \rho_p \dot{r}^2 \quad (5-8)$$

Since \underline{u} represents unsteady flow this represents only a rough approximation.

Elimination of \underline{p} from the above yields a differential equation.

Jet penetration from shaped charges (see Chapter VI) is of particular interest in this study because of research that has been performed on rock. Its possibilities for practical use have not been fully explored.

Spherical and cylindrical projectile behavior has been approximated by jet theory. Because the jet pressure is several times the dynamic strength of target and projectile material, shear resistance is negligible and materials are regarded as incompressible fluids.

As a first approximation Birkhoff (Ref. 51) considers also that the flow is steady with respect to a coordinate system moving with the jet-target interface at a velocity \underline{v} .

The stagnation pressure, by Bernoulli's equation is

$$p = 1/2 \rho_t v^2 = 1/2 \rho_p (v_j - v_i)^2 \quad (5-9)$$

where

p = stagnation pressure

ρ_t = target density

ρ_p = projectile density

v_i = velocity of interface

v_j = jet velocity

Rostoker (Ref. 54) added a factor for target strength k ,

$$1/2 \rho_t v^2 + k = 1/2 \rho_p (v_j - v_i)^2 \quad (5-10)$$

and Eichelberger (Ref. 55) utilizes

$$k = 1/2 \rho_p v_o^2 \quad (5-11)$$

where v_o is the minimum or threshold velocity for cratering to begin. Initial theoretical developments assumed that the velocity of the jet from a conical liner was constant and is of interest because of the basic mechanics involved. For constant velocity v , density ρ_p and length L , most of the penetration h is assumed to occur as a result of steady motion, so, approximately the penetration is simply

$$h = \int_0^{t_1} v dt \quad (5-12)$$

there t_1 is the time from initial impact, i. e.,

$$t_1 = \frac{p+L}{v} \quad (5-13)$$

From these equations

$$\frac{h}{L} = \sqrt{\frac{\rho_p}{\rho_t}} \left\{ \frac{1 - \sqrt{\frac{\rho_p}{\rho_t}} \left[1 - \left(\frac{v_0}{v} \right)^2 \left(1 - \frac{\rho_p}{\rho_t} \right) \right]}{\sqrt{1 - \left(\frac{v_0}{v} \right)^2 \left(1 - \frac{\rho_p}{\rho_t} \right)} - \sqrt{\frac{\rho_t}{\rho_p}}} \right\} \quad (5-14)$$

When the jet has a very high velocity

$$\frac{h}{L} = \sqrt{\frac{\rho_p}{\rho_t}} \quad (5-15)$$

Another hypothesis by Pack, et al., (Ref. 56) utilized the dynamic yield strength \underline{Y} to give

$$\frac{h}{L} = \sqrt{\frac{\rho_p}{\rho_t}} \left(1 - \frac{\alpha_1 Y}{\rho_p v^2} \right) \quad (5-16)$$

where α_1 is an empirical function of the material densities, the correction term being about 0.3 for armor. This last formula does not account for lateral expansion, so another term was added:

$$\frac{h}{L} = \sqrt{\frac{\rho_p}{\rho_t}} \left(1 - \frac{\alpha_1 Y}{\rho_p v^2} \right) + \frac{r}{L} \quad (5-17)$$

Cook (Ref. 3) estimated the radius of the hole by assuming that the impulse received by the target is utilized in lateral expansion, and proposed the formula

$$\frac{\pi}{2} \rho_p (v_j - v_i)^2 r_j^2 \Delta t = (1/2 \rho_t \dot{r}^2 + k) \pi r^2 \Delta t \quad (5-18)$$

where

r_j = radius of jet

r_c = radius of crater

The final cross-sectional is found for $\dot{r}_c = 0$, or

$$r = r_j (v_j - v_i) \sqrt{\frac{\rho_p}{2k}} \quad (5-19)$$

and elimination of v_i from the above equation gives the radius of the hole.

Thermal Penetration

When this mechanism is assumed to dominate, penetration is accomplished by melting or vaporization of the target as the kinetic energy of the projectile is changed to heat.

Whipple (Ref. 57) assumes that the crater is a right circular cone of apex angle 60° and fixes the depth of penetration as

$$h = \left(\frac{9m_p}{2\pi\rho_t} \right)^{1/3} \left(\frac{v_i^2}{Q_t} \right)^{1/3} \quad (5-20)$$

where Q_t is the latent heat of fusion.

Langton's (Ref. 58) theory is similar. It is assumed that if both the target and projectile melt for a hemispherical crater the penetration is

$$\frac{h}{d_e} = \left(\frac{1}{8} \frac{\rho_p}{\rho_t} \right)^{1/3} \left(\frac{v_i^2}{Q_t} - 2 \frac{Q_p}{Q_t} \right)^{1/3} \quad (5-21)$$

Explosive Analogy

This theory, proposed by several investigators, stipulates that the crater formation by high velocity impact is similar to crater formation by high explosives. The theory appears to apply to some materials.

Empirical Relations

Several empirical relations have been proposed in place of inadequate theories. Many of these take the form:

$$h = (km_p)^x (v_p)^y \quad (5-22)$$

where

m_p = projectile mass

v_p = projectile velocity

Some of these apply only to low velocity armor penetration, while others have been applied at higher velocities.

A list of a number of the empirical formulas which have been found to fit data for given materials is summarized in Ref. 49.

Penetration - General

Herrmann and Jones (Ref. 49) give a fairly complete qualitative description of the phenomena occurring in hypervelocity impact as well as a critique of the various formulas.

Photographic and other types of observation indicate that at first impact the conditions may be estimated by one-dimensional shock theory.

Hugoniot conditions govern shock wave phenomena into the target and back into the projectile. Acoustic approximations lead to large errors. A critical velocity exists when projectile velocity exceeds the velocity of the shock back into the projectile, which is a function of densities and compressibilities of the materials.

At low velocities the impact pressure is of the same order as the dynamic yield strength of the target and in this regime penetration is strongly influenced by the relative material strengths and brittleness.

Thus, three regions are commonly defined: 1) a low velocity region where the projectile suffers only minor deformation, 2) a transition region, and 3) a high velocity or fluid impact region. Penetration is nearly proportional to the $4/3$ power of the velocity in the low region and to the $2/3$ power in the high velocity region. Most data available for thick or infinite targets are in the transition region and below.

When impact occurs in the latter region, a fine spray of material is forced out of the crater in ductile materials. Solution of the flow, shock and state equations for an inviscid fluid show shock and rarefaction systems similar to those observed by photography.

Relative shock velocities affect depth of penetration. If the shock in the projectile is carried below the surface, greater penetration is expected. However, if the projectile shock proceeds above the target surface, a wider shallow crater may occur. Brittle targets tend to fracture around the lip due to elastic springback.

Material subjected to intense transient pressure may be heated above the melting point and some of it easily ejected from the crater. Some materials show signs of recrystallization after melting. Severe plastic deformations and shock twinning are also evident.

Of the various hydrodynamic theories Herrmann and Jones (Ref. 49) discuss only Bjork's and Opik's in relation to the available hypervelocity penetration data. Bjork's numerical solutions based on fluid dynamics are (1961)

for only two metallic combinations, Al in Al and Fe in Fe. Solutions contain no adjustable constants, material property constants being evaluated by measurements. The assumption that material strength is negligible makes the theory applicable only at high velocities. Herrmann and Jones plotted all data based on an "equivalent sphere,"

$$d_e = \left[3/2d^2L \right]^{1/3}$$

For low velocities, values for Al and steel targets fall in Bjork's curve, but other alloys fall below. The experimental points also indicate a steeper slope than $(v)^{1/3}$. No data are available to check agreement at higher velocities. Opik's theory contains an adjustable constant for threshold velocity, but agreement between his theory and experimental results is rather poor.

The first order penetration theory for shaped charge jet theory appears to apply only at high velocities, but no other correlations were plotted or postulated by Herrmann and Jones.

Of the thermal penetration theories, Whipple's theory overestimates the penetration in metals, Langton's underestimates it and Grow's theory grossly overestimates penetration at all but lower velocities. None of these theories take mechanical properties into account.

Projectile strength appears to have little effect on penetration above the transition region, where density is a dominant factor. On the other hand, Herrmann and Jones (Ref. 49) state that there is strong evidence to indicate that penetration depends upon target strength over the entire range covered by data available in 1961 for velocities up to 4.7 km/sec. More recent data on metals appear to be largely for thin targets. The diameter of the crater varies

with different materials, the ratio h/d_c increasing with increase in velocity for copper and lead to a value of 0.5. For Al, Mg and nylon projectiles the upper asymptotic value is about 0.4. For tungsten carbide the ratio increases in an anomalous manner to 2.0 for copper target at 3000 ft/sec and decreases to 0.8; to 1.2 for steel 1020 target at 3060 ft/sec and then decreases to 0.9; and 2.3 for a lead target at 1500 ft/sec and decreases to 0.5 for higher velocities.

IMPACT EXPERIMENTS - METALS

There has been a large number of experiments performed in efforts to obtain very high velocity projectiles on a variety of targets, primarily aluminum. Selected results are given from those projects which appeared to have information that would shed some light on the effects of impact of projectiles on rock.

Marnell, et al.

Marnell, et al., (Ref. 59) have classified the nonviscous theories of penetration in which strength is ignored as being (1) hydrodynamic, and (2) explosive shock. The principles utilized in these developments are based upon fluid dynamic formulas which are employed to describe the flow field, upon which are imposed selected criteria to limit the final dimensions of the crater. While strength may be ignored in the flow process, it is often a boundary condition used to stop the flow process. Under such assumed processes the theory as well as the non-unique boundary condition may yield a wide variety of results.

The hydrodynamic approach utilizes Eulerian equations of compressible, inviscid adiabatic flow for continuity, momentum and energy. The configuration is that of a right circular cylinder impacting a semi-infinite medium of the same material. Analytical solutions have not been obtained, so finite difference methods are employed for machine computation.

In Bjork's method (Ref. 60) the limit of the crater is the distance at which a pressure pulse occurs of negligible velocity and pressure. Calculated results are presented in pictographic form, and give for both iron and aluminum the following:

$$h/d = kv^{0.32} \quad (5-23)$$

which implies that the crater volume is proportional to the momentum of the projectile.

Walsh (Ref. 34) on the other hand, while employing the same computational scheme, assumes two scaled impacts of equal potential energy, and that the final crater radii are equal. This results, adjusting for "late stage equivalence" in

$$h/d = kv^{0.62} \quad (5-24)$$

The exponent is independent of the material properties, but the constant k depends upon the strength and thermodynamic properties of the target.

Explosive shock studies are based upon an analysis of a spherical shock in a gaseous medium by Taylor (Ref. 61). He ignores conditions at the instant of the explosion, and assumes a finite amount of energy is generated at a point. For large pressures the same hydrodynamic equations employed by Bjork apply, subject to shock conditions, for an ideal gas at constant specific

heat. The results show that the spatial distribution of the flow-field is independent of time if all radii are scaled to the shock radius.

Ray and Kirchner (Ref. 62) similarly assume a point source of energy on the surface of a semi-infinite mass. Taylor's solution is modified to account for density changes at the shock front, energy conservation being the dominating process, and momentum is not conserved. Their analysis likewise leads to

$$h/d = kv^{2/3} \quad (5-25)$$

where the constant k depends upon target and projectile properties.

Dauids (Ref. 63) employs a model of two moving surfaces, the shock front and the expanding crater. From his analysis there results

$$h/d = kv^{2/5} \quad (5-26)$$

where k is independent of target strength.

In his critique, Marnell (Ref. 59) states that "Bjork uses a no strength criterion. His flow-field calculations may have a bounded stability. Walsh assumes late stage flow-field equivalence and calculates relative penetrations. The procedures are certainly different; both are open to question..."

Marnell (Ref. 59) employs a different approach. He assumes (1) one-dimensional flow-field, (2) negligible strength in flow, but strength criteria for crater limit, (3) flow is inviscid and adiabatic, with viscosity and heat transport in the shock front, and (4) the adiabatic pressure density relationship is $p^{-\gamma} = \text{constant}$. Lagrangian coordinates are used to express flow and shock equations. For appropriate initial and boundary conditions separation of variables, operational or similarity methods of solution are not applicable and a

series expansion method is employed for solution. The tentative criterion for crater depth is the position of the shock front when the pressure drops below the dynamic yield stress, values of which are yet to be determined. The flow-fields determined by this method are non-similar, and it is believed that a spherical geometry will yield more meaningful results.

Riney

Riney (Ref. 64) proposed a viscoplastic model which accounts for inertial, viscous and plastic effects, by introducing viscosity and dynamic yield stress into the ideal fluid equations. Several dimensionless parameters were found which affect the relative importance of properties at various stages in the cratering process. The inertial effect is important during early stages, while target strength is dominant in the final stages of crater formation.

The viscous effect is large near the contact interface immediately after impact. While its magnitude decreases as the strain-rate gradient decreases, it may be important throughout the whole process. Riney also indicates that viscosity also introduces anisotropic stresses which are essential to the strength effect. The assumption of viscosity results in large initial pressure and deformation, the width of the pressure profile is increased.

The shape and size of the final crater, according to this model, are determined by (a) the shape and amplitude of the pressure wave established during the first five or ten microseconds, (b) the resistance of the target to flow, and (c) the continuation of flow until the pressure decreases below the intrinsic yield strength of the target material.

In turn it is proposed by Riney that the shape and amplitude of the pressure wave (a) are strongly dependent on viscosity, (b) the resistance of the target to flow depends on the viscosity and to a lesser extent on the yield strength, and (c) the yield strength factor controls the instant when flow ceases.

Wall (Ref. 65) points out that when a projectile impacts a massive target at greater than "critical fracture" velocity, it breaks up or "shatters." For some materials this consists of extensive fracture, in others deformation without rupture. He also recognizes the low speed, transition and high speed regimes, but his analysis applies to the low speed and transition regimes.

One critical velocity is that at which the impact induced stresses exceed the strength of the projectile material and suggests the following form of equation:

$$v_s = \frac{H\sigma_p}{\rho_t c_t} \left(1 + \frac{\rho_t c_t}{\rho_p c_p} \right) \quad (5-27)$$

where

v_s = critical velocity

σ_p = ultimate strength of projectile

H = projectile shape factor

ρ_t = density of target

ρ_p = density of projectile

c_t = velocity of sound in target

c_p = velocity of sound in projectile

Wall postulates three regimes, a low-speed, a transition and a high-speed regime, and that brittle fracture may occur in any of them depending upon material properties. His mathematical theory is based upon average velocity-density terms, Newton's law, shock parameters and certain material properties. A different law is applied to each regime, the boundaries between regimes depending upon the properties of the projectile and the target. The equations used for low-speed and high-speed are similar.

Wall (Ref. 65) concludes that:

- 1) Penetration depth increases approximately linearly with projectile density, length and impact velocity.
- 2) Depth increases with strength (hardness) of target material.
- 3) Depth is inversely proportional to effective target density and sound speed.
- 4) Projectile shatter velocity varies linearly with projectile strength.

Hopkins and Kolsky

In an earlier (1960) consideration of the mechanics of hypervelocity impact Hopkins and Kolsky (Ref. 66) noted that the unsteady motion produced involves a complex combination of different physical regimes characterized by elastic and plastic deformation, incompressible and compressible flow, and explosion conditions at high velocities. This imposes a severe compromise on the representation of real processes by mathematically tractable theory, and only a limited degree of accuracy is possible. Hopkinson's law of scaling of explosions is suggested as having a possible limited application.

Hopkins and Kolsky also enumerate five sets of physical properties of importance: (1) elastic behavior, (2) plastic behavior, (3) density, (4) variable compressibility, and (5) thermal properties.

They also propose five regimes in which these properties tend to be dominant.

Regime A - elastic. At low velocities with stresses below the yield point these will be elastic rebound or the problem will be of Hertzian character. Three or more types of elastic waves will be generated in the half space (target).

Not mentioned by Hopkins and Kolsky is the elastic region that will exist at higher velocities where the stress waves generated in the target beyond the crater will be lower than the yield stress.

Regime B - plastic. At higher velocities where the stress in the projection target is beyond the yield point plastic deformation will occur. As the velocity is increased progressively more energy will be expended in plastic work. In brittle targets the deformation will take place as the result of fracture due to tensile stresses rather than flow due to shear stresses.

Regime C - hydrodynamic. At progressively higher velocities the stresses are very much beyond the yield point and the target and/or projectile may act as a fluid. This phenomena may occur over a wide range of velocities.

Regime D - sonic impact. As the velocity of impact approaches the velocity of dilatation waves in the target, the stress waves in the target travel only a short distance during impact and such stresses play an important role in the behavior of the impact region.

In brittle materials impact at or near sonic velocity is of interest because the maximum velocity of crack propagation is about one-half of the velocity of dilatation waves. Hence, when penetration velocities are equal to or greater than the dilatation velocity, the hoop (tangential) tensions which cause radial cracks cannot travel far before the projectile passes and the stress is relieved. Hopkins and Kolsky illustrate this phenomena with a block of plastic penetrated by a jet from a shaped charge at 6000 m/sec. In the upper part of the crater, penetrated by the high velocity portion of the jet damage was localized. In the lower part of the crater made by the slower portion of the jet extensive cracks were caused. Slabbing may also be generated by compressive waves reflected from free surfaces as tensile waves where the material is weak in tension.

Regime E - explosive impact. At supersonic velocities the volume of the target affected is comparable with the projectile volume. The kinetic energy of the projectile is sufficient to melt or vaporize both the projectile and a small volume of the target because the energy cannot be dissipated otherwise. For example, a steel projectile with a velocity of 10^4 m/sec has a kinetic energy of 2×10^4 cal/g, which is ten times the energy needed to vaporize the projectile.

Hopkins and Kolsky estimated the transitional velocities for several metals for the above regimes. (Table 5-1).

TABLE 5-1
TRANSITIONAL VELOCITIES (m/sec)

	Steel	Duralumin	Aluminum	Copper	Lead
v_1	46	65	13	8	2
v_1	360	430	190	130	40
v_1	4600	5300	5300	3750	2100

The velocity v_1 is calculated on the plausible assumption that the specific mechanical impedance of the target is ρc_1 , where c_1 is the dilatational velocity $[(k + \frac{4}{3} G)/\rho]^{\frac{1}{2}}$, and then $v_1 = Y(c_0 + c_1)/\rho c_0 c_1$, where $c_0 = (E/\rho)^{\frac{1}{2}}$; $v_2 = (Y/\rho)^{\frac{1}{2}}$ and $v_3 = (k/\rho)^{\frac{1}{2}}$.

Regime (a): $0 < v < v_1$; Regime (b): $v_1 < v < v_2$;

Regime (c): $v_2 < v < v_3$; Regime (d): $v_3 < v < 3v_3$ (approx.);

Regime (e): $v > 3v_3$ (approx.).

IMPACT DATA-METAL TARGETS

Selected data from the compilation by Herrmann and Jones (Ref. 49) were plotted for various types of projectiles and targets.

Data for several types of aluminum targets were employed (Fig. 5-7).

Some selected properties are:

Aluminum	1100F	2014	2024S	24ST	2024T3	2024T4
Density	2.79	2.79	2.80	2.77	2.68	2.77
Bulk Velocity (km/sec)	6.14	6.22	6.24	6.25	5.84	6.71
Brinell Hardness	----	135	110	114	126	120
Yield Strength kg/cm ²	----	2952	3304	----	3515	2881

Typical projectile properties are:

	Aluminum	Tungsten Carbide	Copper	Lead	Uranium	Steel	Nylon	Diamond	Magnesium	Pyrex Glass
Density	2.79	14.96	8.90	11.2	18.69	7.77	1.33	3.24	1.74	2.64
Bulk Velocity	5.84	6.72	4.42	2.0	3.13	6.25	----	----	5.52	----

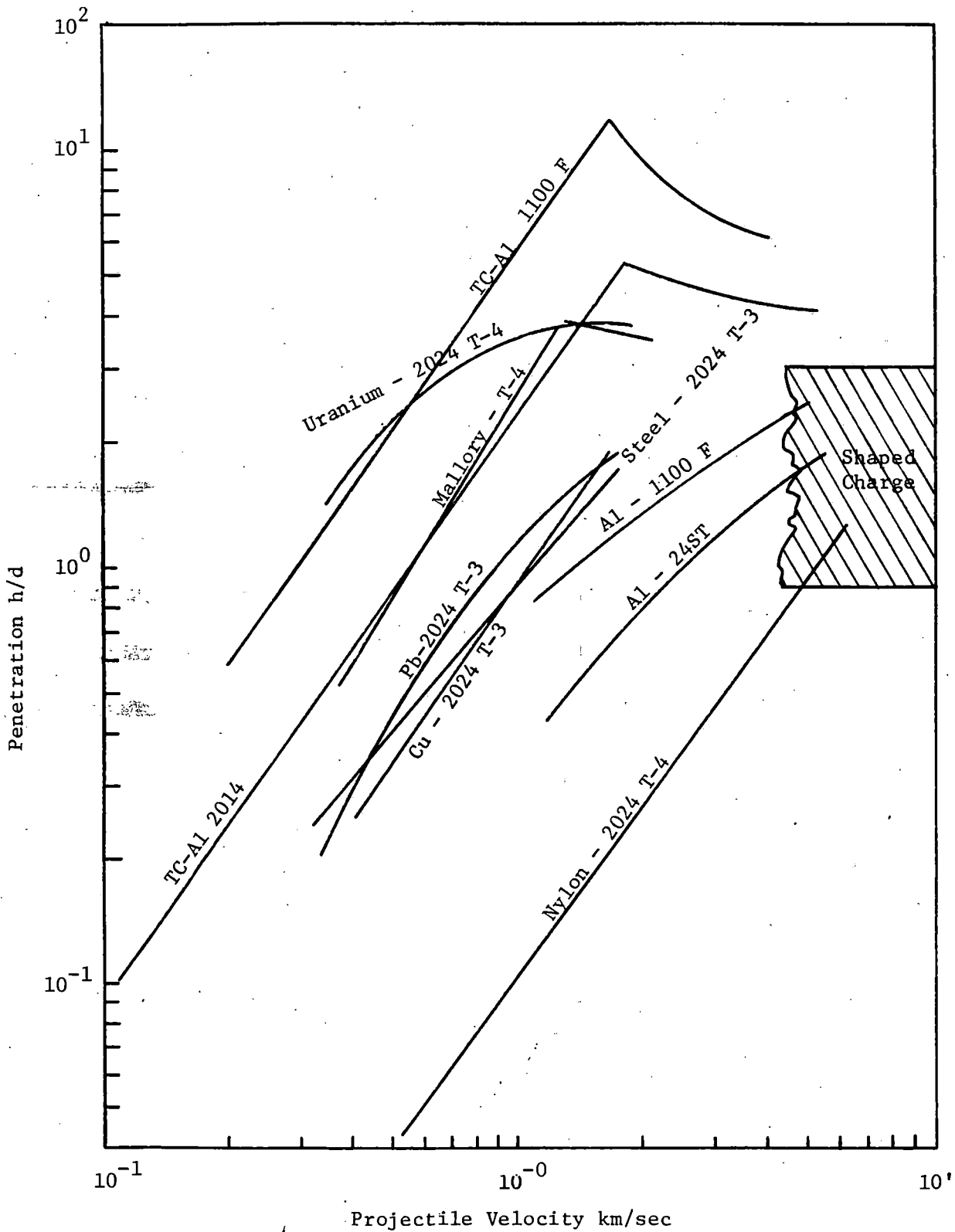


Fig. 5-7. Penetration of aluminum targets.

The penetration (Fig. 5-7) for tungsten carbide projectiles was greatest, which is probably partially accounted for by both its hardness and density. The penetration for uranium was approximately the same, but for a different type of aluminum target. The hardness and yield strength of Al 1100F are not given, but it appears to be softer and weaker than 2024 T-4. The ability to penetrate varies as some increasing function of the projectile density. At the right side of the graph is shown the theoretical penetration for shaped charge jets based upon the first order law, i. e.,

$$h/d = \sqrt{\rho_p/\rho_t} \quad (5-28)$$

for density ratios from about 0.95 to 9.0. It is noteworthy that all of the curves trend in general toward the shaded area for the density law penetration. The latter is known to apply only at very high velocities with an additional correction for target strength.

For lead targets (Fig. 5-8) the curves are less steep and with the exception of brass and copper projectiles. Tungsten carbide again shows the highest penetration. The trend for higher velocities appears to be above the theoretical shaped charge penetration zone. This may be partially due to the low yield strength of lead which is about 82 kg/cm².

For steel and beryllium copper targets (Figs. 5-9 and 5-10) the trend is somewhat similar; with lead projectiles exhibiting an anomalous behavior at low velocities.

Finally, a comparison was made of the effect of nylon projectiles on lead, aluminum and beryllium copper targets (Fig. 5-11). For the relatively low velocities involved the effect of the low strength of lead is apparent.

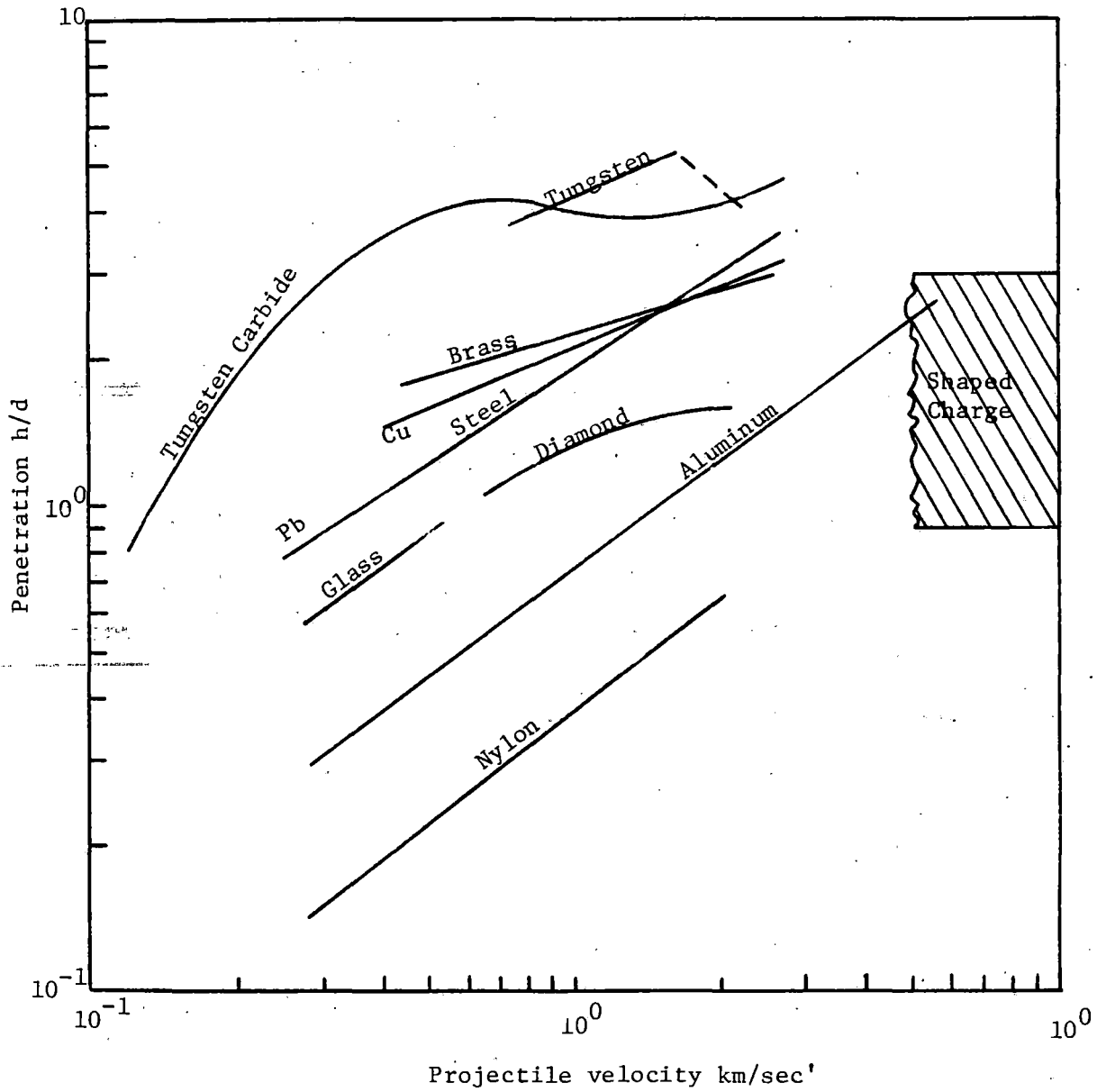


Fig. 5-8. Penetration of lead targets.

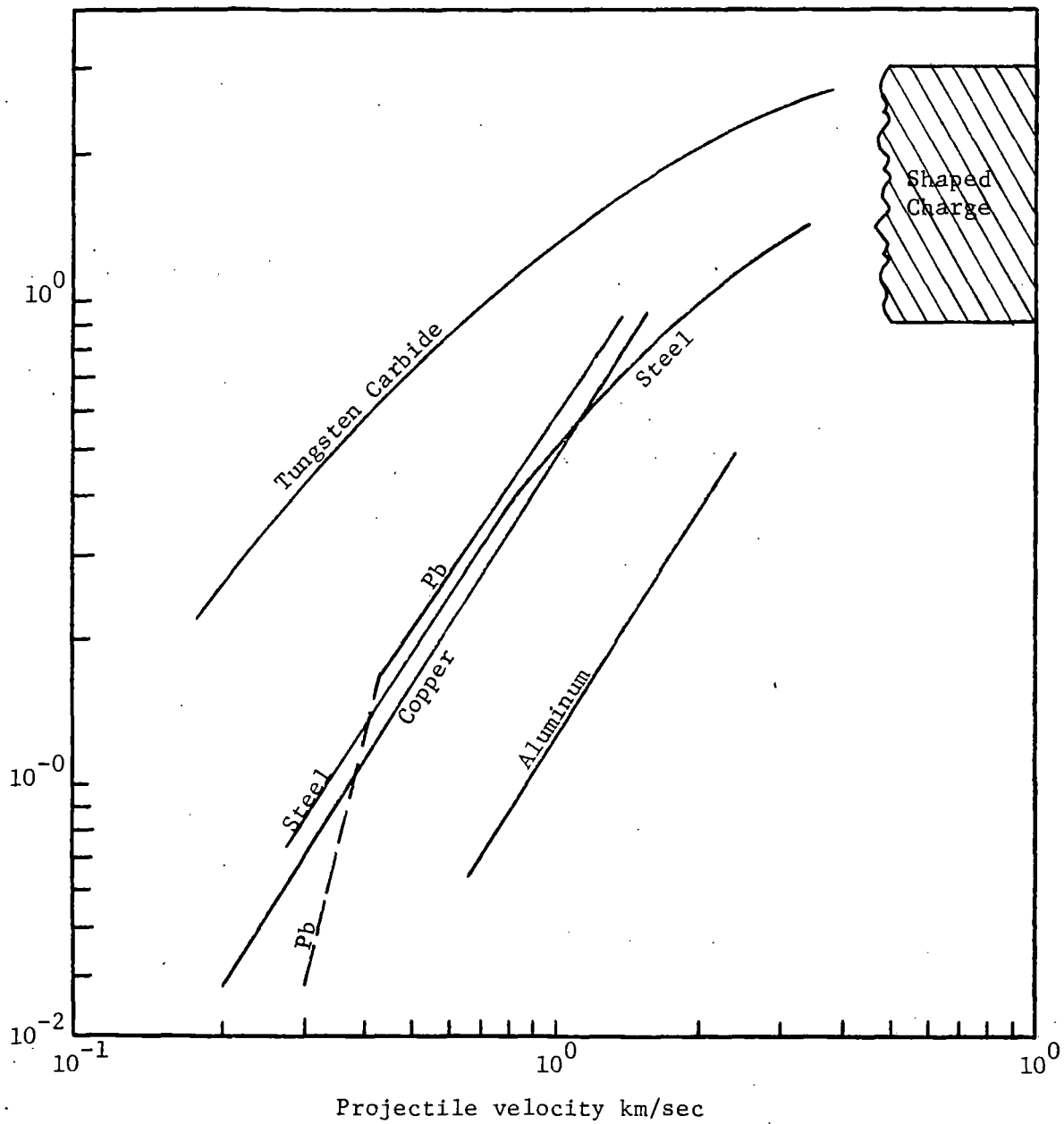


Fig. 5-9. Penetration of steel targets.

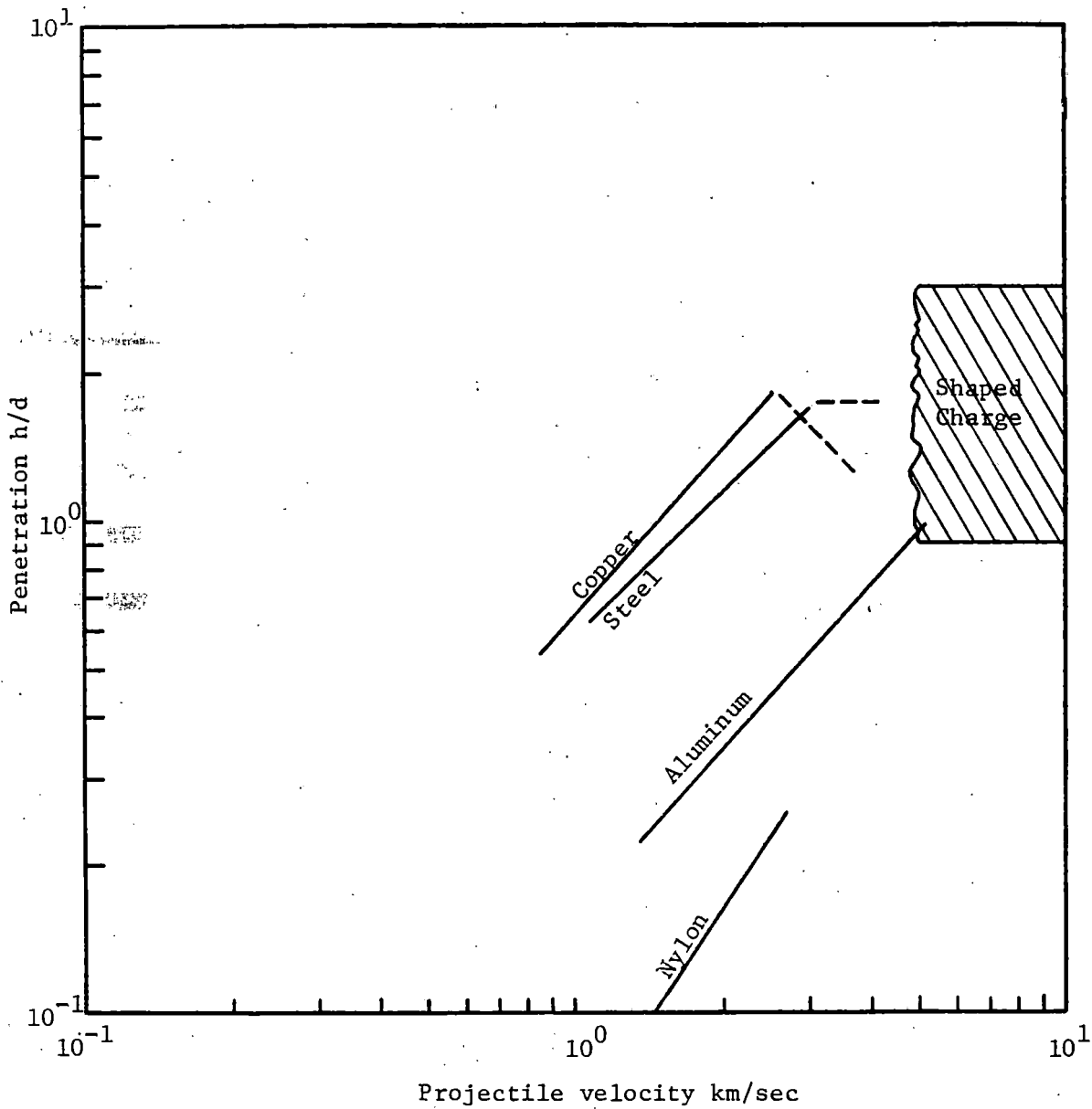


Fig. 5-10. Penetration of beryllium copper targets.

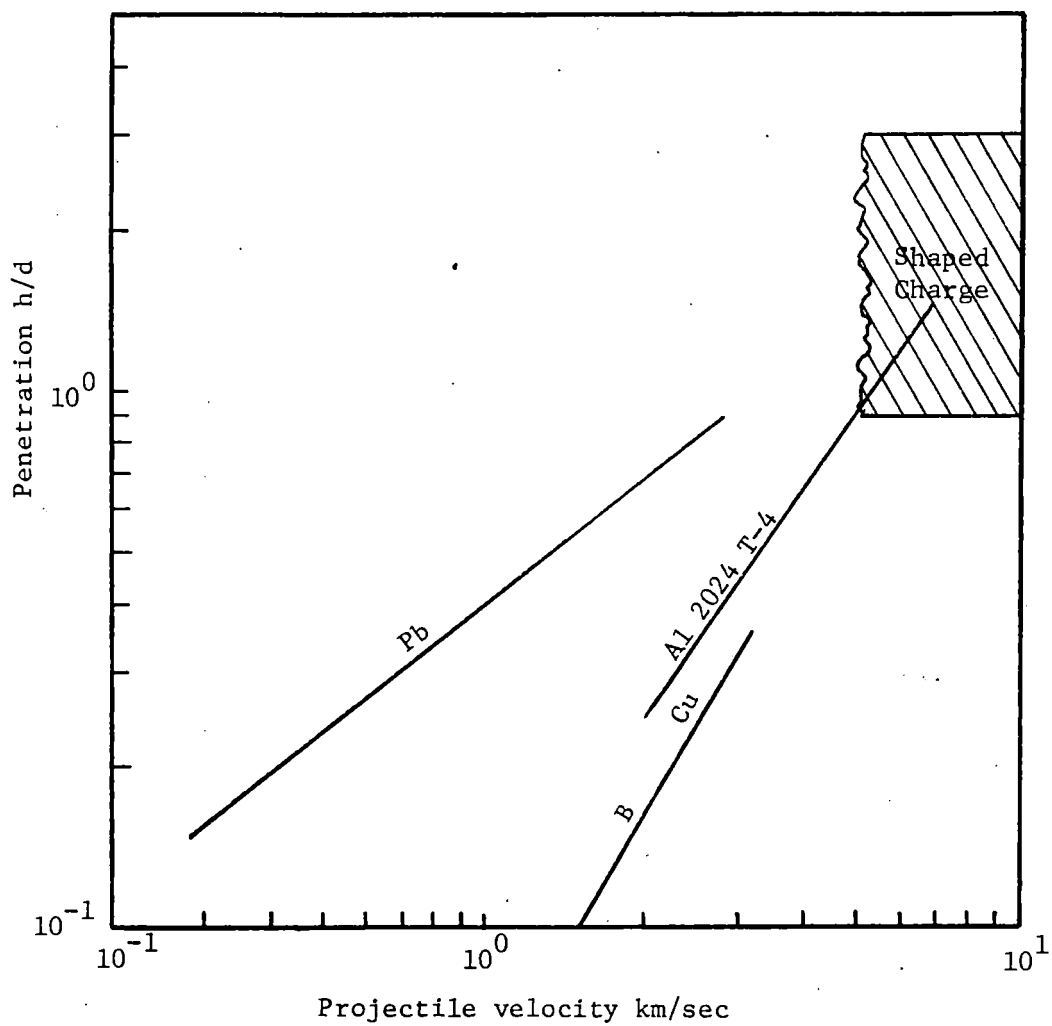


Fig. 5-11. Penetration of nylon in lead, aluminum and beryllium copper.

Other Investigators

Denardo, et al., (Ref. 67) performed experiments with 1/16, 1/8, 1/4 and 1/2 inch Al2017-T4 spheres on 2024-T4 and 1100-0 aluminum targets to determine diameter effects for velocities up to 28,000 ft/sec. The hypervelocity regime of impact was about 13,800 ft/sec. Dimensionless penetration p/d varied as projectile diameter to the 1/18th power. Momentum transfer from projectile to target was higher for the harder (2024-T4) aluminum.

Kinslow (Ref. 68) observed the effects of hypervelocity particles upon transparent lucite targets by Lexan projectiles. At high velocities the projectile embedded itself slightly and then appears to explode. A shock wave is formed accompanied by crushing and melting. The shock decays into an elastic pulse and needle-like fractures are formed. The melt solidifies and contracts producing radial tension fractures. Reflected waves may also cause subsequent fractures.

Because of the explosion-like phenomena it was found that the effects could be simulated by exploding No. 8 blasting caps on the surface of the plastic.

In studies of penetration of semi-infinite targets by rods, Christman, et al., (Ref. 69) found that target strength had a significant effect in the penetration transition region. Crater volumes are not dependent on length/diameter ratios. The crater volume creating efficiency of rods is greater for rods with l/d ratios of 3 than for spheres, and crater volume is not proportional to kinetic energy. Target strength influences cratering up to velocities of 15.7 km/sec, and may not be negligible at higher velocities.

Holloway (Ref. 70) reports that in hypervelocity studies on wax that for impact velocities of 4 km/sec craters reached a maximum depth at about 200 per second and then rebounded to 60 percent of their maximum depth.

Dignam and Rockowitz (Ref. 71) used acoustic impedance as a correlating parameter and found that in oxygen free copper several definite types of projectiles showed that penetration efficiency and cratering efficiency did not increase continuously with increasing projectile acoustical impedance.

Palmer and Turner (Ref. 72) established an energy balance equation for the cratering process:

$$E_k = E_n + E_s + E_r + E_e \quad (5-29)$$

where

E_k = projectile kinetic energy

E_n = heat of deformation, shock heating, and sound

E_s = thermal and kinetic energy of spray material

E_r = recrystallization and strain energy

E_e = lost energy

Techniques were devised to measure these types of energy for chrome-steel balls and lead targets, which are plotted in Fig. 5-12. At low velocities all of the energy goes into recrystallization, the amount going into spray increases as the velocity increases. Above 3.4 km/sec research results predicted that the partitioning remains essentially constant. Other empirical relations were derived.

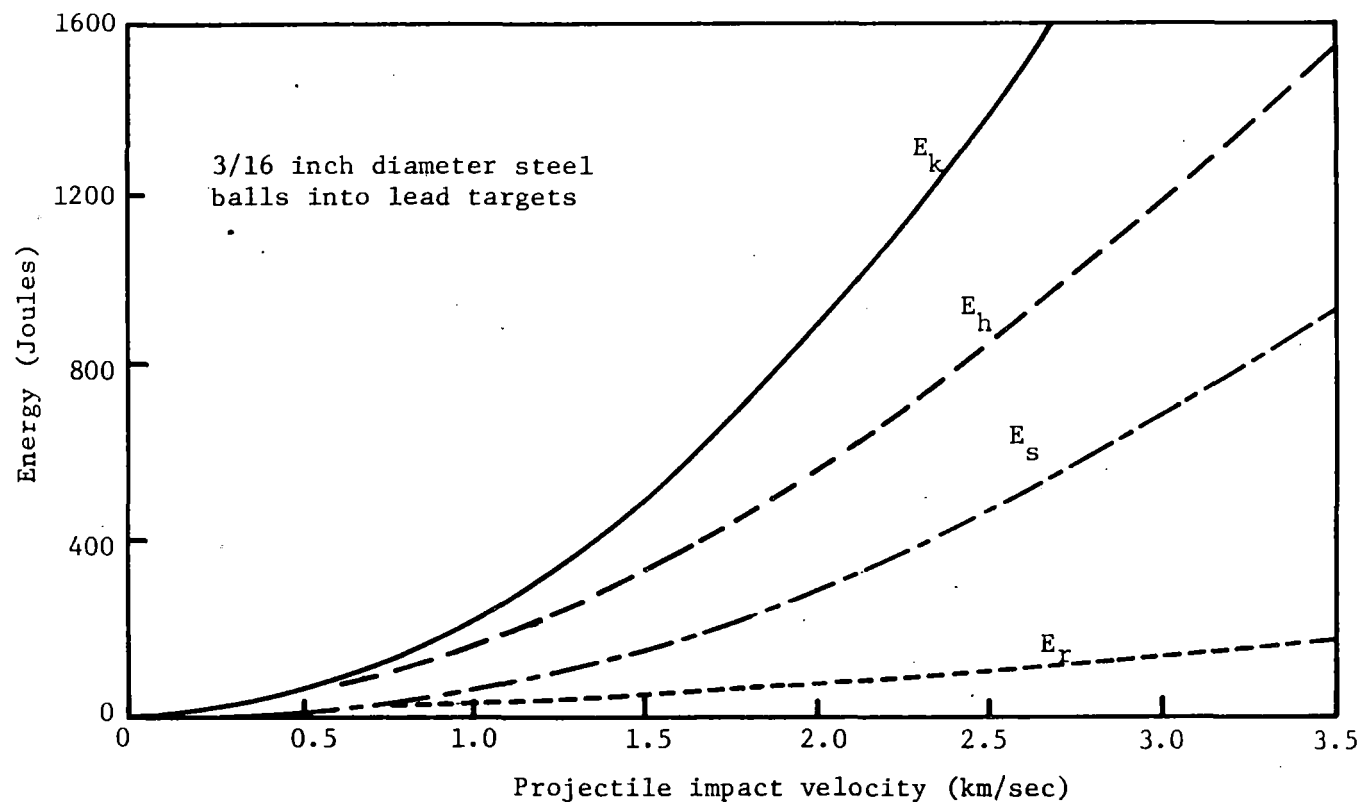


Fig. 5-12. Kinetic energy of impact, target-heating energy, spray-partile energy, and recrystallization energy plotted as functions of impact velocity.

Walsh and Johnson (Ref. 73) used numerical methods (SHELL code) to integrate hydrodynamic flow equations. For thick targets they reached the following conclusions:

(1) Crater dimensions increase as the impact velocity to the 0.58 power for velocities greater than twice target sound velocity.

(2) Above five times target sound velocity for projectile-target density at constant mass does not change target effects.

(3) Spherical and cylindrical (l/d ratio of one) are equivalent in effect except at early times. Larger ratios as large as three have no effect for velocities five times target sound or greater.

(4) Crater size is limited by target strength even at high velocities.

(5) The ratio of the total impact of the target to the momentum of the projectile varies as the impact velocity to the 0.74 power.

Using the PICKWICK code Reney and Heyda (Ref. 74) came to the conclusion that the depth of penetration for similar metals varies with the impact velocity to the 2/3 power.

Impact flash was employed by Rosen and Sully (Ref. 75) to determine the mass, temperature and velocity of projectiles. Color of the flash depended only slightly on projectile mass. Correlations were found between peak flash, velocity and depth of penetration.

Dietrich, et al., (Ref. 76) assume that a critical velocity exists at which the lattice structure of a metal is destroyed and the lattice rupture velocity is expressed by

$$v = \left(\frac{\sigma_m \epsilon_m - \phi}{\rho} \right)^{\frac{1}{2}} \quad (5-30)$$

where

ρ = density

σ_m = rupture stress

ϵ_m = rupture strain

ϕ = dynamic elastic energy

For a simplified model the quantity $(\sigma_m \epsilon_m - \phi)^{-1/3}$ is taken as a material parameter used in a penetration law in place of an empirically determined constant.

Gehring, et al., (Ref. 77) utilizes a phenomenological model for crater formation, divided into four regimes: (1) initial transient including flash, (2) primary penetration, due to direct action of projectile, (3) cavitation during decrease in pressure, and (4) recovery regime including spallation and pressure recovery (Fig. 5-13). Shock pressure, momentum transfer and crater growth measurements were made and some correlations obtained with material properties.

From tests conducted with steel projectiles on aluminum and lead targets, Sorensen (Ref. 78) concluded that the normalized crater volume data may be correlated by an equation involving only the density of the projectile, and the density and static shear strength of the target. Velocities ranged up to 7 km/sec.

This conclusion does not agree with analysis of a wide range of data for a larger number of materials by other investigators.

Among brittle materials that have been tested, beryllium and graphite were impacted with small spheres at 25,000 fps (Ref. 79). Cracking damage

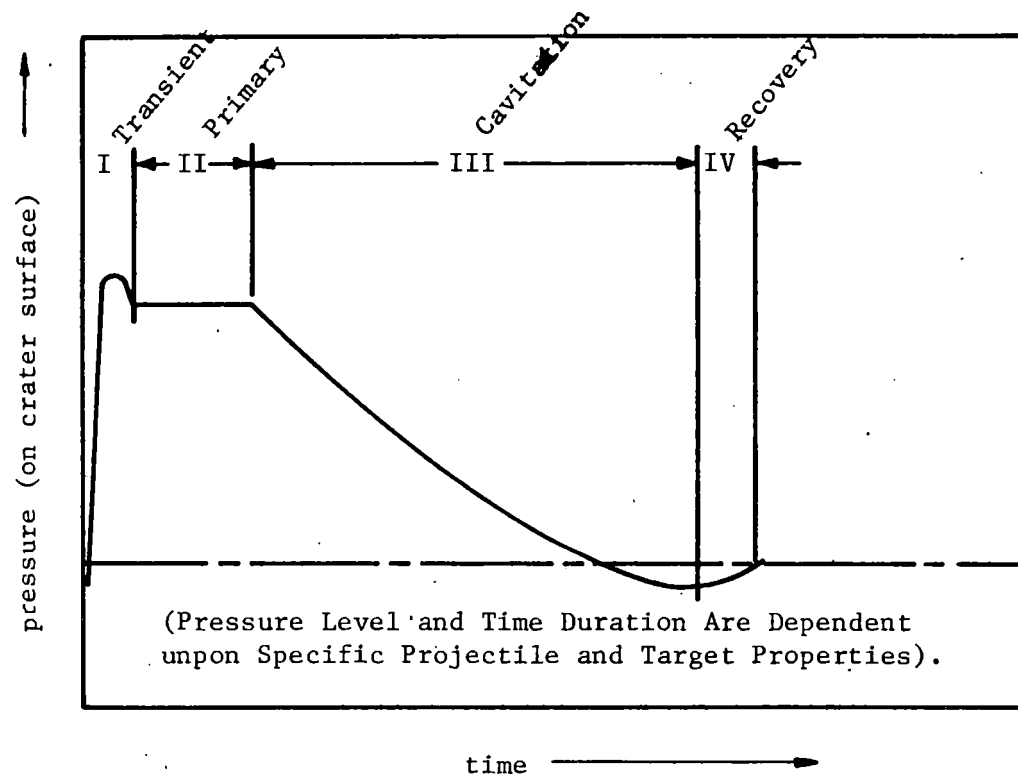


Fig. 5-13. Impact cratering regimes on a pressure-time basis

occurred as well as cratering. Secondary cracking and spall damage was caused by amplification and reinforcement of stress waves. Crater depths in beryllium agree with common criteria law, but those in graphite were only one-half of that expected.

In an examination of threshold penetration of several metals by aluminum spheres, Fish and Summers (Ref. 80) found that no single property could explain the relative performance of the metals.

DIMENSIONAL ANALYSIS

Bouma and Burkitt (Ref. 81) made a multivariable statistical analysis of existing data on penetration of semi-infinite metallic targets by projectiles of different materials. Data were not part of planned statistical programs, i. e., effects of each dimensionless variable and pertinent random errors could not be estimated as accurately as in a planned statistical experiment. Thus, regression and correlation methods were employed in the analysis.

The analysis was planned (in a three year program) to deduce from a statistical analysis of crater depth data for spherical projectiles on semi-infinite targets which material properties are most closely related to crater depth. It was believed that none of the common low temperature, low pressure static properties play a direct part in cratering processes, but some of them would be found to be statistically related.

Velocity effects were the most difficult, but were solved by fitting all data to the functional form:

$$z\left(\frac{h}{d}\right) = \ln \left[1 + (Xv)^2 \right] \quad (5-31)$$

where $z(\frac{h}{d})$ is a dimensionless crater depth, being the product of several dimensionless coefficients of material properties raised to a power. The term $X(v)$ is a dimensionless velocity, also containing the product of different powers of several dimensionless material property ratios (see below). Both X and Z are calculated with a coefficient of multiple correlation 0.84, which amounts to an accuracy of $\pm 25\%$ in this analysis. No high temperature, high pressure property data were employed, since all properties must reflect differences in crystalline or atomic structure.

Multivariable analysis was made of data available to 1965 (Fig. 5-14). The best functional form was found to be that of equation (5-31). The degree of correlation that was achieved is given in Fig. 5-15, and the measured values of X and Z tabulated in Table 5-3.

Inasmuch as the effects of variations in impact velocity are given in equation (5-32) values of X and Z show only the influence of actual properties of materials tested as target and projectiles. The experimental values of X and Z were analyzed by separate regression routines in terms of power laws for the materials given in Table 5-3.

A preliminary evaluation was made to determine the relevance of the material properties, and those which were statistically correlated or strongly related to other properties were eliminated. For example, Poisson's ratio appeared to be a strong variable, but was eliminated because of its relation to other elastic moduli and because of the small range of values, i.e., from 0.30 to 0.45 with the majority at 0.33. The remaining properties were then

TABLE 5-2

LIST OF SYMBOLS

Experimental Variables

B	10^{-2} x Brinell hardness on 500-kg scale kg/mm^2)
c	Mean specific heat of solid, 300°K to melting point (cal/gm°C)
C	Dilatational velocity of sound (km/sec) $C^2 = 9.90 \frac{E_t}{\rho_t} \frac{(1-\nu)}{(1+\nu)(1-2\nu)}$
d	Projectile diameter (cm)
D	Crater diameter (cm)
E	10^{-6} x Young's modulus (kg/cm^2)
f	Shape factor $\left\{ \begin{array}{l} \text{For a spherical projectile harder than the target, } f=2/3 \\ \text{For a spherical projectile not harder than the target, } f=1.0 \end{array} \right.$
F	10^{-2} x latent heat of fusion (cal/gm)
h	Crater depth (cm)
H	10^{-3} x heat to vaporize - sensible heats above 300°K plus latent heats (cal/gm)
H'	10^{-3} x latent heat of vaporization (cal/gm)
k	Thermal conductivity at 20°C (cal/cm sec°C)
K	10^{-6} x bulk modulus (kg/cm^2) = $\frac{E}{3(1-2\nu)}$
K'	10^{-6} x dilatational modulus (kg/cm^2) = $\frac{E(1-\nu)}{(1+\nu)(1-2\nu)}$
m	Projectile mass (gm)
Q	10^{-2} x heat to melt - sensible heat above 300°K plus latent heat of fusion (cal/gm)
U	10^{-3} x ultimate strength (kg/cm^2)
v	Projectile velocity at impact (km/sec)

TABLE 5-3
VALUES OF PARAMETERS X AND Z

Symbol	Projectile	Target	Measured Values		Calculated Values	
			X	Z	Eq (5-32) X	Eq (5-33) Z
+	2024T3	2024T4	.80	1.85	.67	1.63
x	Cu	2024T4	1.50	1.20	1.66	1.34
o	Pb	2024T4	2.00	1.60	1.68	1.19
*	St1	2024T4	2.00	1.70	1.70	1.42
□	HPAL	HPAL	1.35	1.65	1.19	1.37
>	HPCu	HPAL	2.60	1.00	3.50	1.62
△	2024T3	BeCu	.40	2.05	.42	2.93
†	2024T3	BeCu	.28	1.40	.39	1.88
‡	2024T3	Cu	1.30	3.00	1.27	2.86
•	HPAL	HPCu	1.10	2.40	1.19	1.91
•	HPCu	HPCu	1.70	1.50	1.96	1.59
•	Cu(B65)	Cu(B36)	.65	2.01	3.28	2.27
•	Cu(B65)	Cu(B65)	2.10	1.90	1.78	1.67
•	Pb	Cu(B65)	2.00	1.30	1.80	1.56
•	St1	Cu(B65)	3.10	2.20	3.25	2.38
•	2024T3	Pb	4.60	3.10	4.84	2.99
•	Cu(B65)	Pb	12.50	2.40	12.05	2.47
•	Pb	Pb	5.00	1.50	6.84	1.62
•	St1	Pb	14.00	2.40	12.37	2.63
•	2024T3	St1	.78	3.00	.75	2.61
•	2024T3	St1 (1030)	.46	2.00	.46	2.03
•	Cu	St1 (1015)	1.10	1.50	1.05	1.51
•	Pb	St1	1.35	1.80	1.05	1.43
•	St1	St1	1.20	1.80	1.07	1.58
•	2017T4	2024T4	.74	1.74	.72	1.60
•	Zn	2024T4	11.50	2.90	12.02	3.21
•	Zn	Cu(B65)	2.00	1.85	1.77	2.20
•	Zn	Pb	11.50	2.90	12.02	3.21
•	Zn	St1 (1015)	1.10	2.00	1.04	1.98
•	Zn	Zn	1.55	2.00	1.24	1.65
•	2024T3	Zn	.92	2.80	.89	2.47
•	Cu(B65)	Zn	2.50	2.20	2.22	1.70
•	Pb	Zn	.90	.45	1.26	.76
•	St1	Zn	3.00	2.40	2.28	1.80

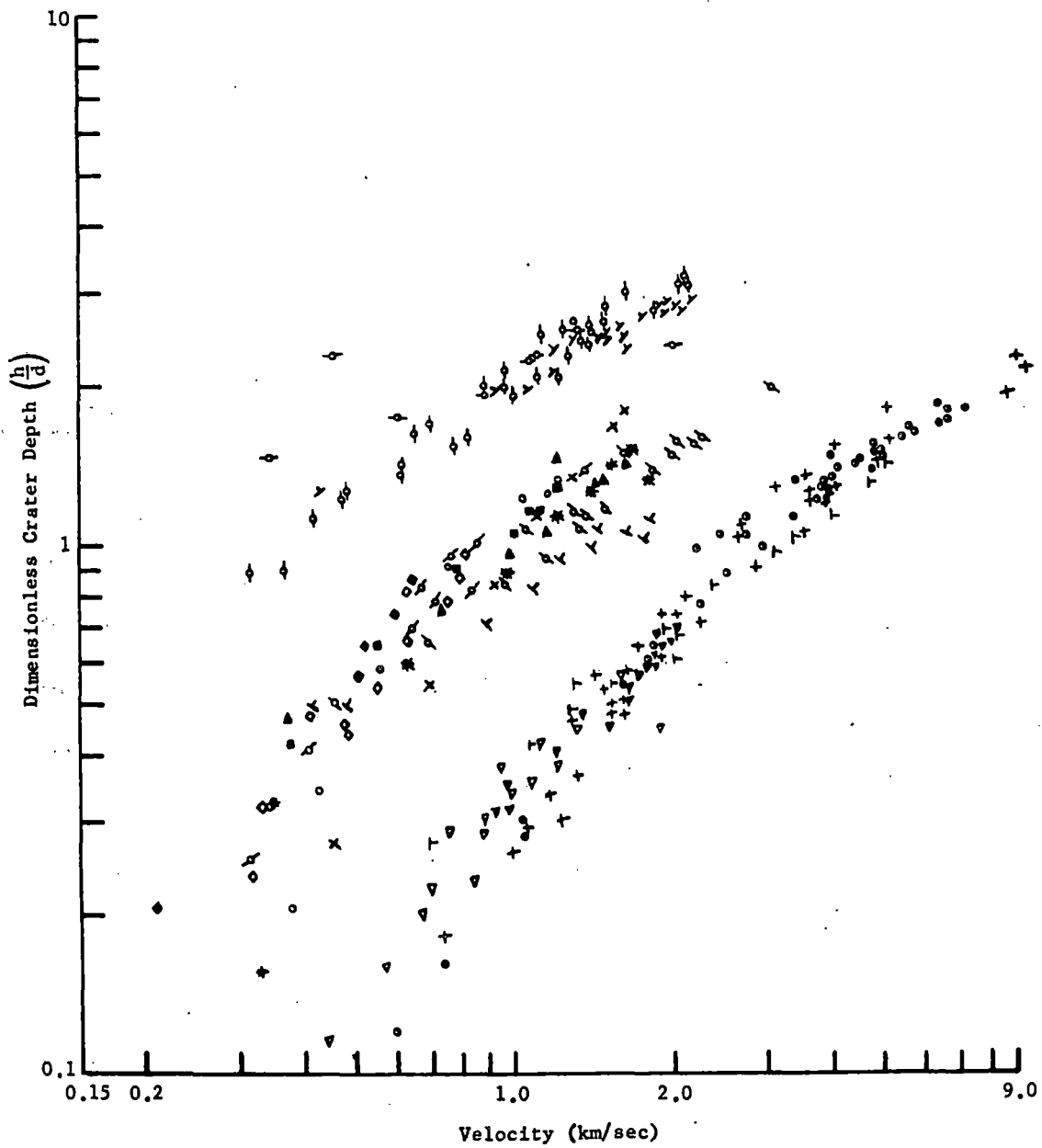


Fig. 2 Dependence of Crater Depth on Projectile Impact Velocity (Without Consideration of the Material Properties)

grouped in dimensionless ratios for final statistical analysis. The parameter X was given dimensions of inverse time so that Xv would be dimensionless, h/d already being dimensionless. The dimensionless qualities used and the resulting equations are:

$$Z = 1.131 (Q_p/Q_t)^{-0.185} (\rho_p/\rho_t)^{-0.36} (E_t/B_t)^{0.073} (E_p/E_t)^{0.149} \\ (Y_t/B_t)^{0.132} \epsilon_p^{-0.053} f^{-0.755} \quad (5-32)$$

Coefficient of multiple correlation = 0.842.

$$X = 0.479 (\rho_t/E_t)^{0.50} (\rho_p/\rho_t)^{0.472} (E_p/B_p)^{0.406} (B_p/B_t)^{0.130} \\ (Y_t/B_t)^{0.253} \epsilon_t^{0.216} f^{-1.44} \quad (5-33)$$

Coefficient of multiple correlation = 0.956.

The measured values of X and Z were tabulated from appropriate plots which were assumed to be the best correlations obtainable. Some brief sets of data were expanded to check on the predictive ability of the method of analysis. The values of X and Z were measured for these data (Table 5-3). Raw data are shown in Fig. 5-14, general correlation in Fig. 5-15 and selected correlations with ranges of application for the power law (Fig. 5-16). The latter depicts data for aluminum projectiles (\square) and copper projectiles (λ) as well as other selected sets of data. The lines of slope 4/3, 2/3 and 1/3 fit the data over a fairly wide range. The main feature is that the data appears to be well represented by a curve over the whole range and not by segments of given slopes.

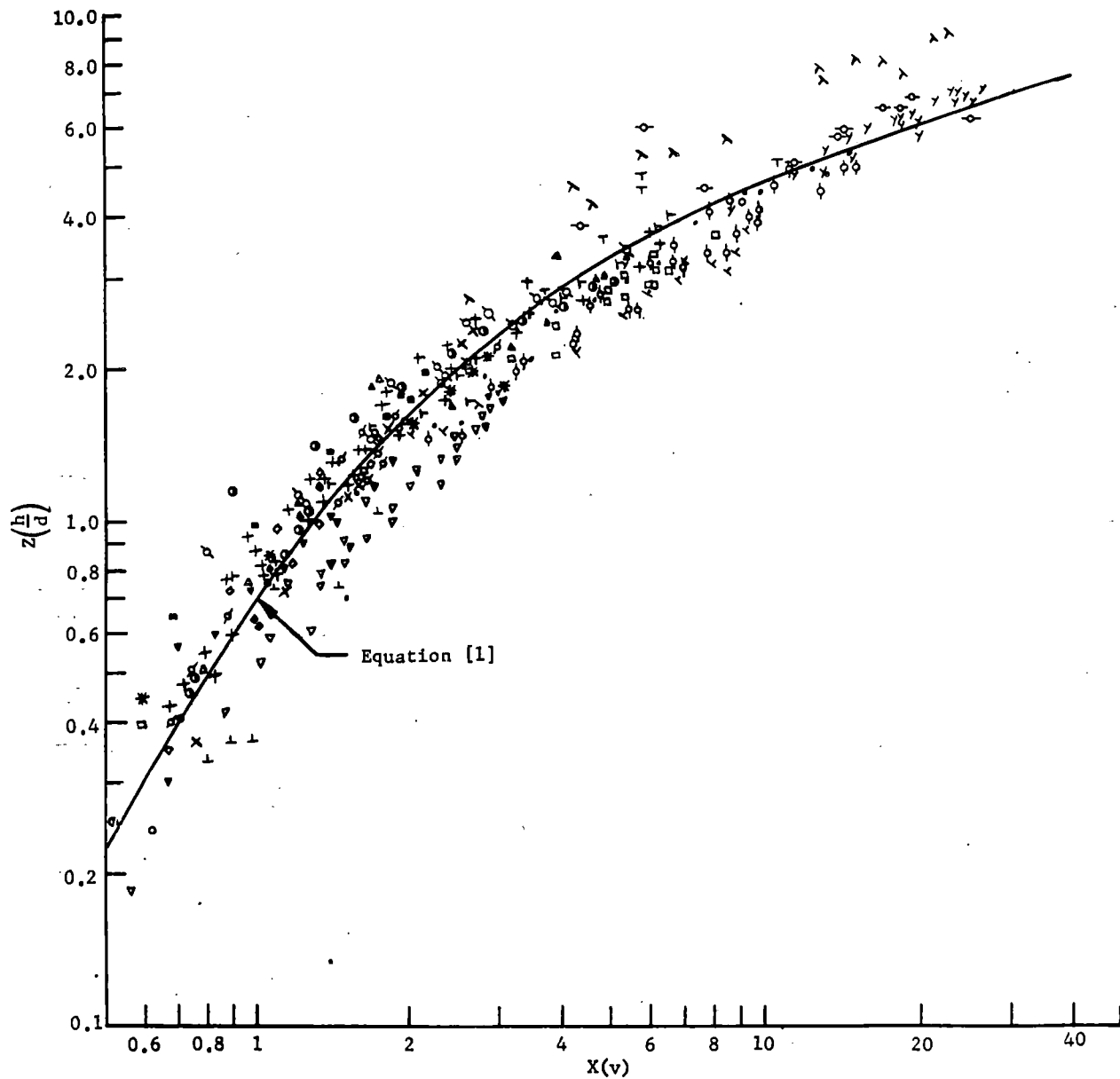


Fig. 4 Comparison of Predicted Crater Depth with Experimental Results Using Equations [1], [2], and [3]

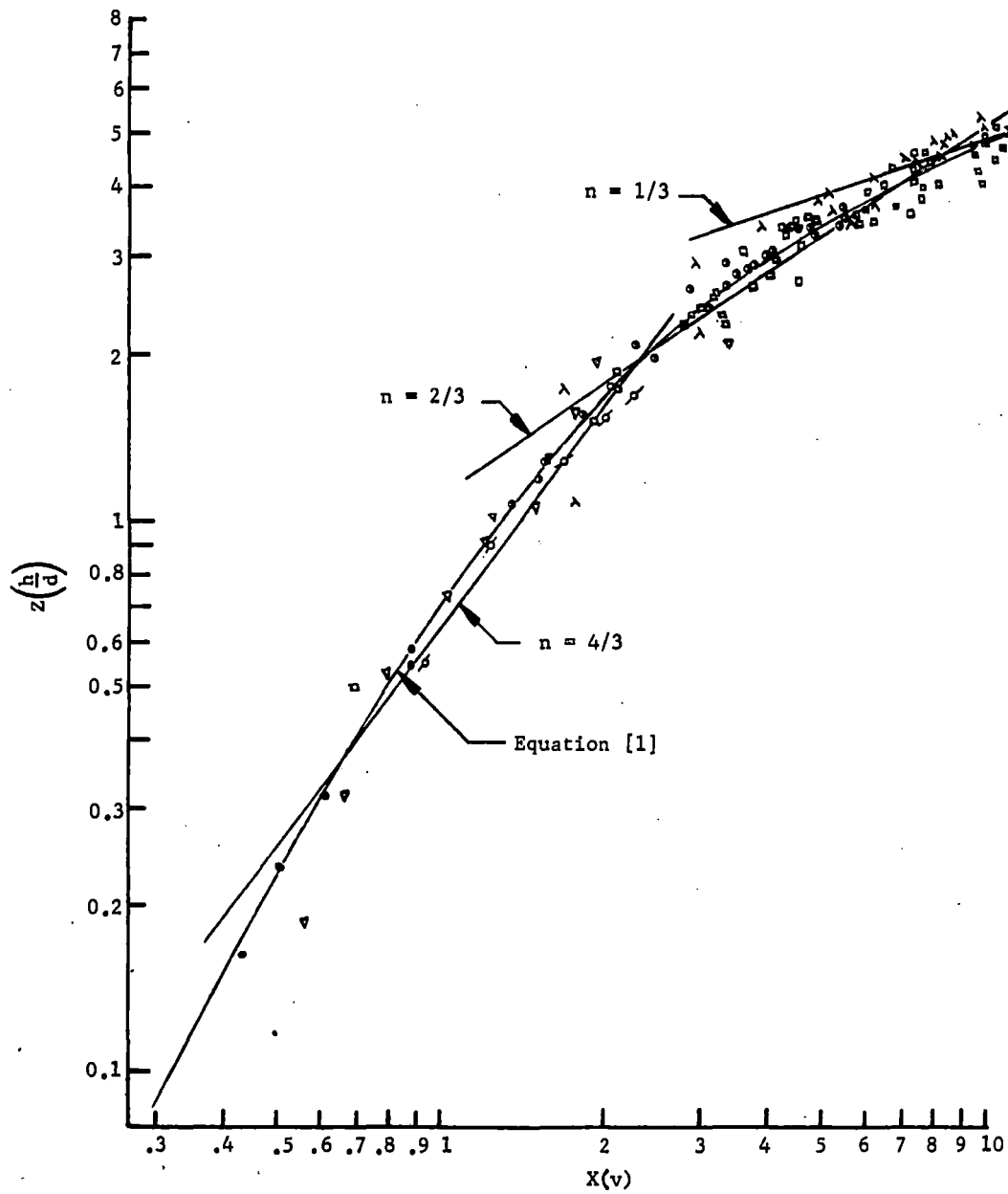


Fig. 5 Composite Variation of Crater Depth with Velocity

When written in dimensionless form it becomes

$$X_v = 0.479 (\rho_t v^2 / E_t)^{0.500} (Y_t / B_t)^{0.253} (\rho_p / B_t)^{0.472} (E_p / B_p)^{0.406} \\ (B_p / B_t)^{0.130} \epsilon_t^{0.216} f^{-1.44} \quad (5-34)$$

which the author (Ref. 76) characterizes as a "compromise between accuracy and complexity." The ratios of (E_t/B_t) and $(\rho_t Q_t/E_t)$ were discarded because they had only a minor effect.

The dominant properties are the Brinell hardness, Young's modulus, density, velocity, ductility of the target and a projectile shape factor. Density is one of the more effective parameters, as well as velocity. Young's modulus and Brinell hardness are effective, or basic atomic or structural properties of the material which they represent.

IMPACT EXPERIMENTS - ROCK

A detailed description of craters formed in several types of rock by hypervelocity projectiles is given by Moore and Lugn (Ref. 82). Basalt, sandstone, dolomite and nephrite were impacted with projectiles (from a light gas gun) of steel, aluminum, pyrex, polyethylene and other materials weighing 0.02 to 0.4 gm at velocities from 14,000 to 23,900 fps. About 20 craters were examined in detail and were found to be roughly conical with crushed and intensely fractured rock at the bottoms. The ejecta from the craters were made up of projectile fragments and pieces of rock from a few microns to several centimeters in dimensions.

Typical craters were shallow cones from 0.6 to 2.4 cm deep and 4 to 12 cm across. The rims of the craters were irregular and the lower sections

more symmetrical, but with irregularities. Crushed rock and (1) shear fractures, (2) radial fractures, (3) spall fractures and (4) concentric fractures were formed.

Crushed rock was found in the bottoms of all craters, individual grains being broken, displaced or pulverized. Microscopic fractures spread and decrease into the rock. Pore spaces are closed in sandstones, and in dense rocks unbroken polyhedra are enclosed in a matrix of crushed rock.

Shear fractures are formed in some craters, and are identified by grooves and striae. Surfaces may be pyramid or cone shaped. Shear fractures in basalt are marked by intensely pulverized rock with weak grooves. Shear failure may be due to difference in principal stresses in plastic flow.

Radial fractures are tensile breaks radiating from the crater axis and nearly perpendicular to the impact surface. In dense rocks the fractures may project beyond the crater, but not in porous rocks.

Spall fractures are tensile in character, formed by reflected rarefaction waves from free surfaces. Fragments are spalled from the surface in larger fragments which may be fitted back into place, and constitute about half of the crater ejecta.

Concentric fractures are present about the rims of some craters, and extend only a fraction of a millimeter below the rock surface.

High speed photography indicates that luminescence is generated at the moment of impact, and as the projectile penetrates a bowl-shaped spray of ejecta grows rapidly with a speed comparable to that of the projectile. The

base of the ejecta expands into a dome which exhibits irregularities which may be related to the large spall fragments, the outermost of which are sometimes not ejected from the crater.

Penetration is postulated to be by means of plastic flow, crushing and shearing, under hydrodynamic conditions. Tensile fractures are formed later and spalling subsequent to reflection of waves. Many of the features described are also present in craters created by high explosives.

Gault and Heitowit (Ref. 83) made a preliminary analysis of the energy partitioning in the impact of aluminum projectiles on basalt in conjunction with extraterrestrial impact of meteorites. They point out the fallacy of explosion theory of impact, i. e., when the kinetic energy of the projectile is equal to the energy of vaporization an explosion occurs. It is shown by their analysis that only a small portion of the energy is trapped as heat of fusion and/or vaporization. Their analysis is based upon both theory and observations with a high speed camera.

The initial stage of impact is considered to be a problem in one-dimensional flow (Fig. 2-1) which may be described by the well-known Rankine-Hugoniot equations

$$\rho_o U = \rho (U-u) \quad (5-35)$$

$$p - p_o = \rho_o Uu \quad (5-36)$$

$$E - E_o = \frac{1}{2} (p+p_o) \left(\frac{1}{\rho_o} - \frac{1}{\rho} \right) = \frac{1}{2} u^2 \quad (5-37)$$

where \underline{U} is the shock velocity in the undisturbed medium, \underline{u} is the mass velocity, and \underline{p} , ρ and \underline{E} are the pressure, density and specific internal energy,

respectively, the subscript \underline{o} indicating conditions in the undisturbed medium. For impact conditions $p \gg p_o$ and equations (5-36 and 5-37) may be written

$$p = \rho_o Uu \quad (5-38)$$

$$E - E_o = \frac{1}{2} p \left(\frac{1}{\rho_o} - \frac{1}{\rho} \right) = \frac{1}{2} u^2 \quad (5-39)$$

Thus, the total work done in shock compression is $p(1/\rho_o - 1/\rho)$. From equation (5-39) the energy of the shock is equally divided between the specific kinetic energy $(1/2u^2)$ and the increase in the specific internal energy $(E-E_o)$.

Only ρ_o is known, hence, the Rankine-Hugoniot expressions provide a system of these equations in four unknowns, and an additional equation is required which will relate thermodynamic properties of the media.

Hugoniot data (p vs. ρ_o/ρ) for aluminum and basalt were plotted as curves, which represent the locus of points for states existing for discontinuous pressure jumps. These curves and the conservation equations permit evaluation of the variables in terms of each other. The following may also be obtained from experimental results:

$$U = a + ku \quad (5-40)$$

The values of the constants $\underline{a} + \underline{b}$ for basalt and Al are given in Fig. 5-18.

To maintain contact at impact (Fig. 5-19)

$$v_i = u_p + u_t \quad (5-41)$$

and

$$p = \rho_o (a + ku)u \quad (5-42)$$

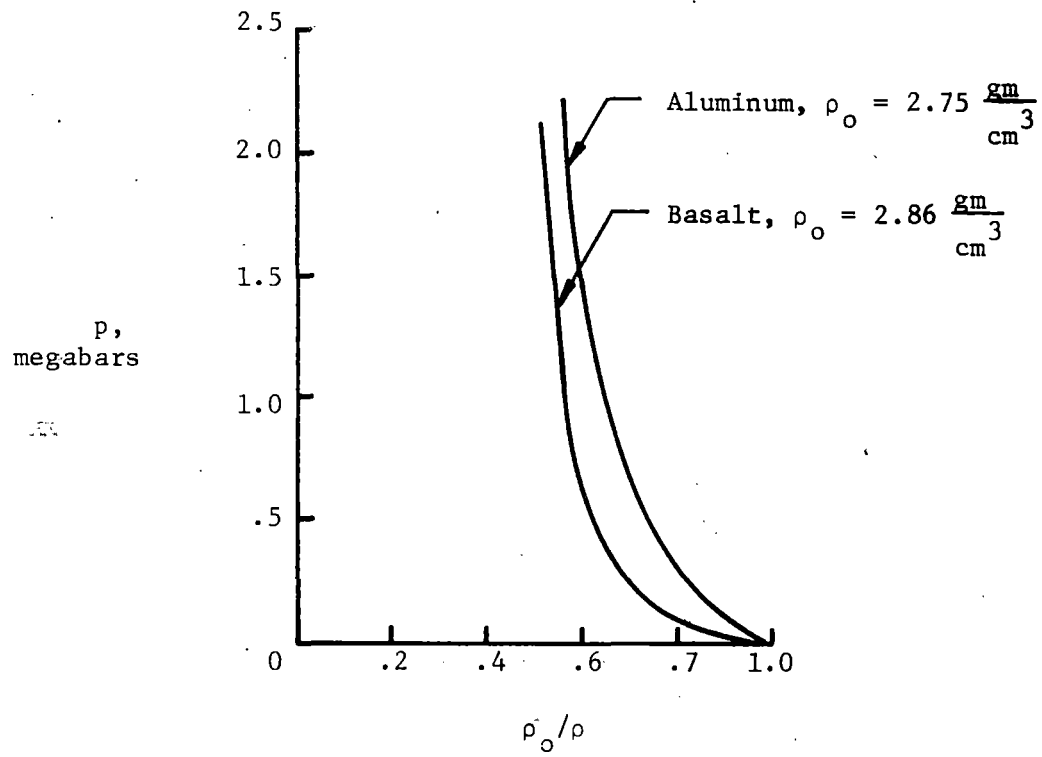


Fig. 5-17. Hugoniot curves for aluminum and basalt. (Gault).

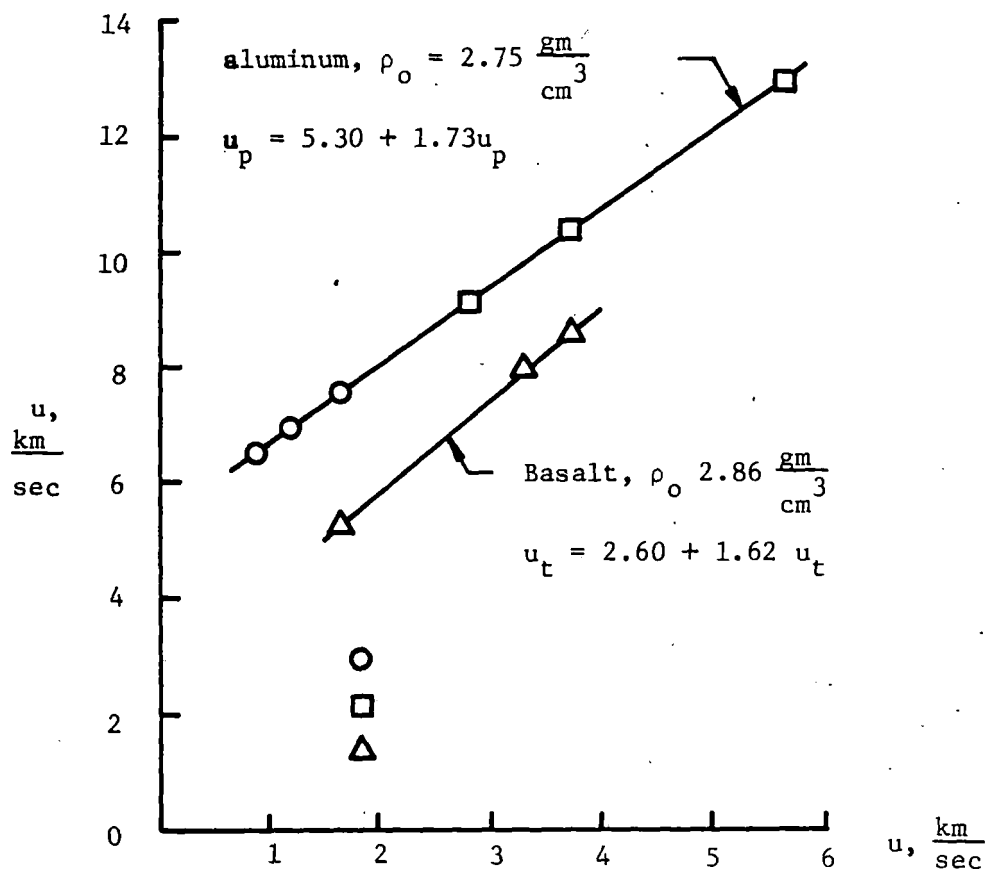


Fig. 5-18. Shock wave and mass velocity relationship for aluminum and basalt. (Gault).

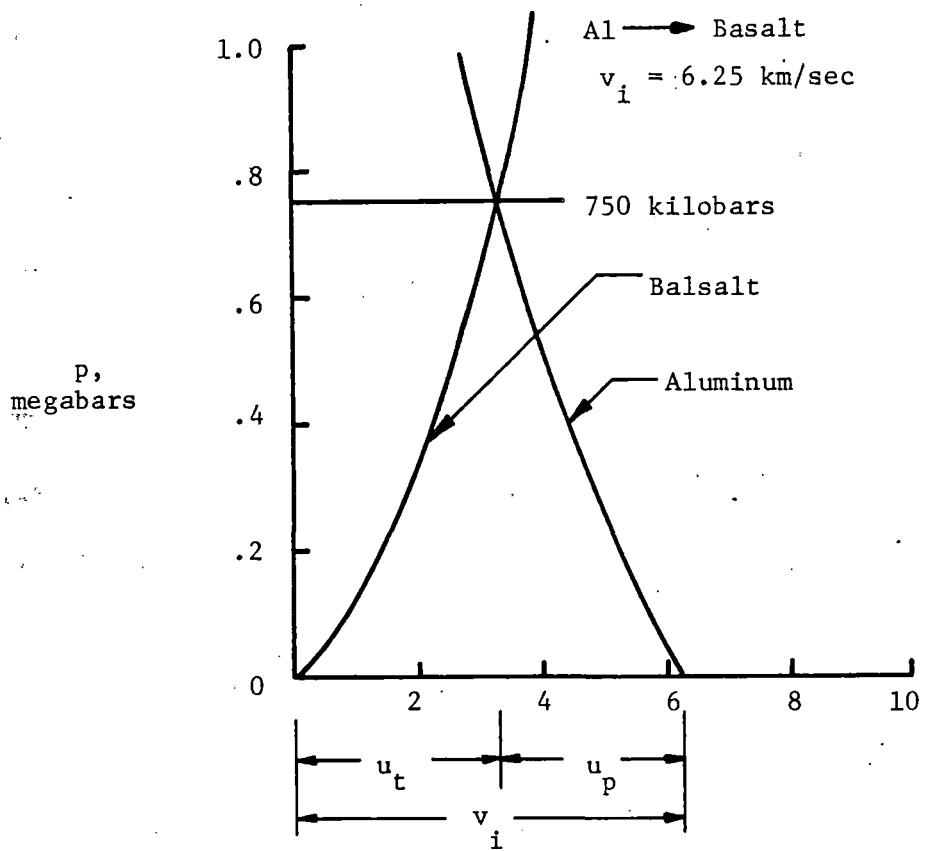


Fig. 5-19. Graphical solution for determining pressures and mass velocities for one-dimensional impact of dissimilar materials. (Gault).

and further

$$p_p = \rho_{op} [a_p + b_p (v_i - u_t)] (v_i - u_t) \quad (5-43)$$

$$p_t = \rho_{ot} (a_t + b_t u_t) u_t \quad (5-44)$$

For equal pressure in the target and projectile

$$[a_p + b_p (v_i - u_t)] (v_i - u_t) = \rho_{ot} (a_t + b_t u_t) u_t \quad (5-45)$$

a quadratic which furnishes a solution for the required parameters.

Likewise the initial energy partition may be expressed

$$\frac{\text{Energy retained by projectile}}{1/2 \rho_{op} v_i^2} = \frac{u_p^2 + u_t^2}{(u_p + u_t)^2} = \frac{1 + (u_p/u_t)^2}{(1 + u_p/u_t)^2} \quad (5-46)$$

and the fraction delivered to the target is

$$\frac{\text{Energy delivered to target}}{1/2 \rho_{op} v_i^2} = \frac{2u_p/u_t}{(1 + u_p/u_t)^2} \quad (5-47)$$

The energy delivered to the target is equally divided between an increase in internal energy and the kinetic energy of the compressed mass behind the shock front, the residual kinetic energy of the projectile is

$$\frac{\text{Residual projectile kinetic energy}}{1/2 \rho_{op} v_i^2} = \frac{1}{(1 + u_p/u_t)^2} \quad (5-48)$$

and the increase of the internal energy of the projectile is

$$\frac{\text{Projectile internal energy}}{1/2 \rho_{op} v_i^2} = \left(\frac{u_p/u_t}{1 + u_p/u_t} \right)^2 \quad (5-49)$$

The above equations indicate that, except for impact of similar materials, the retained projectile energy will never equal that delivered to the target. For higher density projectiles, the fraction of energy delivered becomes smaller.

These formulas and calculations based upon them demonstrate one of the errors involved if the kinetic energy of the projectile is equated to specific internal energy in the projectile material for explosive impact.

Gault, et al., show that for impact of Al and Fe projectiles in basalt the calculated energy is initially partitioned as follows:

		Percent initial proj. energy		
<u>Energy</u>		<u>Al</u>		<u>Fe</u>
Projectile	(Internal, $E_p - E_{op}$)	22.3)		10.5)
	()	50.2)
	(Kinetic, $1/2\rho_p u_p^2$)	27.9)		45.7)
				56.2
Target	(Internal, $E_t - E_{t_0}$)	24.9)		21.9)
	()	49.8)
	(Kinetic, $1/2\rho_t u_t^2$)	24.9)		21.9)
				43.8

After the initial partitioning the process is assumed to be analogous to the compression of a spring. Once the force of the projectile is spent the compressed target mass will expand in release of the compression (rarefaction). The compressed material is capable of work, and the use of energy reduces that which remains at zero pressure (Fig. 5-20) for $ds = 0$.

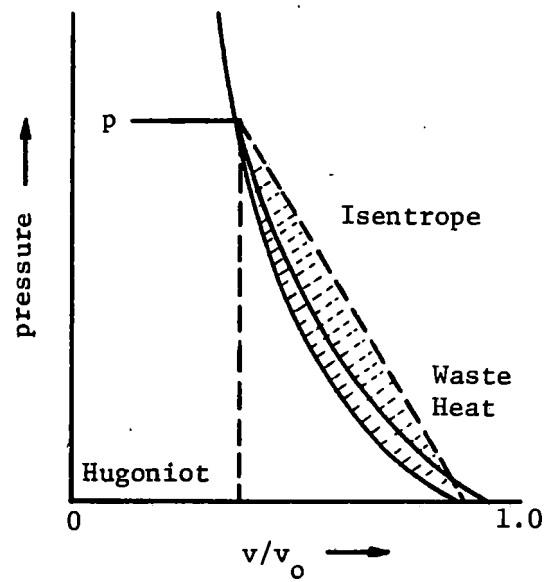


Fig. 5-20. Hugoniot curve and pressure release curve for an isentrope ($ds = 0.$) (Gault).

The isentrope represents a continuous process, the Hugoniot a discontinuous one. The work of expansion is represented by the crosshatched area. The triangular area enclosed by dashed lines represents the total shock compression energy, only a fraction of the energy is available for fusing or vaporization.

Gault, et al., (Ref. 83) following Rice, et al., (Ref. 84) utilize the following equation for (pressure p_a) along an adiabatic release line

$$\frac{dp_a}{d\bar{v}} + \frac{\gamma}{\bar{v}} p_a + \frac{d}{d\bar{v}} \frac{\bar{v}}{\gamma} p_a = \frac{dp_h}{d\bar{v}} + p_h \frac{\gamma}{\bar{v}} \frac{d}{d\bar{v}} \frac{\bar{v}}{\gamma} - \frac{\gamma}{\bar{v}} \frac{dE_h}{d\bar{v}} \rho_0 \quad (5-50)$$

The subscripts a and h refer to conditions on the pressure release and Hugoniot curves, respectively. The quantity $\gamma = \gamma(\bar{v})$ is the Grünesen ratio and $\bar{v} = \rho_0 / \rho$ the ratio of the specific volumes. The relation $p_a = p_a(\bar{v})$ is determined from experimental data and the internal energy trapped in the projectile ΔE_p is given by

$$\Delta E_p = \frac{1}{2} u_p^2 - (pv \text{ work}) \quad (5-51)$$

The value of ΔE_p may be normalized by $E_p - E_{p_0} = 1/2 u_p^2$ (Fig. 5-21). For a velocity of 6.25 km/sec, 19 percent of the increase in specific internal energy, or 4 percent of the total kinetic energy, is expended in irreversible heating. This is enough to partially melt the projectile. Observed melting of projectiles indicates that the above procedure predicts about only 1/3 of the melting which actually takes place.

For the target a hemispherical shock is assumed and combined with an appropriate experimental Hugoniot. A pressure gradient is approximated

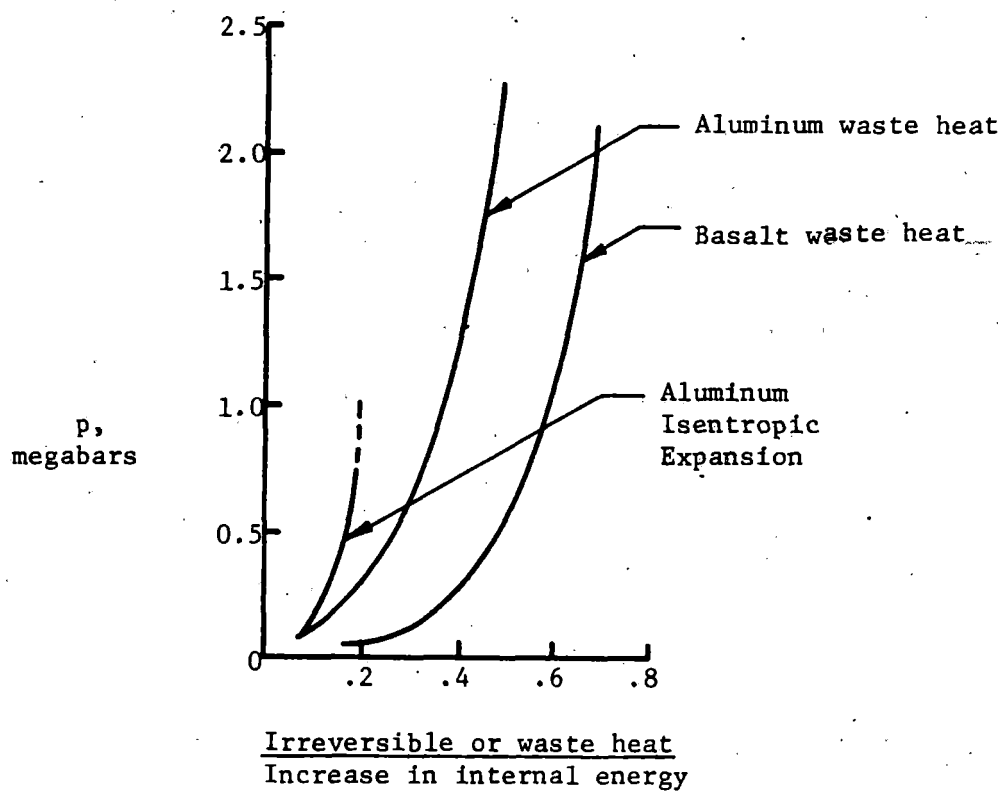


Fig. 5-21. The variation of irreversible and waste heat with pressure. (Gault).

and irreversible heat calculated from appropriate equations by numerical methods. The estimated amounts of heat are sufficient to fuse minerals in basalt, but not to vaporize them.

Comminution of the target consumes an important fraction of the projectile kinetic energy. This is approximated by calculating the new surface energy from a screen analysis of the particle sizes of crater ejecta, and an approximation of the fracturing of target material around the crater. A specific surface energy was assumed for basalt from known values for quartz and limestone. For a given test it was found that about ten percent of the projectile energy was used in comminution of ejected material. Additional crushing and fracturing of the target was estimated at a maximum of ten percent.

Ejecta velocity distribution was estimated from high speed framing camera records. A numerical summation process indicated that about 48±5 percent of the kinetic energy of the projectile was retained in the ejecta.

The spallation of the rear of the target, together with the tensile strength of basalt permitted calculation of elastic energy as being less than one percent of the total projectile energy.

Radiant (flash) energy has been calculated by other investigators to be on the order of 10^{-4} percent of the total kinetic energy of the projectile.

Gault and Hietowit (Ref. 83) analyzed the partitioning of energy in the impact of aluminum projectiles at 6.25 km/sec against homogeneous basalt using shock and thermodynamic equations.

Their results were as follows:

Energy expended for:	Percentage of
(1) irreversible waste heat projectile target	projectile K.E. 4 to 12 19 to 23
(2) comminution	10 to 24
(3) ejecta throwout	45 to 53
(4) miscellaneous residual elastic wave radiant	less than 1 <u>negligible</u>
Total	77 to 113

If their analytical solutions are reasonably correct then hypervelocity projectiles provide an insufficient means of fracturing. Likewise, if ejecta is fine material, considerable energy is wasted in comminution.

Moore, et al., (Ref. 85) conducted a series of 38 impact experiments in basalt at normal incidence. Aluminum, steel and polyethylene projectiles of weight 0.0058 to 4.051 gm were fired from light gas guns, velocities varying from 0.88 to 7.3 km/sec and kinetic energies from 4.9 to 10^3 to 7.4×10^{11} erg.

Basalt properties were:

density - 2.70 to 2.89 g/cm³
compressive strength - 1.56 to 3.69 x 10⁹ dynes/cm²
tensile strength - 0.90 to 2.32 x 10⁸ dynes/cm²
shear strength average computed - 8.6 x 10⁸ dynes/cm²
acoustic velocity - 4.9 to 5.5 km/sec

A least squares fit of the data gave the following equation:

$$M_e = 10^{-10.613} \left[\left(\frac{\rho_p}{\rho_t} \right)^{\frac{1}{2}} E_p \right]^{1.189} \quad (5-52)$$

where

M_e = ejected mass

E_p = projectile energy

ρ_p = projectile density

ρ_t = target density

Target failure conditions are complex, and a comparison of cratering in basalt with that in metals and water lead Moore, et al., to the conclusion that tensile fracture plays a dominant role in cratering in basalt. Spalling creates craters in rock which are about ten times as large as those in metal.

Fluid impact theory predicts that the crater volume or ejected mass for given materials should be proportional to the projectile energy. The results of these experiments indicate that the ejected mass varies as the energy to the 1.2 power. In other words, the effective strength decreases with crater size.

Moore, et al., (Ref. 86) compared the results of impact cratering in lead, copper, aluminum, diatomaceous earth, water and basalt on an energy basis, for the same kinetic energy. The crater volume for diatomaceous earth was largest, basalt next, then copper, aluminum and lead. If the projectile energy is normalized adjusting for density and target strength, the basalt volumes are about three times the others, probably due to tensile spalling. Target strength at high conforming pressures is utilized as a criteria, although

few data are available for the high pressures involved (above 49 kilobars).

Moore (Ref. 85) found in hypervelocity experiments in basalt targets that the mass ejected from a crater increased with the projectile energy, and the square root of the ratio of projectile and target densities. The mass ejected per unit of projectile energy increased with the size of the crater. Theoretically, for constant target strength this figure should be constant. Thus, the effective strength of basalt decreases with increasing size of crater.

Comminution

Several theories have been proposed to give the energy of crushing of solid material to produce a given particle size reduction. The Rittinger theory appears to be the most applicable, and it states that the work required for crushing is proportional to the new surface area formed.

This may be expressed mathematically as follows:

$$E_c = K_r \left[\sum_{40}^1 \text{pct}_i \frac{1}{d_i} - \frac{100}{d_o} \right] \quad (5-53)$$

where

E_c = crushing energy

K_r = a constant

d_i = average diameter of each of forty screen fractions

d_o = diameter of original solid

When particle size distribution is employed as a measure of energy, shape factors may be required if absolute surface energy is determined. Methods

of adsorption and permeability are also employed to determine surface energy of crushed materials.

Specific surface energy increases rapidly with decrease in particle size, and even though considerable fine material is produced by the various methods of impact, for jets only a small part of the total energy is utilized in crushing.

CHAPTER VI

EXPLOSIVE SHAPED CHARGES AND CUMULATION

The high velocity and stagnation pressure of the gaseous products of a chemical explosion can be increased if the explosive charge is first formed into a special shape. In general, the principle of such an explosive shaped charge is to direct the energy from one portion of the explosion products or focus it, thus concentrating energy over a small area of a target which is to be penetrated, cut, or shattered. In the United States and Great Britain this is called the Munroe effect; in Germany and some other European countries it is called the Newmann effect; in the USSR it is referred to as cumulation. There are other methods of velocity augmentation or cumulation, however, that do not make use of explosives.

Although the explosive shaped charge may be formed in any of a number of different geometries, a cylindrical charge with a conical cavity is most commonly used. The explosive column may be tapered at the booster end, giving a beehive shape (Fig. 6-1). When placed with its cavity end against a massive target, the shaped charge excavates a crater or hole whereas cylindrical charge with no cavity causes only superficial surface damage to strong targets such as steel, concrete, or rocks.

A major improvement in the performance of explosive shaped charges occurred in the 1930's with the discovery that lining the cavity with a non-explosive solid increased penetration many times. The term cavity effect is applied to both lined and unlined cavities, whereas the term Munroe effect is

usually restricted to unlined cavities. During World War II, the lined cavity phenomena led to the development of powerful new weapons.

After the war, the mining industry became interested in applying the shaped charge to rock excavation, and studies of shaped charge effects in rock were initiated in the late 1940's (Refs. 87 and 88). It became apparent that the limited existing technology, lack of means of adaptation, and the price of materials discouraged widespread use of shaped charges at that time.

The basic theory for jet formation (uniform velocity) and target penetration was developed during World War II, and appeared in the literature in a paper by Birkhoff, MacDougall, Pugh, and Taylor (Ref. 51). The jet formation theory was generalized and made more applicable to non-uniform jets in a paper by Pugh, Eichelberger, and Rostoker in 1952 (Ref. 89). Called the hydrodynamic theory of jet formation, it is believed by some (Austin, 1959), Ref. 90) to be limited to thin-walled conical and wedged shaped liners with wide apex angles.

Detonation is usually initiated on the end opposite the cavity by an electric blasting cap and/or booster. The detonation wave accelerates and travels toward the cone, approaching a steady state condition and planar geometry if the charge is long enough.

The collapse of a conical liner, as visualized in the generalized hydrodynamic theory, is pictured in Figure 6-2. As the detonation wave passes from the apex to the base of the cone, each successive element of the liner collapses under the detonation pressure, moving at high velocity nearly perpendicular to the original disintegrated liner material. It converges at a junction on the cone axis, then divides into two jets along the axis because of

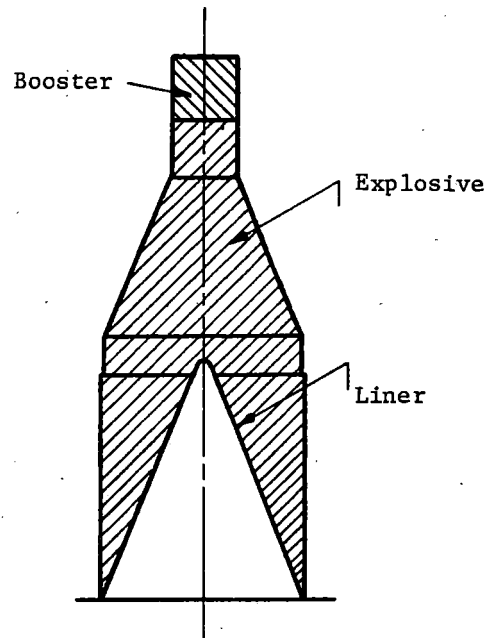


Fig. 6-1. A typical shaped charge with conical liner for use in static experiments. (Birkhoff).

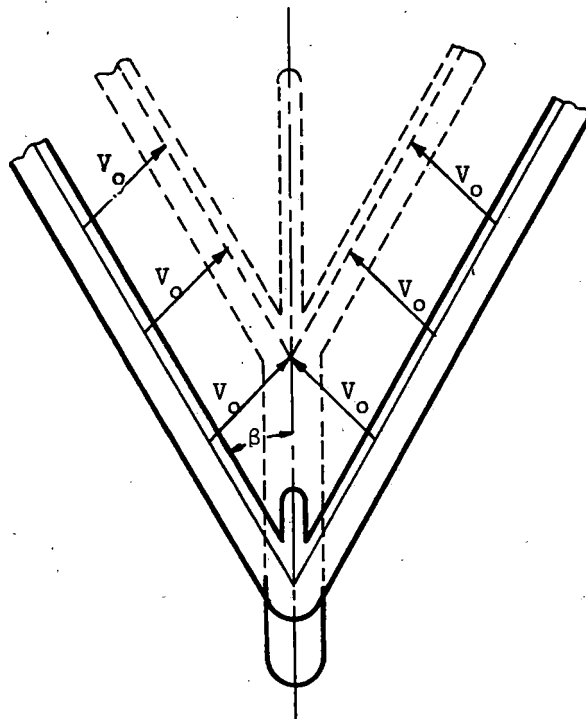


Fig. 6-2. Formation of jet and slug from a cone or wedge-shaped liner whose sides collapse with constant velocity V_0 as a result of the explosion of a charge that was in contact with the outer surface. The solid lines show conditions at an early instant of time, and the dotted lines show conditions after the walls have moved a distance equal to the velocity V_0 , for unit time. (Birkhoff).

the cone's symmetry. Since the junction moves rapidly from apex to base, the absolute velocity of both jets is to the right in Figures 6-2 and 6-3, and the divergence of the two jets results in a relatively slow velocity for the one on the left, called the slug. The fast jet is responsible for all of the penetration.

Because the detonation pressure is many times the strength of the liner, its strength is assumed negligible and is treated as an incompressible ideal fluid. The velocity of a liner element is considered to be constant throughout the collapse process, with no consideration given to acceleration time. The velocity of liner material is assumed to change direction but not velocity at the junction. In the special case in which each cone element collapses at the same velocity, Bernoulli's equation may be applied, leading to the same condition. Application of conservation of mass, energy, and momentum yields for fast jet velocity

$$V_j = V_o \csc (\beta/2) \cos (\alpha + \delta - \beta/2) \quad (6-1)$$

where V_o is the collapse velocity and α , δ , and β are the angles in Fig. 6-4. The fraction of the mass of a liner element which goes into the jet is

$$dm_j/dm = \sin^2 (\beta/2) \quad (6-2)$$

where dm is an element of the original liner's mass and dm_j is the mass contributed to the jet by dm .

The theory at this stage accounts for the presence and shape of both a jet and slug. Further, it provides for a variation in velocity along the length of the jet, and in so doing offers an explanation of lengthening of the jet, the

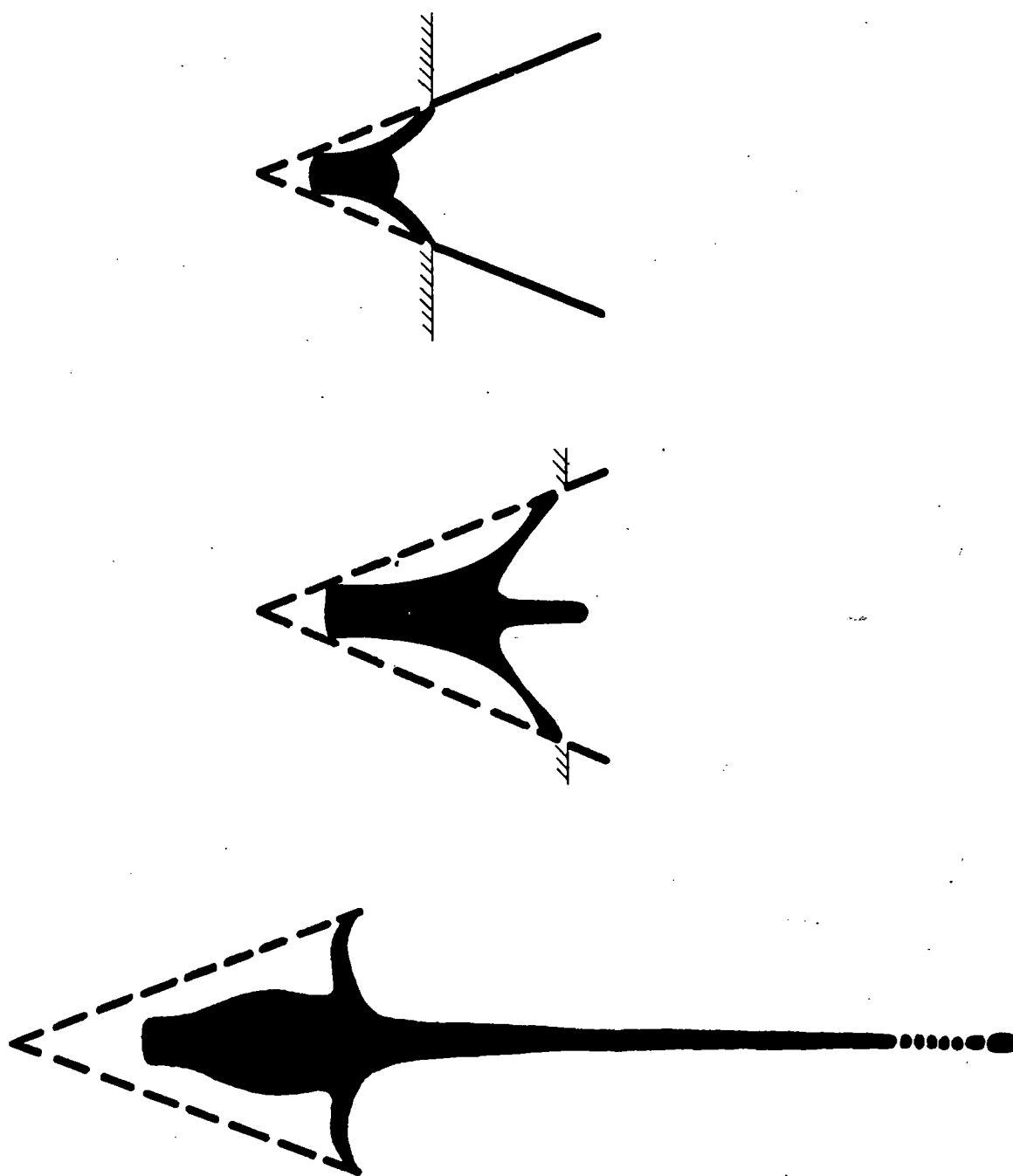


Fig. 6-3. Sketches of computed cone collapse and jet formation.
(Eichelberger).

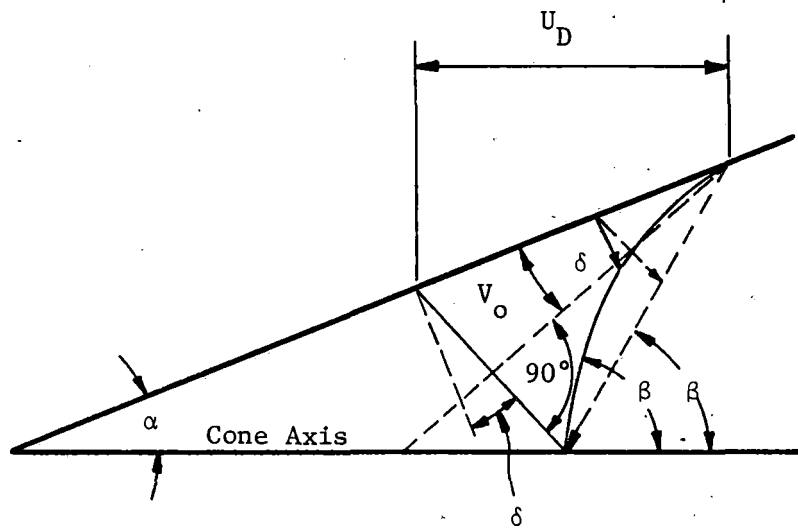


Fig. 6-4. Cross section showing the non-steady collapse process in a conical liner. (Pugh).

illusion of an afterjet and with other considerations the existence of an optimum charge-target separation (standoff). Both theory and experiment reveal a very high velocity at the tip of the jet. Austin (Ref. 90) states that flash x-ray studies, bi-metallic liners, and radioisotope tagging of liners have been used to demonstrate the theory.

Poulter and Caldwell (Ref. 91) proposed a plastic-flow theory for the collapse of thick-walled, conical liners with small apex angles. This mechanism of collapse has been confirmed by the use of flash x-rays and bi-metallic liners (Ref. 88). Poulter and Caldwell also outlined a spherical-convergence theory to explain the collapse of semi-spherical liners. Clark and Bruckner (Ref. 93) earlier proposed, on the basis of indirect observations, that such liners instead turn inside out and then fragment during collapse. This mechanism was further supported by the observations of Kolsky (Ref. 94).

The cavity effect is also a form of cumulation (Ref. 31). In other applications of this process a cylindrical "charge" of inert material such as wax is designed with an internal cylindrical or conical cavity. This is impacted on the closed end with a high velocity cylinder causing a compression wave in the "charge". A jet is formed in the cavity by a process similar to that in the liner of a shaped explosive charge.

Above certain velocities the impact pressure of a jet is many times the strength of solid targets. Consequently, the theory of jet penetration was originally based upon the assumption of steady-state, incompressible, ideal fluid flow (Ref. 51). The jets encountered in practice are imperfect, exhibiting such effects as nonsteady velocity, wavering, and breakup, but basic

theory provides a good approximation. The formula for penetration, the so-called first order theory is

$$\frac{h}{L} = \sqrt{\frac{\lambda \rho_j}{\rho_t}} \quad (6-3)$$

where

h = penetration depth

L = length of jet

ρ_t = target density

ρ_j = jet density

and λ = parameter which depends upon the degree of jet breakup, equal to 1 for continuous jet. The most obvious result of neglecting target strength is the implication that penetration is independent of jet velocity, depending only on jet length.

However, experiments have shown that target strength does affect penetration somewhat, because the rear of the jet travels at a relatively low velocity and so exerts a relatively low pressure on the target. This effect was treated in various ways by Pack and Evans (Ref. 56), and others (Refs. 54, 95, 96). The effect of heat losses was also considered by Cook (Ref. 3).

The various forms of recent theoretical developments account for such additional phenomena as optimum standoff and approximate linear scaling of penetration with charge diameter. A reasonably accurate prediction of penetration in many metals is possible for common standoff distances, and future research may show that similar laws will be applied to rock and other brittle materials.

The first order theory does not account for target strength or after effects such as the lateral expansion of the hole or the shock waves in the target. Nor has an accurate hypothesis been advanced for the energy partitioning of jet impact, either on ductile (metal) or brittle (rock) targets.

Herrmann (Ref. 49) points out that the above first order penetration theory may be expected to apply only at very high velocities. For lower velocities a theory should include a correction for target strength which in turn reduces the predicted penetration. There is some lack of agreement with theory because the major contribution to the penetration process at high velocities may be due to the expansion of the crater.

The similarities which exist between impact effects of projectiles and jets appear to be limited to the initial portion of a jet approximately equal to a cylindrical projectile of the same mass and geometry. In the development of some theories of penetration both spherical and cylindrical projectiles have been considered as short jets. For projectiles at the instant of impact a shock wave is propagated from the point of impact into both the target and the projectile. For a jet of metallic particles or other solid material particles, the stream is made up of separated discrete segments, and is not capable of propagating a shock back into the jet.

In contrast very high velocity projectiles form a hemispherical crater in ductile metals, while craters in rock are enlarged by tensile spalling around the rim.

Design of Shaped Charges with Conical Liners (Ref. 96)

All of the design parameters of the liner and the charge are of primary consideration, some being more critical than others. Cone diameter is approximately proportional to target penetration for a given charge geometry and other parameters. (Effects related to design were observed in steel targets). The effect of liner material is also marked, but more complex, as evidenced by Figure 6-5. In general, penetration is increased by greater liner density and ductility, although other material properties may override these effects, copper versus lead; for example. Cone angle is optimum at about 60° (Fig. 6-6), but is interdependent with standoff, confinement, and liner thickness. Penetration versus thickness (Fig. 6-7) indicates the best thickness to be about 0.02-0.03 diameters. A wall taper, giving a large variation of wall thickness from apex to base, may reduce penetration, but for some designs may reverse it. An explosive shoulder (i.e., a charge diameter greater than the cone O.D.) is generally detrimental. Truncation of the cone is sometimes beneficial. Filling the apex of the liner does not affect penetration, but objects within and nearer the base of the cavity inhibit or prevent jet formation.

Exact cone manufacture is important because many types of defects may greatly affect jet formation and reduce penetration. Ellipticity of 1.7 percent decreases penetration by more than 10 percent. A distorted cone whose apex is off-center relative to its base diameter may give penetration as much as 10 percent less than ideal. Annealing of most metals or other materials to remove the residual stresses is necessary. The bead on a welded cone must be ground flush to the cone on the outside but is not harmful on the inside.

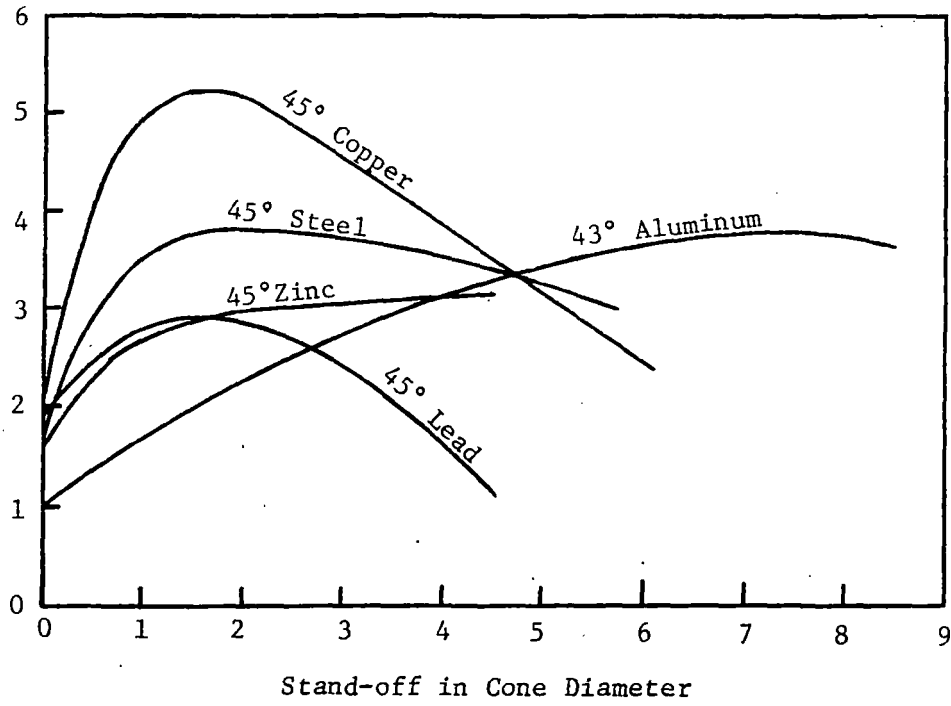


Fig. 6-5. Stand-off vs. penetration by material. (Brimmer).

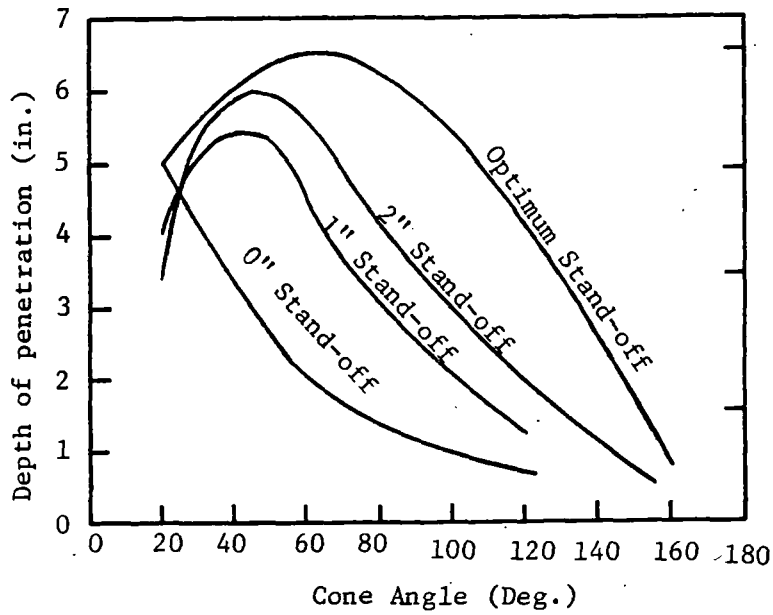


Fig. 6-6. Cone angle vs. penetration by stand-off. (Brimmer).

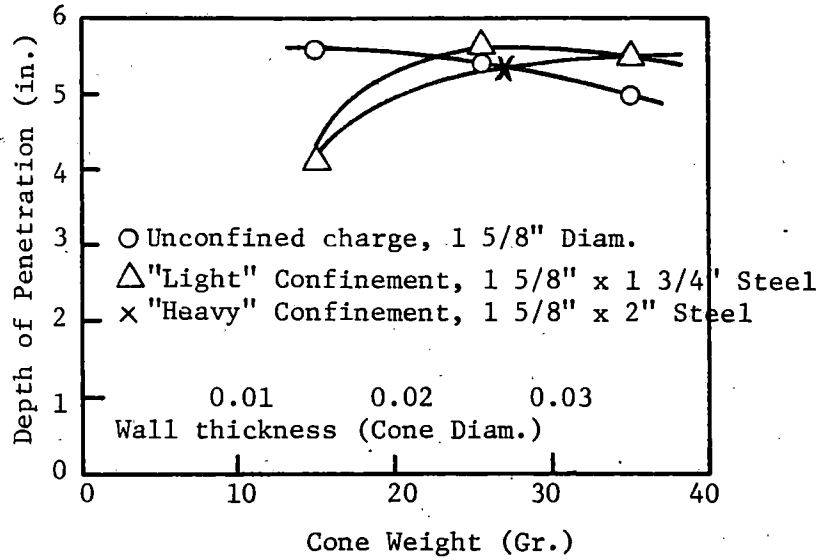


Fig. 6-7. Depth of penetration vs. wall thickness. (Brimmer).

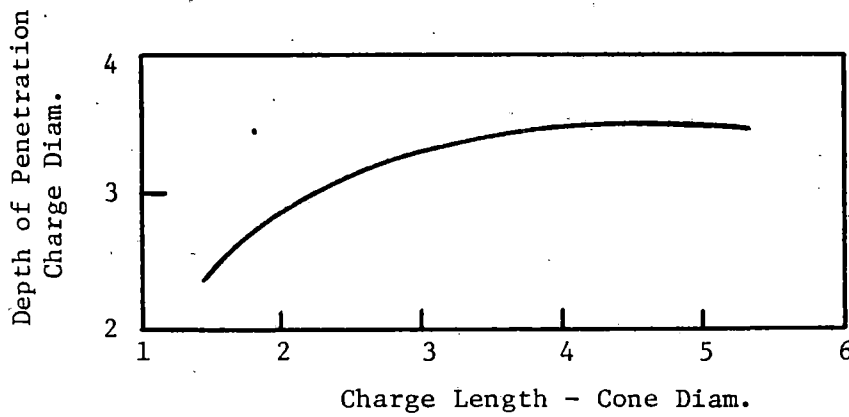


Fig. 6-8. Depth of penetration vs. charge length. (Brimmer)

Waviness along the slant height and wall thickness variation around the circumference may likewise seriously affect penetration. Furthermore, an inclination of more than 0.5 of a degree between the liner and the charge axis causes impairment of effective collapse and jet formation.

The length of the explosive charge also determines the depth of penetration. Greater charge lengths result in greater penetration, with a particularly marked increase up to 2.5 or 3 times the cone diameter (Fig. 6-8). Effectiveness of the shaped charge also depends upon the type of explosive used, with high detonation velocity and pressure being the most important properties. Symmetry is important in charge preparation just as in liner manufacturing and off-center positioning of the detonator by 1/10 of the charge diameter is detrimental in charges of standard lengths.

Other design factors used to enhance penetration include charge confinement and inertia or low velocity charge cores. Confinement enhances penetration only a small amount if the other design variables are adjusted for optimum performance. However, the use of a core of low-velocity explosive on non-explosive material (wave shaped) in the main charge may increase penetration by 25 percent.

Penetration by a perfectly fabricated charge is a function of standoff, i.e., the distance between the end of the charge and the target. Optimum values of standoff for steel targets are from 2-3 diameters (Fig. 6-9), but vary for different cone angles and different liner and target materials.

Jet Penetration of Rock

Lined shaped charges were investigated by Clark (Ref. 88) to evaluate their effect in breaking concrete blocks. Breakage by jets was less than

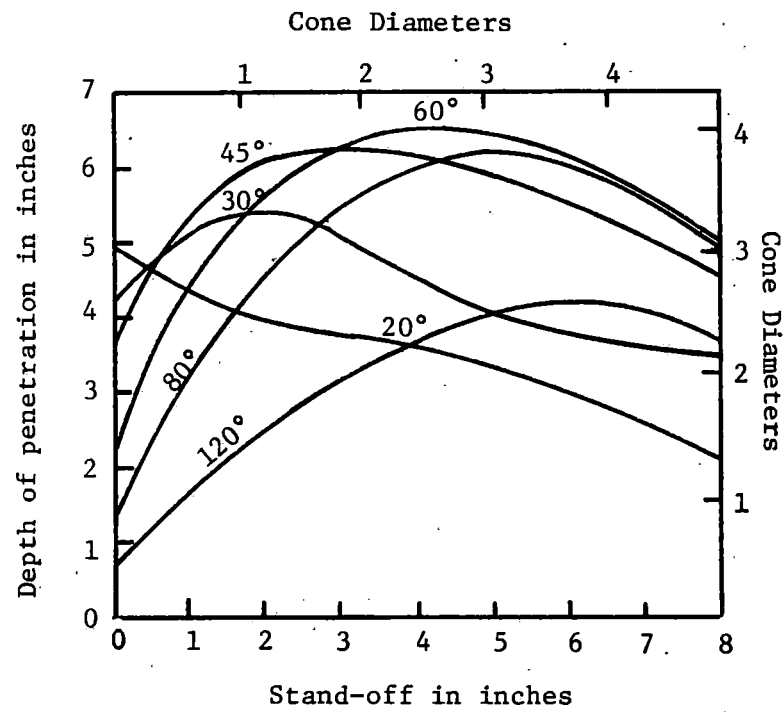


Fig. 6-9. Stand-off vs. penetration in cone angle. (Brimmer).

that achieved by the same amount of explosives in contact with the block, and considerably less than the same amount of explosive with a mud cap. Hopkins and Kolsky (Ref. 66) point out that in penetration of jets into lucite, the velocity of both the jet and penetration interface were so great that penetration was complete before a stress wave of appreciable magnitude and duration could be initiated in the target. These observations would indicate that while the high speed jets themselves are effective for penetration they may not be effective in breakage.

By comparison, for repeated pulsed jets of water the initial impact of the first few shots on rock creates minor cracks and the subsequent shots may cause breakage. The exploitation of the cracks by the water pressure and subsequent fracture represents a different mechanism and requires target defects to be present.

No detailed research results on the scaling of shaped charge penetration appear to have been published although developed equations, which are in fair agreement with observations, indicate that for a given charge material and configuration, the penetration depth should increase with the linear dimension of the charge. That is, the familiar cube root law of explosives applies, which in turn implies energy scaling.

Somewhat like short jets with high velocity, cylindrical projectiles with length/diameter ratios of 3 or greater form cylindrical craters instead of hemispherical. In metals it has been found that there are essentially three velocity regimes of projectile impact. The first is a low velocity region where

the projectile is subjected only to minor deformation. The second is a transitional region which leads into a third or high velocity region where fluid impact and inertia dominate. Several theories have been proposed to explain penetration, such as (1) the rigid projectile theory, (2) hydrodynamic theories, (3) power law postulations. These are summarized by Herrmann and Jones (Ref. 49). (See also Chapter V).

Three analogous regions also may exist for jets, depending upon jet and target properties, including density and velocity of the jet, and density, hardness and strength of the target.

Pack, et al., (Ref. 56) and Rostoker (Ref. 54) proposed jet penetration equations with a correction for target strength, and Cook (Ref. 3) extended these theories to determine the radius of the hole by assuming that the impulse transferred to the target expands the hole laterally.

If Bernoulli's theorem (Ref. 56) is applied to a steady jet impacting a target where the jet-target interface is moving with a constant velocity v the stagnation pressure is

$$p = \frac{1}{2}\rho_j v^2 = \frac{1}{2}\rho_j (v_j - v_i)^2 \quad (6-4)$$

A strength factor k was introduced by Rostoker (Ref. 54) to give

$$\frac{1}{2}\rho_t v^2 + k = \frac{1}{2}\rho_j (v_j - v_i)^2 \quad (6-5)$$

and Eichelberger writes the strength factor in the form

$$k = \frac{1}{2}\rho_j v_0^2 \quad (6-6)$$

where v_0 is the minimum jet velocity to just cause a crater.

The correction for strength used by Pack, et al., (Ref. 56) considered the correction to be expressed in powers of $Y/\rho_j v^2$ yielding a first approximation to which was added a correction term

$$\frac{h}{L} = \sqrt{\frac{\rho_j}{t}} \left[1 - \left(\frac{\alpha_1 Y}{\alpha_j v^2} \right) \right] + \frac{r}{L} \quad (6-7)$$

where Y is the dynamic yield strength of the target, α_1 is an empirical function of jet and target densities, and r is the hole radius.

Cook (Ref. 3) extended the theory for estimation of the hole radius r_1 by assuming that the impulse received by the target causes lateral expansion of the hole

$$\frac{\pi}{2} \rho_j (v_j - v_i) r_j^2 \Delta t = \frac{1}{2} \rho_t (\gamma^2 + k) \pi r^2 \Delta t \quad (6-8)$$

where r_j is the radius of the jet. The final cross-section is found for $\gamma = 0$

$$r = r_j (v_j - v_i) \frac{\rho_j}{2k} \quad (6-9)$$

or eliminating v_i yields

$$r = \frac{\sqrt{\rho_j \rho_t}}{\sqrt{\rho_t} + \sqrt{\rho_j}} \cdot \frac{r_j}{\sqrt{2k}} \quad (6-10)$$

This expression indicates that for a given jet target material combination, the hole radius is proportional to the radius of the jet, which has been borne out in observations of jet holes in rock materials.

Austin (Refs. 90 and 97) carried out the most complete study of jet penetration in rock reported in the literature. Data from his work plus that from experiments by Lewis and Clark (Ref. 87) are plotted in (Fig. 6-10). Density of target materials varies from approximately 1.0 to 9.0. It is noted that the penetration values do not follow the theoretical curve based upon the

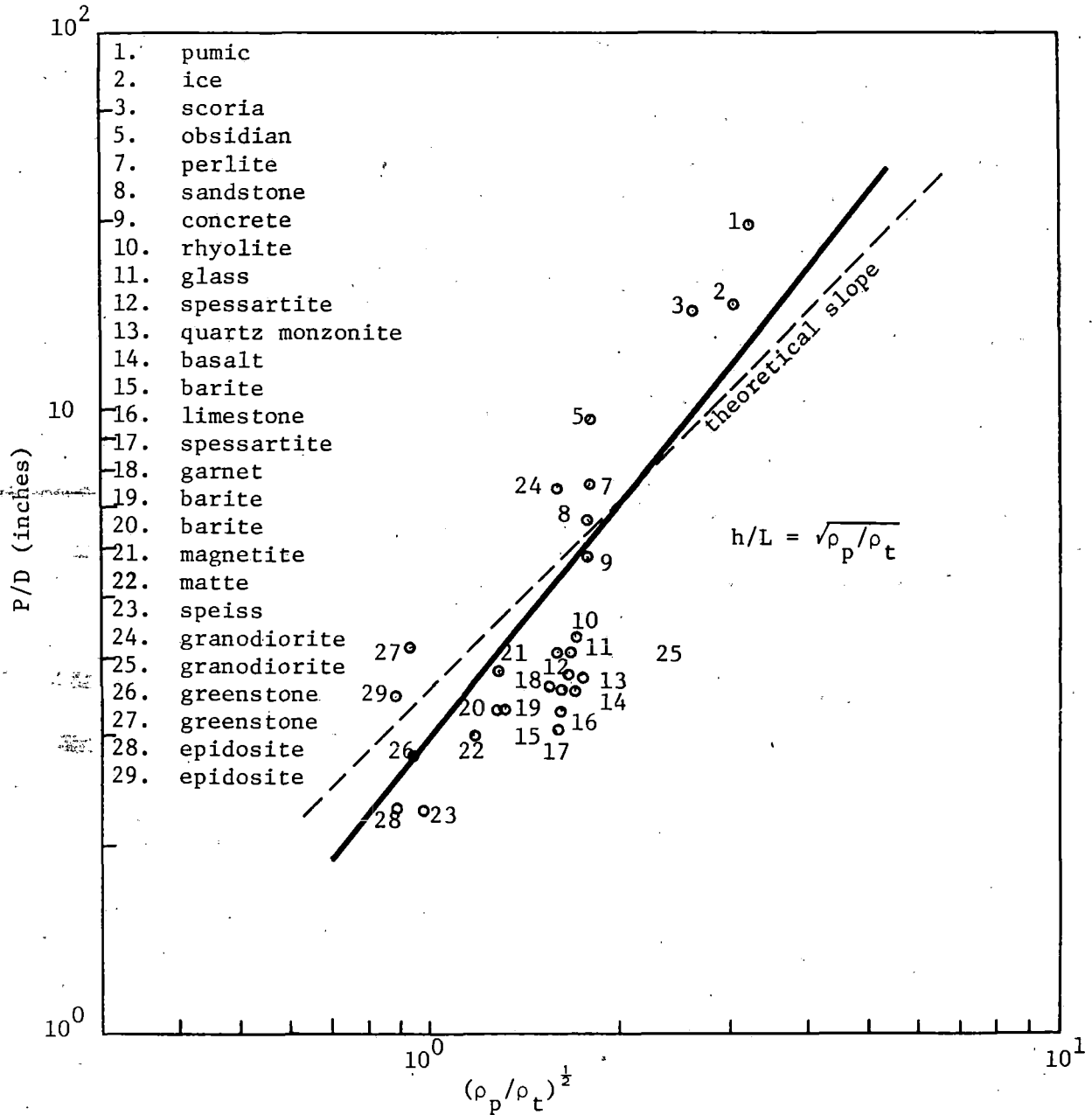


Fig. 6-10. Normalized rock penetration by shaped charge jets vs. square root of density ratio. Nos. 1-25 4" diam. cast iron cones, $\rho_p = 7.2$; Nos. 26-29 7" and 9½" glass cones, $\rho_p = 2.6$.
 P = penetration, D = charge diameter, ρ_p = jet density, ρ_t = target density, L = jet length.

theory by Pack and others. These data confirm the postulate that the effective strength appears to decrease with crater size. It should be noted also that there is considerable scatter in the data.

Draper, et al., (Ref. 98) made a series of tests with standard M-2A3 and M3 military breaking charges against greenstone and epidosite targets to determine possible applicability in conventional drilling and blasting.

	CHARGE DESCRIPTIONS	
	<u>M - 2A3</u>	<u>M3</u>
Wt - total	15	40
Wt of explosive	11.5	28.5
Type of explosive	50 - 50 pentolite	
Cone Material	glass	steel
Cone Angle	?	?
Diameter	7 inches	9½ inches
Length	12 inches	15½ inches
Design	Beehive	Beehive
Stand-off, normal	5½ inches	15 inches

Depths of penetration were 12 to 14 inches in epidosite and 15 to 19 inches in greenstone for the M-2A3, and 32 inches and 29 inches, respectively, for the M3.

Both types of rock were unusually dense and of high strength. Greenstone had a density of 2.96 and a compressive strength of 44,200 psi and epidosite, 3.26 and 63,100 psi, respectively. Both rocks were also unusually hard to drill with both diamond drills and pneumatic drills.

Preliminary tests were made with shaped charges at UMR (1968) to check results of others' investigations. The rock tested is a tough dolomite of density 2.57 and a compressive strength of 11,900 psi. Selected results of the tests by USBM, UMR and those by Austin (Ref. 97) are tabulated below:

AUSTIN'S TESTS

Charge Description:

Wt of explosive	5.5
Type of explosive	C-3
Cone Material	Cast Iron
Cone Angle	55°
Diameter	4 inches
Length	?
Design	cylindrical & beehive
Stand-off, normal	8 ± inches

Penetration:

Cylindrical:

Rhyolite	11-24 inches
Quartz mon.	16-34 inches
Limestone	8-10 inches
Sandstone	23-26 inches

Beehive:

Rhyolite	16-17
----------	-------

UMR TESTS

Charge Description:

Wt of explosive	11 ounces and 3 pounds
Type of explosive	C-4
Cone material	Cast Iron
Cone Angle	45° and 55°
Diameter	1½ and 3 inches*
Length	4½ and 6 inches
Design	Cylindrical
L/d ratio	4 and 3

* 3 inch is a beehive shape

Penetration - Dolomite:

<u>Charge Diameter</u>	<u>Explosive Weight</u>	<u>L/d</u>	<u>Penetration</u>
1½	11 oz.	4	10-12½ in. (45°)
2	1 lb.	3	8-12½ in. (55°)
3	2 lb.	(beehive)	21-24 in. (55°)

An examination of the results indicate that:

(1) The M2-A3 charge is ineffective probably because of the glass liner and other factors of design.

(2) The USBM tests were made on some of the hardest dense, tough rocks available, and are not representative of average rocks encountered.

(3) With a steel liner the M-3 charge was relatively effective in drilling holes.

(4) Austin makes no reference to annealing of his liners, which may be important to consistent, good performance.

(5) Cast iron and steel liners are not the most effective types that can be used. Copper and other metals give somewhat higher penetration.

(6) The military beehive charge is not an optimum design for performance purposes.

(7) Tests at UMR in a tough dolomite showed penetrations of 1-1/8 inch diameter holes of up to 12 in/lb. M-3 penetration varied from 0.8 to 1.0 inches per pound for 2-2½ inch diameter holes and Austin's tests showed from 2-7 inches of depth per pound.

(8) The USBM concludes that costs are approximately \$8.00 per foot of hole (1948). For a 3 inch charge (experimental) at UMR the cost is estimated at about \$5.00 per foot (1968). For production type charges the cost should be considerably less than this.

From the above it appears that no well-designed tests of the feasibility of using shaped charges for drilling and blasting have been made, and those performed have not utilized all of the necessary design standards to obtain optimum performance. No attempt was made to adapt shaped charge

performance to new design. Actually, some reported investigations were conducted under unfavorable conditions.

Recent pilot tests at UMR indicate that properly designed charges may give performance considerably better than those reported in the literature.

Based on this information it becomes evident that more data on closely controlled experiments is needed to establish the laws of high density jet penetration of rock. Most of the data in Figure 6-10 (shots 1-23) were acquired using a 4" diameter charge, 55° cone of cast iron, the charge being loaded with Comp. C-3. The report by Brimmer (Ref. 96) indicates that these liners may have been too thick. Also, no studies have been made on the relative effects of different liner materials on rock. No investigations have been made of the relative effects of metal jet velocity on penetration and/or breakage. The effect of high velocity water jets would be expected to be lower than that for glass.

Energy Partitioning

The categories into which the released explosive energy from a shaped charge is divided by the governing physical and chemical processes have not been quantitatively evaluated.

For an unconfined explosive charge the kinetic energy carried by the products of detonation is utilized in (1) deforming the cavity liner, (2) imparting kinetic energy to the jet and liner, (3) in expanding against atmosphere pressure, and (4) in lost heat. It is estimated that less than five percent of the total explosive energy in a charge with an ℓ/d ratio of five is utilized in forming the jet.

For a confined charge the energy partitioning between cavity and blast effects varies a few percent with the degree of confinement. As the confinement is increased from zero, there is only a small increase in the jet performance (Ref. 96). Much of the energy of a confined charge in a blast borehole is utilized in breaking the rock or imparting kinetic energy in the form of waves or ejected particles. For carefully controlled tests on cubes of concrete this amount has been found to be as high as seventy percent (Ref. 99).

Assuming that only a small portion of the explosive is utilized in jet formation, if shaped charges are employed for penetration only, a large part of the energy of the explosion is lost. On the other hand, if they can be employed to perform both drilling and blasting, the savings in equipment, time, energy consumption and cost should be appreciable. Currently, it is not possible to predict accurately the operational details of such a system.

As stated above, there appears to be little information in the literature available on energy partitioning of the impact kinetic energy utilization of shaped charge jets on semi-infinite targets, particularly of brittle materials. Some preliminary analyses are available for hypervelocity impact of projectiles on rock.

Gault and Hietowit (Ref. 83) analyzed the partitioning of energy against homogeneous basalt by approximate methods. (See Projectile Penetration). Theory showed that less than one percent of the impact energy is transferred into elastic wave energy.

If these approximations are reasonably correct, hypervelocity projectiles provide an inefficient means of fracturing. Likewise, if ejecta is made

up of fine material, considerable energy is utilized in comminution. Also, the largest portion of the initial kinetic energy is still in the form of kinetic energy after the impact process is complete. That is, the projectile retains more than half of its kinetic energy during and after the impact process.

These analyses may be used only as an initial guide for shaped charge jets, but it is probable that energy partitioning is a function of velocity, material properties and other factors as well. Percentages of partitioned energy should be quite similar to that for hypervelocity projectiles.

Target failure conditions due to projectile impact are complex, and a comparison of cratering in basalt with that in metals and water influenced Moore, et al., (Ref. 82), to come to the conclusion that tensile fracture plays a dominant role in total crater formation in basalt. Late spallation creates craters in rock which are about ten times as large as those in metal.

Fluid impact theory predicts that the crater volume or ejected mass for given materials should be proportional to the projectile energy. The results of these experiments indicate that the ejected mass varies as the energy to the 1.2 power of the velocity to the 2.4 power of the kinetic energy. In other words, the effective target strength decreases with crater size.

This would be a factor in favor of generating very high velocity jets or projectiles. If it applies over a wide range of velocities, then the cost per unit kinetic energy of jets and projectiles versus their velocity becomes an important design factor.

It is believed that further research will establish whether this relationship may be found to govern over a range of velocities of interest, and the

relative cost of producing very high velocity impact may be more accurately determined.

Cumulation - Tubular Booster

Cooley, et al., noted that the theory of cumulation jets from tubular cavities is not complete, but assumed that the two-dimensional analysis by Birkhoff (Ref. 51) can be applied. (See shaped charge theory). As noted in the analysis of shaped charges Eichelberger (Ref. 92) found that the agreement of observations from three-dimensional (axisymmetric jets) was largely fortuitous.

A portion of the mass of the booster is assumed to act in a manner analogous to a liner in an explosive cavity and that the material at the cavity surface moves normal to the conical surface of the cavity (Fig. 6-11). From considerations of momentum the jet velocity is found to be twice the shock velocity, and the slug has zero velocity. Calculations are also made for the mass of a hypothetical "slug". Both the theory and applications given by Cooley, et al., are inconclusive and subject to revision.

Cooley, et al., (Ref. 31) utilized a high velocity rifle (.22 caliber, (Fig. 6-12) with cumulation charges of paraffin or solidified glycerin cast in the muzzle. A nylon piston impacted the charge at velocities to 1,000 fps. Aluminum and steel targets were penetrated to moderate depths. Standoff behavior is similar to that for shaped charges (Fig. 6-13).

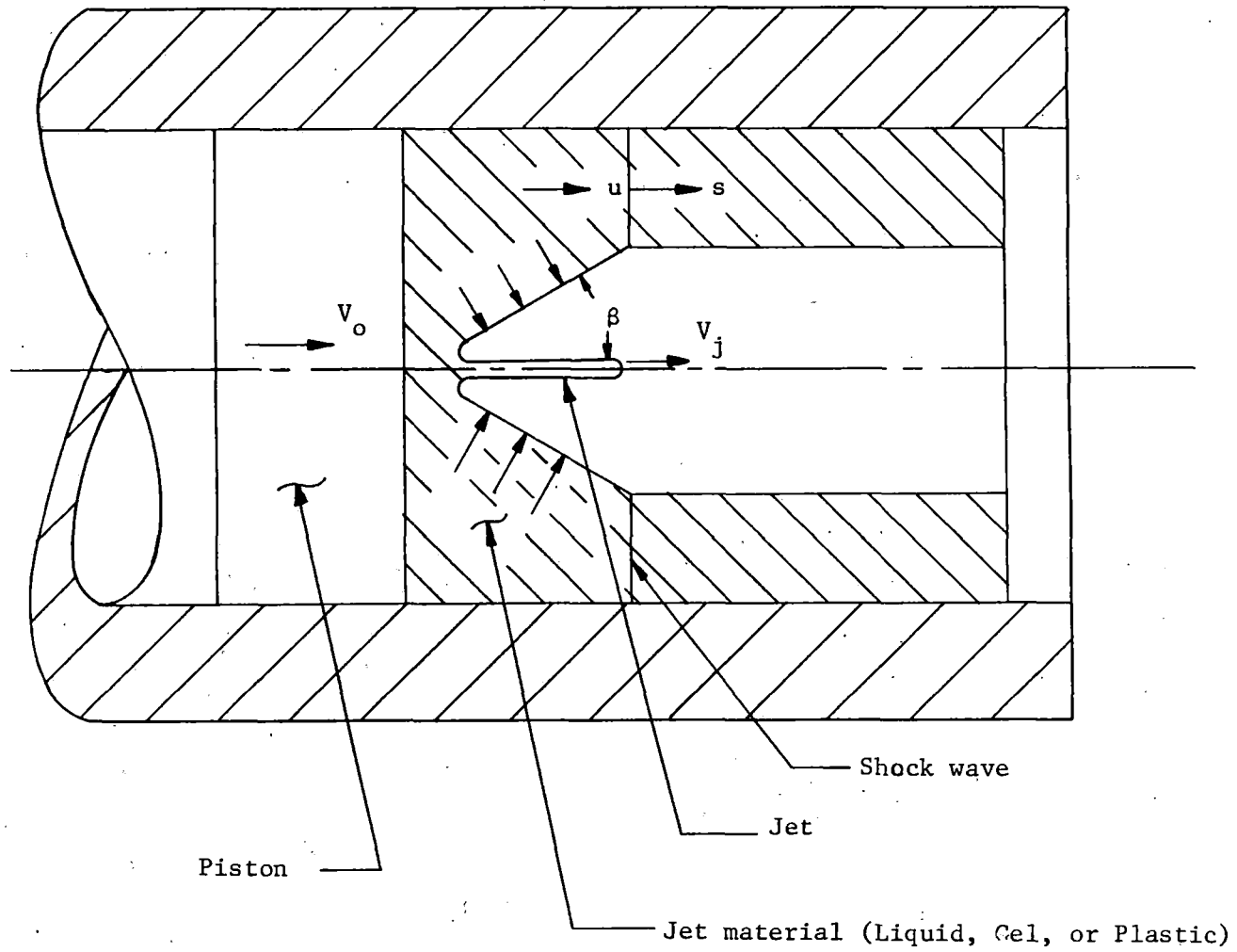


Fig. 6-11. Schematic of cumulation system to produce a jet. (Cooley).

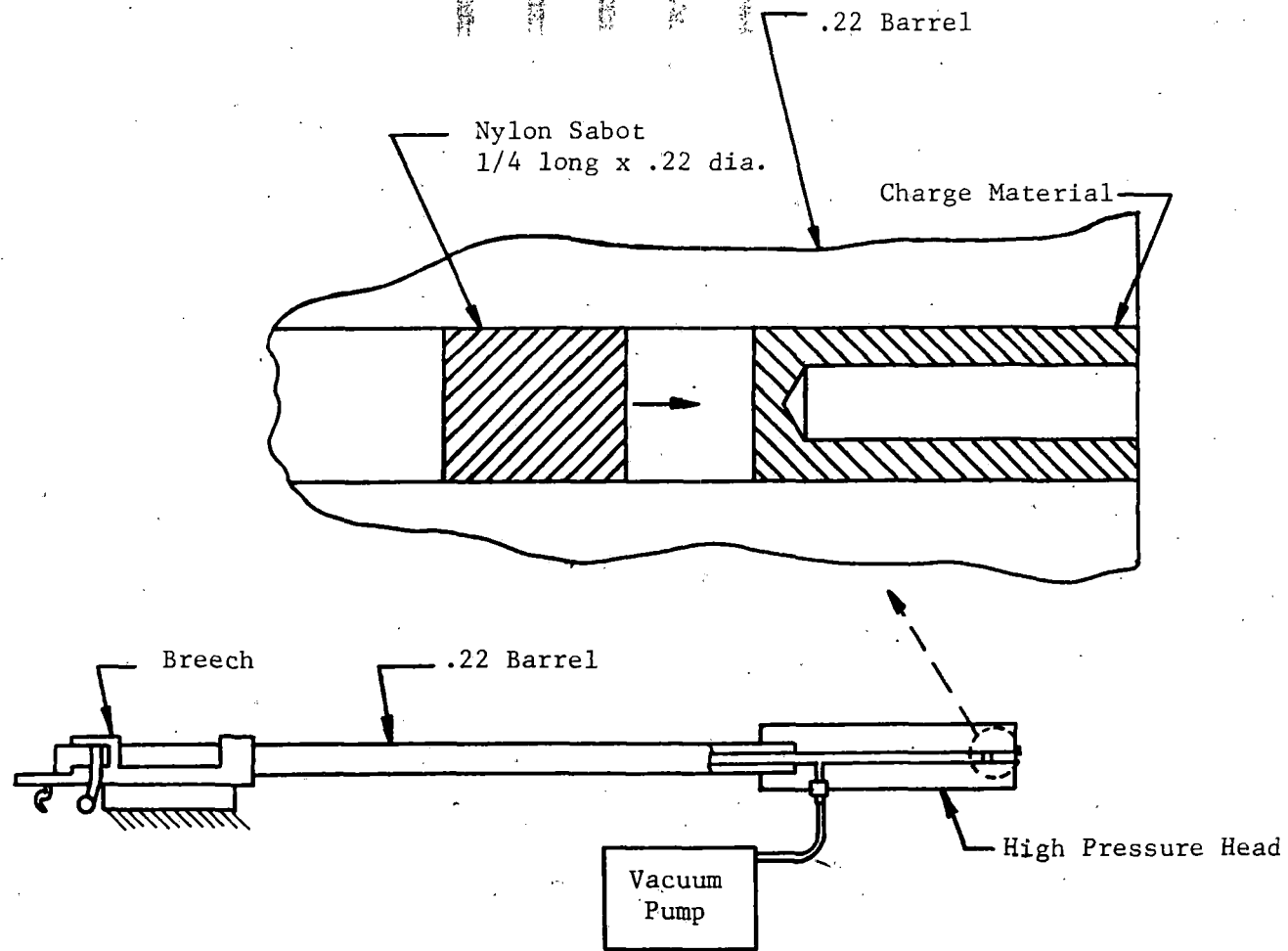


Fig. 6-12. Drawing of Cumulation Jet Test Equipment. (Cooley).

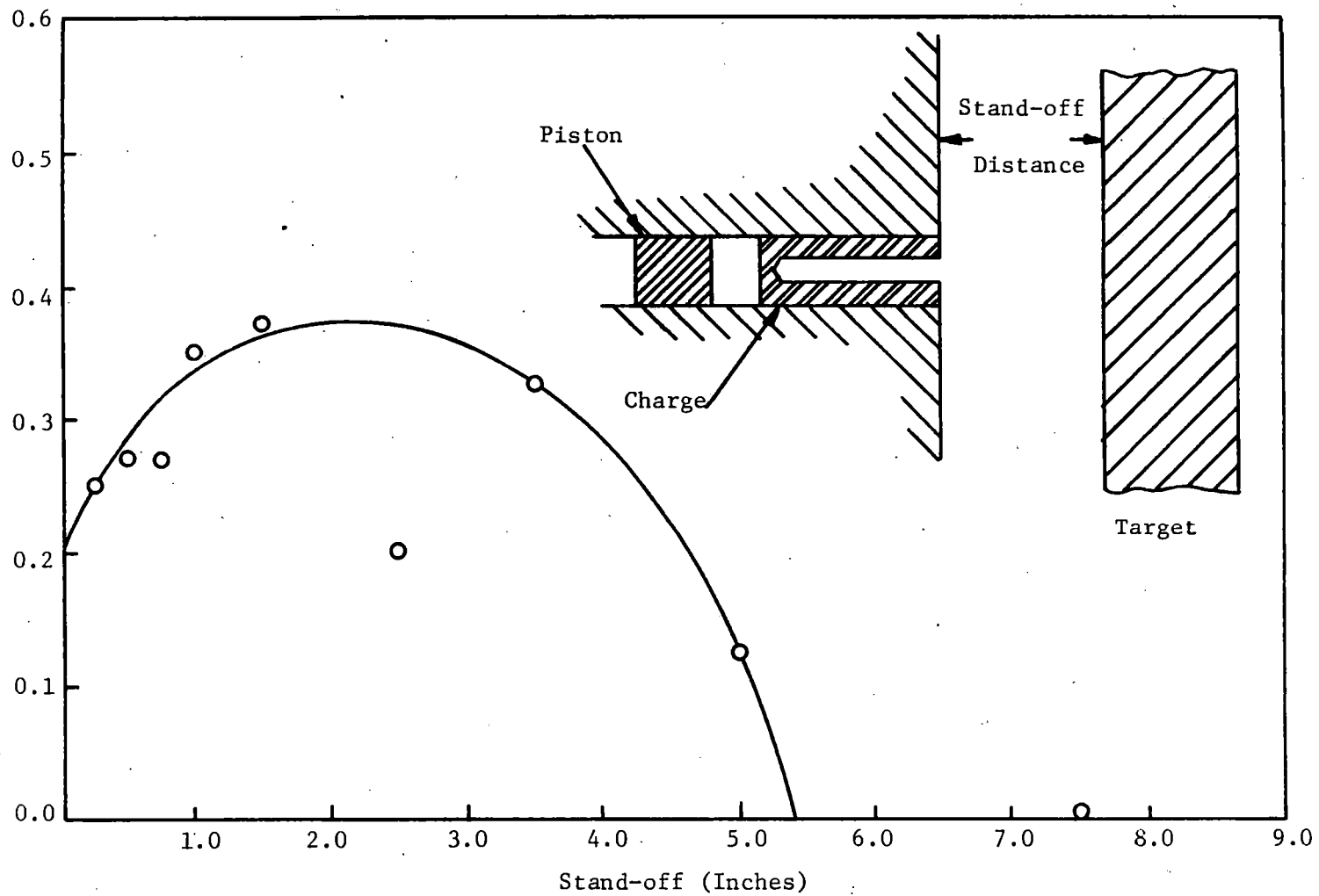


Fig. 6-13. Penetration as a function of stand-off distance for a 1.0 paraffin charge. (Cooley).

Miscellaneous

A method of obtaining isolated hypervelocity pellets of aluminum of 3.2 to 4.0 grams with velocities of 7.57 to 10.95 mm/ μ sec (25,059 and 35,478 ft/sec) from 3.33 inch diameter Comp. B shaped charge has been reported by Merendino, et al., (Ref. 100). A truncated shaped charge (Fig. 6-14) is provided with an inhibitor to prevent the collapse of the lower part of the cone. Copper inhibitors were only partially successful, permitting some high velocity material behind the initial mass to pass. Lucite provided an effective inhibitor (Fig. 6-15) with only a little low velocity debris. This may be deflected to a baffle plate by a semi-annular section of explosive below the base of the shaped charge.

Jet tip velocity varied with the cone angle, being 7.57 mm/ μ sec for 60°, 8.86 for 45°, 9.56 to 9.8 for 37°, 10.4 for 30°, 10.95 \pm for 25° and 11.7 for 20°. This projects to 15.6 mm/ μ sec for 0°, but a 20° apex liner did not produce a consolidated pellet.

In view of the fact that shaped charges follow a linear scale relation, it is suggested that a jet tip of mass of 200 grams would be obtained by increasing the charge diameter to 12 inches. This in turn may provide a simple means of providing high velocity projectiles for hypervelocity impact studies.

Sykes and Vrablik (Ref. 101) report on an explosive system for accelerating 2.2 gram pellets to velocities of 4.2 km/sec. It was accelerated by embedding a flat cylinder of metal in the end of an explosive charge. The whole was used as a final stage of a rocket in an experiment to observe the

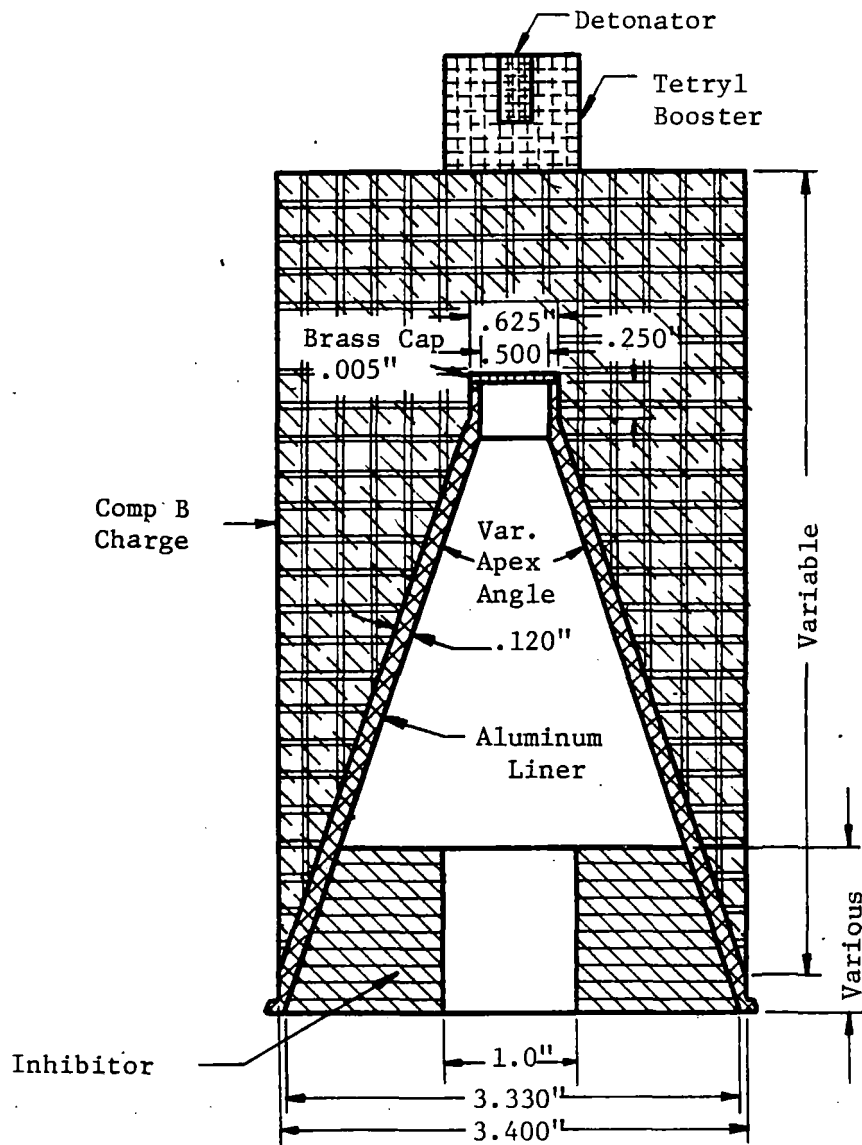
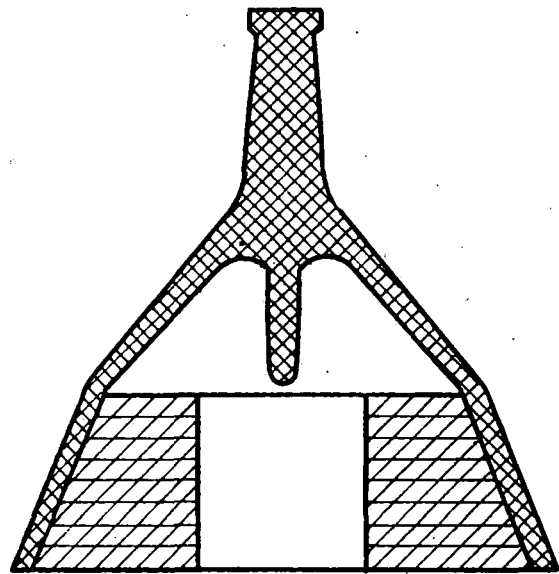
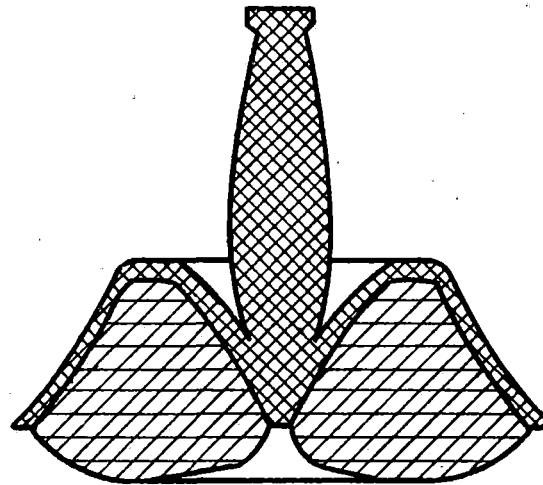


Fig. 6-14. Design of shaped charge used with lucite inhibitor. (Merendino).





"A"

18.0 μ s after detonation
(approx)



"B"

27 μ s after detonation

 Liner Material (Aluminum)
 Inhibiting Material (Lucite)

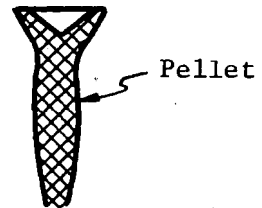


Fig. 6-15. Projectile formation from inhibited shape charge. (Merendino).

light emitted from an artificial nickel-iron meteorite of known mass.

James and Buchanan (Ref. 102) presented the result of a series of penetration tests on steel using a 45° copper liner 0.037 thick, charge (P.E.) five inches long and 1-5/8 inch diameter. Experiments were made (1) for measurement of depth and volumes of craters, and (2) for measurement of velocity of penetration in seven materials. A histogram of penetration indicates a somewhat skew distribution.

Density, tensile strength, shear strength and hardness of target materials were determined. No direct correlation was found between density or target strength and penetration for the whole length of the jets. However, for the higher velocity front portion of the jets there was good agreement in penetration for targets of the same density, but of different strengths. There also were good correlations found between strengths and hole diameter. Penetration velocities were found to be approximately proportional to the jet velocity.

CHAPTER VII

PRESSURE VESSELS

INTRODUCTION

In general the pressures to which a vessel is subjected may range from static or quasi-static to dynamic or impulsive. Static type pressure vessels have been investigated in great detail for cylindrical geometry, and to a lesser extent for spherical geometry. On the other hand very little seems to be known about the response of vessels to dynamic pressures.

This chapter is devoted to the current design principles which may have application to a 500,000 psi vessel having sufficient volume to be useful for high velocity jet formation. Vessels for static applications such as material properties studies and material synthesis under high confining pressures will not be considered. For the latter applications, pressures of the order of 1,000,000 psi are not uncommon. Such pressures are normally generated and contained in a small volume by rams converging on the small volume from various angles. These devices are commonly termed flat-face anvils, tetrahedral apparatus, and cubic apparatus depending on the geometry of the opposing pistons.

Due to their geometry and small volume the above devices do not appear to be applicable to this investigation. The chapter will be devoted to cylindrical vessels which could be employed as reaction chambers, piston-cylinder arrangements, or tubing to transport a high pressure fluid.

DYNAMIC PRESSURE VESSELS

A pressure vessel in its broadest sense is a container which confines the fluid long enough for the desired pressure effects to occur. With this

definition the "strength" of a vessel may be due to its inherent strength for intermediate rate processes, or to its mass or inertia for high rate processes, such as the detonation of an explosive.

An interesting application of the inertial type of vessel is the use of lead jackets around small explosive cores to afford the necessary confinement to sustain the detonation process. In this manner the critical charge diameter below which steady state detonation will not occur can be reduced considerably from that necessary for unconfined charges. Normally in these detonating fuses the "vessel" ruptures shortly after the detonation has passed; however, the desired effect in sustaining the detonation has been accomplished. Techniques have recently been developed for completely containing the reaction products from small explosive cores if necessary. Here the design is both inertial and conventional.

Mackenzie and Dalrymple (Ref. 103) detonated spheres of C4 explosive centrally located in cylindrical containers to determine the maximum amount of explosive which could be detonated in various size cylinders of various materials. Sidewall rupture was the prevalent type of failure. Empirical curves were determined relating the limiting mass of the explosive to the inside diameter and wall thickness for several aluminum alloys and stainless steels. No theoretical analysis was attempted.

In another report on this same problem, Mackenzie, Dalrymple, and Schwartz (Ref. 104) state the commonly measured engineering strengths of materials are of little value in the design of dynamic vessels. The strength

of a material is rate dependent and no simple relation exists between the static and dynamic strengths of any given material. Thus, static characteristics are of no great value in the design of dynamic pressure vessels.

Daugherty (Ref. 105) designed and fabricated a one million psi pressure chamber to contain the pressure of a small detonating explosive charge. The internal volume of this vessel was only 0.275 in.³, and the vessel was of the multi-anvil type. It appears that the design was based solely on static pressurization which may or may not be sufficient for explosive pressurization.

Rate effects in pressure vessels have been analyzed theoretically by Spillers (Ref. 106). His analysis is for an orthotropic viscoelastic thick-walled tube in plane strain subjected to an applied pressure of the form

$$p(t) = p_0 u(t) \quad (7-1)$$

where $u(t)$ is the unit step function. The solution for radial stress σ_r at radius r obtained through the Laplace transformation is given by

$$\sigma_r = -\frac{p_0 a}{r} \left\{ \frac{\ln a}{\ln b} + \frac{2}{\pi} \sum_{n=1}^{\infty} \frac{(-1)^n}{n} \sin \left(n\pi \frac{\ln a}{\ln b} \right) \right. \quad (7-2)$$

$$\left. \left[\frac{\phi(0)}{\gamma_1 \gamma_2} + \frac{e^{\gamma_1 t} \phi(\gamma_1)}{\gamma_1 (\gamma_1 - \gamma_2)} + \frac{e^{\gamma_2 t} \phi(\gamma_2)}{\gamma_2 (\gamma_2 - \gamma_1)} \right] \right\}$$

where γ_1 and γ_2 are the roots of

$$s^2 \left[\ell n^2 b + n^2 \pi^2 \frac{\alpha_{11}}{\alpha_{22}} \right] + s \left[\ell n^2 b (\beta_{22} + \gamma_{11}) + n^2 \pi^2 \frac{\alpha_{11}}{\alpha_{22}} (\gamma_{22} + \beta_{11}) \right] \quad (7-3)$$

$$+ \ell n^2 b \beta_{22} \gamma_{11} + n^2 \pi^2 \frac{\alpha_{11}}{\alpha_{22}} \gamma_{22} \beta_{11} = 0.$$

$$\phi(s) = \frac{\ell n^2 b (s + \beta_{22}) (s + \gamma_{11})}{\ell n^2 b + n^2 \pi^2 \frac{\alpha_{11}}{\alpha_{22}}} \quad (7-4)$$

s is the transform variable,

a and b are the internal and external radii respectively.

α_{11} , α_{22} , β_{22} , γ_{11} and γ_{22} are constants describing the viscoelastic properties of the orthotropic material.

Spillers then discusses the simplifications which are introduced when the material is assumed to be incompressible. An anisotropic material does not have a coefficient of compressibility as an isotropic material does; thus, material incompressibility must be interpreted to mean that the material undergoes no dilatation. The simplification of incompressibility resulted in the Laplace transforms of the responses having the transform-parameter as a rational function. The responses are thus of the same order of complexity as the response of an isotropic thick-walled tube.

STATIC PRESSURE VESSELS

It is desired to design cylindrical pressure vessels to contain static or quasi-static pressure up to 500,000 psi. A cylindrical geometry is generally more useful than a spherical geometry since it lends itself to piston-cylinder and transport (tubing) applications as well as a simple container.

It is shown in Appendix B that a thin-walled vessel (diameter greater than 20 times wall thickness) can contain a pressure of not more than 1/10 of the tensile strength of the material. Thus, even for steels having tensile strengths in the order of 300,000 psi, a thin-walled vessel will sustain, at most, up to 30,000 psi internal pressure.

Higher pressure can be contained, however, by increasing the ratio of wall thickness to diameter. The stresses then vary across the wall and the vessel is termed thick-walled. Lamé developed the classical equations for the stresses in such a thick-walled cylinder assuming elastic behavior and loading by internal and external pressures p_i and p_o respectively (Fig. 7-1). These equations for radial and tangential stresses at radius r , σ_r and σ_θ respectively, are

$$\sigma_r = \frac{a^2 b^2 (p_o - p_i)}{b^2 - a^2} \cdot \frac{1}{r^2} + \frac{p_i a^2 - p_o b^2}{b^2 - a^2} \quad (7-5)$$

$$\sigma_\theta = -\frac{a^2 b^2 (p_o - p_i)}{b^2 - a^2} \cdot \frac{1}{r^2} + \frac{p_i a^2 - p_o b^2}{b^2 - a^2} \quad (7-6)$$

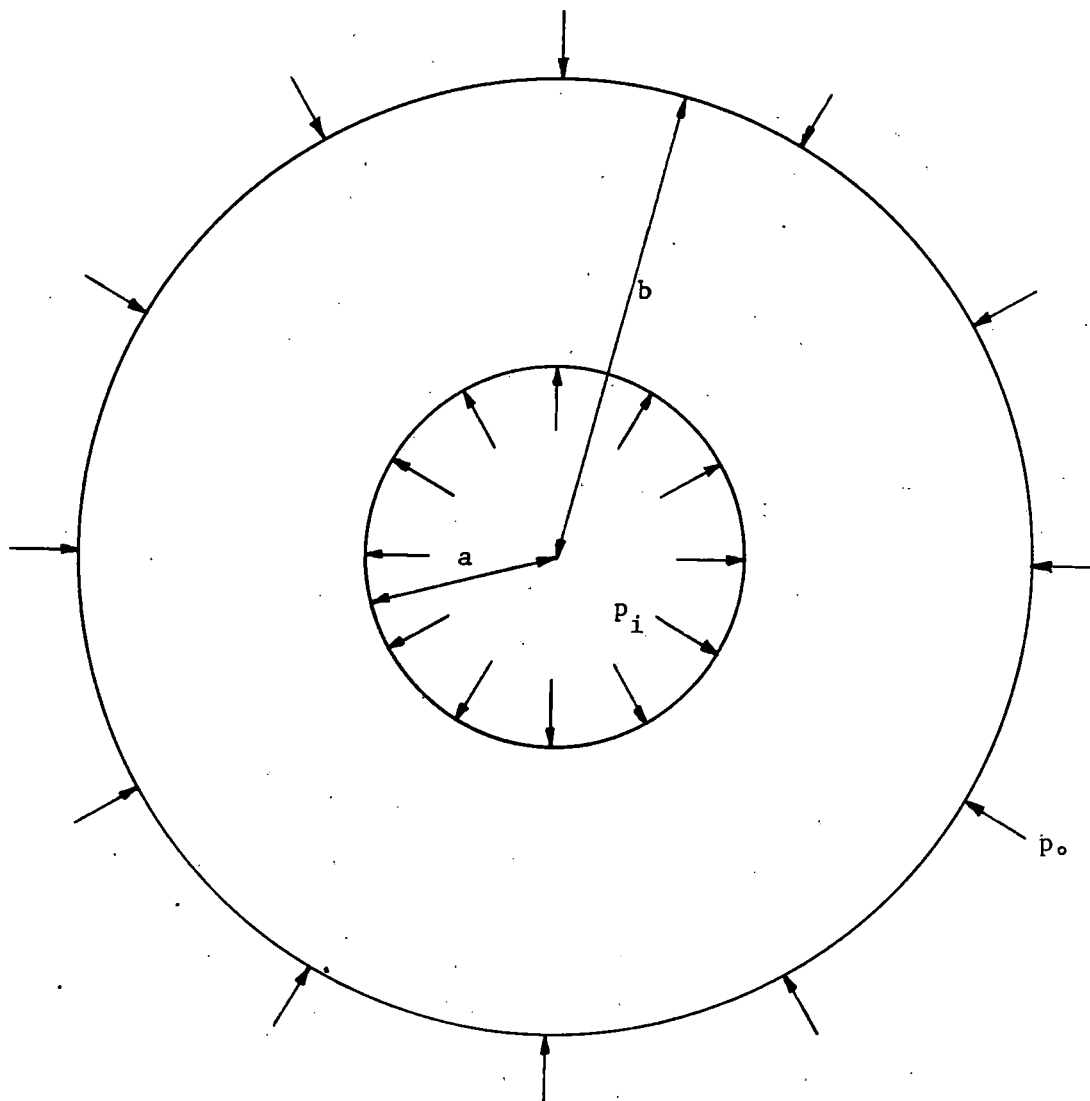


Fig. 7-1. Thick-walled cylinder subjected to internal and external pressures.

When the external pressure is zero the above equations reduce to

$$\sigma_r = \frac{a^2 p}{b^2 - a^2} \left(1 - \frac{b^2}{r^2} \right) \quad (7-7)$$

$$\sigma_\theta = \frac{a^2 p}{b^2 - a^2} \left(1 + \frac{b^2}{r^2} \right) \quad (7-8)$$

where p is the internal pressure. Equations (7-7) and (7-8) indicate that σ_r is everywhere compressive and that σ_θ is always tensile. The stress σ_θ is maximum at the inner surface, where

$$\sigma_{\theta\max} = \frac{p(a^2 + b^2)}{b^2 - a^2} \quad (7-9)$$

As the outer radius b becomes infinite it can be shown that $\sigma_{\theta\max}$ approaches the internal pressure p . Thus, there is a limit to the pressure which can be contained, even with infinitely thick walls.

Equation (7-8) shows that the tangential stress decreases with increase in radius outward from the bore. Thus, the outer material does not contribute as much to the confinement as that near the bore. Various techniques have been developed to create a more nearly uniform stress distribution across the wall thickness. Basically all of these techniques attempt to introduce residual compressive tangential stresses near the opening which will tend to decrease the magnitude of the tensile stresses in this critical region. The various methods for accomplishing this are autofrettage, shrink bands, multiple cylinder configurations, and wire wrapping.

Autofrettage is the most widely discussed technique for introducing residual compressive stresses near the cylindrical cavity. The technique is used in gun barrel manufacture and is applicable to other vessels. It consists of a pressurization beyond the design pressure so that the material becomes partly or fully plastic. Upon release of the pressure a residual stress pattern is created which makes the stress at subsequently applied design pressure more uniform throughout the thickness of the vessel.

Appendix B gives a detailed analysis of the autofrettage process for a material which is elastic up to the yield point and perfectly plastic thereafter. It is assumed that material behaves elastically upon release of the autofrettage pressure and also upon repressurization to any value up to the autofrettage pressure. A maximum shear stress failure criterion is employed. Equations for radial and tangential stresses are developed in Appendix B for the various stages of the autofrettage process for the cases of yielding throughout the entire wall and partial yielding.

Seely and Smith (Ref. 107) state that the assumption of constant maximum shear stress in the plastic region during the initial pressurization is reasonable if there is no increase in strength of the material due to cold working and if the residual stresses do not cause yielding in the reverse direction upon release of the pressure. These conditions are substantially met for materials having a well-defined yield point and for cylinders having dimensions such that the ratio $\frac{b}{a}$ is small to medium in value.

Figure 7-2 is a graph of the ratio of the internal pressure to the tensile elastic strength versus the ratio of the external radius to the internal

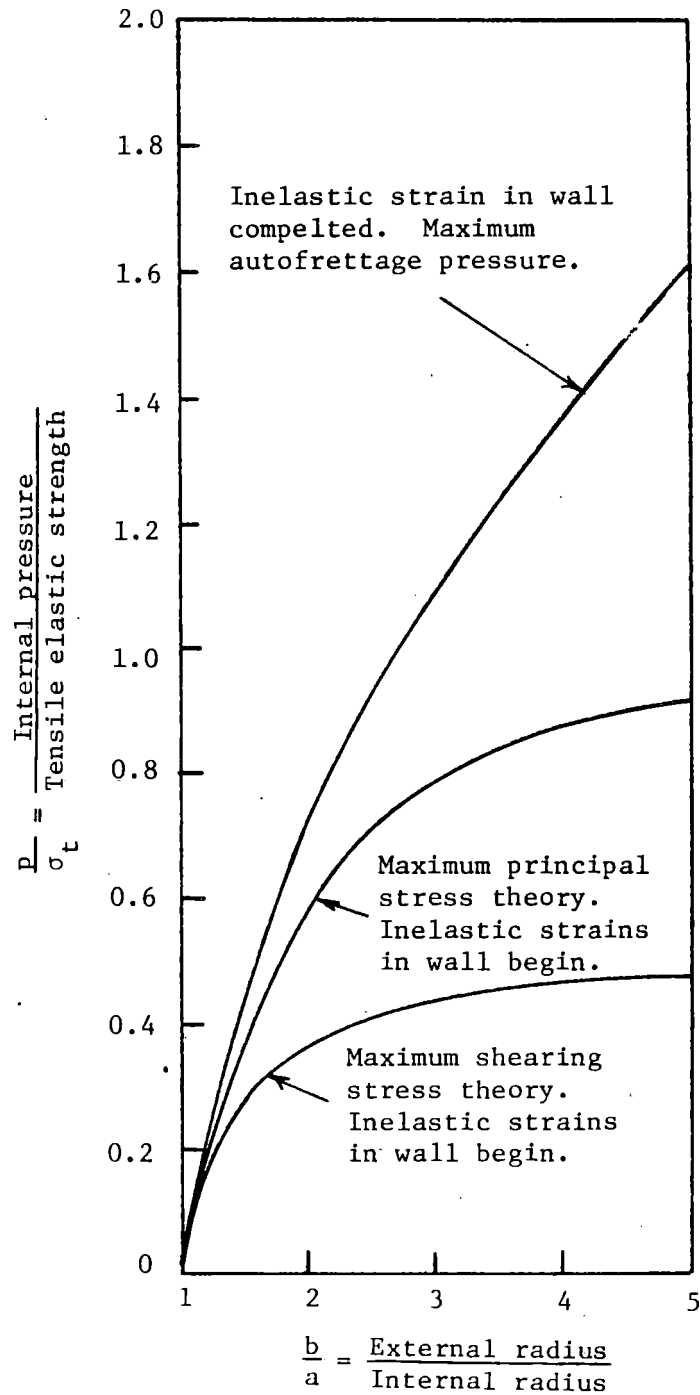


Fig. 7-2. Influence of autofrettage. (Seely and Smith).

radius. The bottom curve is a plot of these ratios when inelastic strains in the wall begin, based on the maximum shearing stress theory; the middle curve shows the ratios when inelastic strains commence but is based on the maximum principal stress theory; the upper curve shows the ratios when the wall becomes entirely plastic at the maximum autofrettage pressure. The middle curve is normally not used since the maximum principal stress theory is not valid for this type of loading. The curves coincide at the origin which corresponds to a thin-walled vessel. For $\frac{b}{a} = 5$ it is seen that the pressure can be increased by a factor of approximately three from the time when the inside wall first becomes plastic to when the entire wall becomes plastic.

Berman (Ref. 108) lists the primary limitations to the autofrettage process and its analysis as:

1. Pressures much higher than the design pressure used to produce autofrettage may be near the burst pressure.
2. Material properties beyond the yield point are difficult to determine and may vary from point to point in the material.
3. The relationship between measured material properties and the multiaxial stresses in those parts of the vessel in the plastic range is approximate.
4. The true residual stress pattern is open to question due to variations of material properties in the plastic range and the approximation in their application.
5. A large portion of the vessel is considerably understressed unless the design pressure is near the fully plastic pressure.

Faupel (Ref. 109) speaks of percent autofrettage and percent overstrain. Full or 100 percent autofrettage is obtained when the theoretical maximum residual stresses are left at the bore. The cylinder is said to be 50 percent autofrettaged when only half of the maximum possible residual stress is left at the bore. Full or 100 percent overstrain occurs when the entire wall becomes plastic; 50 percent overstrain indicates that the plastic zone has penetrated only half of the wall thickness. For some real materials 100 percent autofrettage can be accomplished by only 10 percent overstrain. Optimum design is considered as that producing the maximum residual stress distribution with minimum material.

Faupel also points out the importance of reverse yielding in compression. This phenomenon occurs when the material near the bore yields in compression upon release of the pressure rather than following Hooke's law during the entire release. If the theoretical maximum value of residual stress is governed by von Mises' criterion (constant octahedral shearing stress or maximum distortion energy) it can be shown that the limiting condition for no reverse yielding in a fully overstrained, closed-end cylinder is a diameter ratio $\frac{b}{a} = 2.22$. For an open-end cylinder the limiting ratio is 1.94. For diameter ratios greater than these reverse yielding will occur on release of the autofrettage pressure if the pressure is greater than twice the elastic breakdown pressure for a closed-end cylinder, or 1.83 times the elastic breakdown pressure for a closed-end cylinder.

Prager and Hodge (Ref. 110) present the theory of reverse yielding making the simplifying assumptions of incompressibility and equal values of tensile and compressive yield strength. The elastic range for unloading from

a plastic state and subsequent loading in the opposite sense then equals the elastic range for the original loading. Thus, a pressure release of magnitude Δp will induce reverse yielding of $\Delta p > 2 p_{yp}$, where p_{yp} is the pressure at which the wall begins to yield upon the initial pressurization. Their analysis assumes plane strain conditions and that von Mises' yield criterion applies.

Assume an initial pressurization to cause the vessel to yield out to a radius c so that the region $a \leq r \leq c$ is plastic and the region $c \leq r \leq b$ is elastic. The stresses in the elastic and plastic zones are

$$\sigma_r = \begin{cases} -\tau_{yp} \left(1 - \frac{c^2}{b^2} - 2 \ln \frac{r}{c} \right) & a \leq r \leq c \\ \frac{c^2}{b^2} \tau_{yp} \left(1 - \frac{b^2}{r^2} \right) & c \leq r \leq b \end{cases} \quad (7-10)$$

$$\sigma_\theta = \begin{cases} \tau_{yp} \left(1 + \frac{c^2}{b^2} + 2 \ln \frac{r}{c} \right) & a \leq r \leq c \\ \frac{c^2}{b^2} \tau_{yp} \left(1 + \frac{b^2}{r^2} \right) & c \leq r \leq b \end{cases} \quad (7-11)$$

$$\sigma_z = \begin{cases} \tau_{yp} \left(\frac{c^2}{b^2} + 2 \ln \frac{r}{c} \right) & a \leq r \leq c \\ \tau_{yp} \frac{c^2}{b^2} & c \leq r \leq b \end{cases} \quad (7-12)$$

where τ_{yp} is the yield strength in shear and where the radius c is related to the pressure p by

$$p = \tau_{yp} \left(1 - \frac{c^2}{b^2} - 2 \ln \frac{a}{c} \right) \quad (7-13)$$

Let c' be the radius of the elastic-plastic interface for the reverse yielding which occurs for a pressure release of magnitude Δp , where $\Delta p > 2p_{yp}$.

The radius c' for a given Δp can be determined from

$$2 \ln \frac{b}{c'} + \left(\frac{c'}{b} \right)^2 - 1 = 2 \ln \frac{b}{a} - \frac{\Delta p}{2 \tau_{yp}} \quad (7-14)$$

The changes in the stresses produced by the decrease in pressure Δp

are then shown to be

$$\Delta \sigma_r = \begin{cases} 2 \tau_{yp} \left(1 - \frac{c'^2}{b^2} - 2 \ln \frac{r}{c'} \right) & a \leq r \leq c \\ - 2 \tau_{yp} \frac{c'^2}{b^2} \left(1 - \frac{b^2}{r^2} \right) & c' \leq r \leq b \end{cases} \quad (7-15)$$

$$\Delta \sigma_\theta = \begin{cases} - 2 \tau_{yp} \left(1 + \frac{c'^2}{b^2} + 2 \ln \frac{r}{c'} \right) & a \leq r \leq c' \\ - 2 \tau_{yp} \frac{c'^2}{b^2} \left(1 + \frac{b^2}{r^2} \right) & c' \leq r \leq b \end{cases} \quad (7-16)$$

$$\Delta \sigma_z = \begin{cases} - 2 \tau_{yp} \left(\frac{c'^2}{b^2} + 2 \ln \frac{r}{c'} \right) & a \leq r \leq c' \\ - 2 \tau_{yp} \frac{c'^2}{b^2} & c' \leq r \leq b \end{cases} \quad (7-17)$$

The residual stresses remaining after release of the internal pressure will then be the difference between the stresses given in equations (10), (11), and (12) and the corresponding stresses given in equations (15), (16), and (17).

When the material exhibits strain hardening, the plastic analyses of the stresses in a thick-walled vessel become more complicated and generally involve numerical solutions. Such analyses may be based on either tensile stress-strain diagrams or shear stress-strain diagrams. Jorgensen (Ref. 111) used tensile data to analyze the stresses in elastically strained and partially overstrained thick-walled cylinders since tensile data are more readily available and calculations are somewhat simplified. The equation for the ultimate pressure p_{ult} which best fit the experimental data was

$$p_{ult} = \frac{2}{\sqrt{3}} \frac{\sigma_u + \sigma_o}{2} \ln R' \quad (7-18)$$

where

σ_u = ultimate stress psi

σ_o = outside wall stress taken from the stress-strain diagram.

R' = ratio of outside radius to inside radius in the strained condition.

In a later investigation Jorgensen (Ref. 112) compared experimental data for pressure vessels for steels with numerical calculations based on both tensile and torsional stress-strain data.

Three regions are considered: the outer elastic region $r_y \leq r \leq b$, a perfectly plastic region $r_p \leq r \leq r_y$, and a region of strain hardening $a \leq r \leq r_p$.

The pressure summations p_e , p_y , and p_σ in the elastic, plastic, and strain hardening regions in terms of the tensile stress-strain data are shown to be

$$p_e = \frac{\sigma_y}{\sqrt{3}} \left(1 - \frac{r_y^2}{b^2} \right) \quad (7-19)$$

$$p_y = \frac{2}{\sqrt{3}} \sigma_y \ln \frac{r_y}{r_p} \quad (7-20)$$

$$p_\sigma = \frac{1}{\sqrt{3}} \int_{r=a}^{r=p} (\sigma_m + \sigma_n) \ln \frac{r_n + u_n}{r_m + u_m} \quad (7-21)$$

The corresponding equations for torsional stress-strain data are

$$p_e = \tau_y \left(1 - \frac{r_y^2}{b^2} \right) \quad (7-22)$$

$$p_\tau = \int_{r=a}^{r=p} (\tau_m + \tau_n) \ln \frac{r_n + u_n}{r_m + u_m} \quad (7-23)$$

where r_m, r_n = initial intermediate radii
 u_m, u_n = intermediate radial deformation
 σ_m, σ_n = equivalent true intermediate stresses
 σ_y = true yield stress
 τ_y = yield shear stress

From the discussion at the end of this paper it appears that Jorgensen's analyses may be in error since he used $\epsilon = u/r$, where ϵ is the radial

strain, instead of the correct expression $\epsilon = \partial u / \partial r$. There is also some question as to the validity of assuming constant volume conditions in the elastic portion of the vessel, although there is general agreement that the constant volume assumption is valid in the plastic portion.

Crossland and Bones (Ref. 113) related torsional and tensile test data to the pressure-expansion curves and ultimate pressures of thick-walled cylinders. The problem of yield for materials with an upper yield strength is complicated by the fact that the upper yield strength is a function of the stress gradient. The initial yield stress in a thick-walled cylinder is approximately equal, however, to that found from a torsion specimen with the same stress gradient as in a cylinder. The constant pressure which will cause continued expansion when the cylinder has just become fully plastic but before strain hardening has commenced is termed the "collapse pressure". The experimental results compared favorably with the theoretical curves as evidenced by the curves in Figure 7-3. These curves show the relationships between the collapse pressure and the diameter ratio, and between the initial yield pressure and the diameter ratio for 0.15 percent carbon steel. The initial yield pressure was predicted very accurately when the upper yield shear stress was corrected for shear stress gradient. The pressure-expansion curve (pressure versus tangential strain at outside surface) was obtained by manipulating the following three equations:

$$r + u = \sqrt{r^2 + 2a u_a + u_a^2} \quad (7-24)$$

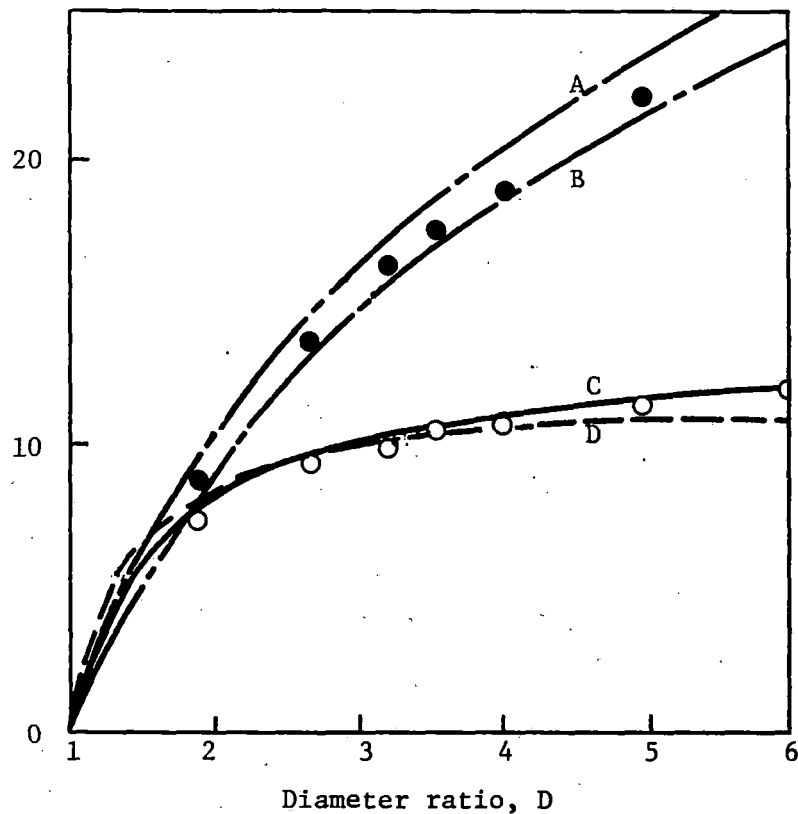


Fig. 7-3. Initial yield and collapse pressures for 0.15 percent carbon steel. (Crossland and Bones).

A, B Theoretical collapse pressure-diameter ratio curves based on plastic yield shear stress, τ_2 (A: $\tau_2 = 7.4$ ton/in²; B: $\tau_2 = 6.8$ ton/in²).

Experimental points for collapse pressure.

C Theoretical initial yield pressure-diameter ratio curve based on an upper yield shear stress corrected for shear stress gradient.

D Theoretical initial yield pressure-diameter ratio curve based on an upper yield shear stress $\tau_1 = 11.5$ ton/in².

○ Experimental points for the initial yield pressure.

$$\gamma_e = 2 \ln \frac{r+u}{r} \quad (7-25)$$

$$p = \int_{a+u_a}^{b+u_b} \frac{\tau}{r+u} d(r+u) \quad (7-26)$$

where

u = radial displacement at radius r

γ_e = equivalent shear strain at radius $r + u$

a, b = inside and outside radii respectively

τ = shear stress at radius r

p = internal pressure

Figure 7-4 shows the relationships between the theoretical ultimate pressure and the diameter ratio, and between the experimental ultimate pressure and the diameter ratio for the 0.15 percent carbon steel. The ultimate pressure is the highest pressure on the pressure-expansion curve. The theoretical curve and experimental points agree closely in Figure 7-4.

Similar graphs showing excellent correlations for initial yield pressures, collapse pressures, and ultimate pressure, were obtained for 0.3 percent carbon steel and for Vibrac.

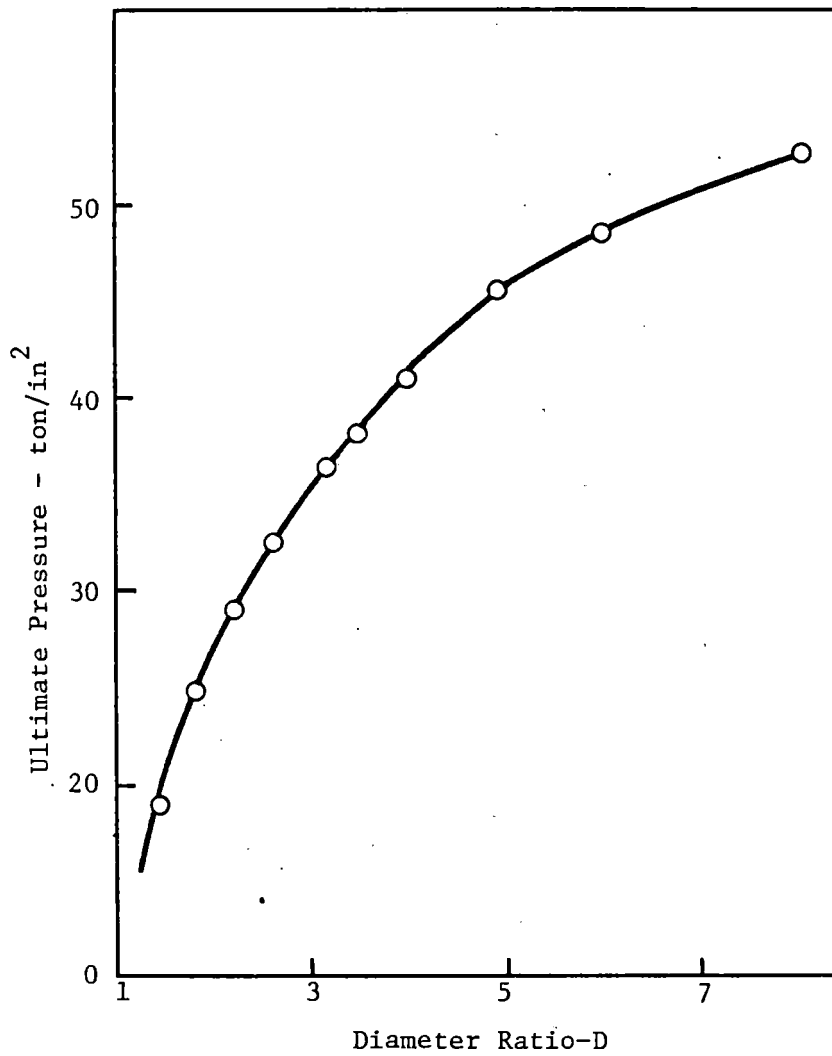


Fig. 7-4. Experimental and theoretical ultimate pressure-diameter ratio curves. (Crossland and Bones).

Dawson (Ref. 114) calculated the expansion (tangential strain at outside surface) and residual stresses in a cylinder of work hardenable material using a method proposed by Nadai (Ref. 115). Dawson deduced the shear stress-strain curve for the available tensile stress-strain curve using the equations:

$$\tau = \frac{\sigma_t}{\sqrt{3}} \quad (7-27)$$

$$\gamma = \frac{3 \epsilon_t}{2} \quad (7-28)$$

It is assumed that the shear strain γ is proportional to $1/r^2$ all through the cylinder at each stage of the expansion. The internal pressure p is then

$$p = \int_{\gamma_b}^{\gamma_a} \tau(\gamma) \frac{d\gamma}{\gamma} \quad (7-29)$$

and the shear strain at the outside surface $r = b$ is given by

$$\gamma_b = \frac{2(1+\nu)}{2-\nu} \epsilon_{t_b} \quad (7-30)$$

where

ν = Poisson's ratio

and

ϵ_{t_b} = tangential strain at $r = b$

The analytical calculation of the expansion which involved a numerical integration agreed within 3.5 percent of the experimentally measured value. Similarly the residual tangential bore stress agreed within four percent.

A comprehensive study of the yield and bursting characteristics of nearly 100 thick-walled, closed-end cylinders was performed by Faupel (Ref. 116).

The elastic breakdown pressures and the bursting pressures were related to the properties of the materials and design equations proposed. The elastic breakdown pressures p_{yp} for open end, closed-end, and restrained end vessels are given by the following equations:

$$p_{yp} \text{ (open ends)} = \frac{\sigma_y (R^2 - 1)}{\sqrt{3R^4 + 1}} \quad (7-31)$$

$$p_{yp} \text{ (closed ends)} = \frac{\sigma_y}{\sqrt{3}} \left[\frac{R^2 - 1}{R^2} \right] \quad (7-32)$$

$$p_{yp} \text{ (restrained ends)} = \frac{\sigma_y (R^2 - 1)}{\sqrt{(3R^4 + 1) + 4\nu(\nu - 1)}} \quad (7-33)$$

where R is the radius ratio $\frac{b}{a}$ and σ_y is the .01 percent offset yield strength.

The closed-end equation was found to describe the behavior fairly well.

Faupel then states that if the cylinder wall yields at a constant stress as is assumed in classical plasticity theory the bursting or ultimate pressure p_{ult} is given by the equation

$$p_{ult} = \frac{2\sigma_y}{\sqrt{3}} \ln \frac{b}{a} \quad (7-34)$$

He then shows that if the ultimate tensile strength σ_u is greater than the yield strength σ_y the bursting pressure is

$$p_{ult} = \frac{2\sigma_y}{\sqrt{3}} \ln \frac{b}{a} \left[2 - \frac{\sigma_y}{\sigma_u} \right] \quad (7-35)$$

where σ_y is here taken as the 0.20 percent offset or lower yield strength.

The above equation predicted the bursting pressure at least 90 percent of the time to better than ± 15 percent of the observed value.

Burrows, et al., (Ref. 117) summarize the various failure criteria used in pressure vessel design. Table 7-1 shows the alternative criteria of elastic failure relating the principal elastic stresses

$$[\sigma_{\theta} > \sigma_z = 0.5 (\sigma_{\theta} + \sigma_r) > \sigma_r] \quad (7-35)$$

in a uniformly thick, infinite, hollow, closed-end cylinder, under internal pressure, to the major principal stress σ_{yp} in a tensile test specimen.

Table 7-1 - Elastic Failure Criterion (Burrows, et al.)

CRITERION	FORMULA
<u>Maximum Stress*</u>	
Lame (1831) Rankine (1888)	$\sigma = \sigma_{\theta}$
<u>Maximum Strain*</u>	
Poncelet (1840) Saint-Venant (1870)	$\sigma = (3/4)(\sigma_{\theta} - \sigma_r) + (1/4)(1 - 2\nu)(\sigma_{\theta} + 3\sigma_r)$
<u>Maximum Shear</u>	
Coulomb (1773) Tresca (1864) Guest (1900)	$\sigma = \sigma_{\theta} - \sigma_r$
<u>Energy</u>	
Beltrami (1885) Haigh (1919)	$\sigma = (3/4)^{0.5}(\sigma_{\theta} - \sigma_r) \left\{ [(5 - 4\nu)/3] + 4(1 - 2\nu)\sigma_{\theta}\sigma_r(\sigma_{\theta} - \sigma_r)^2 \right\}^{0.5}$
<u>Modified Energy</u>	
Huber (1904) Hencky (1924) von Mises (1913-1926)	$\sigma = (3/4)^{0.5}(\sigma_{\theta} - \sigma_r)$
*Least acceptable at present	

Table 7-2 shows these same failure criteria when plasticity is assumed with consequent adoption of constant volume (infinite bulk modulus) so that Poisson's ratio is 0.5.

Table 7-2 - Plastic Failure Criteria (Burrows, et al.)

CRITERION	FORMULA
Maximum Stress	$\sigma = \sigma_{\theta}$
Maximum Strain	$\sigma = (3/4) (\sigma_{\theta} - \sigma_r)$
Maximum Shear	$\sigma = \sigma_{\theta} - \sigma_r$
Energy	$\sigma = (3/4)^{0.5} (\sigma_{\theta} - \sigma_r)$
Modified Energy	$\sigma = (3/4)^{0.5} (\sigma_{\theta} - \sigma_r)$

Burrows, et al., also describe the work of a task force to resolve the differences in points of view on the criteria to be used in calculating the wall thickness required for high pressure steam piping. Thirty-one different equations for pipe-wall stresses are presented along with short descriptions of their applicability. The final equation which was developed is

$$t = \frac{p d}{2S + 2yp} \quad (7-36)$$

where

- t = minimum wall thickness
- p = internal pressure
- d = outside diameter
- S = code allowable S-value
- y = temperature-dependent parameter having a value of 0.4 for ferritic and austenitic steels below 900 degrees F.

The above equation was adopted by the Power Boiler Section of the ASME Boiler Code and was approved by the Power Piping Committee of the ASA B31 Code for Pressure Piping in approximately 1954.

The condition of unrestricted plastic flow of a circular tube in plane strain with internal pressure p and obeying von Mises' failure theory is discussed by Prager and Hodge (Ref. 110). In unrestricted plastic flow the interior and exterior radii a and b increase with time, their initial values being denoted by a_0 and b_0 . The pressure p necessary to keep the widening tube fully plastic will vary with time. The initial value of p_0 is given by

$$p_0 = 2\tau_{yp} \ln \frac{b_0}{a_0} \quad (7-37)$$

where τ_{yp} is the yield strength in shear.

Each particle moves radially during the flow process. The radial velocity v of a particle r distance from axis will be a function of the radius r and the time t . The theory of perfectly plastic materials allows the parameter t to be replaced by the parameter a .

$$v = v(r, a) \quad (7-38)$$

Thus, the radial "velocity" depends on r and on a , which plays the role of the time. The strain rates at the "instant" a are therefore given by

$$\dot{\epsilon}_r = -\frac{a}{r^2}, \quad \dot{\epsilon}_\theta = \frac{a}{r^2}, \quad \dot{\epsilon}_z = 0 \quad (7-39)$$

A particle originally at some distance r_0 from the axis of the tube has stresses acting on it at the time when the interior radius has reached the value

of a given by the equations

$$\sigma_r = \tau_{yp} \ln \frac{r_o^2 + a^2 - a_o^2}{b_o^2 + a^2 - a_o^2} \quad (7-40)$$

$$\sigma_\theta = \tau_{yp} \left(\ln \frac{r_o^2 + a^2 - a_o^2}{b_o^2 + a^2 - a_o^2} + 2 \right) \quad (7-41)$$

$$\sigma_z = \tau_{yp} \left(\ln \frac{r_o^2 + a^2 - a_o^2}{b_o^2 + a^2 - a_o^2} + 1 \right) \quad (7-42)$$

The internal pressure necessary to keep the tube fully plastic and expanding is given by the equation

$$p = \tau_{yp} \ln \left(1 + \frac{b_o^2 - a_o^2}{a^2} \right) \quad (7-43)$$

The above equation indicates that the pressure required for continuing expansion decreases as the inside radius increases or with increasing time.

Bailey (Ref. 118) derives equations for the stresses in a thick-walled cylinder undergoing creep. He states that there is a linear relationship between stress and log rate of creep in shear for steels at temperatures up to approximately 500 degrees C as given by the equation

$$\tau = k_1 + k_2 \log_{10} \dot{\gamma} \quad (7-44)$$

where

$$\tau = \frac{\sigma_r + \sigma_\theta}{2} \quad (7-45)$$

$\dot{\gamma}$ = creep rate in shear (radians per hour)

k_1 and k_2 are experimentally determined constants.

The stresses in the r , θ , and z directions are then shown to be

$$\sigma_r = 2n \ln \frac{r}{a} \ln \frac{r}{a} \ln \frac{r}{b} + p \frac{\ln \frac{b}{r}}{\ln \frac{b}{a}} \quad (7-46)$$

$$\sigma_\theta = 4n \ln \frac{a}{r} + 2n \ln \frac{b}{a} - 2n \ln \frac{r}{a} \ln \frac{r}{b} + p \left(\frac{1 - \ln \frac{b}{r}}{\ln \frac{b}{a}} \right) \quad (7-47)$$

$$\sigma_z = 2n \ln \frac{a}{r} + n \ln \frac{b}{a} - 2n \ln \frac{r}{a} \ln \frac{r}{b} + \frac{p}{2} \left(\frac{1 - 2 \ln \frac{b}{r}}{\ln \frac{b}{a}} \right) \quad (7-48)$$

where $n = .4343 k_2$.

Unfortunately, most creep data is obtained in uniaxial tensile tests rather than torsional type tests. Creep with rupture in a pressure vessel is, however, currently (1968) believed to be reasonably well correlated with tensile creep-rupture data, at least for a range of diameter ratios.

Prager and Hodge (Ref. 110) discuss the conditions for failure of a repeatedly loaded tube. They state that the internal pressure must be sufficiently small to avoid unrestricted plastic flow and to avoid the establishment

of a cycle of plastic deformation. The first condition is satisfied if the internal pressure p is less than the pressure at which the cylinder becomes fully plastic p_{fp} where

$$p_{fp} = 2\tau_{yp} \ln \frac{b}{a} \quad (7-49)$$

The second condition is satisfied when

$$p < p_{fp} = 2\tau_{yp} \ln \frac{b}{a} \quad \text{for } \frac{b}{a} \leq 2.22 \quad (7-50)$$

$$p < 2 p_{yp} = 2\tau_{yp} \frac{(b^2 - a^2)}{b^2} \quad \text{for } \frac{b}{a} \geq 2.22 \quad (7-51)$$

MacLaughlin (Ref. 119) performed a three-dimensional photoelastic analysis of stresses in thick-walled closed-end cylinders using stress-freezing and slicing techniques. He found that the octahedral shearing stresses in hemispherically-ended cylinders were less than half those in flat-ended cylinders. This phenomenon occurred even though the hemispherically-ended cylinders were composed of approximately 40 percent less material in the end region. The octahedral shearing stress was also 13 percent lower in models having end plugs than those without the plugs. Indications were that an optimum end-wall thickness may exist and that further study is warranted.

A cylindrical pressure vessel may be strengthened by shrinking another cylinder around the main cylinder. The outer cylinder is normally heated so that it expands sufficiently to just slip over the main cylinder. As the

outer jacket contracts upon cooling it exerts an external pressure on the inner cylinder. The result is that compressive tangential stresses are generated in the inner cylinder as well as tensile stresses in the jacket. The outer cylinder is referred to as a band if its thickness is small. Such bands are designed to carry only hoop forces. If the outer cylinder is relatively thick the vessel is then referred to as a compound or multilayered vessel.

The elastic stresses in a compound vessel can be analyzed by using Lamé's equations for stresses in thick-walled cylinders and considerations of the displacements at the interfaces. Seely and Smith (Ref. 107) analyze this problem for jacket and cylinder materials having the same values of ν and E , and the same strengths. Letting \underline{a} , \underline{b} , and \underline{c} denote the internal radius of the main cylinder, the external radius of the main cylinder (or internal radius of jacket), and the external radius of the jacket, respectively, (Fig. 7-5) they solve for the values of \underline{b} and \underline{c} such that two simultaneous requirements are satisfied. First, the maximum circumferential stresses in the cylinder and the jacket are equal to the working stress σ_w when the allowable internal pressure \underline{p} is reached, and second, the radius \underline{c} has its minimum possible value, thereby making most effective use of the material. The values of \underline{b} and \underline{c} are then

$$\begin{aligned} b &= ka \\ c &= k^2 a \end{aligned} \tag{7-52}$$

where

$$k^2 = \frac{1 + (p/\sigma_w) + 2\sqrt{1 + (p/\sigma_w)}}{3 - (p/\sigma_w)} \tag{7-53}$$

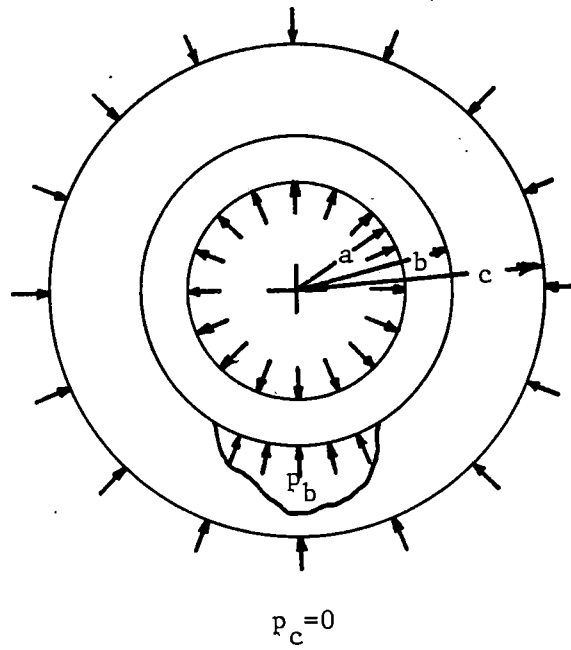


Fig. 7-5. Two-region nomenclature. (Huddleston).

Becker and Mollick (Ref. 120) present a theory for the elastic design of a compound cylinder made by shrinking together several concentric cylinders. In their analysis the cylinders may have different strengths and they may operate at any temperature and under internal or external pressure. The cylinders are further assumed to be homogeneous and isotropic, and to have the same Young's modulus.

Lame's equations for stresses in a thick-walled cylinder are used in conjunction with the maximum shear stress failure criterion. For optimum design all successive rings will reach their yield strengths simultaneously.

Denoting the radii of the boundaries between the cylinders as a , b , \dots , l , and denoting p_a , p_b , \dots , p_l as the radial pressure at the radius designated by the subscript the following equation for internal pressure is derived

$$p_a = \tau_{ab} \left[1 - \left(\frac{a}{b}\right)^2 \right] + \tau_{bc} \left[1 - \left(\frac{b}{c}\right)^2 \right] + \dots + \tau_{kl} \left[1 - \left(\frac{k}{l}\right)^2 \right] + p_l \quad (7-54)$$

where τ_{ab} , τ_{bc} , \dots , τ_{kl} are the yield strengths in shear in the cylinder between the radii designated by the subscripts.

The following equation relates the magnitudes of the various radii for simultaneous yielding to occur

$$\tau_{fg} \left(\frac{f}{g}\right)^2 = \tau_{gh} \left(\frac{g}{h}\right)^2 \quad (7-55)$$

The diametral interference δ_g which is the difference between the diametral deflections at g of the inner and outer cylinders under the action of p_f , p_g , and p_h is given by the equation

$$\delta_g = \frac{4g}{E} [\tau_{gh} - \left(\frac{f}{g}\right)^2 \tau_{fg}] \quad (7-56)$$

Physically δ_g is the sum of the increase in the inner diameter of the outer cylinder and the decrease in the outer diameter of the inner cylinder.

The authors also show that the relative deflections are mating surfaces (the interferences) which are unchanged by changes in the internal or external pressures on the assembly.

Huddleston (Ref. 121) presents the theory of minimum wall-thickness multiregion high-pressure cylinders. The analysis combines the Lamé equations for the stress distribution in thick-walled cylinders with von Mises' yield theory. Results for both plane stress and plane strain conditions are presented in the form of nondimensional radius and pressure parameters for vessels having 1, 2, 3, 4, and 5 regions. The results are typical of the graphs shown in Figures 7-6, 7-7, and 7-8 for five regions in plane stress. The radii to the boundaries of the various regions are $a, b, \dots, r_i, \dots, f$ (going from the inside outward) and the interfacial pressure at these radii are $p_a, p_b, \dots, p_i, \dots, p_e$. Figure 7-6 is a graph of the ratio of the i th radius r_i to the internal radius a versus the ratio of the internal pressure p_a to the yield strength σ_a . Figure 7-7 is a graph of the ratio of the interfacial pressure at radius r_i to the yield strength σ_a versus the ratio $\frac{p_a}{\sigma_a}$. The computational

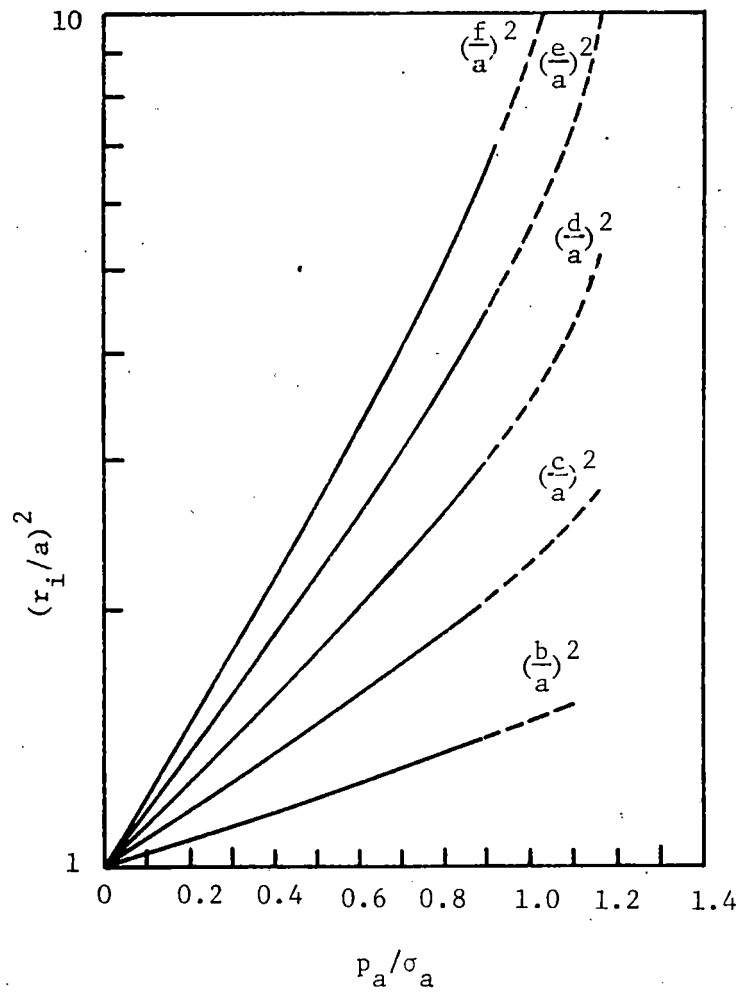


Fig. 7-6. Radius ratios squared versus internal pressure parameter for five regions in plane stress. (Huddleston).

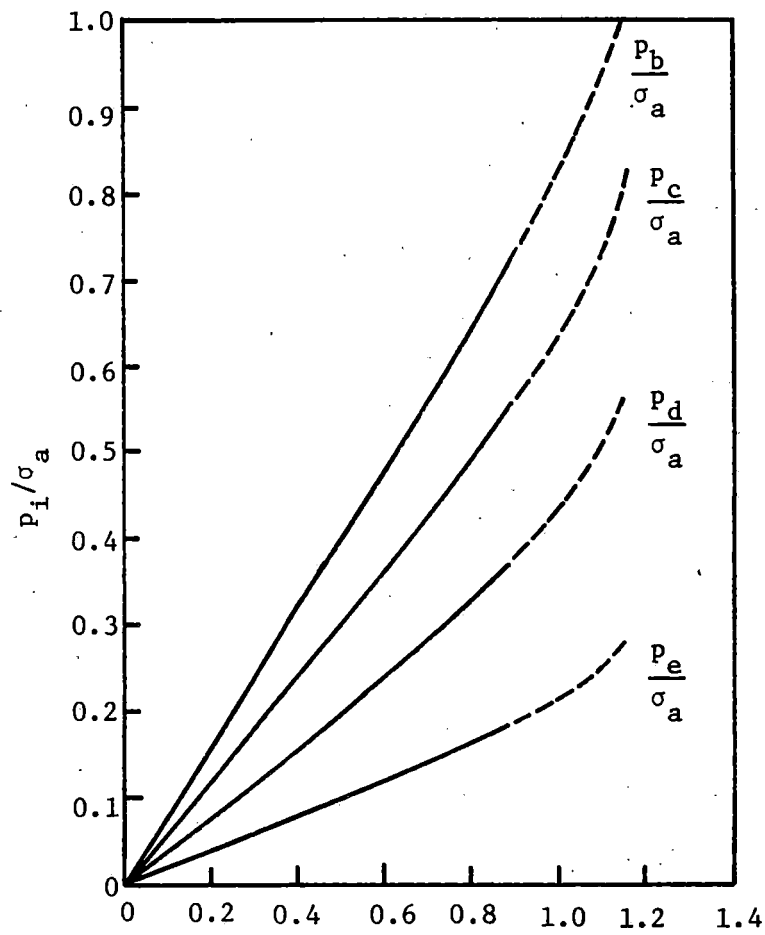


Fig. 7-7. Intermediate pressure ratios versus internal pressure parameter for five regions in plane stress. (Huddleston).

scheme does not include the complications of reverse yielding during fabrication. The dashed portions of the curves represent solutions to the assumed mathematical model but are elastically unstable due to reverse yielding.

Figure 7-8 is a graph of the ratio $\frac{p}{\sigma_a}$ versus the number of regions. The parameter R is the overall outside to inside radius ratio. The shaded portion of the graph is the region of elastic behavior. It is noted that the internal pressure does not exceed the tensile yield strength without reverse yielding occurring.

Pressure vessels may also be strengthened by wrapping them with a high strength wire under tension so that the material near the bore comes under compression. When the vessel is later pressurized the stress near the bore rises from compression to tension and that in the wire rises to a higher tension, all within the elastic limits.

The primary present applications of the wrapping technique involve large-volume thin-walled rocket motor cases (Refs. 122-127). Glass fibers are often used for wrapping such vessels due to their high strength and light weight. The design pressures in the rocket cases are, however, in the order of 1000 psi which is low compared to what can be contained in a thick-walled vessel.

A cascade arrangement can also be used to contain a high pressure. Here one pressure vessel is placed inside another, with the space between them being filled with a fluid pressurized to a value less than that in the inner vessel. A major difficulty with such a system is that the size of the innermost, highest pressure chamber becomes rapidly smaller as the number of

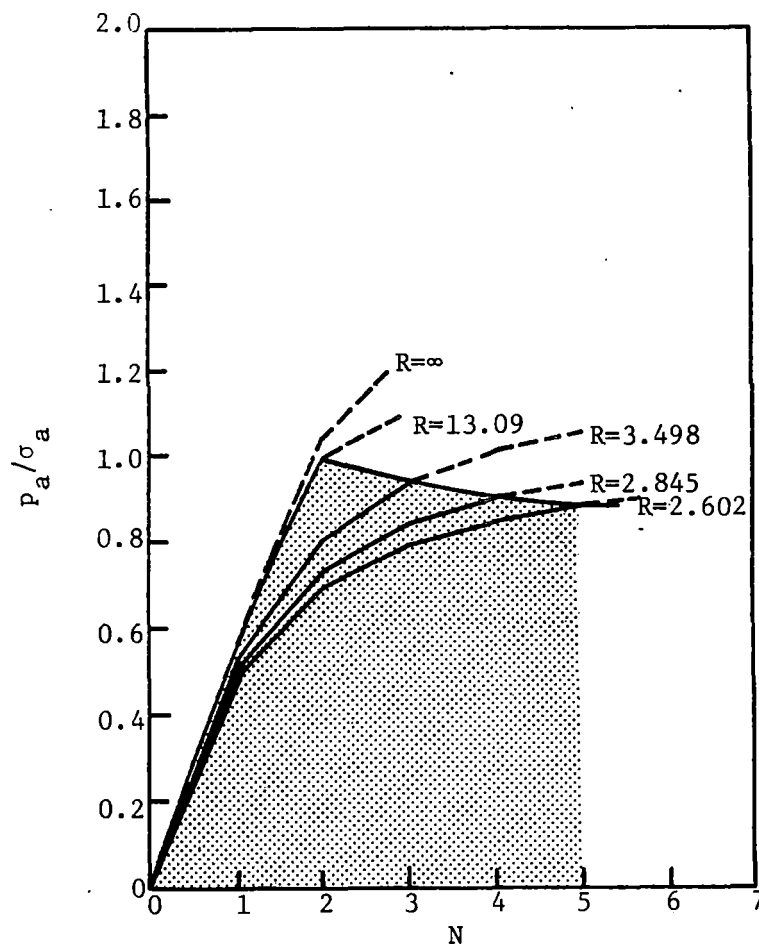


Fig. 7-8. Limiting internal pressure parameter versus number of regions for plane stress ($\nu=0$). (Huddleston).

stages is increased. Bridgman (Refs. 128 and 129) used such a two-stage in some of his compressibility studies. A more recent application is for large volume spherical vessels for nuclear power reactors (Ref. 130). Here the vessel had a large volume (inside radius = 48 in.) and contained water at 600°F pressurized to 1600 psi.

Berman (Ref. 131) proposes a cascade or coaxial design which he believes can be used to 500,000 psi. He suggests as many as five coaxial vessels which are separated by a fluid in which the pressure is externally controlled so that at each pressure each vessel sustains the same maximum stress intensity based on all three principal stresses. Constant material properties are assumed. An important advantage of the controlled fluid-fill design is that materials having a high design stress may be used in the inner layers since a large hydrostatic pressure is created at the inner surface at design pressure. This hydrostatic pressure is about 50 percent greater than that in a comparable shrink-fit vessel.

Semerchan and Plotnikov (Ref. 30) describe a Russian apparatus for generating pulsed jets at 2000 m/sec. The apparatus consists of a pressure multiplier made up of two coaxial cylinders whose pistons are rigidly interconnected. The low pressure cylinder has an inside diameter of 50 mm and operates at a pressure of 80 MN/m^2 (11,600 psi). The high pressure cylinder has an inside diameter of 10 mm and operates at a pressure of 2000 MN/m^2 (290,000 psi). The high pressure cylinder is a single-layer thick-walled vessel made from steel. It is stated that the stresses in the high pressure cylinder computed by the usual methods for a thick-walled tube exceed the

tensile strength of the material. The high pressure piston is made from the same steel as the cylinder and is hardened to a hardness of $R_c = 40-45$. The seal of the high pressure chamber consists of a set of alternating copper and lead rings which are subjected to hydrostatic compression by a yoke and sealing nut. The low pressure cylinder was charged with compressed air and is equipped with a capping seal which works on the uncompensated area principle. This seal consists of a cap placed in the piston aperture and a set of alternating chlorovinyl and textolite rings. The report also describes the method of charging and triggering using a diaphragm burst technique.

Material Considerations

Recent trends in pressure vessel applications involving higher pressures, thicker walls and new materials require a detailed knowledge of the various mechanical properties of the materials which are of importance to the structural safety of the vessels.

Langer and Harding (Ref. 132) state that after making a preliminary decision regarding the acceptance of one or more materials with respect to their availability in required size, shape and thickness in adequate soundness, the ability to be formed or fabricated by convenient techniques and suitability in overall cost in relation to alternatives, the designer must know the effect of various mechanical properties on a specific set of design conditions. The authors state that tensile strength, yield strength and brittle fracture strength are a measure of the initial strength of the vessel, whereas creep strength and stress rupture strength are indicative of the long time service of the vessel. The ductility of the material, which is usually measured by the percent

elongation and reduction of area in the tensile test, must also be considered. Strain-fatigue resistance and resistance to notch sensitivity give a measure of the strength of the vessel to withstand alternating loads and temperatures.

The failures of pressure vessels have been classified by Langer and Harding (Ref. 132) into two main groups: a) shear or cleavage failure and b) failure as the ultimate result of excessive plastic deformation. The extent to which cleavage failure occurs depends on the brittle fracture properties of the material which require the existence of stress, low temperature and a defective notch. However, excessive pressures in a ductile vessel beyond the design value result in plastic deformation.

As noted by Schwartz, et al., (Ref. 133) the basic assumption of a fracture-safe design of the pressure vessel depends on the fact that few, if any, engineering structures are free of internal flaws. Such flaws may develop either during the initial stages of manufacture of the material or during the course of its fabrication. The method of fracture-safe design using the "Fracture Analysis Diagram" developed by Pellini and Puzak (Ref. 134), can be applied for steels at temperatures far below the crack-arrest and nil-ductility temperatures. Care must be exercised to assure that critical combinations of flaw size and stress level are not attained or exceeded. This procedure may not be applicable to steels which do not have distinct transition temperature features. Thus, the designer has either to put a limitation on the working stress or to use steels of lower nil-ductility temperatures. But Langer and Harding (Ref. 132) have commented that this method cannot be used effectively on pressure vessel design, especially when one has to

use a high strength steel, because the available yield strength decreases as the strength increases.

In their discussion on the strength of thick-walled cylinders, Crossland, et al., (Ref. 135) state that before plastic deformation starts the vessel will be initially elastic with the maximum stress at the core. As the pressure increases the core undergoes the plastic deformation, the outer shell still retaining its elastic property. As the deformation increases, the plastic-elastic boundary moves outward until it reaches the periphery of the vessel, the expansion being continued at a constant or collapse pressure until the core gains the strengthening effect of strain-hardening. Finally, when the strengthening effect of strain-hardening becomes equal to the weakening effect of the reduced wall thickness, the failure of the vessel occurs.

Langer and Harding (Ref. 132) point out that since the load fluctuations in a pressure vessel designed for long time service are usually of the order of hundreds of thousands, (10^3 to 10^5 cycles) rather than millions, which falls clearly into the range of low cycle fatigue, the term endurance limit loses much of its significance.

C.F. Tiffany (Ref. 136) states that examinations of the low cycle fatigue failures of pressure vessels indicate the presence of either flaws, notches or some other crack-line defects at the fracture origins. Mills (Ref. 137) states that the fracture toughness is believed to be the important material property governing the rate of growth of these defects. The fracture propagation from small cracks and defects in mild steel is thought to occur as follows.

As the fluid pressure is increased the stress intensification at a crack tip increases linearly with the fluid pressure until at some pressure the crack begins a period of slow growth. During this period the crack extension is self-limiting in that it will not continue unless the nominal stress is increased. This fact is a consequence of the plastic deformation occurring at the tip of the fracture. The amount of crack extension per unit stress increment increases with stress until finally the process ceases to be self-limiting and crack extension continues without further increase in stress. At this point the propagation becomes unstable and rapid failure ensues. To assure against such a failure these unavoidable sharp flaws or crack-like notches must be considerably smaller than the critical size at a given operating stress level.

Goodman (Ref. 138) obtained experimental data to assist in establishing material selection, design and fabrication criteria for reliable lightweight pressure vessels. Although his work was concerned with miniature thin-walled vessel (2 in. I.D.) simulating rocket cases, some of his conclusions appear to be pertinent to thick-walled vessels. He concludes that no simple (coupon) test can accurately predict the significant biaxial behavior and burst stress of a given material in an actual pressure vessel, and that material properties should be performed in biaxial stress fields in which the significant geometrical effects are included. Tensile instability, which is the upper bound on the burst strength, was accurately predicted by a plasticity analysis based on uniaxial stress-strain data. Also, tensile coupons which accompany larger items during heat treatment may not accurately reflect the properties of the larger structure, especially if there are any differences in mechanical history

(such as flattening) or thermal history (such as annealing before heat treatment or mass effect in quenching). Furthermore, the uniaxial tensile test will indicate only gross anisotropy.

Ingraham (Ref. 139) lists some of the serious limitations of the V-notch Charpy impact test. These limitations are (1) its lack of sensitivity at strength levels above 200,000 psi; (2) the size limits imposed by the use of thin sheet materials; and (3) the impact energy value is a combination of both crack initiation and propagation. Ingraham suggests the use of cracked specimens with natural cracks instead of the standard V-notch Charpy specimens.

The pertinent uniaxial mechanical properties of virtually all existing steels having ultimate strengths greater than 250,000 psi have been gathered from the literature and are tabulated in Appendix B. Appendix B also gives the results of biaxial stress determinations on miniature pressure vessels made of AISI 4340 steel, Ladish D6AC steel, 7178 Aluminum and 6Al-4 V Titanium. Effects of triaxial stresses on the mechanical properties of pressure vessels made of a mild steel, which came as commercially hot-rolled round stock of 3/4" diameters, are also given in Appendix B.

The following materials are considered to be most applicable to pressure vessels in general (Mills, Ref. 137):

1. Martensitic Alloy Steels (AISI 4340 and AMS 6434):

High strength is achieved by quenching from above the austenitic transformation temperatures followed by tempering to produce a tempered martensite microstructure.

2. Austenitic Stainless Steels (301, 304, and 310):

Useful for cryogenic environments. These steels have a face-centered-cubic crystal structure and are not subject to low-temperature embrittlement as are body-centered cubic metals.

3. Precipitation-Hardenable Stainless Steels (AM 355, 17-7 PH, and 17-4 PH):

High strength obtained by a complex series of annealing, conditioning, transforming, and aging treatments. The final increase in strength is attributed to the formation of a coherent precipitate in the martensitic matrix upon aging at temperatures ranging from approximately 850 to 1100°F.

4. Maraging Steels (18 Ni):

The alloys having 18 percent nickel are believed to be strengthened by the formation of a precipitate during aging of a low-carbon martensitic structure.

5. Titanium Alloys (Ti-6Al-4V, Ti-5Al-2.5Sn, and Ti-13V-11Cr-3Al):

Moderately high-strength and relatively low density make these materials competitive with steels when weight is an important factor.

6. Aluminum Alloys (2014-T6 and 2219-T81):

Relatively low strength compared to other pressure vessel materials; however, lightweight is advantageous in some applications.

7. Nickel Alloys (Inconel 718 and Rene 41):

Particularly useful under high temperature conditions.

An important aspect of pressure vessel design that is usually neglected is that of the effect of the fluid on the vessel. Beaverson (Ref. 140) lists three kinds of deleterious effects. First, there is permanent damage due to stress corrosion such as occurs when water is pressurized in an alloy-steel chamber of SAE 4340 steel or a maraging steel. For example, chambers that withstand 500,000-600,000 psi internal pressure almost indefinitely when the pressure medium is gasoline can fail (when new) on two one-minute exposures to 100,000 psi when water is the pressure medium. Thus, high water pressure chambers require materials different from the usual SAE alloy steels and maraging steels. Beaverson also mentions an experiment on delayed fracture times for various fluids in contact with precracked specimens of 300 M steel. Failure times in minutes were:

Recording ink	0.5
Distilled water	6.5
Benzene	2247.

Interestingly, prior to about 1960-1963 published literature was obtained on precracked specimens with recording ink in the crack to make the crack propagation more easily visible. Thus, the value of such data should be questioned.

Second, some effects persist after the fluid is withdrawn, but are not permanent. For example, the persisting effects of a hydrogen solution can be removed by a post-treatment called baking-out.

Third, the Rebinder effect sometimes exists when the fluid is in contact with the metal. An example is the lowering of ductility of copper when concentrations of oleic acid in a certain range are present in a surrounding solvent. The effect disappears when the deleterious fluid is replaced by air. Also, fluids cause "porous" metals to be in a more brittle state; for example, pressed-and-sintered beryllium and cast iron exhibit this effect.

CHAPTER VIII

CONCLUSIONS AND RECOMMENDATIONS

GENERAL

Requirements of the excavation industry have made it evident that drilling and blasting cycles must be radically modified and appropriate new techniques adapted to increase excavation rates without increasing costs. Utilization of hypervelocity processes other than conventional blasting with high explosives show some promise of furnishing bases for development of new techniques. However, applications of water jets, metal jets and high-velocity projectiles have been investigated in only a perfunctory manner in the United States. Few attempts have been made to improve known designs of some explosive devices for blasting purposes, or more importantly, to adapt blasting procedures to their use. Most investigations have been based on the plan of using new processes for adaptation to conventional excavation procedures.

The utilization of hypervelocity processes for penetration and disintegration of rock is still in an experimental stage, with the exception of the direct use of high (chemical) explosives for blasting. Although there has been extensive research on hypervelocity water jets reported from the USSR, their current use appears to be restricted to relatively large diameter, low-velocity jets for mining of coal. The most recent books and articles available from Russia do not indicate that very high-velocity capillary jets are in practical use for either cutting or breaking of in situ rock, but a 10,000 atm

20 shot per minute Russian water cannon is reported by Cooley (Ref. 31). Research at moderate velocities has also been performed in Great Britain, but no applications appear to have been made, largely due to the cost of generating the intense pressures necessary to extrude water jets at high velocities. Pressure vessel design is also an important problem for ultrahigh pressures.

Jets from shaped charges are of highest velocities presently attainable and penetrate rocks to depths dependent on pertinent parameters. Hypervelocity projectiles will break blocks of rock, but their effects appear to be limited to near surface fracture, particularly on a semi-infinite solid. Shots from light gas guns at required ultrahigh velocities are costly.

The basic theoretical performance of water cannons and light gas guns is analyzed by somewhat similar mathematical procedures. Most of the processes occurring in each of these devices involve the generation and propagation of shock waves. Solutions in turn require a knowledge of the equations of state which govern material behavior. Performance of water cannons including the behavior of compressed water or the pressure vessels under transient loads has not been completely examined.

EQUATIONS OF STATE

For complete theoretical analyses of most of the processes involved in hypervelocity technology, it is necessary to have reasonably accurate equations of state available for appropriate gases, liquids and solids.

The different gaseous equations are devised to apply at low, intermediate and high pressures and temperatures. The ideal gas equation has

been used with some success in the processes taking place in light gas guns, but it is not wholly applicable. Several equations have been proposed for high pressures such as those occurring in detonation waves, and each appears to be applicable for special cases.

Equations for water are taken largely from the p-V-T data of Bridgman, while shock equations have been developed for a large number of substances by measurement of particle velocity. These, together with the phase diagrams, may be used to predict the formation of ice at high pressures. Analysis by appropriate equations for water indicate that water will freeze above a certain critical shock pressure, although this has not been demonstrated experimentally.

Equations of state for solids include elastic, plastic and shock equations. Each of these has applicability in the particular analyses concerned.

WATER JETS

Several theories have been advanced to explain the behavior of axisymmetric water jets at various velocities, considering the water to be either compressible or incompressible, applying non-viscous or viscous assumptions at either subsonic or supersonic velocities. Temperature effects are usually neglected.

Peak pressures developed in water cannon, and corresponding Mach numbers, however, are much higher than those for which theories have been derived. When a jet emerges from the nozzle, shock waves are set up both in the air and in the water jet. The latter probably are responsible for part of the mixing and dispersion of the jet, and other factors are turbulence and

friction of the air. The relative effects of these are not known.

Experiments with jets have shown that the core is much more persistent than was originally believed, but it is obscured by the droplets and spray of the mixing part of the jet. The unit pressure of the jets diminishes quite rapidly with travel distance, making near zero standoff the most effective distance for cutting and breaking, particularly for pulsed jets.

Use of equation of state data and proper thermodynamic theory indicate that water may freeze at about 26 kilobars dynamic pressure. However, the freezing pressure is affected by other factors, including temperature and impurities in the water. No experiments have been conducted to determine whether instantaneous freezing of water does occur at the theoretical critical pressure. Other liquids are known to exhibit freezing, and if water does freeze it will present a serious obstacle if it cannot be corrected with antifreeze or additives or by other means.

WATER JET IMPACT

Several methods have been devised for producing high speed water jets, including compressors, hydraulic rams, water cannons, and by external augmentation. The cost of compressing water to large pressures is not given in the literature, but it appears to be high. The efficiency of producing jets by any of the other methods is likewise not given, although none of the presently described processes appears to be efficient. In some, much of the high pressure water is lost in the production of jets. Although impressive horsepower is stipulated at the nozzle, the cost of input energy has not been

presented in print. Comparisons with drilling and blasting are also made in a nozzle-horsepower basis. Hence, no reliable information on overall efficiencies has been found in the literature.

The impact effects of water jets on rock vary with their diameter and velocity. Large jets of three cm diameter and larger are utilized to mine coal, largely by a washing and eroding action. Much smaller capillary jets of diameters of one to two mm are employed in very high velocity jets only in the laboratories. One of the reasons is that only small volumes of water can be compressed to required high pressure.

Jets of velocities as low as 200 m/sec will cut soft rocks such as sandstone and limestone, but will not cut harder rocks such as marble and anhydrite, which require velocities to and higher than 500 m/sec. There appears to be a critical velocity for each type of rock below which cutting or penetration will not take place either for stationary or transverse jets. Water pressures necessary for initial cutting vary from about 20,000 to 30,000 psi, and depths of cutting by transverse jets are limited to a few centimeters. Thus, it is difficult to visualize a mechanical scheme whereby cutting narrow slots in a rock face could be utilized for effective breakage and excavation.

Pulsed jets are more effective for breakage of rock than continuous jets, especially in porous or cracked rocks. However, all reported experiments were made on blocks of rock and not in solid faces of rock. For the latter geometry and for strong hard rock, breakage was not reported, but would be limited in comparison with breakage of blocks of weaker rock.

Both British and Russian investigators suggest that high speed jets could be used for cutting rocks at the face of a tunnel. One method would involve cutting both normal and parallel to the face, but estimated power requirements at the nozzle are greater than mechanical methods were for the soft sandstone tested. No calculations were made for harder or more dense rocks. The use of traversing jets requires the movement of the pressure vessel or nozzle at speeds of about 1 cm/sec or greater. Pressure vessels are very heavy and would require a heavy traversing mechanism. Also, the efficiency of compression methods is very low. No method is given for cutting parallel to a working face nor are combined methods described.

Russian investigators suggested that they were cutting rocks at a working face, slotting it and then breaking it away by "known means". However, no successful methods of utilizing high velocity capillary jets for continued excavation have been reported in available literature. It would appear, therefore, that there are many mechanical, technical and economical problems which may be difficult of solution. These include efficiency of producing high pressures, design of equipment usable underground and adaptation of jets for cutting and breakage of rock on a working face.

There is little understood about the basic mechanisms involved when high velocity water jets cut slots in solid rock, i.e., whether grains are fractured, eroded or simply washed out. Energy partitioning for impact of water jets has not been investigated, and water jet action at velocities of 1000 m/sec is considerably different than that of shaped charge jets, for example, whose velocity may be as high as 10,000 m/sec. Limited energy is transmitted to the

rock even at high velocity. The instantaneous pressure in a detonation wave in high explosives, on the other hand, may be as much as 10^6 psi or higher. For confined explosives these pressures exist long enough within the rock to generate pulses which will fracture it.

In summary, if water jets are of high enough velocity to cut rock, they appear to do so without generating strong shock or stress waves in the rock. The very high volume of breakage reported for pulsed jets was for a porous sandstone only. Thus, breakage may be limited to this type of rock, and none was reported for harder rocks. Ultrahigh velocity jets appear to utilize most of their usable energy in cutting. That is, penetration processes, coupling, etc., are such that only weak shock and stress waves are generated in the rock.

Water, compared to higher density materials, is an inefficient cutting agent because of its low density. Metallic jets are much more effective, particularly at velocities where inertia effects dominate penetration processes, i.e., from 7,000 to 10,000 m/sec, depending upon material properties.

HYPERVELOCITY PROJECTILES

The impact of hypervelocity projectiles of a wide range of densities has been studied extensively, and empirical equations set up to attempt to describe the behavior of target and projectile materials. Three regimes of velocity are described, but the projectile velocities of interest for rock targets appear to be in the high range.

The most common method of accelerating hypervelocity projectiles is by means of light gas guns. Other types of projectors utilize electric, explosive and combinations of techniques. Most hypervelocity research has

been to simulate micrometeorite impact on space vehicles. However, for very high velocity, small projectiles of light materials must be used. The most used target material has been aluminum because of interest in meteorite effects on space vehicles.

In the higher velocity regions, theory indicates that strengths may be almost negligible, and density is the most important material property. However, rock strength properties do affect depth of penetration even at highest velocities which have been achieved.

There have been several investigations performed on rocks, primarily basalt, to simulate the effects of micrometeorites on rocks on the moon. For short projectiles whose l/d ratio is two or less, a small hemispherical crater is formed at impact by the initial processes, followed by tensile slabbing around the crater. Much larger craters are formed in rock than in metals because of this latter process, which is also due to the fact that rocks are generally weak in tension. Other secondary types of fracturing are also caused, such as minor radial and circumferential fractures. However, these are usually fine cracks occurring only near the surface of the rock.

Where blocks of rock are used as targets some of the major fracturing is due to the presence of the reflecting faces of the rock. However, if rock is part of a solid working face, this type of damage to the rock would be minimal and limited to initial impact and relaxation effects.

Many of the effects of a short high velocity projectile can be simulated by a small surface charge of high explosive, cratering in metals is somewhat similar, but hemispherical craters are not formed by high explosives. Efficiency

of the impact-breakage process has not been evaluated, although the amount of energy that is utilized in producing stress waves is estimated to be less than one percent of the total projectile kinetic energy. Considering the analogous effects of a small unconfined surface charge, the estimated very small percentage of energy appears to be of the correct order of magnitude. Thus, hypervelocity projectiles have a very low energy efficiency both in drilling and breaking of rock.

In view of the size and cost of light gas guns, a much smaller type projectile accelerator would be required for possible underground applications. This could include use of small explosive charges for projecting small missiles at high velocities. These, however, have the same disadvantage as unconfined shaped charges, i.e., much of the explosive energy is required to set up stable detonation conditions and may not be used in the projectile or jet. Unless an inexpensive, efficient method can be found for accelerating projectiles, and a technique can be found to improve their breaking and drilling efficiency, this method appears to have little promise for practical application in rapid excavation.

PRESSURE VESSELS

The static analyses of cylindrical pressure vessels having sufficient internal volume to be of use in high-velocity jet applications indicate that 500,000 psi is a practical goal with present materials and technology, although such a design would probably be an upper limit.

The critical stress in a simple pressurized thick-walled cylinder is in the tangential direction, is maximum at the inside radius and decreases away

from the bore. Various strengthening techniques may be employed to create a more uniform stress distribution throughout the cylinder wall. They are autofrettage, shrink bands, wrapping, and multiple cylinder configurations. Stress analyses of these structures involve plastic as well as elastic behavior. The maximum shear stress criterion and von Mises' criterion are considered to be the most applicable measures of failure. The most refined analyses include the effect of strain hardening and as a result require a numerical approach.

The development in the last five years of substantial number of high strength steels having ultimate tensile strengths in the order of 300,000 psi will be most significant if the relatively low ductilities of these steels is not a limiting factor. The analyses by Berman (see Chapter VII) indicates that a coaxial multiple cylinder arrangement with externally controlled fluid pressure between the cylinders can make safer use of these high strength steels due to the higher hydrostatic pressures near the bore.

The effect of the pressurized fluid on the strength of the vessel must also be considered at extreme pressures. For example, the stress corrosion effect of water on SAE 4340 steel and maraging steel decreases the pressure which the vessel can withstand to only 1/5 of that when the pressurized fluid is gasoline.

Very little theoretical work has been done on pressure vessels to determine their response to dynamic or rapidly changing internal pressures. Some research in this area must have been done in gun design, although very little of this information is found in the literature. A proper design of a dynamic-pressure vessel would include, among other things, an analyses of the effects

on material properties. Repeated extension of the vessel by high order pressure pulses and the resultant creep are also limiting factors.

SHAPED CHARGES AND CUMULATION

Early use of military breaching charges on concrete shows that they would effectively drill holes in rocklike material. However, no complete tests have been conducted to ascertain all of the parameters involved, i.e., type of liner, strength of explosives, cone geometry, and other related factors for rock targets.

Shaped charges also provide a relatively inexpensive means for study of the effects of high speed jet impact with liners (jets) of a wide range of densities. Special designs of charges generate short, essentially single particle large mass jets. Hence, where the exact size and shape of the projectile is not important, lined shaped charges offer a means of generating high velocity projectiles. Cumulation by impact on hollow (inert) charges appears to have some promise of producing liquid jets, but requires further investigation.

Shaped explosive charges have been investigated for their ability to drill holes in rock and to fracture rock materials. Large (40 lb.) military type breaching charges were tested for this purpose by the Bureau of Mines in two types of unusually dense strong rocks. The conclusion drawn, on the basis of drilling holes for conventional tunnel blasting rounds, was that drilling costs were too high. However, no attempts were made to design a new type of blasting procedure around the performance of shaped charges. Current tests indicate that the latter procedure may prove feasible.

For breakage purposes, shaped charges are much less effective than the same amount of explosive used as a conventional mud-cap. This is in keeping with the theory that high velocity penetration is largely dependent on densities of the jet and the target, and that penetration takes place too rapidly to generate strong, persistent pulses in the rock.

DISCUSSION

Results of water jet research in Britain and USSR indicate that both steady and pulsed high velocity jets of water per se may be useful in cutting and/or breaking rocks in the laboratory. However, the production of high velocity water jets by means of mechanical or other types of compressors is costly and requires heavy equipment. Likewise, the production of hypervelocity projectiles by means of light gas guns requires elaborate, sophisticated equipment, and the cost per shot is great, particularly when high velocities are required. Production cost per shot of controlled shaped charge jets is only a small fraction of that of the other methods of hypervelocity generation.

There are several important differences between the phenomena of hypervelocity projectiles, the mechanism of shaped charge jets, and those of water jets, in respect to their use, mechanics of velocity generated and impact effects on various targets. The effect of a projectile is largely localized with respect to breakage, usually producing only a shallow crater with spallation around the rim of the crater. Very high velocity projectiles may produce additional fracture and spallation, although inertial effects dominate at the ultrahigh velocities.

Shaped charge and water jet effects are also localized in a plane normal to the axis of the jet, but penetrate to depths more than an order of magnitude greater than conventional cylindrical projectiles or comparable diameters. In the high velocity regime water jets are much less effective in penetration than metal jets because penetration in a given target is proportional to the square root of the jet density. The holes produced by metal jets are subject to subsequent use for further explosive breakage, while projectile craters are too shallow for further usage.

Rock breakage by both water jets and projectiles reported in the literature have been limited to finite blocks. For solid, semi-infinite rock some of the reflection mechanisms would not be present to cause tensile fracturing. Many of the effects of a hypervelocity projectile can be simulated by a small surface charge of high explosive. Both are surface phenomena and involve limited transmission of energy into the target.

There are certain similarities in the effects of the impact of projectiles and jets. At very high velocities, the penetration depends almost exclusively on the relative densities of targets and impacting agents. Partitioning of energy for the two types may be analogous although the similarities have not been quantitatively defined. Significant differences between projectile and jet impact are primarily due to the greater length and physical character of the jet.

Cavity charges will drill usable holes, hence, research and development should be aimed toward the design of economical drilling and blasting procedures around their performance characteristics. Water jets of the same

velocity theoretically drill much smaller holes. Projectiles excavate shallow craters only.

There is a limited amount of data available on the effects of hypervelocity impact on rock by either jets or projectiles. In simulation of micro-meteorites, it is considered necessary that projectiles not be deformed by the accelerating pressure. In research with rock targets this may not be a stringent requirement. Hence, explosive acceleration of projectiles, in which they are usually partially deformed or eroded, may be acceptable.

SUMMARY - STATUS OF RESEARCH AND DEVELOPMENT

A. Water Jets

1. Production

a. Compressors

Theory - Theory of gas compressors is well established. There was little information found in the literature on the theory or the operation and efficiency of high pressure water compressors.

Development - Two or three versions of piston compressors have been developed in the USSR. Other types of compressors or multipliers are used in Britain and the United States.

Application - Very large horsepower motors are required, water losses in jet formation are high, upper range of pressures is limited, pulsed jets cause machinery breakdown.

Cost - Actual operation costs are not given, but they appear to be excessive.

b. Water Cannons

Theory - Theory is well developed and is similar to that for piston type light gas guns.

Development - Large models have been developed in USSR and smaller ones in the United States.

Application - These have had considerable experimental development in USSR and some in the United States. No actual excavation applications are reported.

Cost - Cost of experimental models has been high.

c. Nozzles

Theory - Streamline theory for nozzles is well-known, but can be approximated only in capillary sizes.

Experimentation - For velocities to 1000 m/sec small entry angles of about 13° with a straight section of two to three diameters has been proven a good design.

d. Augmentation

Theory - Theory of small jet formation has been well developed.

Experimentation - Preliminary experiments only have been conducted. Theory has been partially verified.

Application - No applications have been made.

Cost - No cost figures are given. Efficiency depends on a number of yet undetermined factors.

2. Stability

Theory - Theory established for low velocity jets only. No well developed theory was found for capillary jets at high Mach numbers.

Experimentation - Pressure, continuity and velocity distribution have been measured for jets to 1000 m/sec.

3. Jet Impact

Theory - The basic mechanisms of water jet impact in rock for experimental velocities have not been reported. Ultrahigh velocity mechanisms would be the same as for metallic jets.

Experimentation - Action of moderately high velocity jets is cutting and penetration. Good breakage occurs for porous, cracked rocks with pulsed jets. Coupling and stress wave transmission appear to be very limited.

Application - No actual applications to excavation processes are reported in the available literature.

B. Metallic Jets

1. Jet Formation

Theory - The theory of jet formation from lined shaped charges was developed on a two-dimensional basis, which serves as a qualitative measure only.

Experimentation - Extensive experimentation on velocity and mass distributions in jets has been performed. Design parameters are well-known for military purposes only.

2. Jet Impact

Theory - Theory is based upon first order formula which prescribes penetration to be proportional to square root of density. Inertial effects dominate with minor correction for target strengths.

Experimentation - Extensive tests have been made on metal targets, and a very few on rock. Theory offers a good approximation for both types of targets.

Application - Shaped charges have had extensive military applications. Perfunctory tests only have been made in rock with no imaginative effort to utilize jet properties.

Cost - Estimates of costs for drilling only are high. Other drilling and blasting applications have not been investigated. Shaped charges provide a low cost method of generating hypervelocity jets and projectiles.

C. Hypervelocity Projectiles

1. Projection

Theory - The theory of light gas guns and various other means of accelerating projectiles is well developed.

Experimentation - Extensive experimentation has been performed on the various methods of accelerating projectiles. The present limit appears to be about 40,000 fps.

Cost - The cost of producing hypervelocity projectiles with light gas guns may be as high as \$1000 per shot for highest velocities. Lower velocities are less expensive.

2. Projectile Impact

Theory - Several empirical formulas only have been developed which have limited application at lower velocities. The first order jet theory is believed to apply at very high velocities.

Experimentation - Extensive experimentation has been performed on metals, and a few on rock targets. Many projectile impact effects can be simulated by small charges of high explosives.

Application - Hypervelocity projectiles appear to be relatively ineffective for either penetration or breakage of rocks because impact processes all take place at or near the surface of the rock. Coupling and wave generation are limited.

Cost - See Projection (C-1) above.

RECOMMENDATIONS

1. Further research is needed into the theory of the stability of hypervelocity axisymmetric water jets where the pressure difference between that behind and that in front of the nozzle is very large, i.e., at high Mach numbers.

2. If the economic use of high velocity water jets appears feasible, then more basic research will be required on the stability of hypervelocity capillary jets, and their effectiveness in cutting and breakage of rock in situ.

3. The efficiency of processes required to produce high velocity water jets should be established in theory and experiment. There is not sufficient information currently available to evaluate relative costs.

4. The results of impact of projectiles on rock should be compared with the effects of small surface explosive charges. The latter are less expensive by several orders of magnitude.

5. Measurements should be made of strain energy in rocks caused by projectile impact to verify the analysis of Gault, et al., which states that less than one percent goes to strain wave energy.

6. The potentialities of shaped explosive charges should be developed further to utilize their value as drilling agents. Procedures should be adapted to their capabilities rather than attempting to adapt them to conventional procedures. Previous tests of shaped charges were in dense, hard rock, and were conducted to determine relative drilling costs only.

7. Further research in rapid excavation techniques should consider the use of radical new methods other than the current conventional cyclic

system of drilling, loading and blasting, but should fully utilize known techniques in drilling and blasting where they may be applied.

8. For use underground, relatively low cost, lightweight equipment for producing water jets would be required if this method proves feasible for cutting or breaking rock.

9. Combined methods of water jet cutting and explosive breakage may be required, because jets cannot be used to cut parallel to a working face.

10. If water jets are found to be applicable for cutting rocks at ultra-high velocities, techniques will be required for prevention of freezing at high transient pressures.

11. Energy partitioning at various velocity levels for jets and projectiles needs to be more clearly defined.

12. The relative effectiveness of jets of water and more dense materials should be investigated with respect to their relative effect on rocks, particularly with reference to the energy requirements for producing the jets and their energy partitioning on impact.

13. Most of the high order breakage obtained by water jets was with pulsed flow on porous or relatively soft, cracked rock. Such spectacular breakage was not reported for hard, compact dense rocks such as granite. Effects of pulsed jets on hard rocks should be determined.

APPENDIX A

Symbols, Appendix A

a	sound speed of the gas
A, A_1	cross-sectional area of barrel
c	velocity of disturbance
D_0	diameter of chamber
D, D_1	diameter of barrel
G	mass of propellant gas in a PP gun
l	barrel length
M	projectile mass
m	molecular weight
R	universal gas constant
S	slope
s	entropy
T	temperature
t	time
u	gas velocity
u_{esc}	escape velocity
u_0	velocity of a projectile propelled by a constant pressure p_0
u_p	projectile velocity
u_{p1st}	velocity of projectile when first wave reflected from breech reaches it
v	muzzle velocity of projectile

x	distance coordinate
x_0	length of chamber in PP gun
x_p	position of projectile
γ	ratio of specific heats
ρ	density
σ	Riemann function defined from $d\sigma \equiv (dp/a\rho)_s$

APPENDIX A

Theory of Single Stage Light Gas Guns

Most of the theory outlined in this Appendix is summarized from the treatment by Seigel (Ref. 145). Material from other sources is referenced as it is used. Unless otherwise indicated the pressure is furnished by a pre-burned propellant, i.e., no gas is added or no additional combustion takes place after the projectile starts to move.

Projectile Velocity

The differential equation of motion for a projectile in the barrel of an ideal gun is

$$M \frac{du_p}{dt} = Mv_p \frac{du_p}{dx_p} = p_p A \quad (\text{A-1})$$

which may be integrated to give

$$Mv^2/2 = A \int_0^{\ell} p_p dx_p \quad (\text{A-2})$$

If the effective average pressure is defined as

$$\bar{p} = \frac{1}{L} \int_0^{\ell} p_p dx_p \quad (\text{A-3})$$

then the projectile velocity is given by

$$v = \sqrt{2\bar{p} A\ell/M} \quad (\text{A-4})$$

Velocity-Constant Base Pressure

For constant base pressure along the whole barrel integration of equation (A-2) yields

$$u_o^2 = \frac{2p_o A\ell}{M} \quad (\text{A-5})$$

which for a spherical projectile, for example, becomes

$$u_o = \sqrt{\frac{2p_o A \ell}{M}} = \sqrt{\frac{2p_o (\pi d^2/4) \ell}{(\pi d^3/6) \rho_p}} = \sqrt{\frac{3p_o}{\rho_p} \left(\frac{\ell}{d}\right)} \quad (\text{A-6})$$

If a constant pressure could be maintained behind the projectile the velocity would be given by

$$u_o = \sqrt{2p_o A \ell / M} \quad (\text{A-7})$$

(Such a condition is not obtainable in actual practice in a single stage gun.)

Pressure Disturbances

In a constant diameter gun the first movement of the projectile causes a rarefaction wave which is reflected from the breech. In a gun with chambrage, part of the rarefaction is reflected from the enlargement section as a compression wave and the remainder from the breech as a rarefaction.

For the system shown in Fig. A-1 the conservation of mass yields

$$A(c - u)\rho dt = A(c - u - du)dt (\rho + d\rho) \quad (\text{A-8})$$

while application of Newton's law results in

$$\underbrace{A dp}_{\text{net force}} = \underbrace{A \rho (c - u) dt}_{\text{mass}} \underbrace{\frac{du}{dt}}_{\text{acceleration}} \quad (\text{A-9})$$

and elimination of $\frac{du}{dt}$ from Equations (A-8) and (A-9) yields

$$(c - u)^2 = \frac{dp}{d\rho} \quad (\text{A-10})$$

The wave passage is assumed to be isentropic (reversible and adiabatic) and hence,

$$\frac{dp}{d\rho} = a^2 \quad (\text{A-11})$$

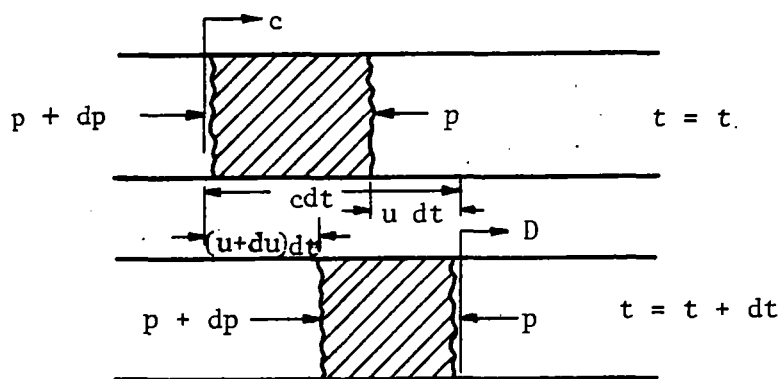


Fig. A-1. Schematic of disturbance in gas in chambers.

or the square of the speed of sound in the gas, thus

$$c = u \pm a \quad (\text{A-12})$$

or the disturbance travels with the speed of sound relative to the gas.

Substitution of (A-12) in (A-9) gives

$$dp = a \rho du \quad (\text{A-13})$$

which is the fundamental expression for a "u + a" (downstream) disturbance.

For a disturbance traveling upstream it is readily shown that

$$dp = - a \rho du \quad (\text{A-14})$$

The above expressions may be derived more rigorously as follows.

Consider the layer of gas (Figure A-2) in a constant diameter tube.

For small infinitesimal changes due to a change in x at a given t ,

$$\left. \begin{aligned} dp &= (\partial p / \partial x) dx \\ du &= (\partial u / \partial x) dx \\ d\rho &= (\partial \rho / \partial x) dx \end{aligned} \right\} \quad (\text{A-15})$$

Similarly,

$$d(\rho u) = \frac{\partial(\rho u)}{\partial x} dx \quad (\text{A-16})$$

and the continuity equation is

$$\rho u = \rho u + d(\rho u) + \frac{\partial \rho}{\partial t} = \rho u + \frac{\partial \rho u}{\partial x} dx + \frac{\partial \rho}{\partial t} \quad (\text{A-17})$$

or

$$\rho \frac{\partial u}{\partial x} + u \frac{\partial \rho}{\partial x} + \frac{\partial \rho}{\partial t} = 0$$

The acceleration of the layer of gas is given by

$$\frac{du}{dt} = \frac{\partial u}{\partial t} + u \frac{\partial u}{\partial x} \quad (\text{A-18})$$

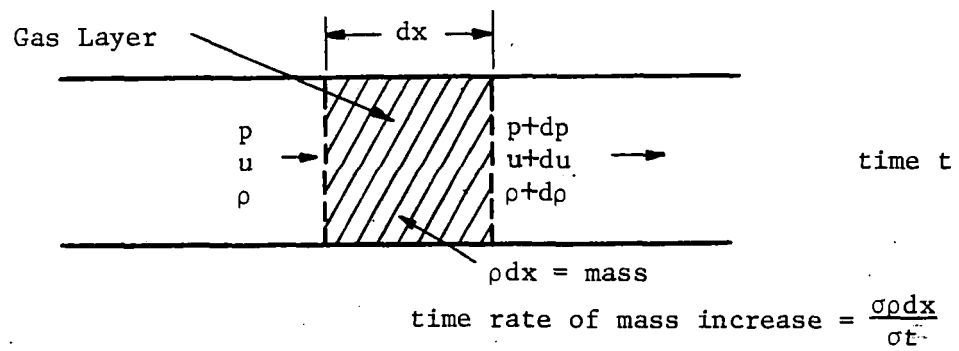


Fig. A-2. Schematic for change of properties across a layer of gas.

while the momentum equation is

$$\rho \frac{du}{dt} = p - (p + dp) = p - \left(p + \frac{\partial p}{\partial x} dx \right) \quad (\text{A-19})$$

or

$$\frac{\partial u}{\partial t} + u \frac{\partial u}{\partial x} = - \frac{1}{\rho} \frac{\partial p}{\partial x}$$

Assuming that the process is isentropic, the speed of sound \underline{a} and the Riemann Function \underline{g} are defined

$$a^2 = \left(\frac{\partial p}{\partial \rho} \right)_s \quad (\text{A-20})$$

$$d\sigma = \left(\frac{a}{\rho} d\rho \right)_s \quad (\text{A-21})$$

or

$$d\sigma = \left(\frac{1}{a\rho} dp \right)_s \quad (\text{A-22})$$

For constant entropy (A-20) and (A-21) may be written

$$a^2 = \frac{dp}{d\rho}, \quad s \text{ constant} \quad (\text{A-23})$$

$$d\sigma = \frac{a}{\rho} d\rho = \frac{1}{a\rho} dp, \quad s \text{ constant} \quad (\text{A-24})$$

Equation (A-24) may be written for differential changes in pressure or density

$$d\rho = \frac{\rho}{a} d\sigma \quad (\text{A-25})$$

$$dp = a\rho d\sigma \quad (\text{A-26})$$

From these one may write

$$\frac{\partial \rho}{\partial t} = \frac{\rho}{a} \frac{\partial \sigma}{\partial t} \quad (\text{A-27})$$

and

$$\frac{\partial \rho}{\partial x} = \frac{\rho}{a} \frac{\partial \sigma}{\partial x} \quad (\text{A-28})$$

$$\frac{\partial p}{\partial x} = a \rho \frac{\partial \rho}{\partial x} \quad (\text{A-29})$$

Thus, the gradient of the Riemann Function σ may be substituted for the gradients in $\underline{\rho}$ and \underline{p} . Substitution in (A-17) and (A-19) results in

$$\frac{\partial u}{\partial t} + u \frac{\partial u}{\partial x} + a \frac{\partial \sigma}{\partial x} = 0 \quad (\text{A-30})$$

$$\frac{\partial \sigma}{\partial t} + u \frac{\partial \sigma}{\partial x} + a \frac{\partial u}{\partial x} = 0 \quad (\text{A-31})$$

The "characteristics equations" are obtained by adding and subtracting (A-30) and (A-31)

$$\frac{\partial}{\partial t} (u + \sigma) + (u + a) \frac{\partial}{\partial x} (u + \sigma) = 0 \quad (\text{A-32})$$

$$\frac{\partial}{\partial t} (u - \sigma) + (u - a) \frac{\partial}{\partial x} (u - \sigma) = 0 \quad (\text{A-33})$$

and, utilizing the notation

$$\frac{d}{dt} = \frac{\partial}{\partial t} + (u \pm a) \frac{\partial}{\partial x} \quad (\text{A-34})$$

these equations may be written

$$\frac{d}{dt} (u \pm \sigma) = 0 \quad (\text{A-35})$$

The characteristic equations (A-32) and (A-33) are equivalent to the continuity and momentum equations provided the gas pressure is determined by density alone, i.e., the expansion process is isentropic.

Characteristic Theory

The characteristic equation (A-35) indicates that the time rate of change of $\underline{u} \pm \underline{\sigma}$ along a path of slope $\underline{u} \pm \underline{a}$ is zero. That is, to an observer traveling with velocity $\underline{u} \pm \underline{a}$ there is no change in the gas. In the x - t plane two sets of lines are obtained, one with a slope of $\underline{u} + \underline{a}$ along which $\underline{u} + \underline{\sigma}$ is constant and one with a slope of $\underline{u} - \underline{a}$ along which $\underline{u} - \underline{\sigma}$ is constant. The two sets intersect and form a characteristic net.

The lines are interpreted as paths of disturbance waves and the net is considered as a net of intersecting disturbances. Because of the fact that the quantity $\underline{u} \pm \underline{\sigma}$ remains constant along the lines of $\underline{u} \pm \underline{a}$, the behavior of the gas and projectile in a constant diameter gun can be formed by use of the characteristic net by means of numerical procedures. In some cases analytical solutions are possible.

Simple Wave Region - Constant Diameter

When the projectile begins to accelerate, a " $u - a$ " rarefaction moves toward the breech with a velocity $-a_0$, i.e., $(u-a) = a_0$ (Fig. A-3). As the projectile moves with a velocity described by A-B-C-D-E (Fig. A-4) it continues to initiate a whole series of such rarefactions. The region AOL (Fig. A-5) is a region of rest or undisturbed gas in which $\underline{u} = \underline{0}$ and $\underline{\sigma} = \underline{\sigma}_0$. For a $(u+a)$ characteristic which extends into this region

$$\underline{u} + \underline{\sigma} = \underline{\sigma}_0 \quad (\text{A-36})$$

which applies to all of the $(u+a)$ characteristics that extend into the rest region, as well as along their full length, i.e., all of those in AOLE (Fig. A-6).

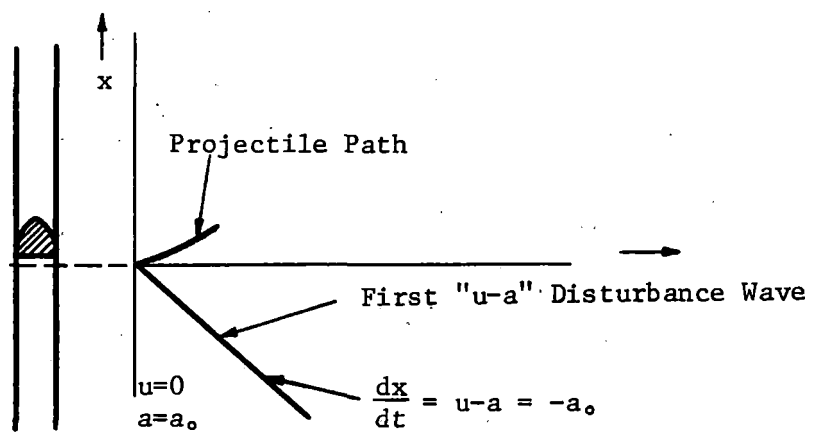


Fig. A-3. Projectile path and disturbances in the x - t plane.

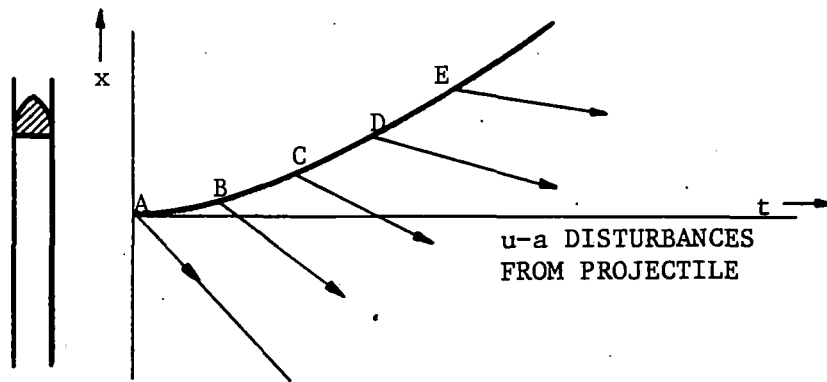


Fig. A-4. Subsequent projectile path and disturbances.

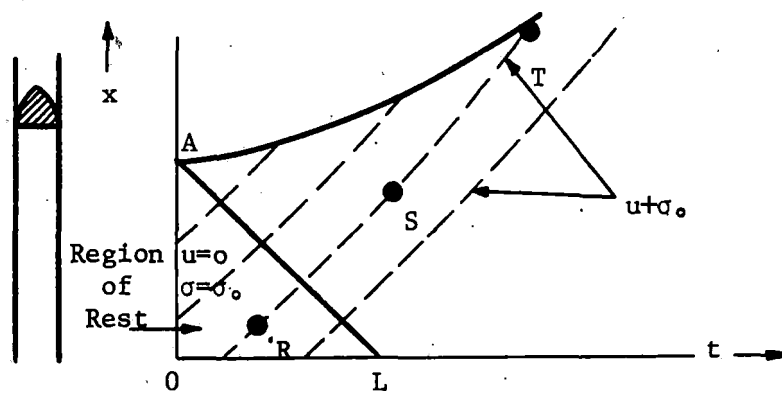


Fig. A-5. Plot of $u+\sigma$ characteristic lines.

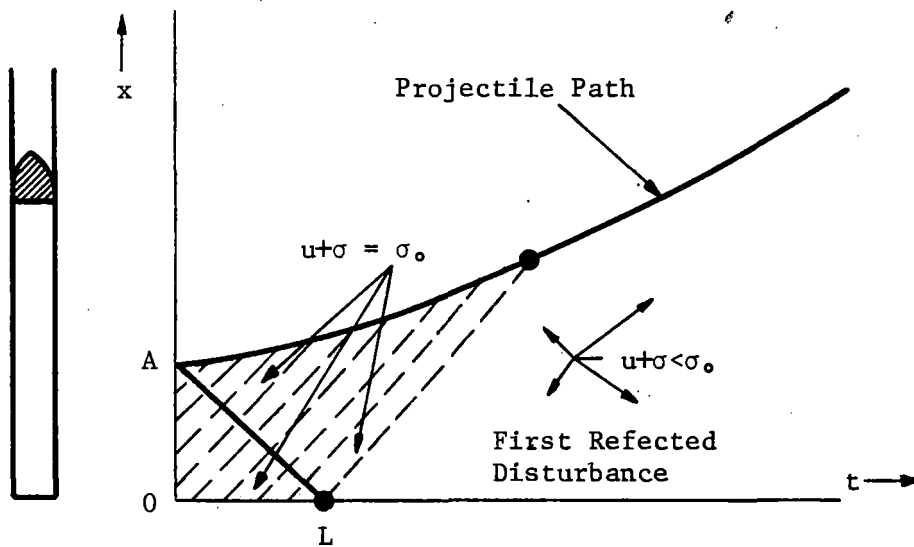


Fig. A-6. Characteristics up to point E where first reflected disturbance reaches projectile.

This area is known as the "simple wave" region. In the region of rest A-O-L (Fig. A-7) characteristics are straight lines with a slope a_0 , but outside they are not. (Fig. A-9).

Further, the (u-a) characteristics each have a $(u-\underline{\sigma})$ equal to a constant along them, e.g., for the characteristic BM (Fig. A-8).

$$u - \sigma = u_B - \sigma_B \quad (\text{A-37})$$

It can be shown that all of the (u-a) lines originating at the projectile and extending into the region of rest are likewise straight lines.

Numerical Calculations

Equations (A-32), (A-33), and (A-34) plus the relations

$$p = p(\rho) \quad \text{for the given entropy} \quad (\text{A-38})$$

$$a = a(p) \quad \text{for the given entropy} \quad (\text{A-39})$$

$$\sigma = \sigma(p) \quad \text{for the given entropy} \quad (\text{A-40})$$

The last three isentropic relations used by Seigel were obtained from thermodynamic data for gases and were employed in graphical form.

Small segments of the curves are assumed to be straight lines and accuracy depends upon the smallness of the segments. The net, therefore, consists of quadrilaterals, and if the conditions (u, v, x, t, p and a) at the points A and B (Fig. A-10) are known, then the conditions at C can be calculated.

From the characteristic equations it is known that

$$u_c - \sigma_c = u_A - \sigma_A, \quad u_c + \sigma_c = u_B + \sigma_B \quad (\text{A-41})$$

and therefore

$$u_c = \frac{1}{2} (u_B + u_A + \sigma_B - \sigma_c) \quad (\text{A-42})$$

$$\sigma_c = \frac{1}{2} (u_B - u_A + \sigma_B + \sigma_A)$$

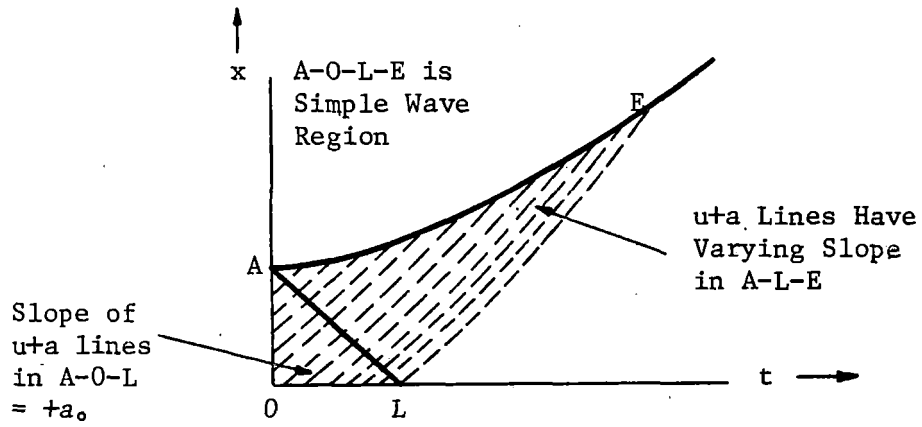


Fig. A-7. Simple Wave region.

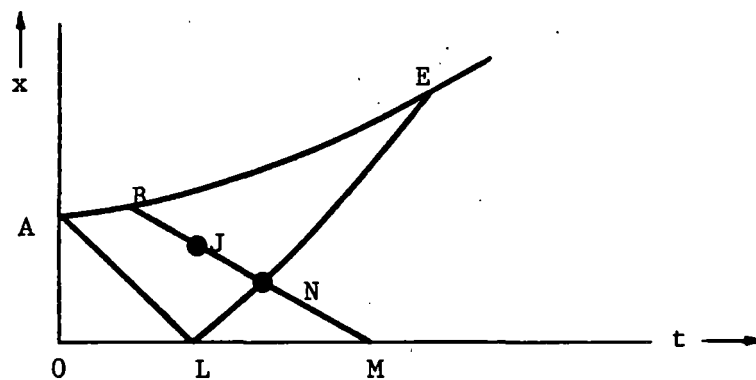


Fig. A-8. A u-a line, B-N in simple wave region, -BNM is a straight line.

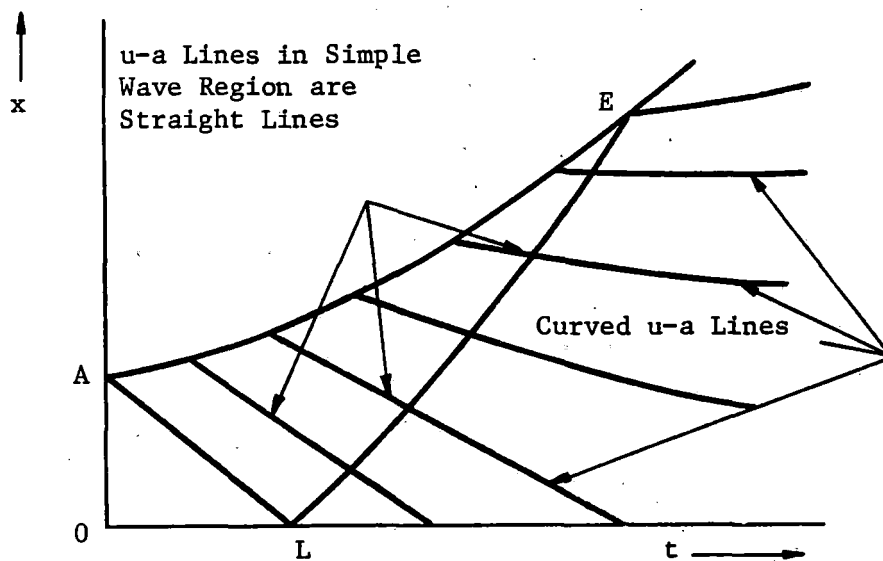


Fig. A-9. Sketch showing curvature of u-a lines outside of simple wave region.

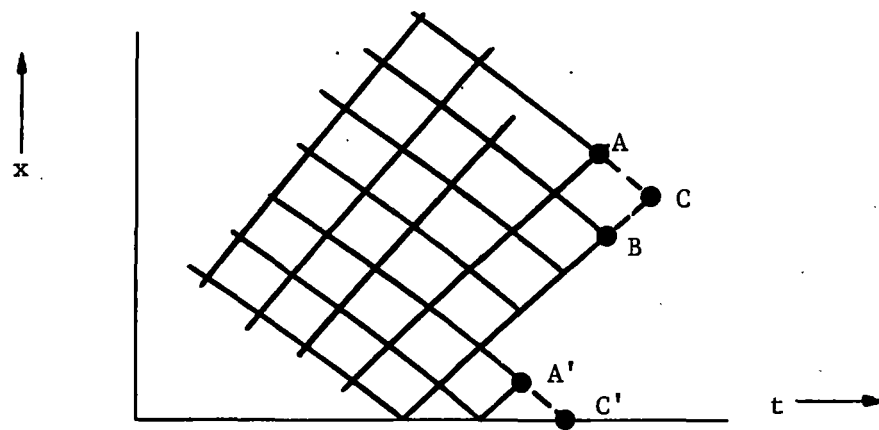


Fig. A-10. Net of quadrilaterals, approximating actual curves.

From σ_c the velocity of sound and pressure at C may be determined. The slopes of the lines AC and BC are calculated as the means of the slopes at A and C, and at B and C:

$$\begin{aligned} (\text{slope})_A = S_A &= \frac{1}{2}[(u_A - a_A) + (u_c - a_c)] \\ S_B &= \frac{1}{2}[(u_B + a_B) + (u_c + a_c)] \end{aligned} \quad (\text{A-43})$$

The coordinates of C are then

$$\begin{aligned} x_c &= \frac{S_A(x_B - S_B t_B) - S_B(x_A - S_A t_A)}{S_A - S_B} \\ t_c &= \frac{(x_B - S_B t_B) - (x_A - S_A t_A)}{S_A - S_B} \end{aligned} \quad (\text{A-44})$$

Thus, the conditions at C are all determined.

For the special case when the unknown point c' is on the t axis (at the breach), only one known adjacent point is required.

$$\begin{aligned} \sigma_{c'} &= (\sigma_A - u_{A'}) \\ S_{A'} &= \frac{1}{2}(u_{A'} - a_{A'} - a_{c'}) \\ t_{c'} &= t_{A'} - \frac{x_{A'}}{S_{A'}} \end{aligned} \quad (\text{A-45})$$

First Reflected Wave

The point at which the first reflected wave reaches the projectile is described by point E (Fig. A-11) which is the intersection of the projectile path, determined by the simple wave equations and the first wavelet ALE. The first leg of the wavelet path is drawn from $x = x_0$ with a slope of $-a_0$.

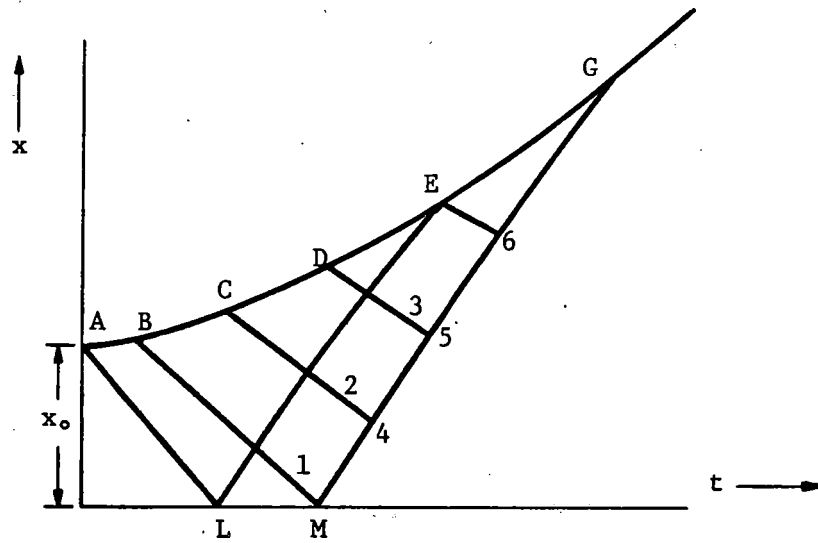


Fig. A-11. Scheme for calculating intersection of curves.

The conditions at L are:

$$\sigma = \sigma_0, \quad u = 0, \quad x = -x_0, \quad t = x_0/a_0, \quad a = a_0 \quad (\text{A-46})$$

Points of known parameter values are selected at B, C, D and E, (v-a) rays drawn and the conditions at points 1 to 6 calculated by the method given above. Completion of the row of quadrilaterals gives the values at point E.

Projectile Path - Post - Reflection

Points M, 4, 5, 6 are determined by a continuation of the network.

The point G is formed by an iterative process subject to the following:

a) The point G is the intersection of a line through E of slope which is the average of the slopes at E and G, and a line through 6 of slope whose average of the slopes at 6 and G is:

$$\text{slope E-G} = S_E = 1/2 (u_E + u_G)$$

$$\text{slope 6-G} = S_6 = 1/2 (u_6 + u_G + a_G + a_6) \quad (\text{A-47})$$

b) Newton's law requires that

$$\frac{u_G - u_E}{t_G - t_E} = \frac{A}{M} (p_G + p_E) \left(\frac{1}{2}\right) \quad (\text{A-48})$$

The first approximation of the time at G is the intersection of the extension of the curves DE and 5-6. a_G is provisionally assumed to be a_E and the approximation of the velocity is

$$u_G^{(1)} = u_E + (t_G^{(1)} - t_E) (p_E) \frac{A}{M} \quad (\text{A-49})$$

and the iterative procedure is given by

$$\begin{aligned}
 s_E^{(2)} &= \frac{u_E + u_G^{(1)}}{2} \\
 s_6^{(2)} &= \frac{(u_6 + a_6) + (u_G^{(1)} + a_G^{(1)})}{2} \\
 t_G^{(2)} &= \frac{(x_6 - s_6^{(2)}) t_6 - (x_E - s_E^{(2)}) t_E}{s_E^{(2)} - s_6^{(2)}} \\
 u_G^{(2)} &= u_E + (t_G^{(2)} - t_E) \frac{p_E + p_G^{(1)}}{2} \frac{A}{M} \\
 \sigma_G^{(2)} &= (u_6 + \sigma_6) - u_G^{(2)}
 \end{aligned} \tag{A-50}$$

The values of $p_G^{(2)}$ and $a_G^{(2)}$ are obtained from (A-39) and (A-40)

$$s_E^{(3)} = \frac{u_E + u_G^{(2)}}{2}, \quad s_6^{(3)} = \frac{(u_6 + a_6) + (u_G^{(2)} + a_G^{(2)})}{2} \tag{A-51}$$

Convergence is rapid, and effect of counterpressure may be introduced.

Isentropic Expansion - Constant Diameter

For one-dimensional adiabatic flow, without friction and heat loss as an approximation, simple solutions are obtainable for some interior ballistics problems. The characteristic equations, written in terms of the Riemann Function σ , defined by

$$d\sigma = (dp/ap)_s \tag{A-52}$$

are

$$du + d\sigma = 0 \quad (\text{A-53})$$

along $dx/dt = u + a$, and

$$du - d\sigma = 0 \quad (\text{A-54})$$

along $dx/dt = u - a$. As shown above they may be written

$$\frac{d}{dt} (u \pm \sigma) = 0 \quad (\text{A-55})$$

which is integrated to yield

$$u \pm \sigma = \text{constant} \quad (\text{A-56})$$

along paths $u \pm a = dx/dt$, respectively (Fig. A-10).

Infinite Chamber

For an effectively infinite chamber, constant diameter, the region behind the initial position of the projectile is the "simple wave" region and the entire region is described by

$$du + d\sigma = 0 \quad (\text{A-57})$$

or

$$du + dp/a\rho = 0 \quad (\text{A-58})$$

which is integrated to give

$$u + \int dp/a\rho = 0 \quad (\text{A-59})$$

or, in terms of

$$u + \sigma = \sigma_0 \quad (\text{A-60})$$

where \underline{u} is zero at $\underline{p} = p_0$ and $\underline{\sigma} = \sigma_0$.

In a gun where the chamber is sufficiently long that the first reflection does not reach the projectile before it leaves the gun, the chamber is effectively of infinite length, or $x_0 = \infty$.

Acoustic Inertia - Infinite Chamber

For $x_0 = \infty$ equation (A-58) may be written

$$dp = -a_p du \quad (\text{A-61})$$

which applies only to a (u+a) disturbance. Equation (A-61) indicates that the drop in pressure is directly proportional to a ρ . The velocity at any point is given by

$$u = \int_p^{p_0} \frac{dp}{a_p} \quad (\text{A-62})$$

which holds only for a preburned propellant gun of constant diameter and of effectively infinite chamber length. The equation of motion of the projectile is given by equation (A-1).

Ideal Gas

The equations for an ideal isentropic gas are

$$p = \rho RT \quad (\text{A-63})$$

$$p = \rho^\gamma p_0 / p_0^\gamma \quad (\text{A-64})$$

where subscript $\underline{0}$ indicates the initial rest state. The acoustic impedance during isentropic expansion is

$$a_p = p_0 \sqrt{\frac{\gamma}{RT_0}} \left(\frac{p}{p_0}\right)^{\frac{\gamma+1}{2\gamma}} = \frac{\gamma p_0}{a_0} \left(\frac{p}{p_0}\right)^{\frac{\gamma+1}{2\gamma}} \quad (\text{A-65})$$

The sound velocity is

$$a^2 = \frac{\gamma p}{\rho} = \frac{\gamma \bar{RT}}{m} = \gamma RT \quad (\text{A-66})$$

and the Reimann Function becomes

$$\sigma = \frac{2}{\gamma-1} a \quad (\text{A-67})$$

From equations (A-56) and (A-65) the projectile velocity is related to the velocity u by:

$$\frac{p}{p_0} = \left(1 - \frac{u}{\frac{2}{\gamma-1} a_0} \right)^{\frac{2\gamma}{\gamma-1}} \quad (\text{A-68})$$

and in the limit of $\gamma = 1$ the equation assumes the form

$$\frac{p}{p_0} = e^{-u/a_0} \quad (\text{A-69})$$

From the above equation it becomes apparent that the dimensionless pressure p/p_0 depends upon the dimensionless velocity v/a_0 . For low speed guns where $v/a_0 \ll 1$ the pressure drop is small, but for high speed guns the drop becomes critically large. The effect of γ on the pressure drop is shown in Fig. A-12. The higher the initial value of sound velocity a_0 , the smaller the pressure drop (Fig. A-13).

From equation (A-68) the pressure drops to zero when the gas velocity reaches the "escape velocity," i.e.,

$$u_{\text{esc}} = 2a_0/(\gamma-1) \quad (\text{A-70})$$

and equation (A-68) can be rewritten as

$$\frac{p}{p_0} = \left(1 - \frac{u}{u_{\text{esc}}} \right)^{\frac{2\gamma}{\gamma-1}} \quad (\text{A-71})$$

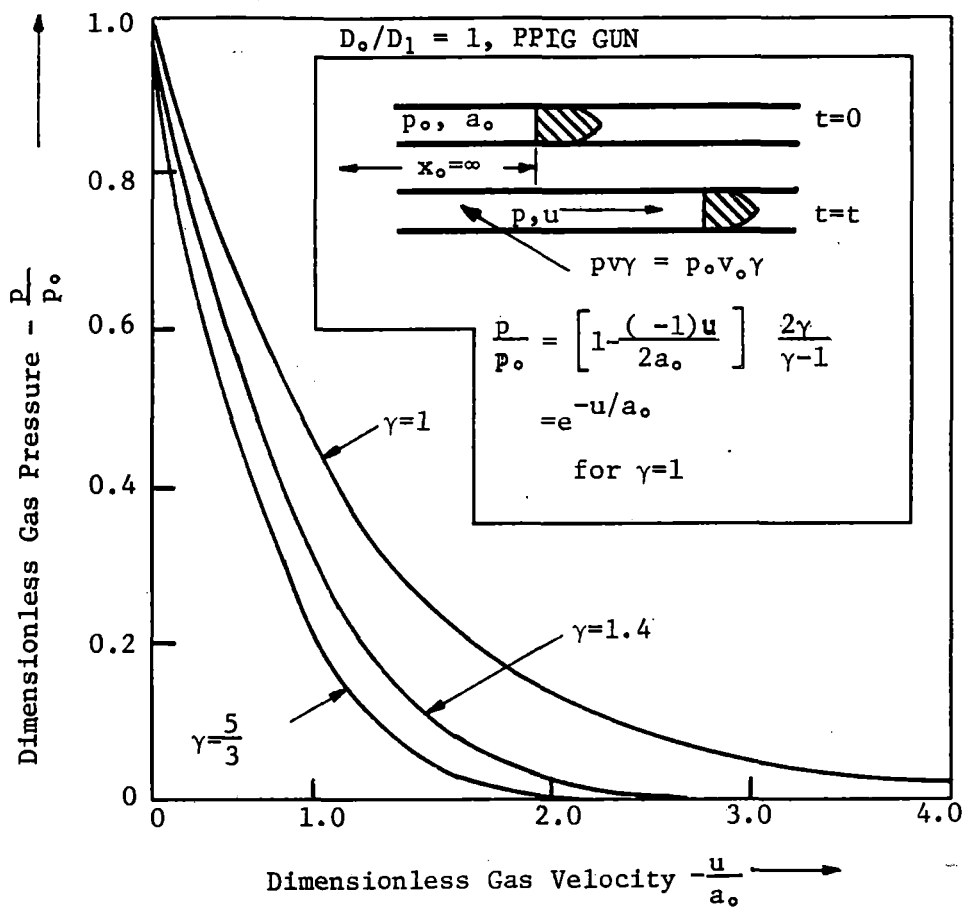


Fig. A-12. Variation of pressure with velocity as u function of γ .

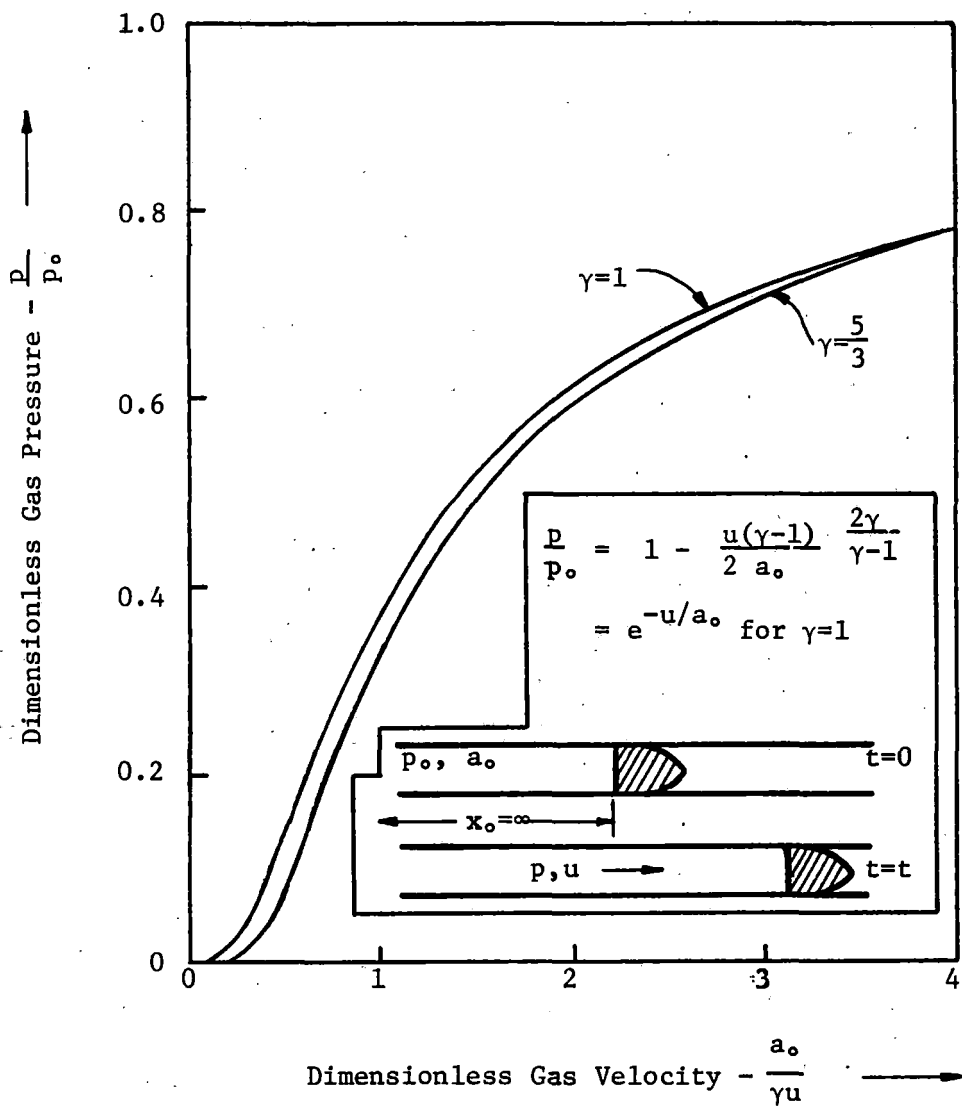


Fig. A-13. Dimensionless gas velocity vs. dimensionless gas pressure.

Actual projectile velocities rarely exceed one-half of the escape velocity. The plot of (A-68) Fig. A-13, with p/p_0 as a function of $a_0/\gamma u$ is nearly a single curve for all values of γ and is approximated by

$$\frac{p}{p_0} = e^{-\gamma u/a_0} \quad (\text{A-72})$$

Hence, the pressure drop is also a function of a_0/γ . The ratio of specific heats cannot be easily changed but a_0 can be increased by using a light gas at high temperatures.

Projectile Equations

If equation (A-68) is combined with (A-1) and the resulting equation integrated, the distance traveled is given in terms of the projectile velocity:

$$\frac{p_0 A_1 x_p}{Ma_0^2} = \frac{2}{\gamma+1} \left\{ \frac{\frac{2}{\gamma-1} - \frac{\gamma+1}{\gamma-1} \left[1 - \frac{u(\gamma-1)}{2a_0} \right]}{\left[1 - \frac{u(\gamma-1)}{2a_0} \right] (\gamma+1)/(\gamma-1)} + 1 \right\} \quad (\text{A-73})$$

or

$$\frac{p_0 A_1 x_p}{Ma_0^2} = e^{u/a_0} \left(\frac{u}{a_0} - 1 \right) + 1 \quad (\text{A-74})$$

The plot of dimensionless velocity versus dimensionless travel distance shows that smaller heat capacity ratios increase the velocity (Fig. A-14).

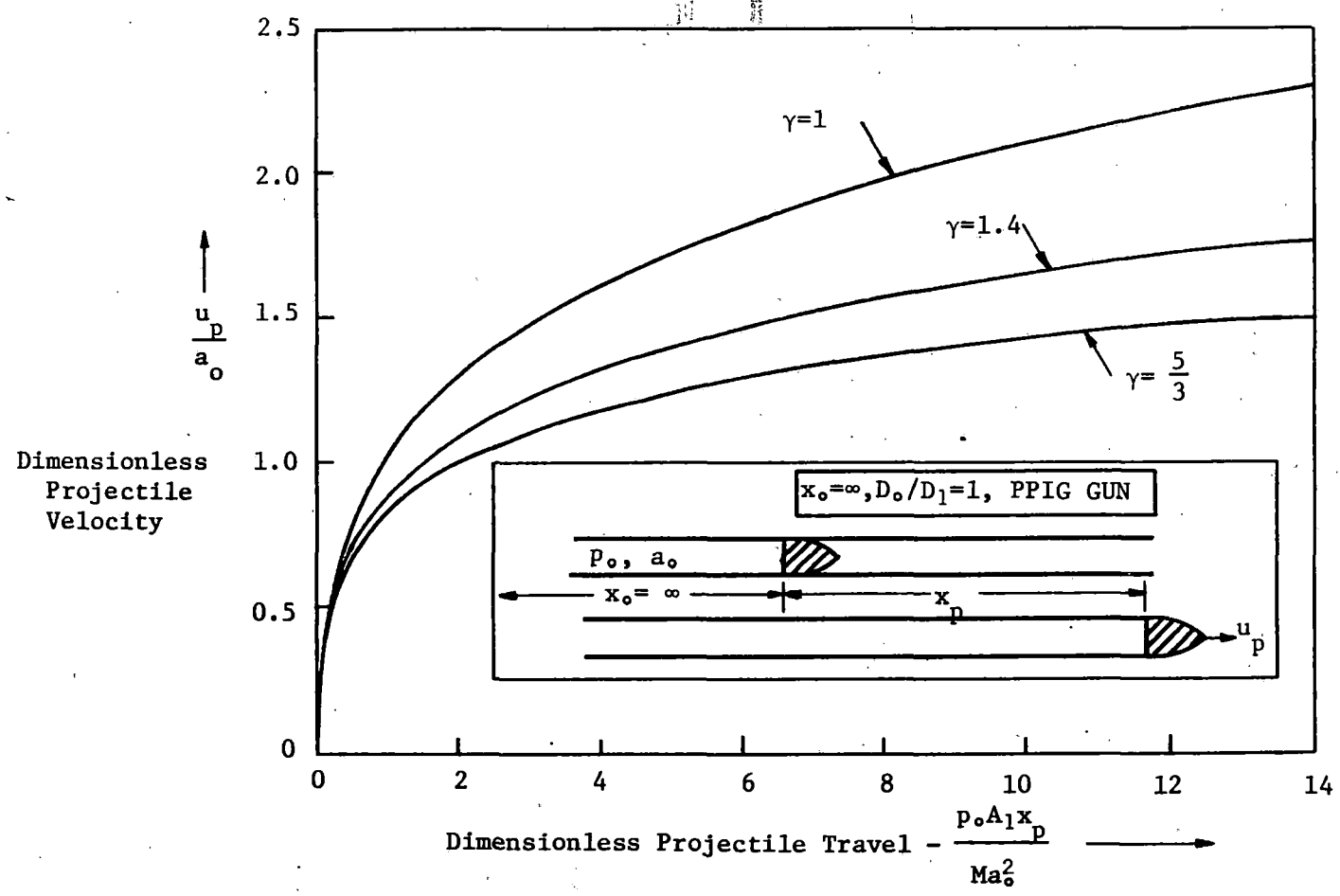


Fig. A-14. Dimensionless projectile travel as a function of dimensionless projectile velocity.

As noted above projectiles seldom exceed one-half the escape velocity because the pressure becomes so low that frictional and back pressure resistance are equal to the pressure on the rear of the projectile.

A curve for dimensionless projectile velocity u_p/u_o versus dimensionless sound speed $a_o/\gamma u_o$, (Fig. A-15) shows the maximum attainable velocity is $u_o = (2p_o A x_p/M)^{1/2}$ for a constant pressure p_o . Thus u_p/u_o is a measure of the efficiency, a high value being obtainable when the initial sound velocity a_o is large.

The projectile velocity of a given gun with an initial propellant pressure p_o is a function of a_o/γ only (Fig. A-15). As indicated above, a high efficiency requires a high value of a_o/γ , which means a_o should be as large as possible and γ as small as possible. The heat capacity ratio γ can be varied only from 1 to 5/3, hence the only way to obtain a significant increase in projectile velocity is to increase a_o .

Finite Length Chamber

For a gun wherein the projectile does not leave the barrel before the first reflection reaches it, the solution is more complex than described for an effectively infinite chambered gun.

An analytical expression relating x_o to the velocity of the projectile at the arrival of the first reflection was obtained by Heybey (Ref. 145) and transformed by Seigel:

$$\frac{p_o A_1 x_o}{M a_o^2} = \frac{2}{\gamma+1} \left\{ \frac{1}{\left[1 - \frac{u_{p1st} (\gamma-1)}{2a_o} \right]^{(\gamma+1)/2(\gamma-1)}} - 1 \right\} \quad (A-75)$$

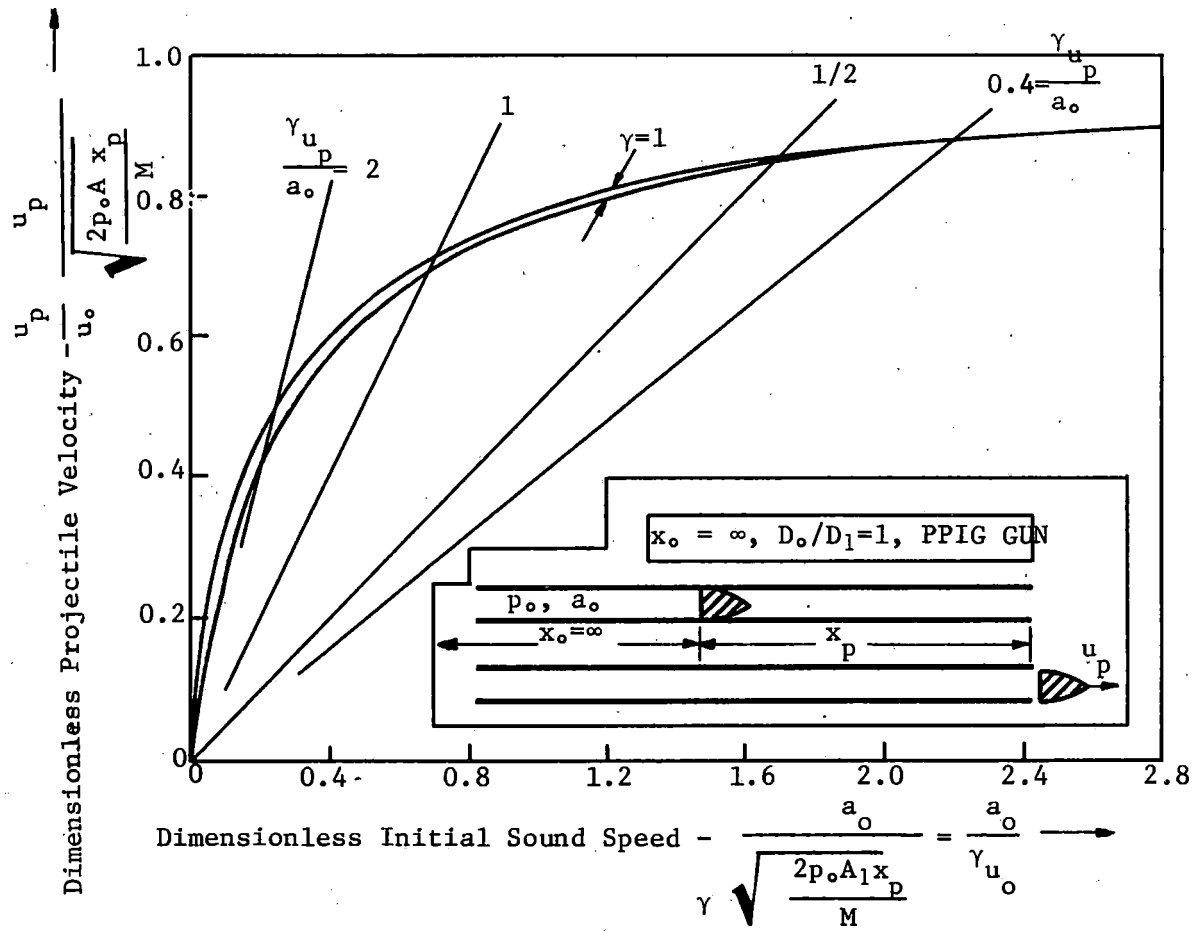


Fig. A-15. Dimensionless initial sound speed vs. dimensionless projectile velocity.

which is for $\gamma = 1$

$$\frac{p_o A_1 x_o}{Ma_o^2} = e^{u_{p1st}/2a_o} - 1 \quad (\text{A-76})$$

When x_{p1st}/x_o is plotted against the left-hand member of equation (A-76),

(Fig. A-16) it is found that

$$\frac{x_{p1st}}{x_o} \approx 2.5 \frac{p_o A_1 x_o}{Ma_o^2} \quad (\text{A-77})$$

The effect of the reflected disturbances is to decrease the pressure on the projectile (Fig. A-17) and (Fig. A-18). For $x_o = \infty$ the projectile performance is analyzed by plotting u_p/a_o versus $p_o A x_p / Ma_o^2$. Where x_o is finite a numerical solution is determined for each assumed chamber length as in Fig. A-19 for $\gamma = 1.4$. The points of departure from the $x_o = \infty$ curves are found from equation (A-75).

Also, the ratio G/M (mass of gas/mass of projectile) may be introduced to give

$$\frac{x_o}{x_o} = \frac{p_o A_1 x_o}{Ma_o^2} = \frac{G}{\gamma M} \quad (\text{A-78})$$

PPIG Gun $d_o/d_1 = 1$

where $\gamma p_o / \rho_o = a_o^2$. Typical curves for different ratios of G/M for a $\gamma = 1.4$ gas are shown in Fig. A-20. Similar curves can be drawn for other parameters including guns with enlarged chambers.

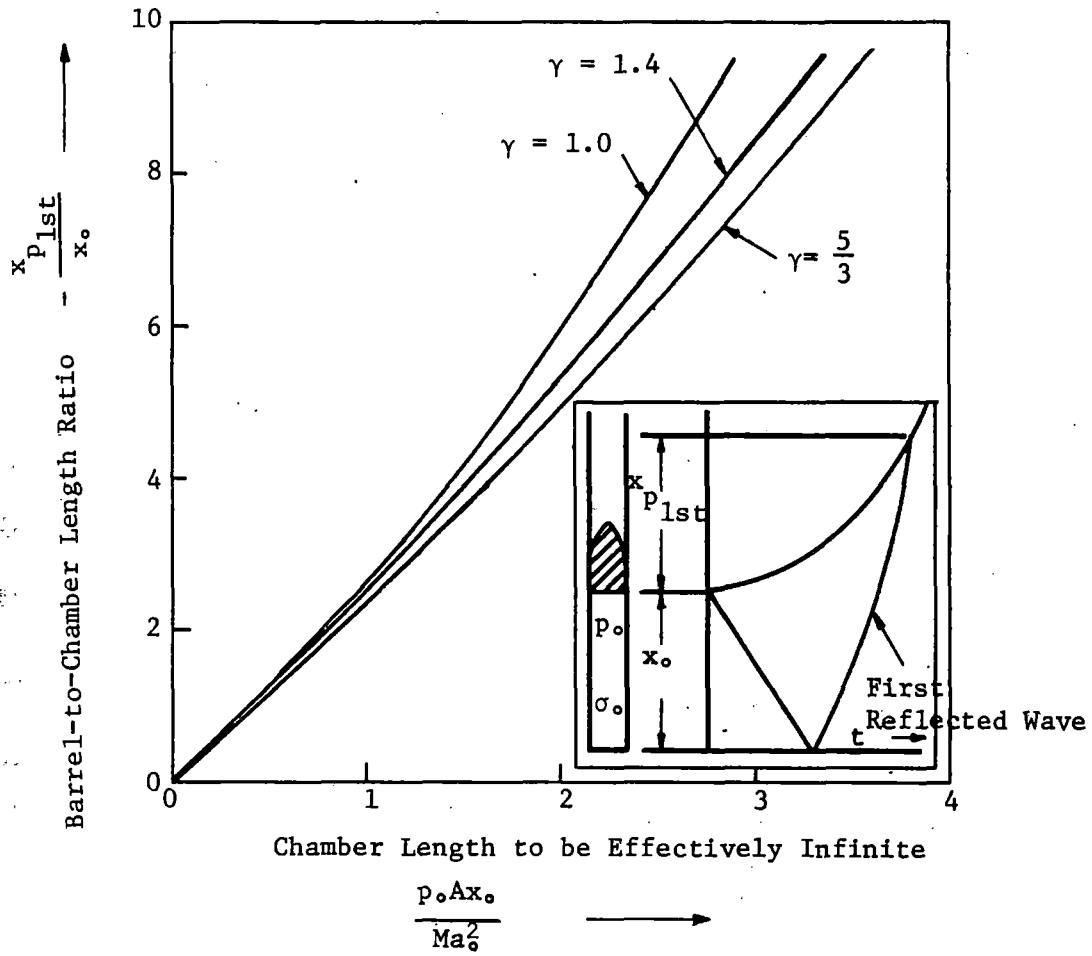


Fig. A-16. Chamber length vs. chamber length ratio.

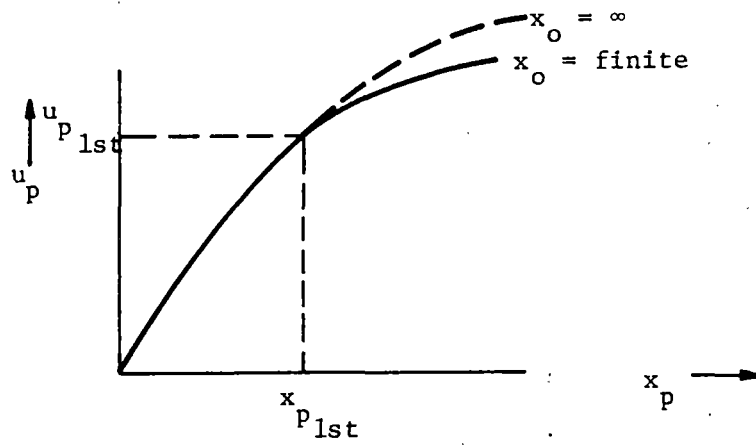


Fig. A-17. Effect of reflected wave vs. pressure.

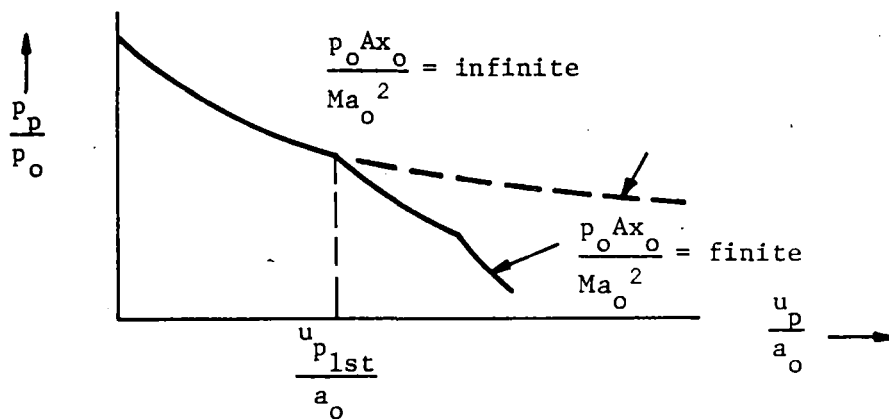


Fig. A-18. Effect of reflection on projectile velocity.

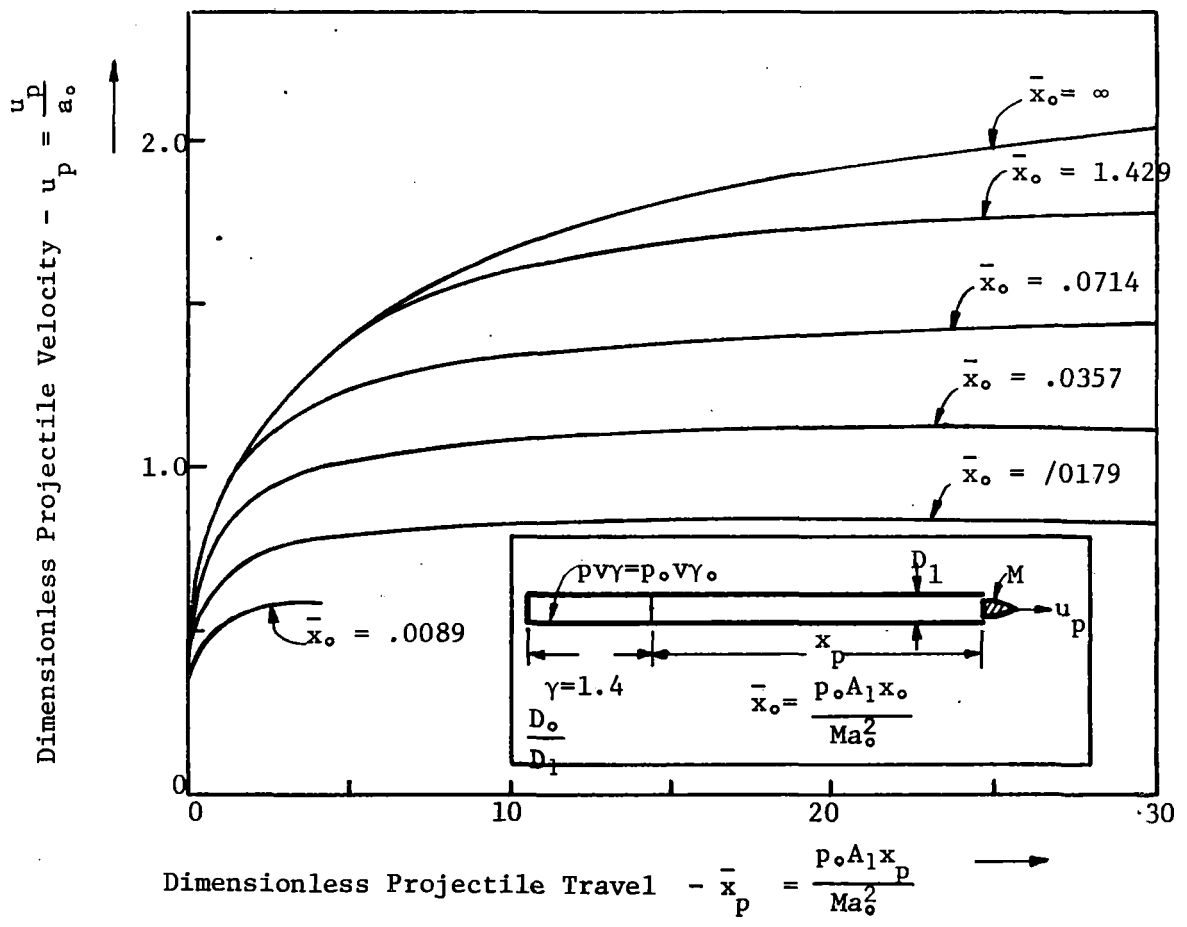


Fig. A-19. Dimensionless projectile velocity vs. dimensionless projectile travel.

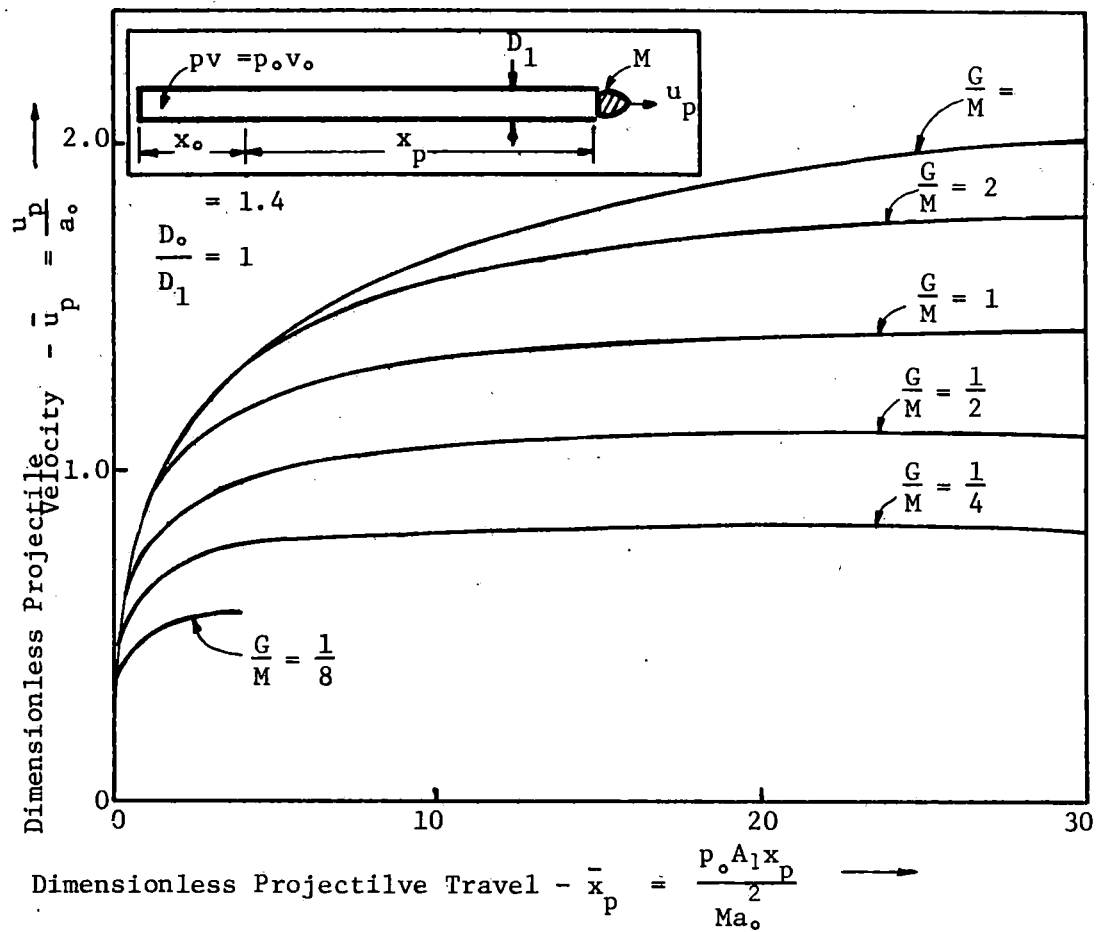


Fig. A-20. Dimensionless projectile velocity vs. dimensionless projectile travel.

Chambered Gun

The flow in the transition section of a chambered gun is two-dimensional, but may be solved by assuming it can be approximated by one-dimensional flow. One method of solution is by means of the characteristic equations, while another more direct method assumes that the change of mass and energy in the transition section are negligible. A comparison of the results of the last method with experimental results (Fig. A-21) shows good agreement for certain specific test conditions.

It can readily be shown by means of the characteristic function that $\underline{u} + \underline{\sigma}$ increases in the transition section, which in turn increases the projectile velocity above that of a non-chambered gun. This result is achieved regardless of the equation of state of the gas. However, the "ap" is applicable to both types of guns for ideal gases only. For non-ideal gases the performance is not determined by the sound speed.

The analysis of pressure pulses, reflection, projectile acceleration, etc., for a chambered gun is somewhat similar to that for a constant diameter gun (Ref. 145). This includes the assumption of a chamber of effectively infinite length for isentropic behavior of ideal gas.

For a gun with an infinitely long chamber, $x_0 = \infty$, it can be shown that the value of $u + \sigma$ is greater than σ_0 while in a constant diameter gun $\underline{u} + \underline{\sigma}_0$. The projectile velocity in the chambered gun is, consequently, greater in the chambered gun.

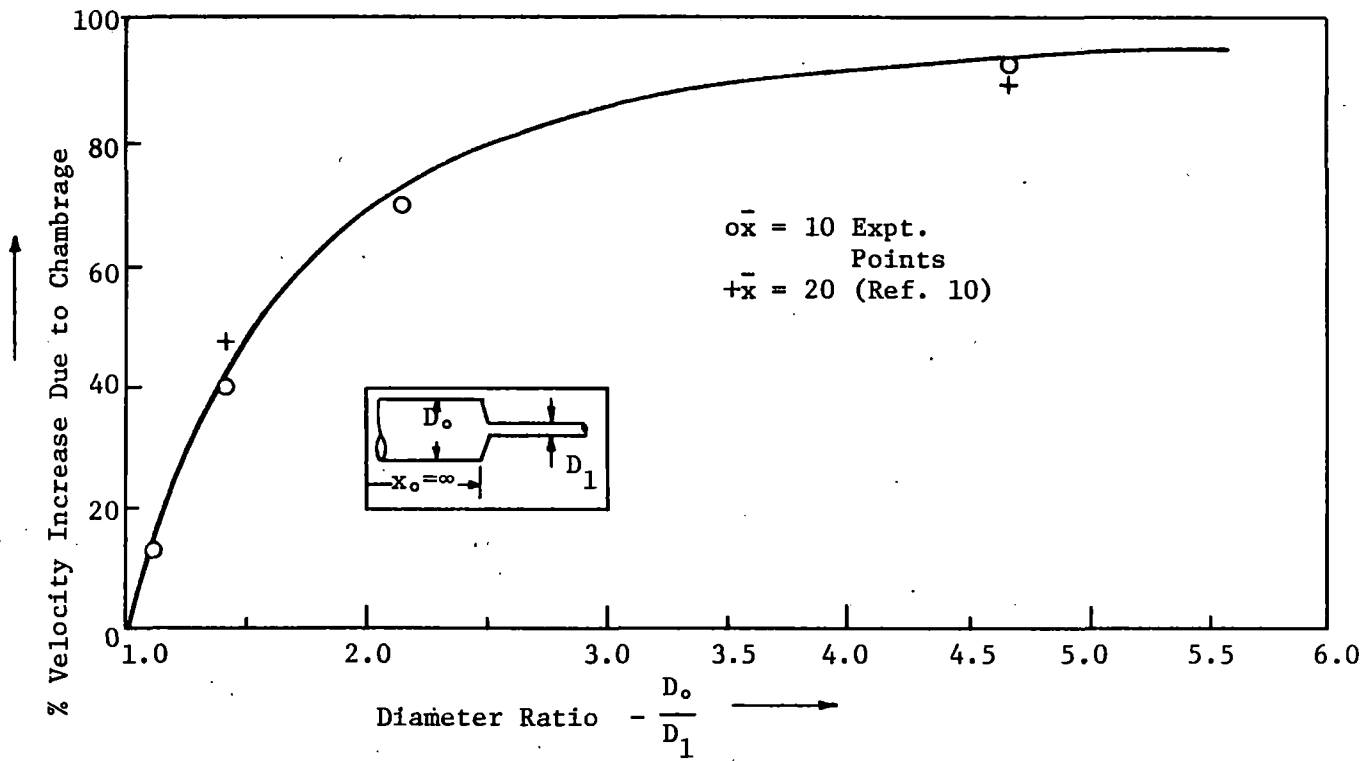


Fig. A-21. Comparison of experimental and theoretical velocity increase due to chambrage.

For a chamber of infinite diameter all of the characteristic lines for the chamber have a slope of $\pm a_0$, and hence numerical computations need be carried out only for the barrel, and the length of the chamber has no influence.

The escape velocity for a gun with $x_0 = \infty$ is found to be

$$u_{\text{esc}} = \sqrt{\frac{\gamma+1}{2} \frac{2a_0}{\gamma-1}} \quad (\text{A-79})$$

while the increase in escape velocity is

$$\Delta u_{\text{esc}(\infty)} = u_{\text{esc}(D_0/D_1=\infty)} - u_{\text{esc}(D_0/D_1=1)} = 1 \left(\sqrt{\frac{\gamma+1}{2}} - 1 \right) \frac{2a_0}{\gamma-1} \quad (\text{A-80})$$

In the limit as $\gamma = 1$ the difference approaches $0.5 a_0$, and shows also that the increase in escape velocity is approximately equal to half of the speed of sound a_0 for all values of γ between $5/3$ and 1 . This also yields almost a straight line relationship between Δu_{en} and $(D_1/D_0)^2$ for all values of γ (Fig. 22).

The performance of a constant diameter $x_0 = \infty$ gun has been shown to depend upon the parameter a_0/γ . For a chambered gun if Δu_p is plotted against $(\gamma u_p/a_0)$ for a constant diameter gun, the curve may be approximated by two straight lines (Fig. A-23) for all values of γ . Also, the relationship between percent increase in escape speed due to chambrage and the ratio of $(D_1/D_0)^2$ is approximately a straight line:

$$\Delta u_p = \Delta u_{p\infty} [1 - (D_1/D_0)^2] \quad (\text{A-81})$$

This may be utilized to approximate the effect of chambrage within a few percent.

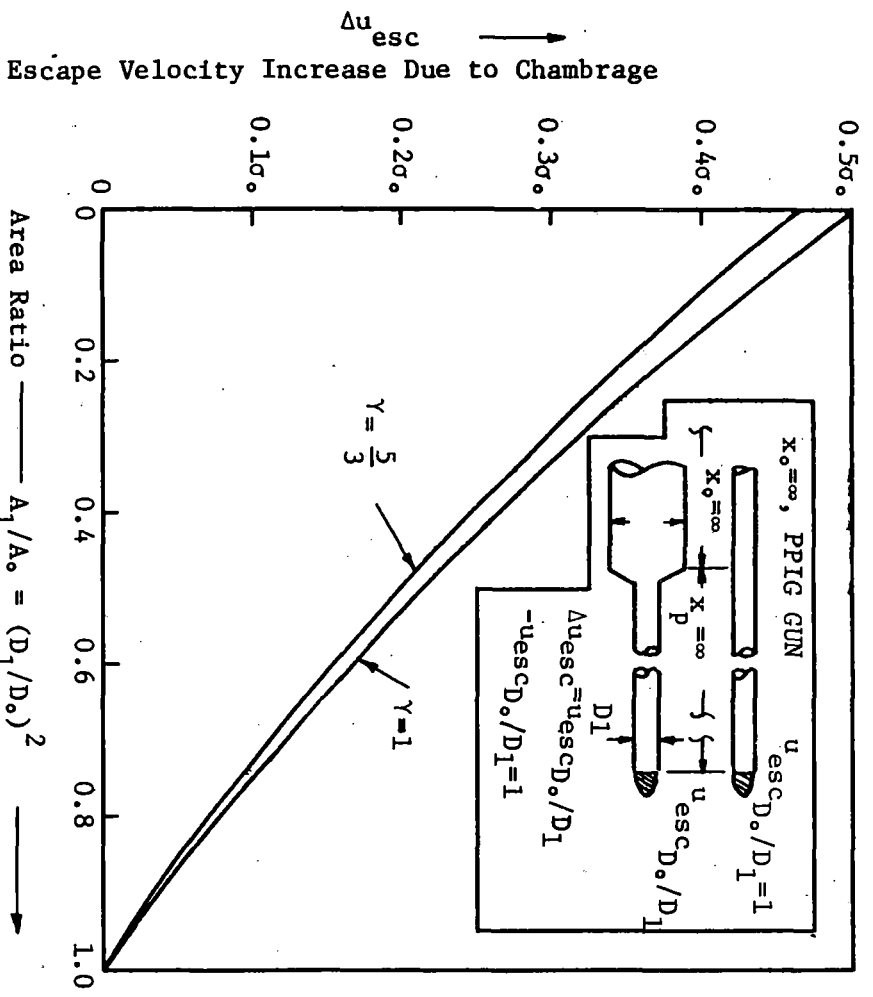


Fig. A-22. Escape velocity vs. chambrage as a function of γ .

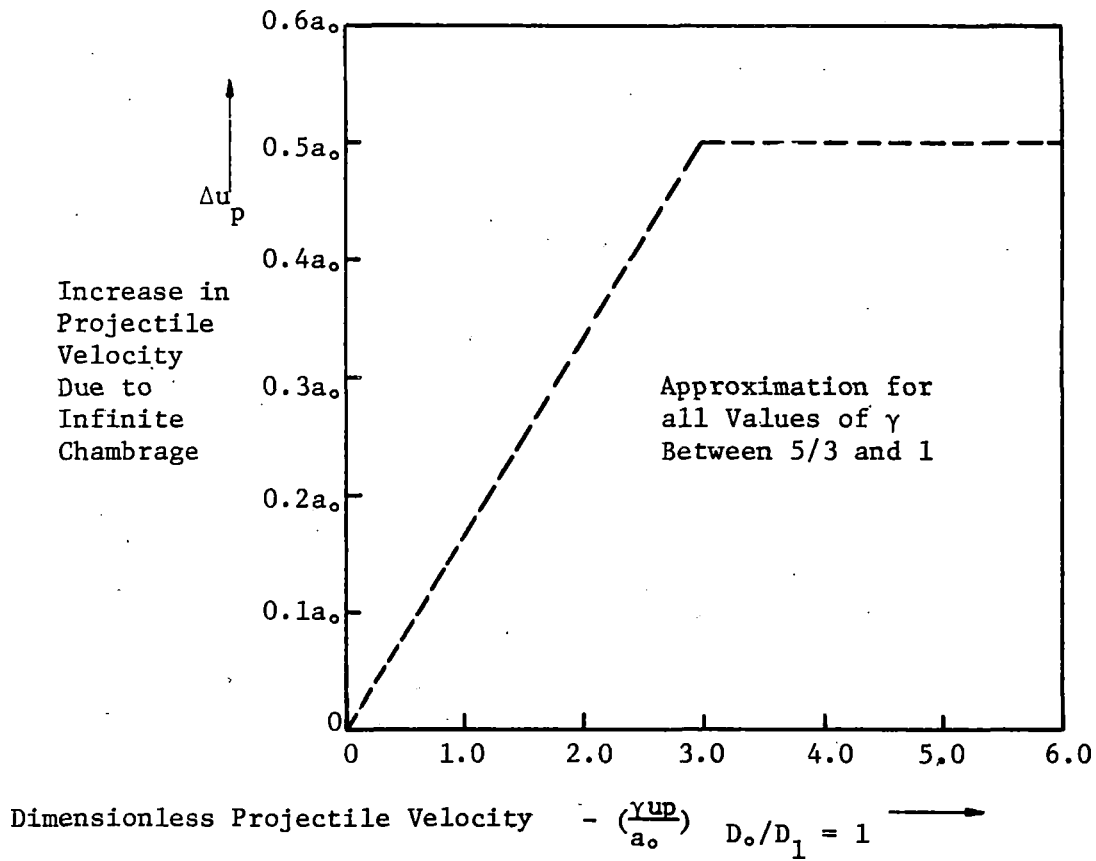


Fig. A-23. Increase in projectile velocity vs. dimensionless projectile velocity.

Pressure-velocity relationships and the sonic flow of gas into the barrel may be determined from appropriate equations and the effects of reflections of waves from the breech where $x_0 \neq \infty$. The characteristic equations may be utilized in a manner similar to that employed for a constant diameter gun to calculate the first reflected disturbance. The relationships for different values of chambrage length and diameters, reflections and effectively infinite chambrage are shown in Figs. (A-24) and (A-25).

Two methods of computation are employed to determine projectile behavior. The first is the method of characteristics described above. The second utilizes a Lagrangian scheme of dividing the gas into small layers. Pressure pulses are assumed to vary negligibly over small times, and the movement of the sides of each layer determines the new volume and pressure. The process is then repeated and motion determined.

Back Pressure of Gas in Barrel

One-dimensional gas equations are required to determine the retarding effect of gas in the barrel. For details of theory see Seigel (Ref. 145). In this case the solution requires the use of

1. The characteristic equations applied to the propellant gas
2. The characteristic equations applied to the gas in front of the projectile
3. Shock equations
4. Newton's equation applied to the projectile

Projectile Velocity as a Function of the Length of Chamber to be Effectively Infinite

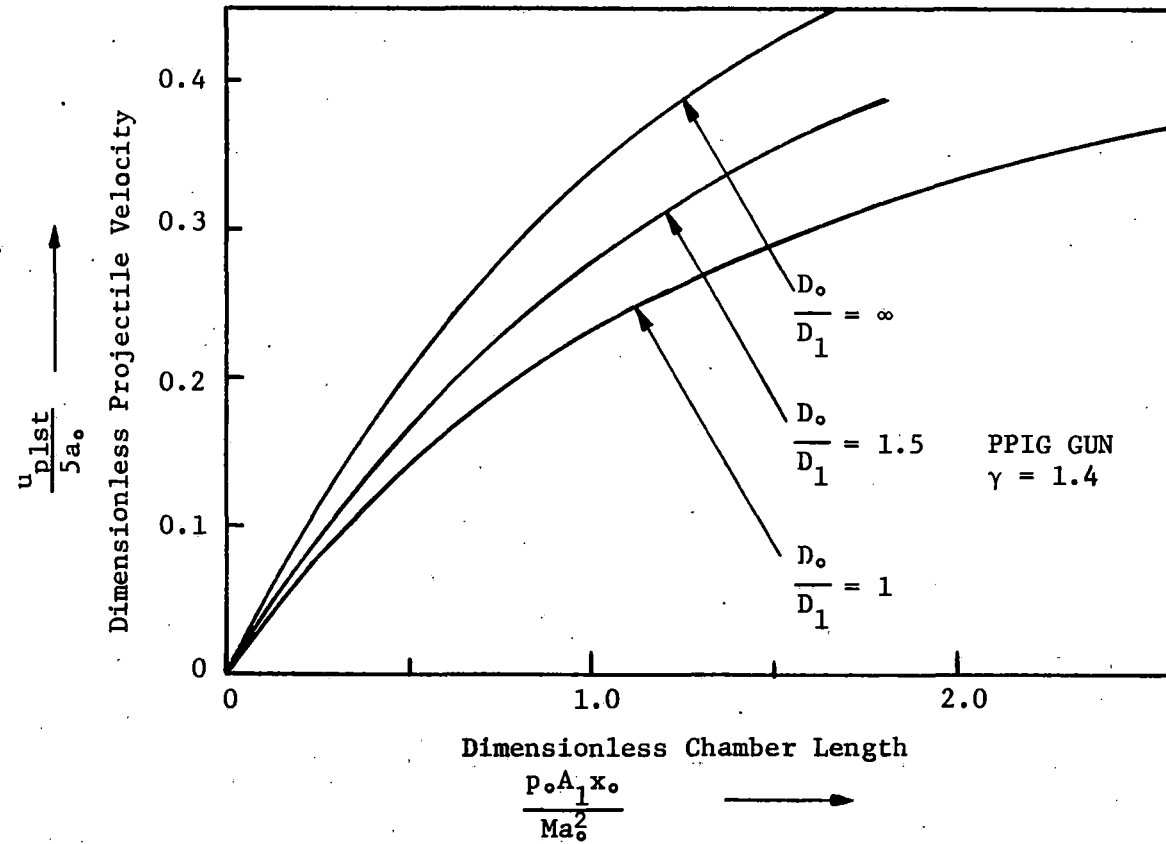


Fig. A-24. Velocity vs. chamber length.

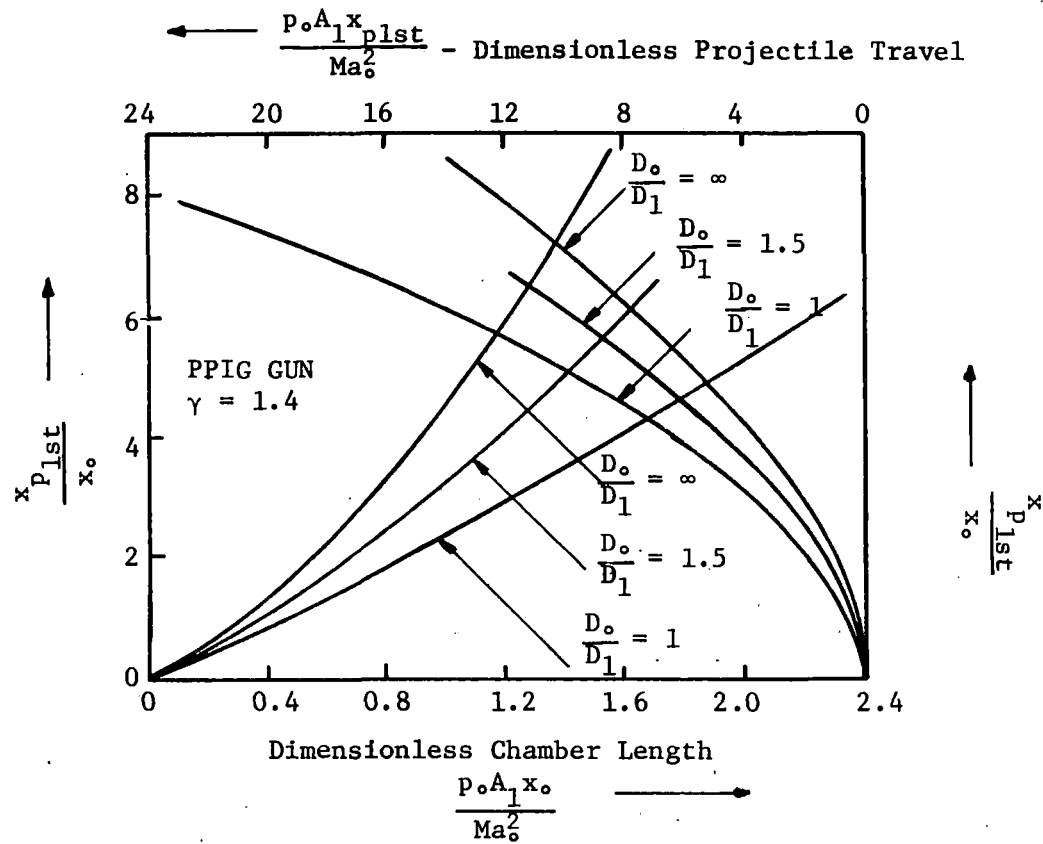


Fig. A-25. Dimensionless distance vs. dimensionless chamber length.

Using approximations the theoretical retardation of a projectile may be calculated and effects of friction are somewhat similar.

Heating Propellant Gas

Effective acceleration requires a light gas with a low acoustic inertia. Hydrogen and helium are both used. Increase of temperature enhances performance, also.

Heat may be obtained from chemical reactions, such as the combustion of hydrogen and oxygen. Heating of hydrogen by an electric arc discharge is used in some laboratories. Heating by shock wave has been attempted with moderate success.

The two-stage gun contains a back chamber and a piston chamber. A high pressure is built up in the back chamber until a calibrated diaphragm bursts, causing the piston to move forward into the pump tube, heating the light gas and compressing it. The piston provides an efficient means of transferring the energy from the back chamber to the propellant gas to high internal energies and more persistent pressures. Details of computation are similar in principle to those of a single stage gun, although additional factors must be considered such as shock waves in the propellant chamber, etc. (See Seigel, Ref. 144, pages 82-100).

Most of the theoretical developments outlined concerning guns have been based on the assumption of an ideal gas equation of state. Real gas may deviate considerably from this type of behavior. An Abel equation of state has been employed by some investigators with considerable success. Also, van der Waal's equation is employed for dense gases.

APPENDIX B

PRESSURE VESSELS

APPENDIX B - I
STRESS ANALYSIS

Thin-Walled Vessels, Elastic Analysis

Low pressures can be contained by vessels having wall thicknesses which are small compared to the overall diameter of the vessel. It can be shown that strains are then approximately uniform across the section and therefore the stresses are also uniform.

The circumferential stress σ_c and the longitudinal stress σ_l in the thin-walled vessel shown in Fig. (B-1) are given by the familiar equations

$$\sigma_c = \frac{p d_i}{2t} \quad (B-1)$$

$$\sigma_l = \frac{p d_i}{4t} \quad (B-2)$$

Equations (B-1) and (B-2) are valid when the radius of the vessel is at least ten times the wall thickness or $\frac{d_i}{t} \geq 20$.

Thus,

$$\sigma_c = \frac{p d_i}{2t} \geq \frac{p(20)}{2} = 10p \quad (B-3)$$

and

$$\sigma_l \geq 5p \quad (B-4)$$

A thin-walled vessel, therefore, cannot contain a pressure greater than 1/10 of the tensile strength of the material. The radial stress σ_r on the inside surface is equal to the pressure p and is usually neglected since it is small compared to the other stresses.

Thick-Walled Vessels, Elastic Analysis

Higher pressures can be contained by increasing the wall thickness of a thin-walled vessel. However, after a certain point the assumptions of

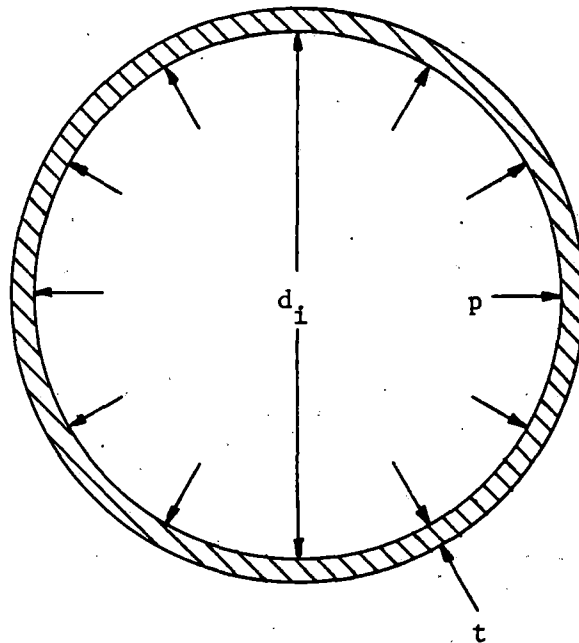


Fig. B-1. Thin-walled pressure vessel.

uniform strain and stress across the section are no longer valid.

The general equations for the radial and tangential stresses, σ_r and σ_θ , in a thick-walled cylindrical vessel, (Fig. B-2) subjected to internal and external pressures, p_i and p_o , are derived in several texts on the theory of elasticity and advanced mechanics of materials (Refs. 116, 140 and 141).

These equations, attributed to Lamé, are:

$$\sigma_r = \frac{a^2 b^2 (p_o - p_i)}{b^2 - a^2} \frac{1}{r^2} + \frac{p_i a^2 - p_o b^2}{b^2 - a^2} \quad (\text{B-5})$$

$$\sigma_\theta = \frac{a^2 b^2 (p_i - p_o)}{b^2 - a^2} \frac{1}{r^2} + \frac{p_i a^2 - p_o b^2}{b^2 - a^2} \quad (\text{B-6})$$

For a thick-walled vessel subject only to an internal pressure $p = p_i$, $p_o = 0$, equations (B-5) and (B-6) then reduce to:

$$\sigma_r = \frac{a^2 p}{b^2 - a^2} \left(1 - \frac{b^2}{r^2} \right) \quad (\text{B-7})$$

$$\sigma_\theta = \frac{a^2 p}{b^2 - a^2} \left(1 + \frac{b^2}{r^2} \right) \quad (\text{B-8})$$

where tensile stresses are considered positive.

Equations (B-7) and (B-8) indicate that σ_r is everywhere compressive and that σ_θ is everywhere tensile. σ_θ is maximum at the inner surface, where

$$\sigma_{\theta \max} = \frac{p(a^2 + b^2)}{b^2 - a^2} \quad (\text{B-9})$$

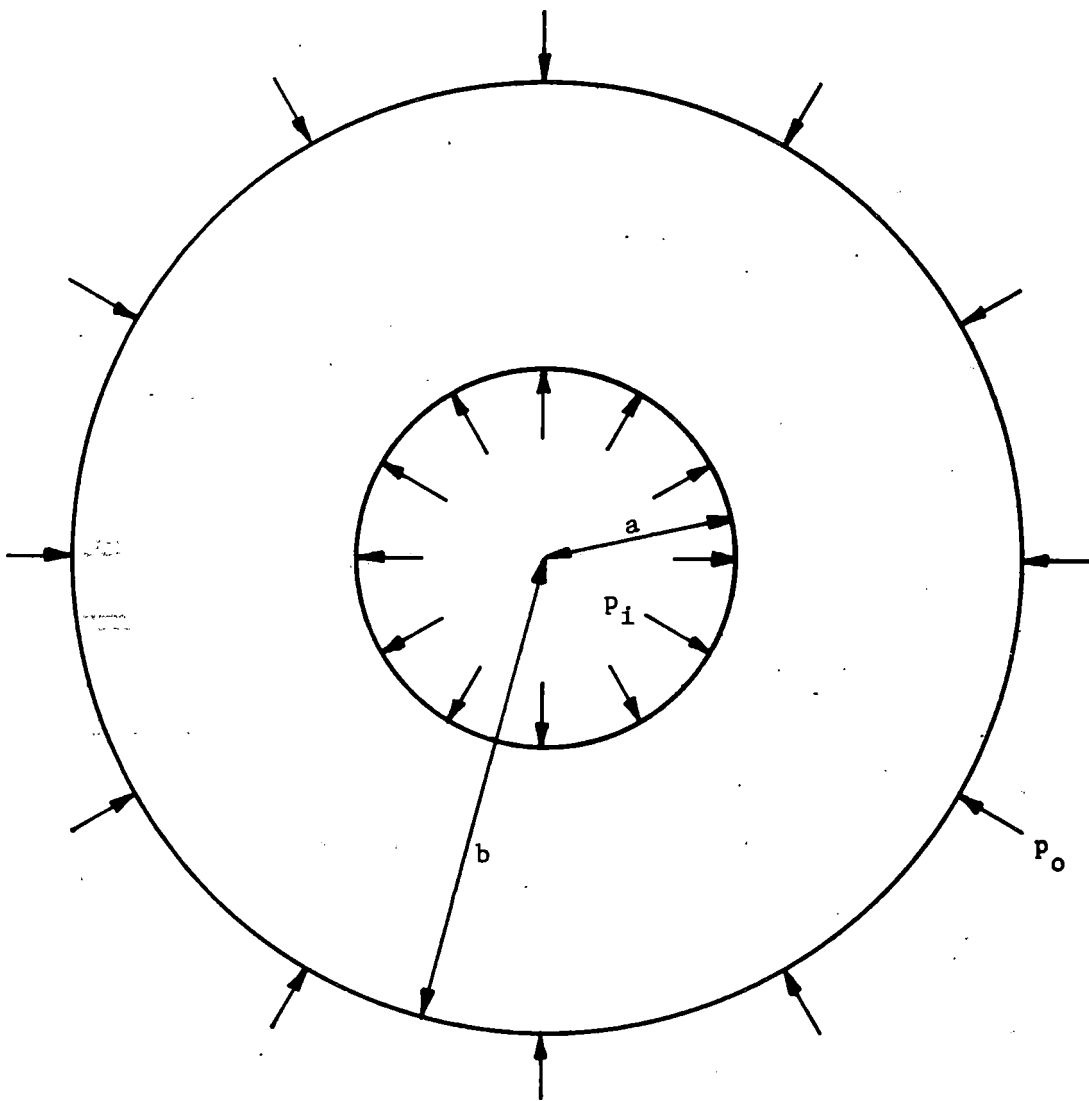


Fig. B-2. Thick-walled cylinder subjected to internal and external pressures.

As the outer radius b becomes infinite it can be shown that the $\sigma_{\theta \max}$ approaches the internal pressure p . If the vessel is loaded only by the internal pressure in the radial direction, and if the cylinder is free to expand along its length, the axial stress σ_z will be zero. However, if the cylinder is completely restrained in the axial direction

$$\sigma_z = 2\nu \frac{a^2 p}{b^2 - a^2} \quad (\text{B-10})$$

Axial stress will also be introduced if the pressure p is allowed to act on the ends of the vessel, in which case

$$\sigma_z = \frac{a^2 p}{b^2 - a^2} \quad (\text{B-11})$$

Autofrettage - Theoretical Analysis

Timoshenko (Ref. 142) rigorously analyzes the stresses produced by the autofrettage process. His analysis is based on a maximum shear stress failure criterion and he assumes that the vessel is loaded only by pressure acting radially. The material is assumed to behave elastically up to the yield point, and perfectly plastic thereafter.

As the autofrettage pressure increases the inside wall first becomes plastic at a pressure p_{yp} given by

$$p_{yp} = \tau_{yp} \frac{b^2 - a^2}{b^2} \quad (\text{B-12})$$

where

$$\tau_{yp} = \frac{\sigma_{\theta} - \sigma_r}{2} \quad (\text{B-13})$$

and a and b are the inner and outer radii respectively.

As the pressure is increased further the plastic deformation penetrates deeper and deeper into the wall of the cylinder. The pressure necessary to cause the entire wall to yield is

$$p_{ult} = -2 \tau_{yp} \ln \frac{a}{b} \quad (B-14)$$

and the radial and tangential stresses are

$$\sigma_r = 2 \tau_{yp} \ln \frac{r}{b} \quad (B-15)$$

$$\sigma_\theta = 2 \tau_{yp} \left(1 + \ln \frac{r}{b} \right) \quad (B-16)$$

If the internal pressure is now removed, residual stresses remain in the wall of the cylinder. Assuming the material follows Hooke's law during unloading, the stresses which are to be subtracted are given by the equations

$$\Delta\sigma_r = \frac{a^2 p_{ult}}{b^2 - a^2} \left(1 - \frac{b^2}{r^2} \right) \quad (B-17)$$

$$\Delta\sigma_\theta = \frac{a^2 p_{ult}}{b^2 - a^2} \left(1 + \frac{b^2}{r^2} \right) \quad (B-18)$$

The residual stresses after release of the pressure will then be the difference between equations (B-15) and (B-17) for σ_r and equations (B-16) and (B-18) for σ_θ . If the cylinder is then repressurized to p_{ult} the resultant stresses will again be given by equations (B-15) and (B-16). However, this time the material will be working only in its elastic range.

Timoshenko calculates the various stresses for the particular case where $b = 2a$ and where the autofrettage pressure is sufficient to cause yielding throughout the entire wall thickness. The results are shown in graphical

form in Figure (B-3), in terms of the shear yield stress τ_{yp} . The σ_r and σ_θ stress distributions when the cylinder is first brought to the autofrettage pressure are shown by the curves mln and st respectively. The stresses to be subtracted upon release of the autofrettage pressure are shown by curves $s_1 t_1$ and mkn. The residual stresses are shown by the shaded areas, the plus sign indicating residual tensile stresses, and the negative signs indicating residual compressive stresses. If the cylinder is again loaded by an internal pressure p_{ult} the resulting tangential stress will be the sum of that shown by curve $s_1 t_1$ and that shown by the shaded areas; this sum being shown by curve st. The maximum resultant stress is seen to be $2 \tau_{yp}$; and no yielding occurs during this second pressurization to p_{ult} .

Timoshenko also considers the case where the ultimate pressure is reduced so that only a portion of the wall is plastically deformed. The pressure p' sufficient to cause yielding out to a distance $r = c$ is given by the equation

$$p' = -2 \tau_{yp} \ln \frac{a}{c} + \tau_{yp} \frac{(b^2 - c^2)}{b^2} \quad (B-19)$$

The corresponding tangential and radial stresses in the inner plastic region are given by the equations

$$\sigma_\theta = 2 \tau_{yp} \ln \frac{r}{c} + \tau_{yp} \frac{b^2 + c^2}{b^2} \quad a \leq r \leq c \quad (B-20)$$

$$\sigma_r = 2 \tau_{yp} \ln \frac{r}{c} + \tau_{yp} \frac{c^2 - b^2}{b^2} \quad a \leq r \leq c \quad (B-21)$$

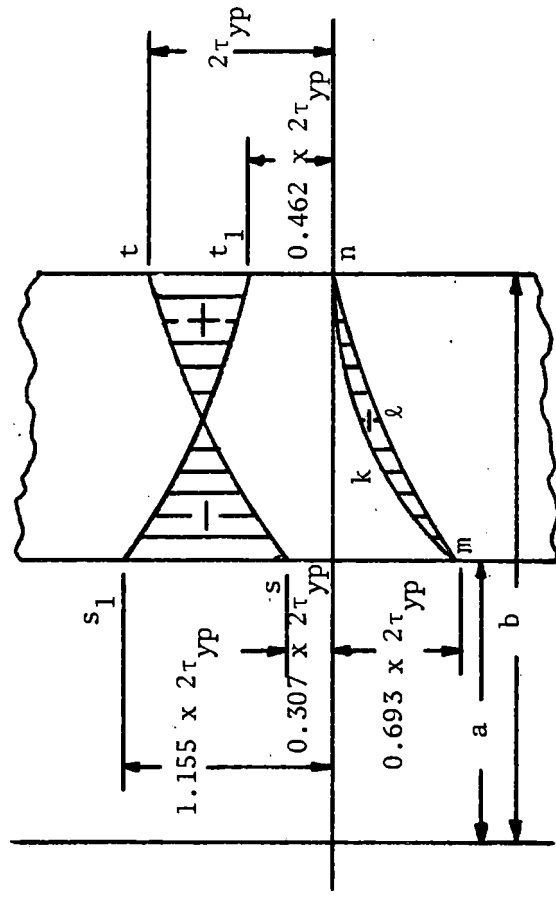


Fig. B-3. Stress distributions for autofrettage.

The tangential stress in the outer elastic portion can be determined by evaluating σ_r in equation (B-21) at the boundary between the elastic and plastic regions $r = c$, and treating the elastic portion as a vessel with inside radius c and outside radius b . The value of σ_r at $r = c$ is given by the equation

$$\sigma_r = -\tau_{yp} \frac{b^2 - c^2}{b^2} \quad (\text{B-22})$$

and the tangential and radial stresses in the elastic region are

$$\sigma_\theta = \frac{c^2}{b^2} \tau_{yp} \left(1 + \frac{b^2}{r^2}\right) \quad c \leq r \leq b \quad (\text{B-23})$$

$$\sigma_r = \frac{c^2}{b^2} \tau_{yp} \left(1 - \frac{b^2}{r^2}\right) \quad c \leq r \leq b \quad (\text{B-24})$$

The stresses to be subtracted upon release of the pressure p' can be calculated simply if the material follows Hooke's law during the release. The cylinder can be treated as two concentric cylinders with the boundary conditions

$$\left. \begin{array}{l} p_i = p' \\ p_o = \tau_{yp} \frac{(b^2 - c^2)}{b^2} \end{array} \right\} \begin{array}{l} \text{at } r = a \\ \text{at } r = c \end{array} \quad \left. \begin{array}{l} \\ \\ \end{array} \right\} \begin{array}{l} \text{inside} \\ \text{region} \end{array} \quad (\text{B-25})$$

$$\left. \begin{array}{l} p_i = \tau_{yp} \frac{(b^2 - c^2)}{b^2} \\ p_o = 0 \end{array} \right\} \begin{array}{l} \text{at } r = c \\ \text{at } r = b \end{array} \quad \left. \begin{array}{l} \\ \\ \end{array} \right\} \begin{array}{l} \text{inside} \\ \text{region} \end{array} \quad (\text{B-26})$$

being applied to equations (B-5) and (B-6). The residual stress will then be the difference between the stress at the initial pressurization to p' and the stress change during release of the pressure. Upon repressurization to pressure p' the material is assumed to behave elastically with the tangential and

radial stresses again being given by equations (B-20) and (B-21), and (B-23) and (B-24) for the inner and outer regions respectively.

APPENDIX B - II

TABULATION OF MATERIAL PROPERTIES

Table B2-1. Uniaxial Properties for Metals Having Strengths Greater than 250,000 psi.

Footnotes to Table B2-1

Table B2-2. Biaxial Stress Tests of Miniature Pressure Vessels, Source: Goodman (Ref. 137)

Table B2-3. Material Specifications for Biaxial Stress Tests

Table B2-4. Triaxial Strength Properties of Mild Steel, Source: Hu, et al. (Ref. 143)

Table B2-1 - Uniaxial Properties for Metals Having Strengths Greater than 250,000 psi.

MATERIAL	HEAT TREATMENT	DENSITY AT 20°C (68°F) lbs/cu in.	COEFFICIENT OF LINEAR THERMAL EXPANSION micro-in./in./°F	ROCKWELL HARDNESS NUMBER	BRINELL HARDNESS NUMBER	MODULUS OF ELASTICITY 10 ⁶ psi
9Ni-4Co-0.25C Steel	High Strength Steel (9Ni-4Co) Plate 1/2 to 1 in thick Normalized 1600F, 1 hr, air cooled, austenitized 1500F, 1 hr, quenched and tempered as indicated below Oil or water quenched Air quenched					
9Ni-4Co-0.45C Steel	Sheet up to 1/4 in thick Normalized (1600F, 1 hr), air cooled, austenitized (1475F, 1 hr) oil quenched and tempered as indicated below. Tempered at 400F (martensite) Tempered at 600F (martensite) Plate 1/4 to 1 in thick Tempered 400F (martensite) Tempered 600F (martensite) Normalized (1600F, 1 hr), air cooled, austenitized 1475F, 1 hr, salt (or other media) quenched at temperatures indicated below (4-8 hr), air cooled Quenched at 455F (bainite) Quenched at 475F (bainite) Quenched at 500F (bainite)					
9Ni-4Co-0.45C Steel	Forgings Normalized (1600F, 1 hr), air cooled, austenitized (1475F, 1 hr) oil quenched, tempered at temperatures indicated below Tempered at 400F (martensite) Tempered at 600F (martensite) Normalized 1600F, 1 hr, air cooled, austenitized (1475F, 1 hr) salt (or other media) quenched at temperatures indicated below Quenched at 475F (bainite) Quenched at 500F (bainite)					
9Ni-4Co-.25C Steel	Cold rolled sheet Austenitized at 1550F, oil quenched, pretempered at 300F, cold rolled 25% to 0.08 in thick sheet and retempered at temperature indicated below Retempered room temperature Retempered 300F Retempered 400F Retempered 500F Retempered 700F					

Table B2-1 (cont.) - Uniaxial Properties for Metals Having
Strengths Greater than 250,000 psi.

MATERIAL	ULTIMATE TENSILE STRENGTH ksi	YIELD STRENGTH* ksi	ELONGATION IN 2 in.** percent	ENDURANCE LIMIT ksi $\sqrt{\text{in.}}$	FRACTURE TOUGHNESS ksi	NOTCH TOUGHNESS ft. lbs. I = IZOD C = CHARPY C _V = CHARPY V-NOTCH	REFERENCE***
9Ni-4Co-0.25C Steel	300 260-270	165(a) 170(a)	12-14(b) 12-14(b)			C = 25 C _V = 34	ME Dec 66
							ME Dec 66
9Ni-4Co-0.45C Steel	280-300 240-260 280-310 240-260	245-260 (a) 220-230 (a) 245-260 (a) 220-230 (a)	10-12(d) 10-12(d) 6-8(d) 10-12(d)			50 65 50 65	C = 25
							C _V = 30
							C _V = 23
							C _V = 30
ME Dec 66							
9Ni-4Co-0.45C Steel	270-285 260-280 250-260	225-230 (a) 220-235 (a) 215-225 (a)	11-13(d) 12-14(d) 12-14(d)			70-90 75-100 85-110	C = 25
							C _V = 30
							C _V = 30
							C _V = 30
ME Dec 66							
9Ni-4Co-0.25C Steel	260-280 250-260	225-235 (a) 215-225 (a)	7-12(d) 7-13(d)			75-100 85-100	C = 25
							C _V = 25
							C _V = 25
							C _V = 25
ME Dec 66							
9Ni-4Co-.25C Steel	314 317 305 300 252	300 315 301 295 248	4 3.5 4 3.5 3.5			80 90 93 93	ME Dec 66
							ME Dec 66
							ME Dec 66
							ME Dec 66
							ME Dec 66

Table B2-1 (cont.) - Uniaxial Properties for Metals Having Strengths Greater than 250,000 psi.

MATERIAL	HEAT TREATMENT	DENSITY AT 20°C (68°F) lbs/cu in.	COEFFICIENT OF LINEAR THERMAL EXPANSION micro-in./in./°F	ROCKWELL HARDNESS NUMBER	BRINELL HARDNESS NUMBER	MODULUS OF ELASTICITY 10 ⁶ psi
Mar-Strained Alloy Steels						
300M D6AC	Austenitized 1650F, salt quenched, tempered 600F, retempered 400F Austenitized 1550F, salt quenched, tempered 600F, retempered 400F					
WCM-1 WCM-4	Austenitized 1650F, air quenched, tempered 600F, retempered 400F Austenitized 1650F, air quenched, tempered 600F, retempered 400F					
Mod. S-5 WHC	Austenitized 1650F, salt quenched, tempered 575F, retempered 400F Austenitized 1650F, air quenched, tempered 600F, retempered 400F					
HY-Tuf. Vascojet-1000	Austenitized 1600F, air quenched, tempered 550F, retempered 400F Austenitized 1850F, air quenched, tempered 1000F, retempered 800F					
AM 355 422	Austenitized 180F, air quenched, tempered 850F, retempered 700F Austenitized 1900F, air quenched, tempered 800F, retempered 750F					
Chromium-Nickel-Molybdenum Steels						
AISI 4340 " Ladish D6AV " 300-M	Tempered 400F Tempered 600F Bar 1.5-2 in dia, tempered 300F Tempered 600F Bar 1 in dia, tempered 200F				520 490	
300-M " USS Strux " "	Bar 1 in diam tempered, 600F Bar 1 in dia, tempered, 800F Forged bar 1 in dia, tempered 450F Tempered 550F Tempered 650F				525 425	
HS-260 " AMS 6434 Rocoloy 270 "	Tempered 400F Tempered 600F Sheet .109 in thick, tempered 400F Tempered 400F Tempered 700F			C54 C50 C58 C56		

Table B2-1 (cont.) - Uniaxial Properties for Metals Having Strengths Greater than 250,000 psi.

MATERIAL	ULTIMATE TENSILE STRENGTH ksi	YIELD STRENGTH* ksi	ELONGATION IN 2 in.** percent	ENDURANCE LIMIT ksi $\sqrt{\text{in.}}$	FRACTURE TOUGHNESS ksi	NOTCH TOUGHNESS ft. lbs. I = IZOD C = CHARPY C _v = CHARPY V NOTCH	REFERENCE***
Mar-Strained Alloy Steels							
300M		280					ME July 63
D6AC		277					ME July 63
WCM-1		340					ME July 63
WCM-4		306					ME July 63
Mod. S-5		328					ME July 63
WHC		318					ME July 63
HY-Tuf.		240					ME July 63
Vascojet-1000		276					ME July 63
AM 355		215					ME July 63
422		235					ME July 63
Chromium-Nickel-Molybdenum Steels							
AISI 4340	287	270(a)	11				ME Mar 63
"	255	235(a)	12				ME Mar 63
Ladish D6AV	299	211(a)	8.5				ME Mar 63
"	267	247(a)	8.1				ME Mar 63
300-M	340	180(a)	6				ME Mar 63
300-M	289	245(a)	9.5				ME Mar 63
"	260	215(a)	8.5				ME Mar 63
USS Strux							
"	291	243(a)	10				ME Mar 63
"	281	243(a)	11				ME Mar 63
"	265	253(a)	10				ME Mar 63
HS-260	290	253(a)	12				ME Mar 63
"	263	236(a)	8				ME Mar 63
AMS 6434							
"	266	218(a)	8				ME Mar 63
Rocoloy 270	332	240(a)	7				ME Mar 63
"	308	265(a)	5.3				ME Mar 63

Table B2-1 (cont.) - Uniaxial Properties for Metals Having Strengths Greater than 250,000 psi.

MATERIAL	HEAT TREATMENT	DENSITY AT 20°C (68°F) lbs/cu in.	COEFFICIENT OF LINEAR THERMAL EXPANSION micro-in./in./°F	ROCKWELL HARDNESS NUMBER	BRINELL HARDNESS NUMBER	MODULUS OF ELASTICITY 10 ⁶ psi
Chromium-Nickel-Molybdenum Steels (Cont.)						
Rocoloy 270 HP-9-4-25 HP-9-4-45 "	Tempered 1000F Tempered 400F Tempered 400F Tempered 600F			C52		
Nickel-Iron-Cobalt-Alloy						
8084 8087 8894 8895 8896	Forged 9/16 in bar Cold rolled 45% Cold rolled 45% Cold rolled Cold rolled Cold rolled					
Maraging Steels						
18 Ni Grade 250 18 Ni Grade 300 16-17.5 Ni Cast 18 Ni	Maraged Maraged Homogenize for 4 hr at 2100F and age 3 hr at 900F Cast Grade - Marage 900F			C52 C54		
20 Ni " " "	Refrigerate at -100F for 16 hr + marage 850F Refrigerate -100F for 16 hr + marage 850F cold work 50% Refrigerate at -100F for 16 hr + marage 900F Refrigerate at -100F for 16 hr + marage 900F, cold work 50%					
25 Ni " 25 Ni	Refrigerate -100F for 16 hr + marage 800F, cold work 25% Ausage at 1300F for 4 hr + refrigerate -100F for 16 hr + marage 850F Refrigerate -100F for 16 hr + marage 850F + cold work 50%					
18 Ni	Solution annealed for 1 hr at 1500F, air cooled and aged for 3 hr at the indicated temperatures 800F 850F 900F 950F 1000F			C52 C55 C58 C59 C58		

Table B2-1 (cont.) - Uniaxial Properties for Metals Having
Strengths Greater than 250,000 psi.

MATERIAL	ULTIMATE TENSILE STRENGTH ksi	YIELD STRENGTH* ksi	ELONGATION IN 2 in. ** percent	ENDURANCE LIMIT ksi	FRACTURE TOUGHNESS ksi $\sqrt{\text{in.}}$	NOTCH TOUGHNESS ft. lbs. I = IZOD C = CHARPY C _V = CHARPY V NOTCH	REFERENCE***
Hocoloy 270 HP-9-4-25 HP-9-4-45 "	266	232 (a)	7.3				ME Mar 63
	250	220 (a)	12				ME Mar 63
	290	250 (a)	7				ME Mar 63
	250	235 (a)	9				ME Mar 63
Chromium-Nickel-Molybdenum Steels (Cont.)							
8084 8087 8894 8895 8896	262	239	3(b)				ME Nov 65
	266.5	252	2(b)				ME Nov 65
	253	228	1.0(b)				ME Nov 65
	250	237	1.0(b)				ME Nov 65
	254	240	1.0(b)				ME Nov 65
Nickel-Iron-Cobalt Alloy							
18 Ni Grade 250 18 Ni Grade 300 16-17.5 Ni Cast 18 Ni	255	245	10				USS
	295	290	8				USS
	240-260	225-250	5-11 (b)			C _V -9-15	ME Jan 63
	240-260	225-250	5-11 (b)				ME Mar 63
Manganese Steels							
20 Ni	264	256	6(b)				ME Mar 63
"	273	264	4.2(b)				ME Mar 63
"	256	244	4.5 (b)				ME Mar 63
"	281	273	4(E)				ME Mar 63
25 Ni	268	254	4(b)				ME Mar 63
"	272	258	4.5 (b)				ME Mar 63
25 Ni	273	262	4(b)				ME Mar 63
18 Ni	276	256	5(d)				ME Feb 67
	310	294	7(d)				ME Feb 67
	340	350	8(d)				ME Feb 67
	363	356	10(d)				ME Feb 67
	350	350	11(d)				ME Feb 67

Table B2-1 (cont.) - Uniaxial Properties for Metals Having Strengths Greater than 250,000 psi.

MATERIAL	HEAT TREATMENT	DENSITY AT 20°C (68°F) lbs/cu in.	COEFFICIENT OF LINEAR THERMAL EXPANSION micro-in./in./°F	ROCKWELL HARDNESS NUMBER	BRINELL HARDNESS NUMBER	MODULUS OF ELASTICITY 10 ⁶ psi
Hot Work Die Steels						
5Cr-Mo-V Air craft quality	Tempered 1075F					
H-11	Tempered 1100F					
H-13	Tempered 950F					
	Tempered 1050F					
	Tempered 900F					
	Tempered 1000F					
Vascojet-1000 Potomac A, Dynaflex	Tempered 950F					
	Tempered 1050F					
Crucible 56	Tempered 1000F					
Unimach 1, Thermold A	Tempered 975F					
	Tempered 1050F					
Unimach 11, Thermold J	Tempered 975F					
	Tempered 1050F					
Vascojet-MA, CVM	Tempered 975F					
	Tempered 1025F					
	Tempered 1075F					
Vascojet-1000 5 Temper	Tempered 950F					
	Tempered 1050F					
Ultra High Strength Steels - Wrought						
Modified H-11		0.281	7.4			30
Mx-2		0.276	5.68			29.4
300-M			7.61			
D-6A		.283				30
4340	Austenitized at 1550F, oil quenched, tempered at 400F	.283	6.3			30
9Ni-4Co-0.30C	Austenitized at 1500-1550F, water or oil quenched, double tempered at 1000F	.283	6.2			28.6
Nickel and Nickel Alloys						
54Ni-39Cr-4Mo-2Ti-1 AL Alloy	Wrought					

Table B2-1 (cont.) - Uniaxial Properties for Metals Having
Strengths Greater than 250,000 psi.

MATERIAL	ULTIMATE TENSILE STRENGTH ksi	YIELD STRENGTH* ksi	ELONGATION IN 2 in.** percent	ENDURANCE LIMIT ksi	FRACTURE TOUGHNESS ksi $\sqrt{\text{in.}}$	NOTCH TOUGHNESS ft. lbs. I = IZOD C = CHARPY C _v = CHARPY V NOTCH	REFERENCE***
Hot Work Die Steels							
5Cr-Mo-V Air craft quality	260	205 (a)	8				ME Mar 63
	280	220 (a)	7				ME Mar 63
H-11	311	241 (a)	3.3				ME Mar 63
	268	226 (a)	8.5				ME Mar 63
H-13	290	228 (a)	3.5				ME Mar 63
	276	224 (a)	8				ME Mar 63
Vascojet-1000 Potomac A, Dynaflux	311	241 (a)	3.3				ME Mar 63
	268	226 (a)	8.5				ME Mar 63
Crucible 56	310	262 (a)	6				ME Mar 63
Unimach 1, Ther- mold A	304	255 (a)	5				ME Mar 63
	260	227 (a)	4.5				ME Mar 63
Unimach 11, Ther- mold J	310	268 (a)	3.8				ME Mar 63
	276	236 (a)	4.1				ME Mar 63
Vascojet-MA CVM	362	293 (a)	6				ME Mar 63
	346	292 (a)	7				ME Mar 63
	322	280 (a)	6.5				ME Mar 63
Vascojet-1000 5 Temper	325	270 (a)	5				ME Mar 63
	270	235 (a)	7				ME Mar 63
Ultra High Strength Steels - Wrought							
Modified H-11	295-311	241-247	6.6-12	130-135		C=15-22	ME Oct 67
Mx-2	279	239	10	110		C=18	ME Oct 67
300-M	289	242	10	116		C=22	ME Oct 67
D-6A	284	250	7.5	110		C=14	ME Oct 67
4340	287	270	11	107			ME Oct 67
9Ni-4Co-0.30C	220-260	190-210	10-16	110-120		C=15-30	ME Oct 67
Nickel and Nickel Alloys							
54Ni-39Cr-4Mo-2Ti- 1 AL Alloy	250	190 (a)					ME July 66

Table B2-1 (cont.) - Uniaxial Properties for Metals Having Strengths Greater than 250,000 psi.

MATERIAL	HEAT TREATMENT	DENSITY AT 20°C (68°F) lbs/cu in.	COEFFICIENT OF LINEAR THERMAL EXPANSION micro-in./in./°F	ROCKWELL HARDNESS NUMBER	BRINELL HARDNESS NUMBER	MODULUS OF ELASTICITY 10 ⁶ psi
Matreloy	Chromium and Chromium Alloys					
H-11 Steel	High Strength Low Alloy Steels 4 1/2" thick plate Tempered 400-500F Tempered 1000F Tempered 1050F					
AISI 4140 Mx-2 Air Steel X-200	Chromium-Molybdenum Steels Bar 1 in dia, tempered 400F Sheet, tempered 525F Sheet 0.60 in thick, tempered 400F Tempered 700F			C51 C55 C53	520	
316 440C 440F	Stainless Steels Cold drawn depending on size and amount of cold reduction Tempered at 600F Tempered at 600F			C57 C57	580 580	
302 440A 440B	Cold drawn depending on size and amount of cold reduction Tempered 600F Tempered 600F			C51 C55	510 555	
Vasco MA Steel H-11 Steel TBA-2	Ausformed Steels Ausforming vacuum melted steel and tempered at 1000F Ausformed Bearing race steel-ausformed			C65		

Table B2-1 (cont.) - Uniaxial Properties for Metals Having Strengths Greater than 250,000 psi.

MATERIAL	HEAT TREATMENT	DENSITY AT 20°C (68°F) lbs/cu in.	COEFFICIENT OF LINEAR THERMAL EXPANSION micro-in./in./°F	ROCKWELL HARDNESS NUMBER	BRINELL HARDNESS NUMBER	MODULUS OF ELASTICITY 10 ⁶ psi
MIL-S-46052(MR) Class 260-210	High Strength Steel Castings					
PH14-8Mo Custom 455 AFC-77	<p>Precipitation Hardening Stainless Steels</p> <p>Cold rolled, aged at 900F for 1 hr. Cold worked prior to aging Austenitized at 1800-2000F, air cooled or oil quenched to room temperature, refrigerated at -100F and double tempered (for 2 hr each) at either 900 or 1100F</p>					

Table B2-1, Footnotes

- * Yield Strength, ksi
0.2% offset, except values denoted by (a) for which offset is not specified in source.

- ** Percent Elongation
in 2 inches except values denoted by
 - (b) unspecified in source
 - (c) in 4 times the diameter
 - (d) in 1 inch

- ***Reference
 - MH-61 - Metals Handbook, Properties and Selection of Metals, Vol. 1, 8th Edition, American Society for Metals, Novelty, Ohio, 1961.
 - ME-Jan 67 etc, Materials Engineering, called Materials in Design Engineering prior to March 1967, Reinhold Publishing Co., New York.
 - USS - United States Steel Corporation Pamphlet, Maraging Steel, ADUSS-94034, no date.

Table B2-2 - Biaxial Stress Tests of Miniature Pressure Vessels.

Spec. Code	Stress Field a:c	Rockwell Hardness Number R _C	Nominal Ulti- mate Tensile Strength ksi	Nominal Yield Strength ksi
AISI 4340 Bar Stock Steel				
Tempered at 475°F				
A 2	2:1	49.6	291	250
A 9	2:1	----	290	253
A 12	1:2	50.2	277	244
A 4	1:2	50.8	277	250
A 10	1:2	50.8	270	245
A 8	1:1	49.8	261	223
A 11	1:1	49.3	264	223
A 7	1:0	49.4	263	225
A 5	0:1	49.9	258	223
Tempered at 700°F				
B 1	2:1	44.1	247	228
B 2	2:1	44.1	246	224
B 5	2:1	44.0	244	221
B 6	1:2	45.0	231	216
B 9	1:2	45.3	230	221
B 11	1:2	45.3	233	220
B 3	1:1	43.9	214	198
B 8	1:1	44.4	214	200
B 10	1:1	44.0	214	200
Tempered at 950°F				
C 2	2:1	37.1	188	184
C 11	2:1	37.0	185	175
C 9	1:2	38.1	185	180
C 7	1:2	36.3	185	172
C 6	1:1	36.6	171	161
C 12	1:1	37.2	170	161
C 1	1:0	36.1	178	163
C 3	1:0	35.9	175	161
C 10	0:1	37.0	169	158
Tempered at 550°F				
D 8	2:1	48.5	273	246
D 10	2:1	48.2	270	236
D 13	1:2	50.1	259	233
D 12	1:2	----	255	233
D 6	1:1	48.4	242	219
D 5	1:1	----	241	219
D 7	1:0	48.3	248	226
D 1	1:0	47.7	249	220
D 3	0:1	48.1	240	219
Tempered at 350°F				
E 2	2:1	53.1	281	257
E 14	2:1	53.1	312	250
E 11	2:1	54.1	314	260
E 4	1:2	53.7	282	257
E 8	1:2	----	---	245
E 12	1:2	53.1	298	250
E 3	1:1	53.8	276	225
E 5	1:1	53.9	248	230
E 9	1:1	54.2	280	225

Table B2-2 (cont.) - Biaxial Stress Tests of
Miniature Pressure Vessels.

Spec. Code	Stress Field a:c	Rockwell Hardness Number R _C	Nominal Ulti- mate Tensile Strength ksi	Nominal Yield Strength ksi
AISI 4340 Bar Stock Steel (Cont.)				
Tempered at 400°F				
F 2	2:1	52.3	308	258
F 8	2:1	52.4	310	250
F 5	1:2	53.0	279	257
F 13	1:2	53.1	295	256
F 9	1:1	51.9	272	226
F 4	1:1	53.1	270	225
F 17	1:0	52.5	285	224
F 7	0:1	52.2	266	230
Tempered at 625°F				
G 2	2:1	47.5	270	246
G 3	2:1	47.7	272	248
G 10	1:2	48.0	254	243
G 1	1:2	48.1	253	240
G 8	1:1	47.3	239	221
G 6	1:1	47.0	242	220
G 9	1:0	47.2	244	219
G 4	0:1	46.5	239	212
G 5	0:1	48.4	234	215
AISI 4340 Bar Stock - Dimensional Variations				
Tempered at 700°F				
XA 1	1:2	44.8	237	234
XA 6	1:2	42.7	232	230
XD 30	1:2	43.0	235	235
XD 9	1:2	44.7	240	230
AS 1	1:2	45.3	239	230
DS 1	1:2	46.3	239	---
XAS 1	1:2	44.7	235	229
XDS 1	1:2	45.2	235	---
AISI 4340 Bar Stock with Girth Uniweld				
Tempered at 800°F				
Z 1	2:1	43.3	229	221
Z 4	2:1	43.0	229	219
Z 2	1:2	43.0	223	216
Z 3	1:2	43.1	224	218
Z 5	1:1	41.7	202	193
Z 8	1:1	42.4	206	195
Z 7	1:0	----	205	195
Tempered at 675°F				
Y 3	2:1	47.5	271	157
Y 4	2:1	48.0	271	255
Y 2	1:2	47.9	247	---
Y 5	1:2	47.9	258	250

Table B2-2 (cont.) - Biaxial Stress Tests of
Miniature Pressure Vessels.

Spec. Code	Stress Field a:c	Rockwell Hardness Number R _C	Nominal Ulti- mate Tensile Strength ksi	Nominal Yield Strength ksi
AISI 4340 Bar Stock with Girth Uniweld (Cont.)				
Tempered at 675°F				
Y 1	1:1	47.1	239	226
Y 6	1:1	47.5	237	225
Y 10	1:0	----	241	225
Tempered at 400°F				
W 4	2:1	53.6	313	262
W 3	2:1	52.9	276	259
W 8	2:1	52.1	305.	262
W 1	1:2	53.0	268	258
W 2	1:2	53.1	287	258
W 7	1:2	52.8	289	260
W 5	1:1	----	227	---
W 6	1:1	53.5	278	241
W 11	1:1	52.9	270	243
W 95	1:2	53.7	261	255
W 105	1:2	53.2	294	253
AISI 4340 with RDCA Heat Treatment				
AOS 1	2:1	----	317	225
AOS 5	2:1	----	327	232
AOS 3	1:2	52.7	308	239
AOS 4	1:2	----	300	220
AOS 2	1:2	----	305	230
SB 16	2:1	----	315	235
SE 6	2:1	52.4	312	231
SB 13	1:2	53.9	287	225
SE 1	1:2	----	299	230
SB 4	1:1	52.8	277	225
Ladish D6A Steel				
Bar Stock Tempered at 1075°F				
A1 1075	2:1	41.8	223	211
B1 1075	2:1	42.4	232	213
B5 1075	2:1	42.5	225	207
A2 1075	1:2	42.4	218	204
B6 1075	1:2	43.1	219	202
Ladish D6AC Steel Extruded Forgings				
Tempered at 500°F				
J 4	2:1	50.8	298	265
J 8	2:1	50.9	302	270
J 3	1:2	50.7	291	263
J 6	1:2	50.8	295	265
J 5	1:1	50.8	265	235

Table B2-2 (cont.) - Biaxial Stress Tests of
Miniature Pressure Vessels.

Spec. Code	Stress Field a:c	Rockwell Hardness Number R _c	Nominal Ulti- mate Tensile Strength ksi	Nominal Yield Strength ksi
Ladish D6AC Steel Extruded Forgings (Cont.)				
Tempered at 500°F				
J 10	1:1	51.5	272	240
J 2	1:0	50.8	270	233
J 9	1:0	51.2	275	240
Tempered at 1000°F				
K 10	2:1	44.7	238	223
K 13	2:1	44.5	232	220
K 1	1:2	44.6	239	225
K 9	1:2	43.6	232	221
K 12	1:2	44.1	232	219
K 7	1:2	45.0	238	224
K 6	1:0	45.2	219	202
K 8	1:1	44.5	213	198
K 3	1:0	46.1	218	200
K 5	1:0	----	220	201
Tempered at 400°F				
L 1	2:1	52.4	319	275
L 2	2:1	52.7	320	275
L 7	2:1	53.1	319	273
L 3	1:2	51.7	302	270
L 5	1:2	52.4	300	271
L 12	1:2	52.6	306	266
L 4	1:1	52.5	286	244
L 8	1:1	52.1	284	240
L 13	1:1	52.9	285	238
L 11	1:0	52.6	285	241
Tempered at 1075°F				
M 1	2:1	44.1	238	224
M 3	2:1	43.7	240	224
M 5	2:1	43.8	238	226
M 12	2:1	43.9	237	223
M 2	1:2	43.7	232	219
M 4	1:2	43.7	228	216
M 8	1:2	44.6	229	194
M 6	1:2	44.3	219	195
M 7	1:1	43.9	216	202
M 10	1:1	44.6	216	201
M 9	1:0	45.5	217	201
M 11	0:1	43.4	213	201
Tempered twice at 1075°F				
N 6	2:1	42.7	220	205
N 5	2:1	43.2	230	214
N 3	1:2	43.2	227	215
N 8	1:2	43.7	225	208
N 2	1:1	42.3	200	185
N 11	1:0	42.1	205	187
N 9	1:0	----	205	180

Table B2-2 (cont.) - Biaxial Stress Tests of
Miniature Pressure Vessels.

Spec. Code	Stress Field a:c	Rockwell Hardness Number R _c	Nominal Ulti- mate Tensile Strength ksi	Nominal Yield Strength ksi
Ladish D6AC Steel Extruded Forgings (Cont.)				
Tempered at 300°F				
P 10	2:1	56.5	351	218
P 12	2:1	56.8	357	222
P 5	1:2	56.4	335	228
P 11	1:2	57.4	343	225
P 8	1:1	56.0	315	199
P 9	1:1	57.4	317	200
P 1	1:2	----	327	281
P 6	1:0	57.0	320	210
P 7	1:0	56.8	317	199
Tempered at 800°F				
Q 1	2:1	49.1	269	245
Q 7	2:1	47.5	267	241
Q 3	1:2	48.2	261	241
Q 4	1:2	48.3	260	245
Q 5	1:1	48.1	239	220
Q 6	1:1	47.6	236	216
Q 2	1:0	47.7	244	220
Q 8	1:0	47.5	245	221
Tempered at 600°F				
R 6	2:1	49.3	285	257
R 8	2:1	50.5	285	260
R 13	2:1	49.5	282	260
R 3	1:2	50.0	272	252
R 5	1:2	49.9	279	255
R 11	1:2	49.9	280	255
R 1	1:1	49.0	260	233
R 2	1:1	49.9	255	230
R 7	1:1	50.6	256	227
R 9	1:0	49.4	261	235
Marquenched - Tempered at 400°F				
S 1	2:1	51.5	301	250
S 7	2:1	53.0	320	269
S 8	1:2	53.3	311	269
S 12	1:2	53.1	304	264
S 3	1:1	52.3	273	220
S 4	1:1	52.4	277	225
S 10	1:0	52.9	285	230
7178 Aluminum Extruded Bar-Heat Treated to T6 Condition				
U 2	2:1	----	104	98
U 4	2:1	----	104	96
U 1	1:2	----	84	80
U 10	1:2	----	81	80
U 5	1:1	----	83	77/81
U 14	1:1	----	83	77/82
U 7	1:0	----	106	97

Table B2-2 (cont.) - Biaxial Stress Tests of
Miniature Pressure Vessels.

Spec. Code	Stress Field a:c	Rockwell Hardness Number R	Nominal Ulti- mate Tensile Strength ksi	Nominal Yield Strength ksi
7178 Aluminum Extruded Bar-Heat Treated to T6 Condition				
U 6	1:0	----	106	97
U 3	0:1	----	82	78
6 Al - 4V Titanium Bar Stock				
V 1	2:1	----	202	186
V 2	2:1	----	197	177
V 7	2:1	----	202	184
V 5	2:1	----	179	---
V 3	1:2	----	180	169
V 4	1:2	----	175	169
V 6	1:2	----	176	175
V 8	1:1	----	177	160
6 Al - 4V Extruded Forgings Medium Oxygen Content				
T 2	2:1	----	196	181
T 3	2:1	----	190	180
T 1	1:2	----	189	185
T 6	1:2	----	193	188
T 10	1:2	----	175	157
T 11	1:2	----	148	---
T 7	1:1	----	72	---
T 8	1:1	----	184	164
T 4	1:0	----	180	171
T 5	1:0	----	177	166
T 9	0:1	----	175	160
Low Oxygen Content				
AA 3	2:1	----	187	167
AA 4	2:1	----	179	163
AA 11	1:2	----	189	179
AA 12	1:2	----	190	179
AA 5	1:1	----	175	157
AA 6	1:1	----	170	151
AA 2	1:0	----	171	157
AA 1	0:1	----	173	160
AA 10	0:1	----	171	160

Table B2-3 - Material Specifications for
Biaxial Stress Tests.

Identification Code	Material	Heat Treatment
A B C D E F G XA, XD SB, SE (AOS) W Y Z	AISI 4340 Steel AISI 4340 Steel AISI 4340 Steel AISI 4340 Steel AISI 4340 Steel	Normalized at 1625F for 10 min, air cooled, austenitized at 1525F for 10 min, oil quenched, tempered for 4 hr. SAME AS ABOVE Special heat treatment by the Research Development Corp. of America, Gardena, Calif. SAME AS ABOVE Normalized at 1625F, hardened at 1500F, oil quenched, tempered.
J K L M N P Q R S A-1075 B-1075 U V	Ladish D6AC Steel Ladish D6A Steel Ladish D6A Steel 7178 Aluminum 6Al-4V Aluminum	Normalized at 1650F for 45 min, air cooled, austenitized at 1550F for 45 min, fan air quenched, tempered 4 hr, air cooled. SAME AS ABOVE Tempered at 1075F T-6 condition, solution 30 min at 870F, aged 24 hr at 250F. Solution treated 30 min at 1750F, cold water quenched, aged 4 hr at 1000F.
T AA	6Al-4V Aluminum	Solution treated 20 min at 1725F, cold water quenched, aged 4 hr at 1000F. SAME AS ABOVE

NOTES:

1. Stress Field
Nominal axial to circumferential stress field. 1:0 is uniaxial tension, 1:2 is internal pressure only, 0:1 is hoop tension only.
2. Nominal Ultimate Stress
Calculated from measured maximum load and pressure and original dimensions of the vessel.
3. Nominal Yield Stress
Equivalent offset yield strain in biaxial stress fields corresponding to 0.2 percent in uniaxial tension
= 0.20 percent for 1:0 and 0:1 stress fields
= 0.173 percent for 1:2 stress fields
= 0.10 percent for 1:1 stress field
4. Hardness of Wall
Rockwell "C" Hardness of wall vessel measured on button cut from wall.

Table B2-4 - Triaxial Strength Properties
of Mild Steel.

Specimen No.	Pressure ksi	Prestress ** ksi	Yield Stress* ksi	Nominal Ultimate** Strength ksi
Test Results of Series 1				
4	10	none	42.21	57.4
6	20	none	41.94	56.9
13	30	none	42.65	57.0
17	40	none	40.57	56.9
35	40	none	43.98	56.97
18	50	none	43.17	59.5
Test Results of Series 2				
14	10	46.8	48.87	57.3
20	20	47.1	48.24	58.0
21	30	47.1	46.93	57.8
34	30	47.87	48.6	57.27
22	40	46.8	47.66	57.1
15	50	47.06	47.06	57.3
Test Results of Series 3				
29	5	51.3	54.66	57.16
27	10	51.97	54.46	57.12
30	15	52.11	55	57.32
5	20	52.0	52.63	57.3
36	20	51.77	54.51	57.57
31	25	51.77	55.43	57.26
8	30	52.00	52.1	57.6
32	35	52.38	52.91	57.3
16	40	52.0	54.07	56.6
28	40	51.83	54.45	57.02
19	50	52.31	53.1	57.07

NOTES:

Specimens were made of a mild steel which came as commercially hot-rolled round stock of 3/4" diameter.

In the second series of tests specimens were prestressed in tension at about 8200 psi above the lower yield point.

In the third series of tests specimens were prestressed in tension at about 12,600 psi above the lower yield point.

*Strain rate about 1×10^{-2} in/in/sec, lower yield stress for test results of series 1.

**Strain rate about 6.7×10^{-4} in/in/sec.

APPENDIX C

Shock Waves - Water Cannon

Cooley (Ref. 31) has given a method of solution of shock wave propagation for the water and piston in a water cannon. The basic equations and method of solution are similar to those used in light gas guns. (See also APPENDIX A).

Piston-Water Impact (Ref. 31)

The geometry is cylindrical and concerns the impact of a steel piston on a stationary mass of water confined in a heavy finite cylinder with an orifice in the closed end. The piston is a single cylinder with or without a plunger attached (Fig. C-1). The problem is to determine the stresses, waves, and mass velocities of the piston and water, and the history of the jet.

Impact disturbances are both multiply-reflected shock and sound waves in the water and the piston, which alter velocities and pressures and affect the jet as it issues from the orifice. After impact the velocity of the piston decreases as the water is accelerated, and in some cases rebound occurs.

Equations

The necessary equations for definition of piston behavior are:

(1) Continuity:

$$\frac{\partial \rho u}{\partial x} + \frac{\partial \rho}{\partial t} = 0 \quad (C-1)$$

(2) Momentum:

$$\frac{du}{dt} - \frac{1}{\rho} \frac{\partial p}{\partial x} = 0 \quad (C-2)$$

(3) Equation of State:
(elastic deformation)

$$\sigma = E \left[\frac{\rho_0}{\rho} - 1 \right] \quad (C-3)$$

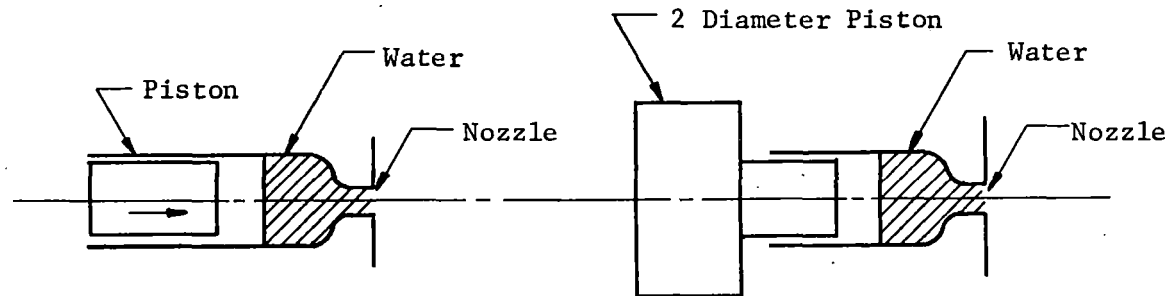


Fig. C-1. Piston without and with enlargement. (Cooley).

which may be combined to yield the characteristic equations:

$$\frac{\partial}{\partial t} \left(u - \frac{\sigma}{\rho_o c_o} \right) + (u+c) \frac{\partial}{\partial x} \left(u - \frac{\sigma}{\rho_o c_o} \right) = 0 \quad (C-4)$$

$$\frac{\partial}{\partial t} \left(u + \frac{\sigma}{\rho_o c_o} \right) + (u-c) \frac{\partial}{\partial x} \left(u - \frac{\sigma}{\rho_o c_o} \right) = 0 \quad (C-5)$$

These equations require that the quantity $\left(u - \frac{\sigma}{\rho_o c_o} \right)$ along lines whose slope is $\frac{dx}{dt} = u+c$, and that the quantity $\left(u + \frac{\sigma}{\rho_o c_o} \right)$ along lines of slope $\frac{dx}{dt} = u-c$ should be constant. Where a cylinder and a plunger of different diameters are used the force at their juncture is common, i.e.,

$$\sigma_1 A_1 = \sigma_2 A_2 \quad (C-6)$$

where the σ 's and the A's are stresses and cross-sectional areas, respectively.

For the water the equations are similar to those for the steel piston:

(1) Continuity:

$$\frac{\partial \rho u}{\partial x} + \frac{\partial \rho}{\partial t} = 0 \quad (C-7)$$

(2) Momentum:

$$\frac{du}{dt} + \frac{1}{\rho} \frac{\partial \rho}{\partial x} = 0 \quad (C-8)$$

(3) Equation of State:

$$\frac{p + 3000}{3001} = \left(\frac{\rho}{\rho_o} \right)^7 \quad (C-9)$$

where p is in atmospheres (Ref. 146).

Again these equations may be combined to yield the required characteristic equations:

$$\frac{\partial}{\partial t} (u+R) + (u+c) \frac{\partial}{\partial x} (u+R) = 0 \quad (C-10)$$

$$\frac{\partial}{\partial t} (u-R) + (u-c) \frac{\partial}{\partial x} (u-R) = 0 \quad (C-11)$$

where \underline{R} is defined as

$$\int dR = \int \frac{dp}{\rho c} \quad (C-12)$$

and the same conditions apply as in the case of characteristic equations for the piston.

The requisite boundary conditions are:

$$\sigma_o = 0 \quad (C-13)$$

where σ_o = stress on free end of piston

$$\sigma_2 A_2 = p_w \quad (C-14)$$

and where σ_2 = stress in piston at water surface,

$$(C-15)$$

A_2 = area of piston at water surface.

For the orifice of the nozzle, continuity requires that

$$\rho_w u_w A_n = \rho_j u_j A_j \quad (C-16)$$

where

ρ_w = density of water

ρ_j = density of jet

u_w = velocity of water

u_j = velocity of jet

A_n = area of nozzle

A_j = area of jet

$$(C-17)$$

For initial conditions for a specified piston geometry and orifice size, the initial velocity of the piston is required for computation by numerical methods. (See also Light Gas Gun equations). The sketch (Fig. C-2) indicates the complexity of the possible shock wave pattern for multiple reflection.

When the piston is of constant length and is long relative to the water volume, the numerical solution is simplified. The characteristic equations for the piston reduce to

$$u + \frac{\sigma}{\rho_o c_o} = v_o \quad (C-18)$$

where v_o is the initial velocity. As a first approximation the piston is considered to be a rigid mass. Hence, the equation of motion for the piston is

$$M \frac{du}{dt} = - pA \quad (C-19)$$

where p is the water pressure at the piston water interface.

The pressure in the water may be expressed in terms of the Reimann function R

$$p = \rho_o R (a+bR) \quad (C-20)$$

where

$$R = \int_{p = 1 \text{ atm}}^p \frac{dp}{\rho c} \quad (C-21)$$

The letters a and b represent constants, $a = 4800$ ft/sec, and $b = 2$.

Thus, R may be calculated from the assumed equation of state for water

$$\frac{p + 3000}{3001} = \left(\frac{\rho}{\rho_o} \right)^7 \quad (C-22)$$

as

$$R = \frac{c}{3} - \frac{c_o}{3} \quad (C-23)$$

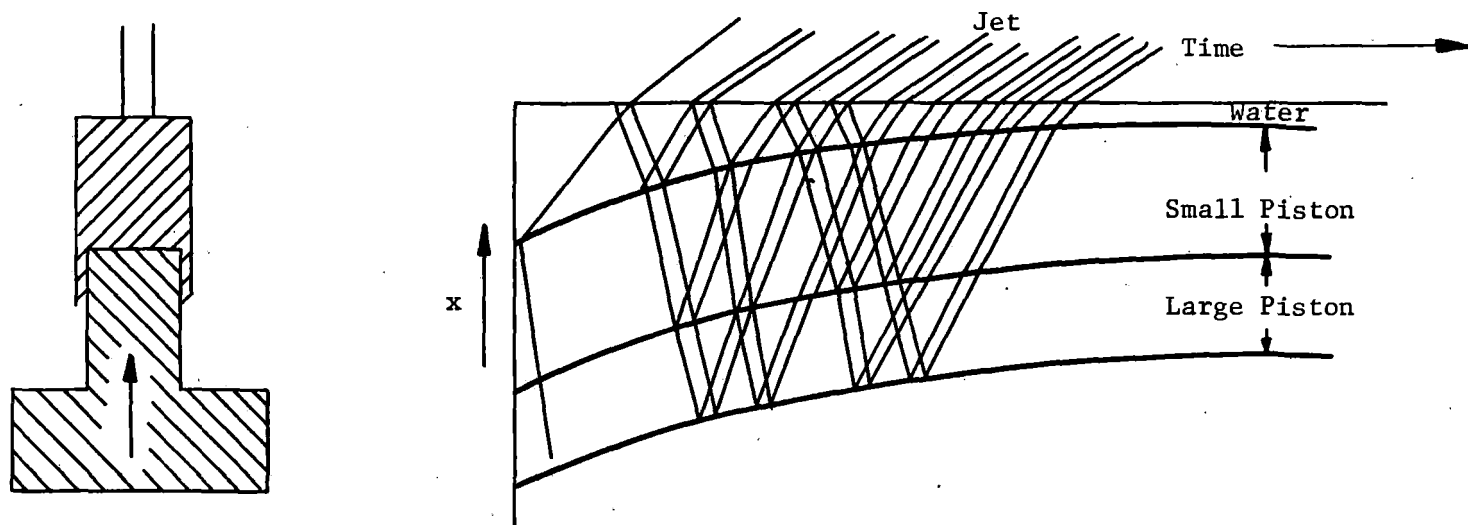


Fig. C-2. Reflection of shock waves in water and piston. (Cooley).

where c = speed of sound in the water at pressure p .

c_o = speed of sound in the water at 1 atm (4800 ft/sec)

For a given $(u-c)$ pulse in the water (illustrated by Regions 4 and 5 in Figure C-3)

$$(u-R)_5 = (u-R)_4 = K_4 \quad (C-24)$$

where K_4 and R_4 are assumed to be known quantities.

Thus, from equations C-21 and C-24 one obtains

$$p = \rho_o (u-K_4) [a+b(u-K_4)] \quad (C-25)$$

$$M \frac{du}{dt} = -A\rho_o (u-K_4) [a+b(u-K_4)] \quad (C-26)$$

Integration of equation (C-26) yields the velocity u_B .

$$u_B = \frac{a}{\left[\frac{a}{u_A - K_4} + b \right] \frac{aA\rho_o (t_B - t_A)}{M} - b} + K_4 \quad (C-27)$$

All of the quantities on the right side of equation C-27 are known except t_B , which may be found as follows.

The average velocity in Region 5 is given

$$\begin{aligned} \bar{u}_5 &= \frac{A \int_A^B u dt}{t_B - t_A} \\ &= K_4 + \left[-\frac{a}{b} + \frac{M}{A\rho_o b(t_B - t_A)} \ln \frac{u_A - K_4}{u_B - K_4} \right] \end{aligned} \quad (C-28)$$

where t_B is still unknown. An iterative procedure is utilized to obtain its correct value. From equation C-24 an average value of R_5 is calculated:

$$\bar{R}_5 = \bar{u}_5 - K_4 \quad (C-29)$$

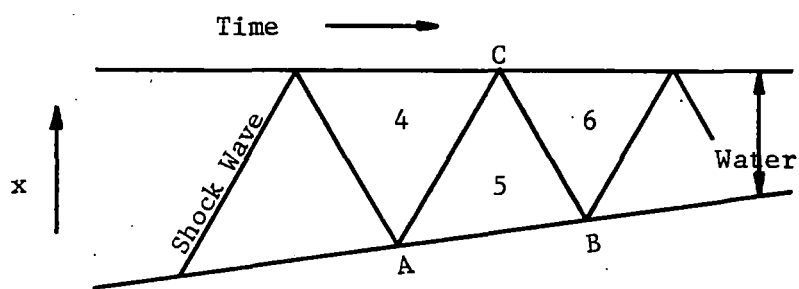


Fig. C-3. Shock wave reflection in water. (Cooley).

Continuing from Region 5 to Region 6

$$\bar{u}_6 + \bar{R}_6 = \bar{u}_5 + \bar{R}_5 = H_6 + c_o/3 \quad (C-30)$$

The point C is found from the slope of the line AC.

If $(u+c)_4 > (u+c)_5$ then the slope is taken to be

$$1/2 \left[(u+c)_4 + (u+c)_5 \right] \quad (C-31)$$

If $(u+c)_4 < (u+c)_5$ then the slope is taken to be $(u+c)_5$.

The point C may then be found from

$$\frac{x_C - x_A}{t_C - t_A} = \text{slope of A-C} \quad (C-32)$$

At the orifice the energy and continuity equation are combined with the equation of state

$$M_{Exit}^2 = 1/3 \left\{ \frac{1+3M_6^2}{\left[(1+3M_6) \frac{c_o}{3H_6} \right]^2} - 1 \right\} \quad (C-33)$$

$$M_6 = \frac{M_{Exit}}{A_6/A_{Exit}} \left[\frac{c_o (1+3M_6)}{3H_6} \right]^{4/3} \quad (C-34)$$

where M is the Mach number and the velocity of the sound at the exit is C_o .

From equations C-33 and C-34 the two unknowns M_6 and M_{Exit} may be obtained and

$$u_{Exit} = M_{Exit} c_o \quad (C-35)$$

$$\bar{u}_6 = u_{Exit} \frac{M_6}{M_{Exit}} \sqrt{\frac{1 + 3 M_{Exit}^2}{1 + 3 M_6^2}} \quad (C-36)$$

$$\bar{c}_6 = c_o \sqrt{\frac{1 + 3 M_{Exit}^2}{1 + 3 M_6^2}} \quad (C-37)$$

$$p_6 = 3000 \left[\left(\frac{1 + 3 M_{Exit}^2}{1 + 3 M_6^2} \right)^{7/6} - 1 \right] \quad (C-38)$$

From C-37, C-23, C-36 and C-30 \bar{R}_6 and \bar{u}_6 are calculated. The slope of the line CB is then determined. If $(u_5 - C_5) < (u_6 - C_6)$ the slope is taken to be

$$1/2 \left[(u_5 - c_5) + (u_6 - c_6) \right] \quad (C-39)$$

If $(u_5 - C_5) > (u_6 - C_6)$ then the slope is taken as being equal to $(u_6 - C_6)$. Point B is found from

$$\text{slope } C - B = \frac{X_B - X_C}{t_B - t_C} \quad (C-40)$$

$$\text{slope } A - B = \bar{u}_5 = \frac{X_B - X_C}{t_B - t_C} \quad (C-41)$$

The values of t_B and X_B are calculated and iterated with equation C-27. The procedure is repeated until the values of u_B converge.

Piston-Water Impact with Air

When a volume of air is enclosed with the water the behavior of both masses (Fig. C-4) must be determined. The orifice is closed until a pressure p_z is reached and then it is opened. At the initial movement of the piston shock waves are generated and reflected in the air and water and a stress (elastic) wave in the piston, the latter traveling at the speed of sound. The piston decelerates after impact, and may rebound. Air and water are initially accelerated, and the increased pressure forces a jet of water through the orifice at increasing velocities.

Equations

The basic equations for the piston are similar to those for the case without air including the characteristic equations:

(1) Continuity:

$$\frac{\partial \rho u}{\partial x} = \frac{\partial \rho}{\partial t} = 0 \quad (C-42)$$

(2) Momentum:

$$\frac{du}{dt} - \frac{1}{\rho} \frac{\partial \sigma}{\partial x} = 0 \quad (C-43)$$

(3) Equation of State:
(Elastic)

$$\sigma = E(\rho_o/\rho - 1) \quad (C-44)$$

The characteristic equations become:

$$\frac{\partial}{\partial t} \left(u - \frac{\sigma}{\rho_o c_o} \right) + (u+c) \frac{\partial}{\partial x} \left(u - \frac{\sigma}{\rho_o c_o} \right) = 0 \quad (C-45)$$

$$\frac{\partial}{\partial t} \left(u + \frac{\sigma}{\rho_o c_o} \right) + (u-c) \frac{\partial}{\partial x} \left(u + \frac{\sigma}{\rho_o c_o} \right) = 0 \quad (C-46)$$

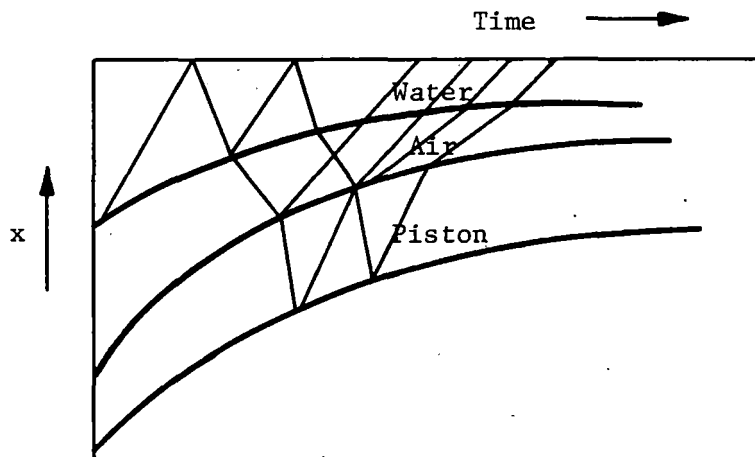


Fig. C-4. Shock waves in a piston-water-air system. (Cooley).

Equations for the shock waves in air are:

(1) Continuity:

$$\frac{\partial \rho u}{\partial x} + \frac{\partial \rho}{\partial t} = 0 \quad (C-47)$$

(2) Momentum:

$$\frac{du}{dt} + \frac{1}{\rho} \frac{\partial p}{\partial x} = 0 \quad (C-48)$$

(3) Isentrope Equation of State:

$$\frac{p}{p_0} = \left(\frac{\rho}{\rho_0} \right)^\gamma \quad (C-49)$$

As in the case of steel the equations are utilized to obtain characteristic equations:

$$\frac{\partial}{\partial t} \left[u + \frac{2c}{\gamma-1} \right] + (u+c) \frac{\partial}{\partial x} \left[u + \frac{2c}{\gamma-1} \right] = 0 \quad (C-50)$$

$$\frac{\partial}{\partial t} \left[u - \frac{2c}{\gamma-1} \right] + (u-c) \frac{\partial}{\partial x} \left[u - \frac{2c}{\gamma-1} \right] = 0 \quad (C-51)$$

These equations require that the quantity $[u+2c/(\gamma-1)]$ remain constant along the curves $dx/dt = u-c$. The usual equations for the conservation of mass, momentum and energy apply to the shock waves, as well as the equation of state for gases:

(1) Continuity:

$$\rho_1 u_1 = \rho_2 u_2 \quad (C-52)$$

(2) Momentum:

$$p_1 + \rho_1 u_1^2 = p_2 + \rho_2 u_2^2 \quad (\text{C-53})$$

(3) Energy:

$$h_1 + u_1^2/2 = h_2 + u_2^2/2 \quad (\text{C-54})$$

(4) Equation of State:
(for an ideal gas)

$$h = \gamma p / (\gamma - 1) \rho \quad (\text{C-55})$$

The equations for the water are the same as for the piston-water case.

Boundary conditions are as follows:

1) $\sigma_o = 0$

σ_o = stress on free end of piston

2) $\sigma_1 = p_a$

σ_1 = stress in piston at water-piston interface

p_a = pressure in water at water-piston interface

3) $v_p = v_a$

v_p = piston velocity at interface

v_a = air velocity at interface

4) $p_a = p_w$

p_a = pressure of air at air-water interface

p_w = pressure of water at air-water interface

5) $v_{a1} = v_w$

v_{a1} = velocity of air at air-water interface

v_w = velocity of water at air-water interface

6) Orifice conditions are quasi-steady state:

$$\text{Continuity: } \rho_w u_w A_c = \rho_j u_j A_j$$

ρ = density of water or jet

u = velocity of water or jet

A = cross-sectional area of water or jet

Initial conditions must specify:

- 1) Geometry of piston orifice, air and water, including lengths and/or diameters
- 2) Initial pressure of air
- 3) Pressure of water at initial ejection
- 4) Initial piston velocity

The above equations are normally solved by numerical computer methods. For a piston long relative to the water the characteristic equation for the piston again becomes:

$$u + \frac{\sigma}{\rho_o c_o} = v_o \quad (C-56)$$

where v_o is the initial velocity of the piston.

Certain approximations are used to simplify calculations. The air column is small and it is assumed to be all at the same conditions of pressure, velocity, etc., as well as obeying the isentropic law in view of the fact that the shocks are relatively weak:

$$pQ^\gamma = p_o Q_o^\gamma \quad (C-57)$$

where Q_o and Q are initial and varying air column lengths.

For a rigid mass piston, the equation of motion is

$$- M \frac{du}{dt} = pA \quad (C-58)$$

where p is the pressure at the piston-air interface.

The water pressure is expressed in terms of the Riemann function R as before for the same equation of state. This parameter R is then found in terms of the pressure to be:

$$R = \frac{a}{2b} \left[\sqrt{1 + 4pb/\rho_o a^2} - 1 \right] \quad (C-59)$$

By means of a system of iteration similar to the case without air the values of velocity and other parameters may be calculated.

Figures C-5 to C-16 show the relationships which exist between various water cannon parameters for assumed values as shown.

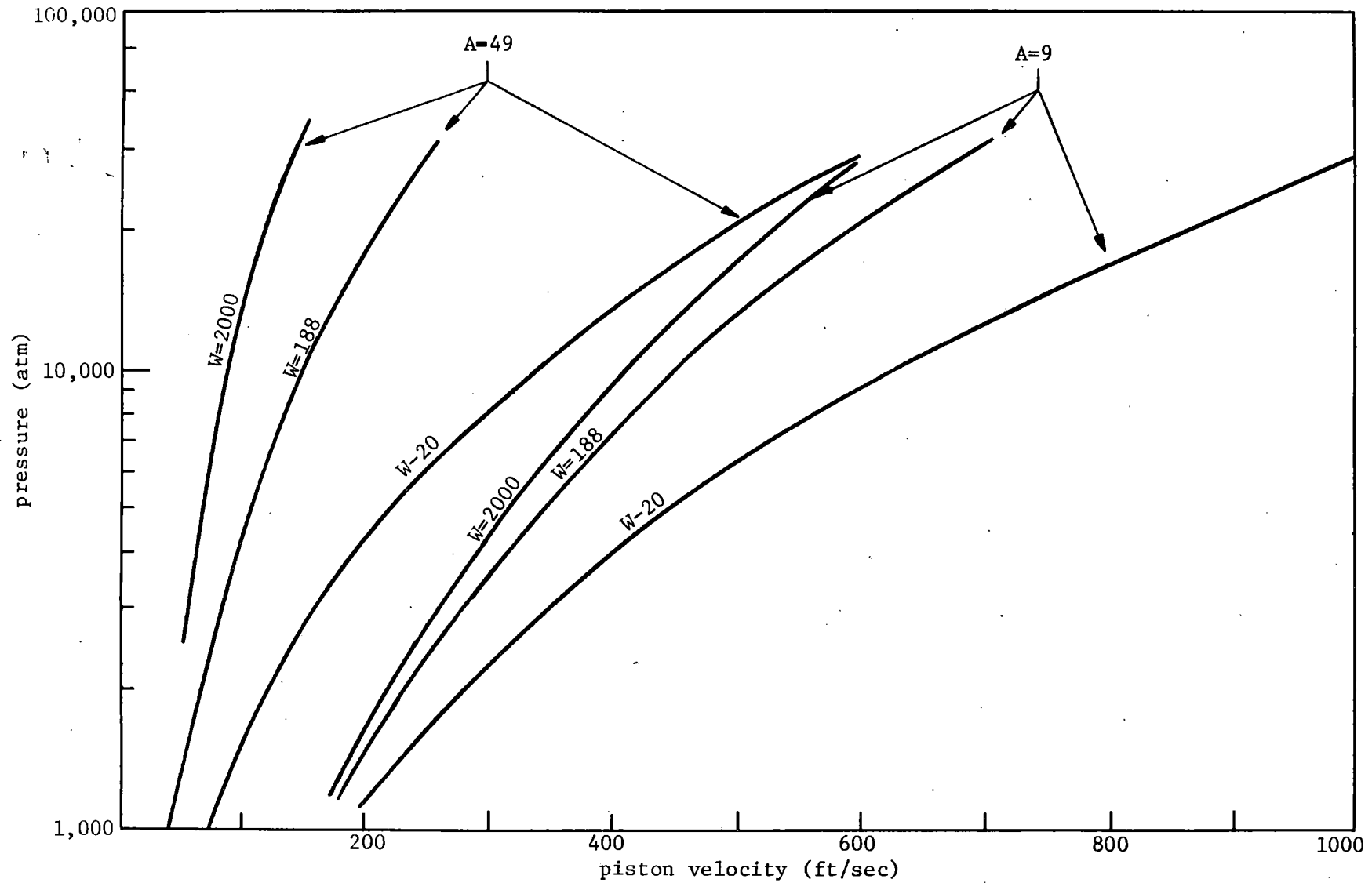


Fig. C-5. Pressure vs. piston velocity for various weight and area ratios. (Cooley).

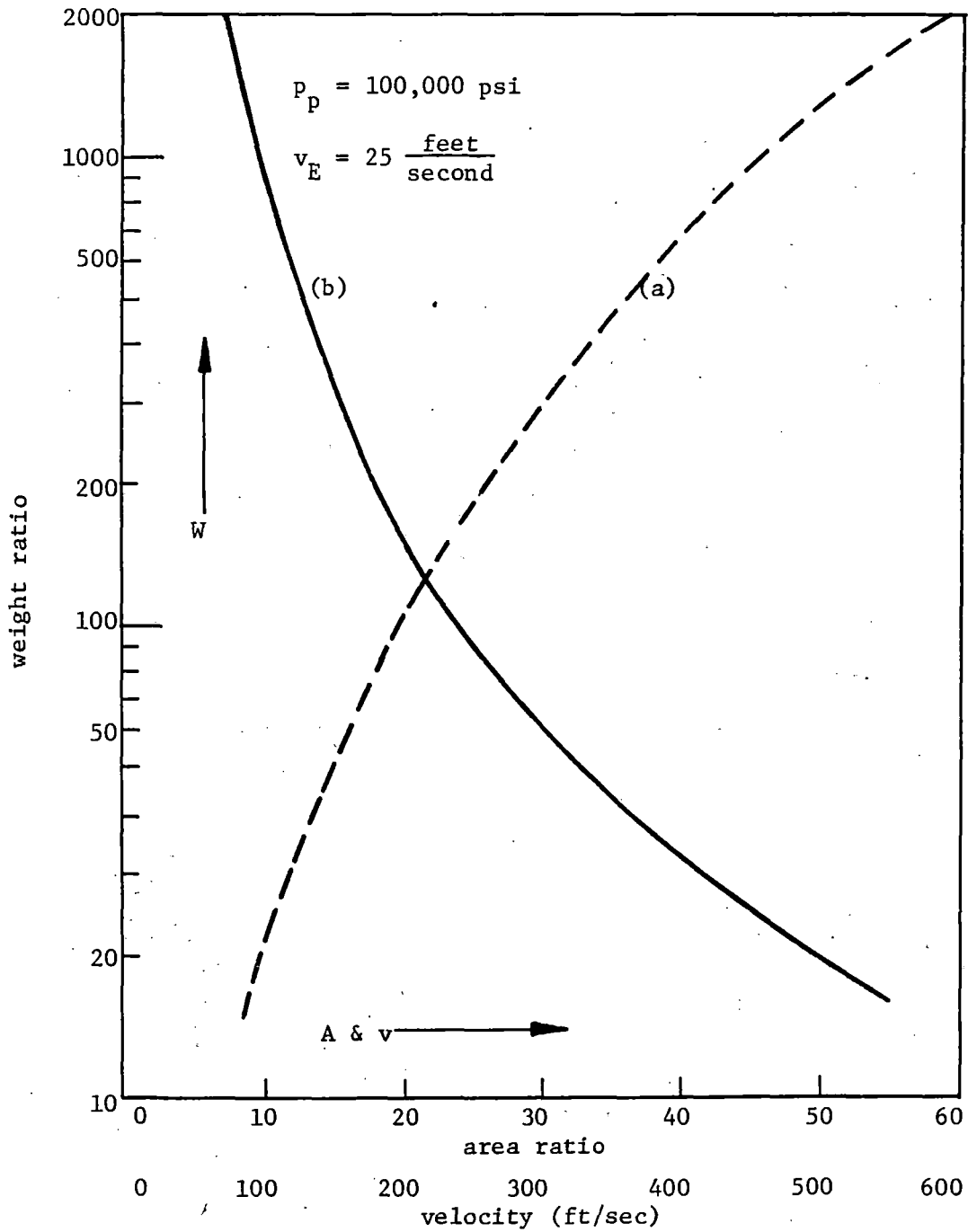


Fig. C-6. (a) Weight ratio vs. area ratio, and (b) weight ratio vs. piston velocity. (Cooley).

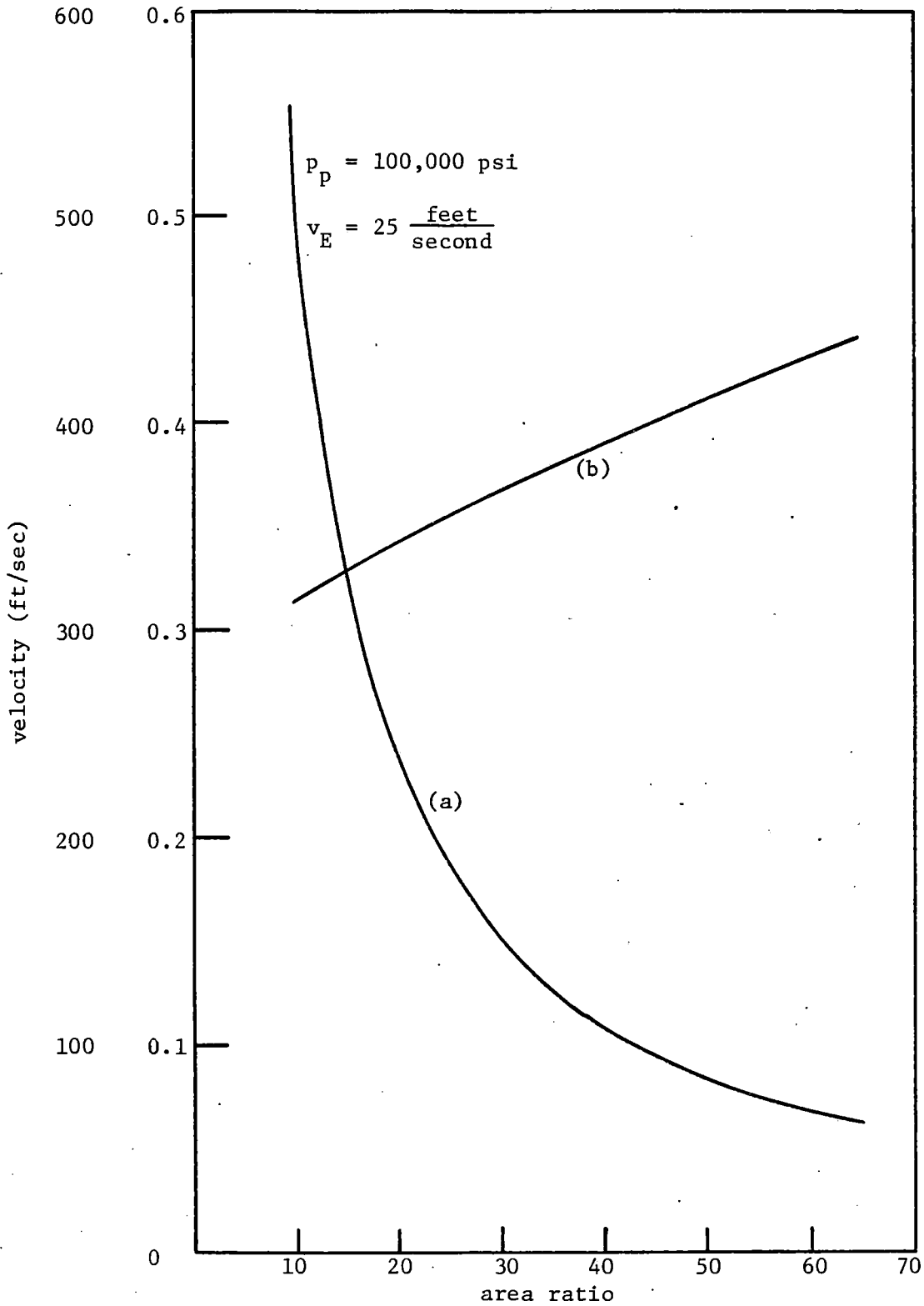


Fig. C-7. (a) Piston velocity and (b) piston position at maximum pressure vs. area ratio. (Cooley).

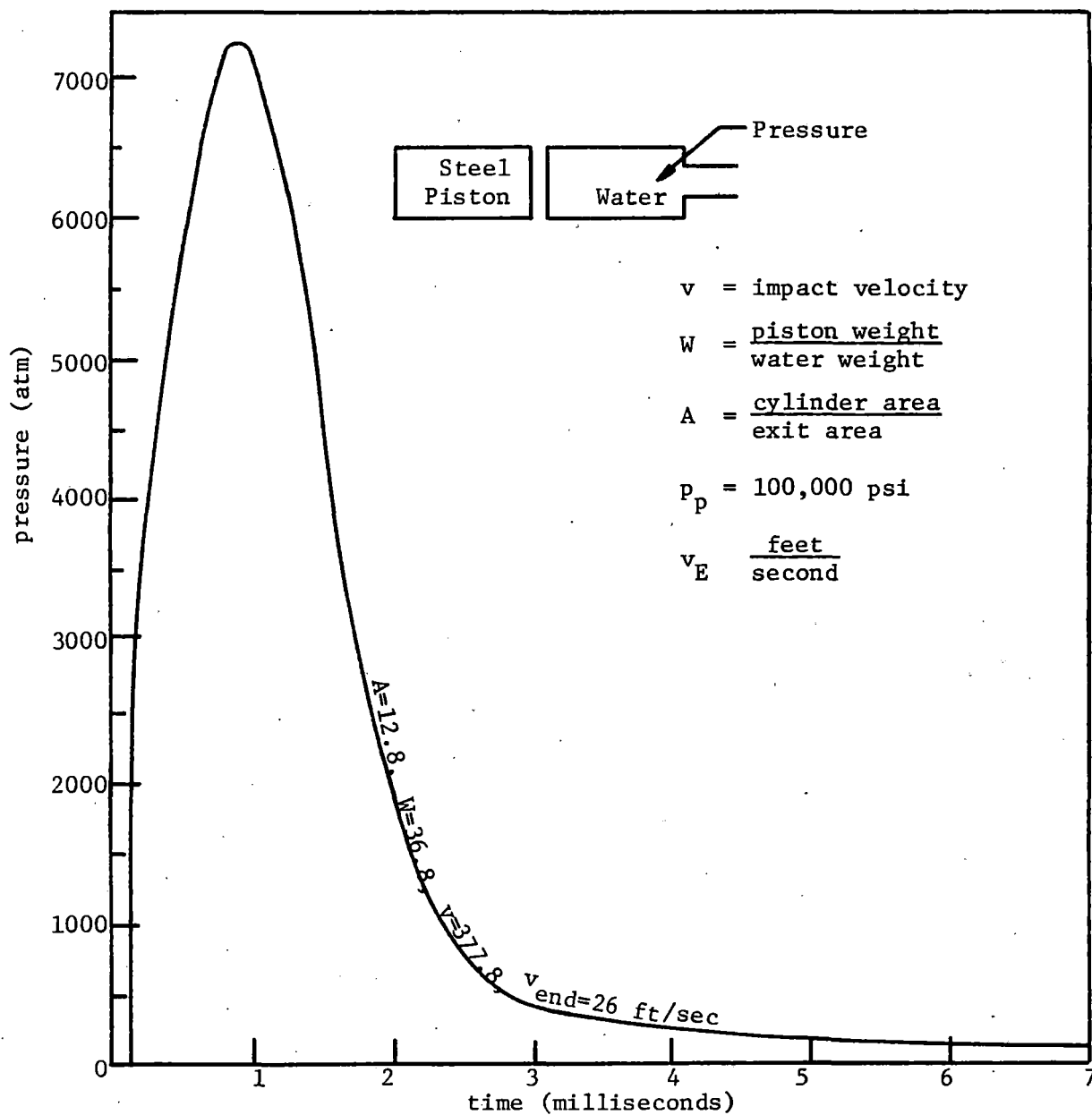


Fig. C-8. Pressure versus time. (Cooley).

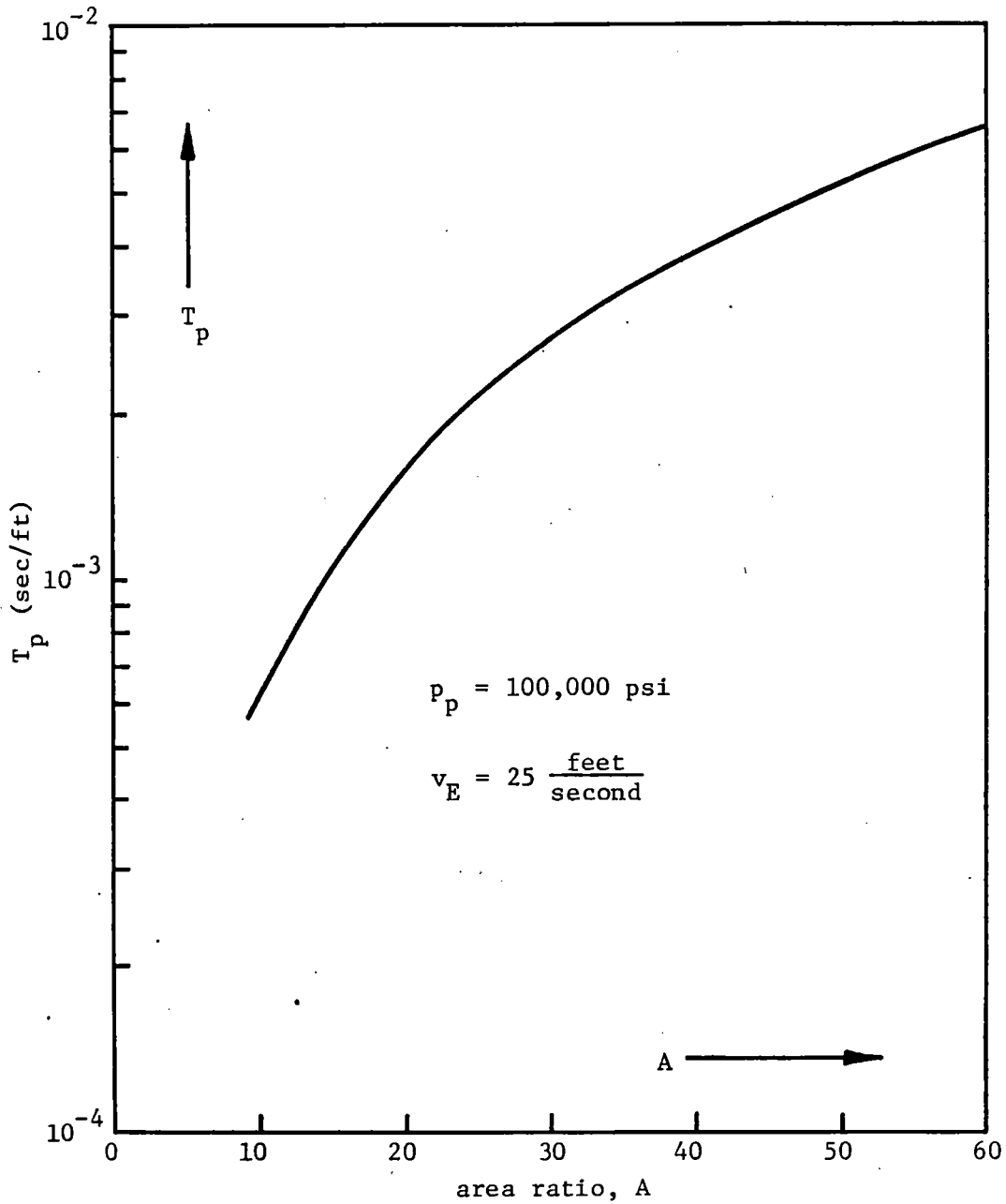


Fig. C-9. Time to reach peak pressure vs. area ratio. (Cooley).

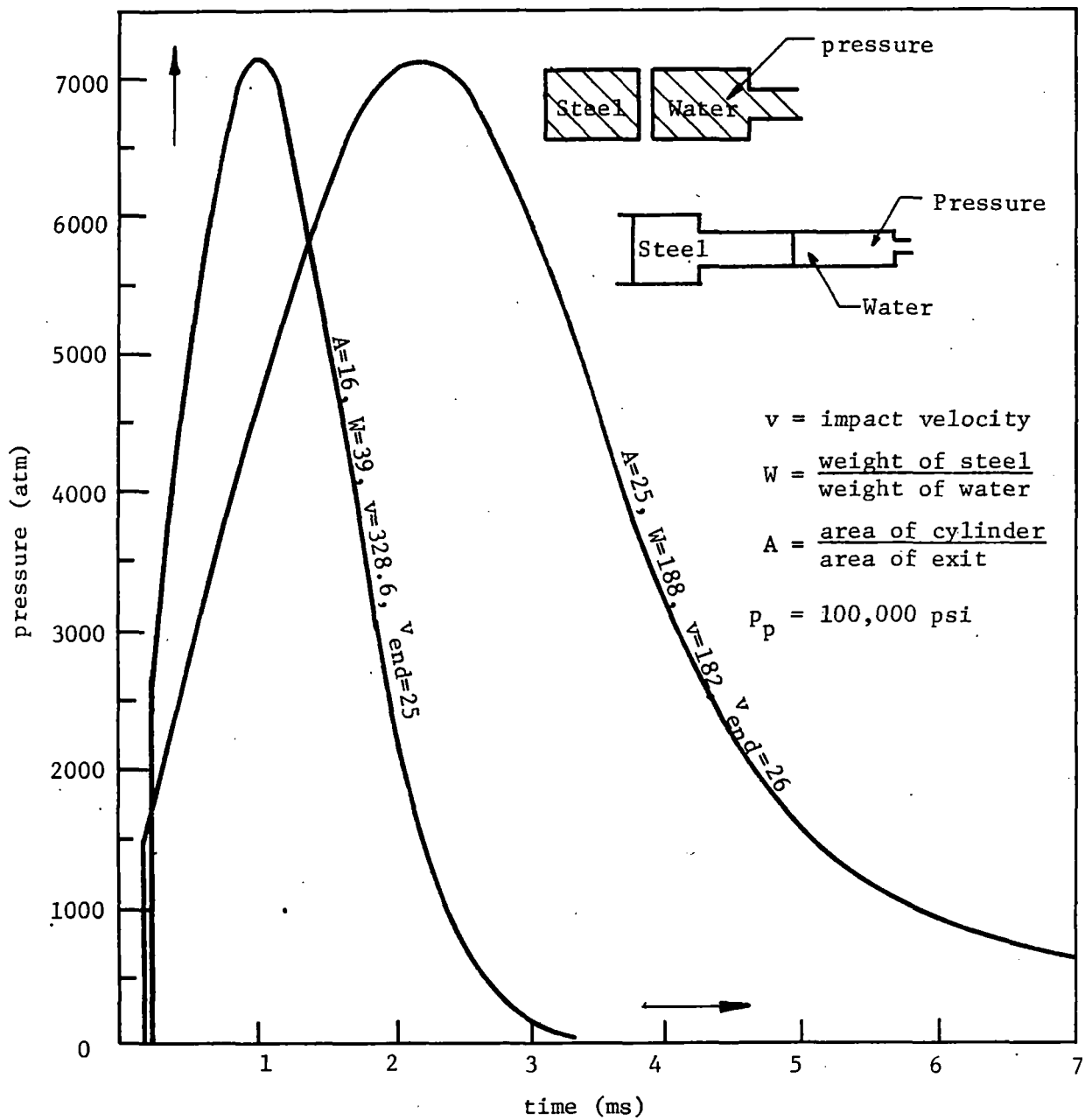


Fig. C-10. Pressure-time curves for single and double diameter pistons. (Cooley).

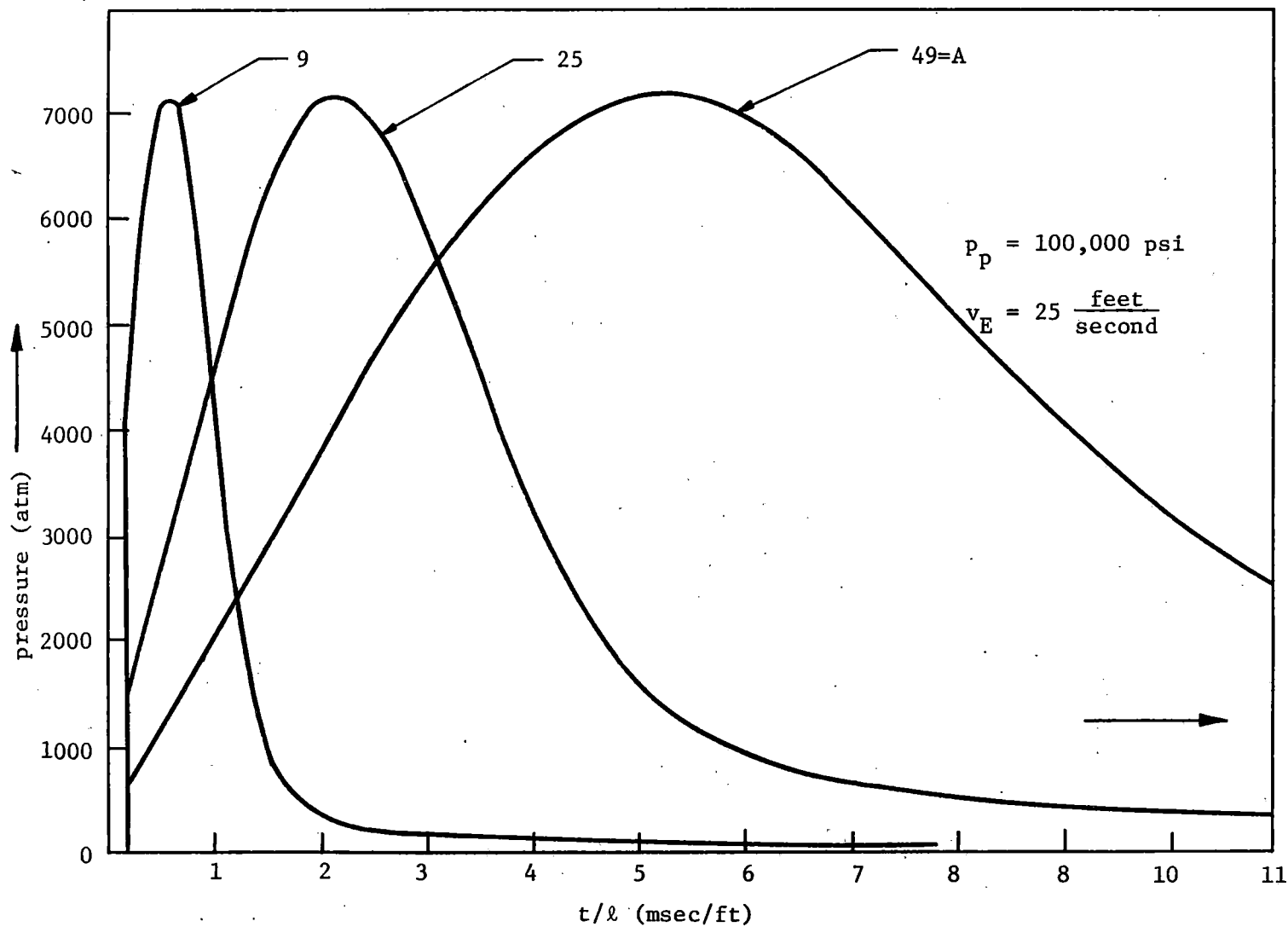


Fig. C-11. Effect of variation of area ratio on pressure pulse. (Cooley).

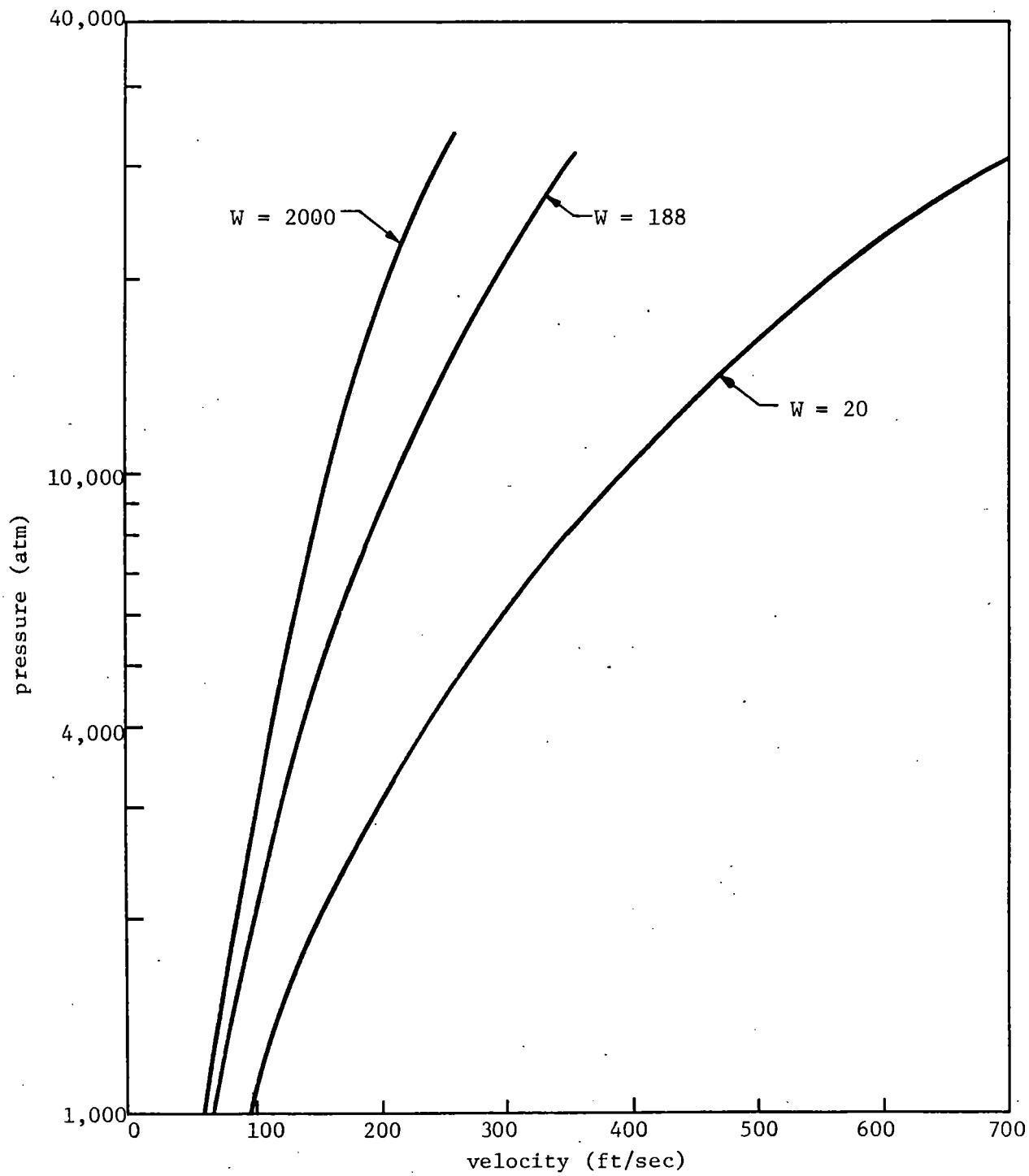


Fig. C-12. Pressure versus piston velocity for various weight ratios at area ratio $A = 25$.

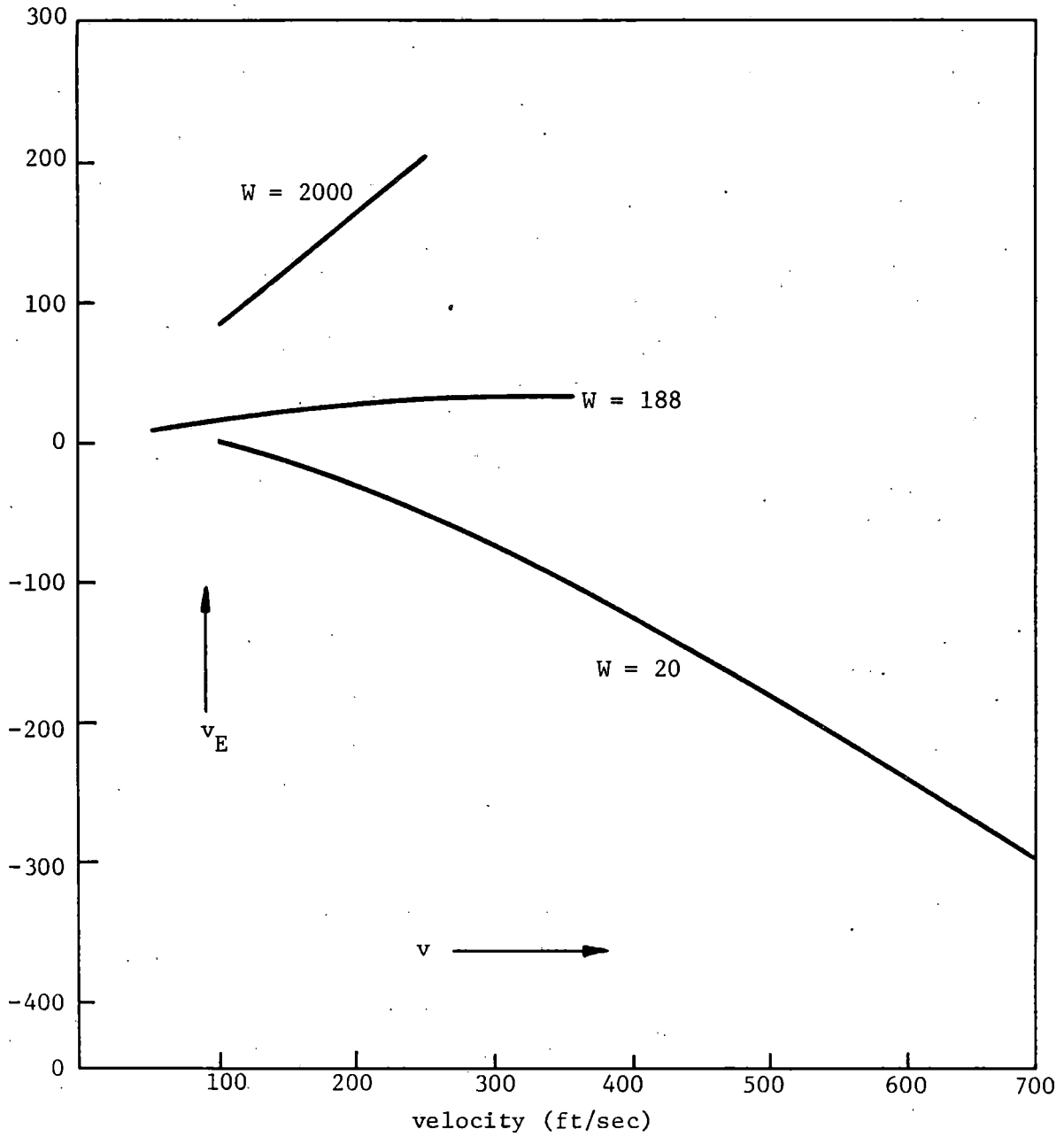


Fig. C-13. Piston end velocity versus initial velocity for various weight ratios, area ratio $A = 25$. (Cooley).

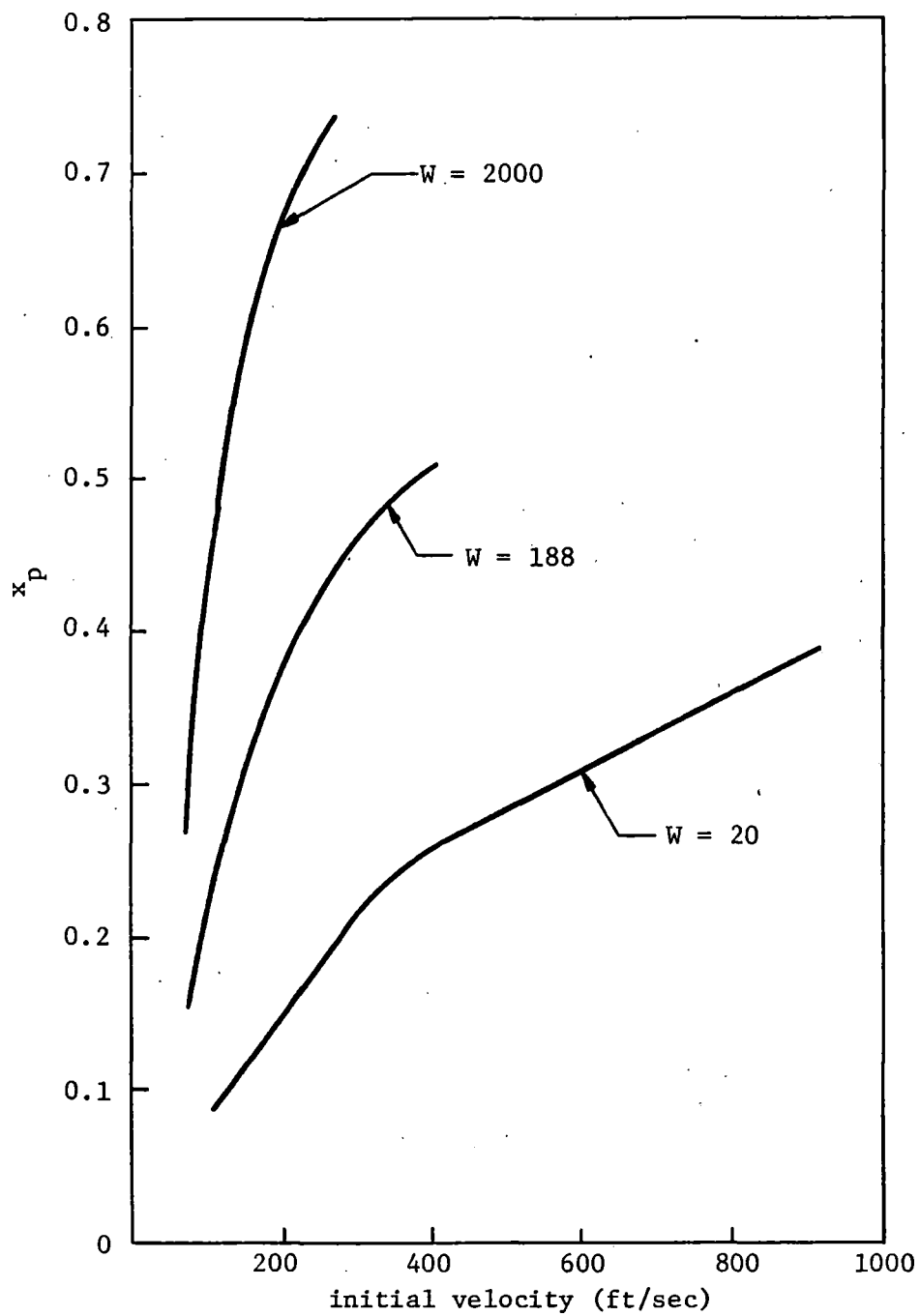


Fig. C-14. Piston position at maximum pressure versus piston velocity for various weight ratios at area ratio $A = 25$. (Cooley).

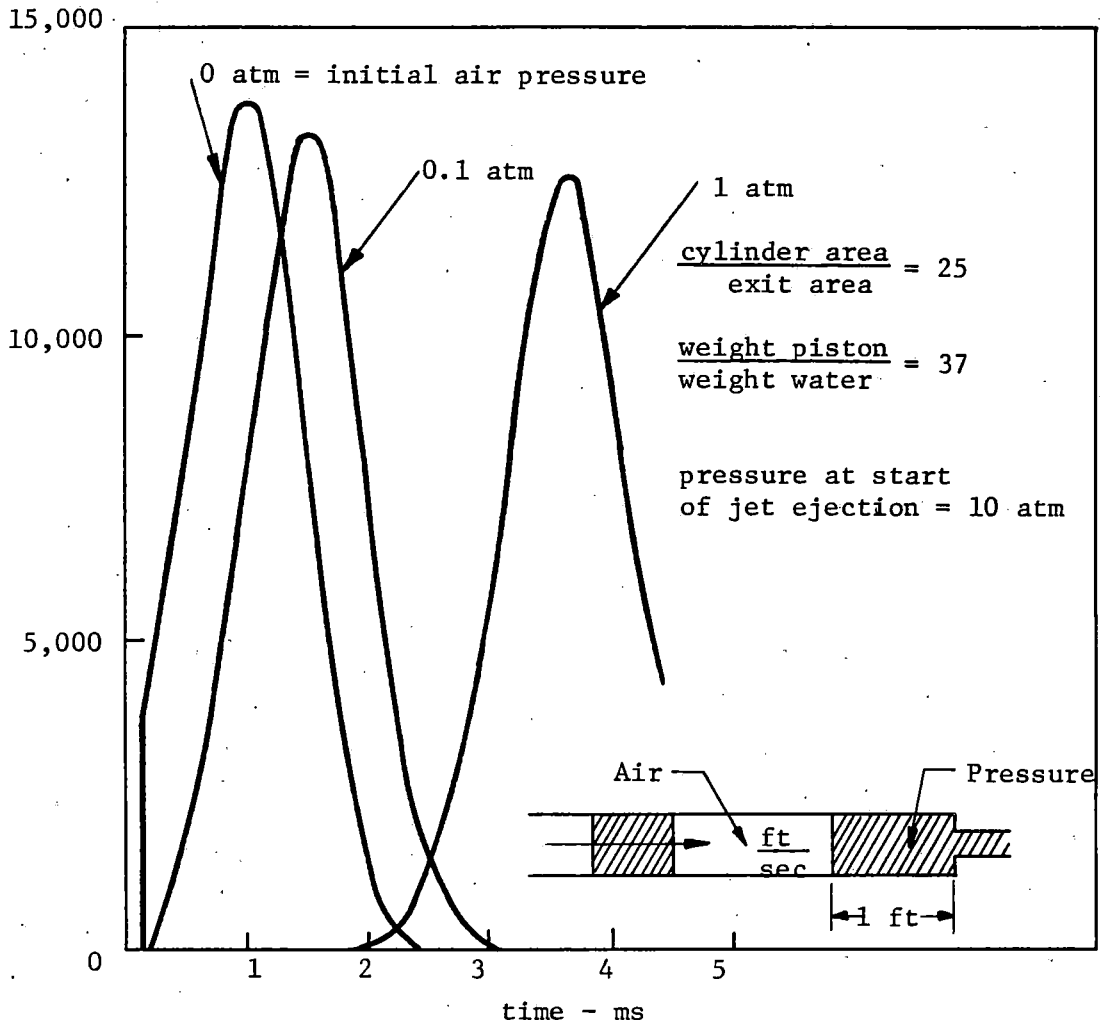


Fig. C-15. Effect of air on pressure pulse. (Cooley).

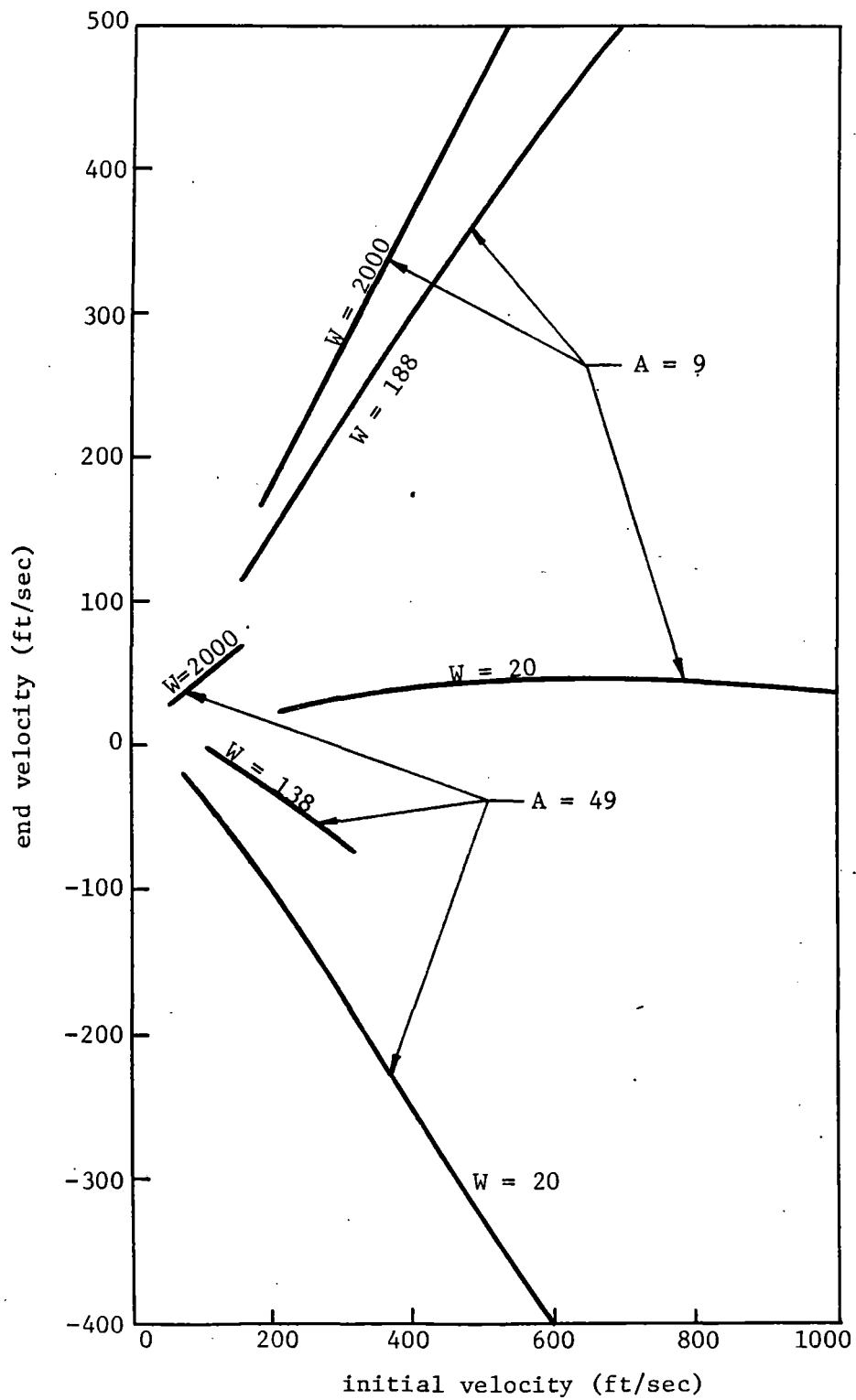


Fig. C-16. Piston end velocity versus initial velocity for various weight and area ratios. (Cooley).

REFERENCES

1. Kamlet, M.J., and Jacobs, S.J., "The Chemistry of Detonation. I. A Simple Method for Calculating Detonation Properties of C-H-N-O Explosives," NOL TR-67-66, USNOL, White Oak, Md., August 1967.
2. Fickett, W., and Cowan, R.D., "Equations of State for High Explosives Based on the Kistiakowsky-Wilson Equation of State for the Product Gases," Rept. No. LA-1865 del, Los Alamos Scientific Lab., December 1954.
3. Cook, Melvin A., "Mechanism of Cratering in Ultra-High Velocity Impact," Inst. of Metals & Explos. Res., U. of Utah, AF OSR-TN-59-50, AD 209 413, January 1959.
4. Chapman, D.L., *Phil. Mag.* (5), Vol. 47, 1899.
5. Jouget, E., "Mechanique des Explosifs," *J. Math.*, 1905, 1906, Paris, 1907, *Chaleur et ind*, January 1939.
6. Becker, R., *Z. Physik*, Vol. 8, page 321, 1922.
7. Rinehart, J.S., "Compilation of Dynamic Equation of State Data for Solids and Liquids," NOTS TP 3798, May 1965.
8. Pai, Shih-I, Fluid Dynamics of Jets, D. Van Nostrand Co., Inc., New York, 1954.
9. Rayleigh, Lord, The Theory of Sound, Dover Publications, Vol. II, 1949.
10. Leach, S.J., and Walker, G.L., "The Application of High Speed Liquid Jets to Cutting - Some Aspects of Rock Cutting by High Speed Water Jets," *Phil. Trans., Roy. Soc., London*, Vol. 260, pp. 295-308, 1966.
11. Lyshevskiy, A.S., "The Use of Super High Pressure Liquid Jets for Cutting Rocks," *Works of the Novocherkask Polytechnical Institute*, Vol. 148, 1963.
12. Tollmien, W., "Berechnung der turbulenten Ausbreitungsvorgange," *ZAMM* Bd. IV, p. 468, 1926; also translated as NACA TM 1085, 1945.
13. Sauer, Robert, Introduction to Theoretical Gas Dynamics, Edwards, 1947.
14. Vereshchagin, L.E., et al., "On the Problem of the Breakup of High Speed Jets of Water," *Soviet Physics-Tech. Physics*, Vol. 4, No. 1, pp. 38-42.

15. Khamyak, I., "Concerning the Mechanism of the Breaking-up of a Jet into Large Drops," *Engineering Physics Journal*, Vol. X, No. 5, pp. 681-82, 1966.
16. Kuklin, I.S., and Shtukaturov, K.M., "Advances in the Methods of Studying the Structure of Hydromonitor Jets," *Works of the Inst. of Min., Acad. of Sci., USSR*, Issue 3, pp. 63-69, 1962.
17. Semerchan, A.A., et al., "Distribution of Momentum in a Continuous Liquid Jet of Supersonic Velocity," *Soviet Physics*, Vol. 3, pp. 1894-1903, 1958.
18. Dunne, B., and Cassen, B., "Velocity Discontinuity Instability of a Liquid Jet," *Jl. of Appl. Phys.*, Vol. 27, No. 6, pp. 577-582, 1956.
19. Dunne, B., and Cassen, B., "Some Phenomena Associated with Supersonic Liquid Jets," *Jl. of Appl. Phys.*, Vol. 25, No. 5, pp. 569-572, May 1954.
20. Zelenin, A.N., et al., "Rock Breaking with Jet Stream under Pressure up to 2000 atm," in book Problems of Mining, Moscow, 1958.
21. Murakami, M., and Katayama, K., "Discharge Coefficients of Fire Nozzles," *Trans. ASME, Jl. of Basic Eng.*, ASME Paper No. 66-EE-6, December 1966.
22. Farmer, I.W., and Attewell, P.B., "Experiments with Water as a Pressure Medium," *Mine & Quarry Eng.*, December 1963.
23. Farmer, I.W., and Attewell, P.B., "Rock Penetration by High Velocity Water Jet," *Intl. Jl. Rock Mech. Min. Sci.*, Vol. 2, pp. 135-153, July 1965.
24. Voytsekhovskiy, V.P., et al., "Some Results of the Destruction of Rocks by Means of a Pulsed Water Jet," *News of the Siberian Dept. of the Acad. of Sci., USSR, Series of Tech. Sci.*, No. 1, Novosibirsk, pp. 7-11.
25. Vereshchagin, L.F., et al., "On the Problem of Friction of a Stream of Water Against the Walls of a Nozzle at Ultrasonic Speeds," *Soviet Physics*, Vol. 2, pp. 1472-3, 1957.
26. Schweitzer, P.H., "Mechanism of Disintegration of Liquid Jets," *Jl. of Appl. Phys.*, Vol. 8, pp. 513-521, August 1937.
27. Konyashin, Yu G., and Veselev, G.M., "Concerning the Use of Impulse Jets," *Sci. Info., Inst. of Min.*, Vol. 20, 1963.

28. Ostrovskii, A.P., "Deep Hole Drilling with Explosives," Gostoptikhsizdat, Moscow, 1960.
29. Vereshchagin, L.F., et al., "Effect of the Reservoir on the Flow of a Stream of Water at Supersonic Speed," Soviet Physics-Tech. Physics, pp. 2451-56, 1957.
30. Semerchan, A.A., and Plotnikov, M.A., "A Method of Liquid Blowout Under High Pressure," Inzhenerno-Fizicheskiy Zhurnal (Russian), Vol. 6, No. 8, pp. 82-87, 1963.
31. Cooley, W.C., et al., "Design Studies of High Velocity Liquid Jet Equipment," Exotech Inc., Rept. Tr-RD-021, Vol. I, 1967.
32. Sims, J.S., et al., "A Study of External Augmentation of the Velocity of Fluid Jets," Bowles Eng. Corp., December 1967.
33. Bridgman, P.W., "The Phase Diagram of Water to 45,000 kg/cm²," Jl. of Chem. Phys., Vol. 5, p. 964, December 1937.
34. Walsh, J.M., and Rice, M.H., "Dynamic Compression of Liquids from Measurements of Strong Shock Waves," Jl. of Chem. Phys., Vol. 26, pp. 815-823, April 1957.
35. Snay, H.G., and Rosenbaum, J.H., "Shock Wave Parameters in Fresh Water for Pressures up to 95 Kilobars," NAVORD Report, 2383, 1952.
36. Bridgman, P.W., "Freezing Parameters and Compression of Twenty-one Substances to 50,000 kg/cm²," Proc. of the Amer. Acad. of Arts and Sci., 74, pp. 399-424, 1942.
37. Bridgman, P.W., "Water in the Liquid and Five Solid Forms under Pressure," Proc. of the Amer. Acad. of Arts and Sci., 47, pp. 441-558, 1912.
38. Bridgman, P.W., "The Volume of Eighteen Liquids as a Function of Pressure and Temperature," Proc. of the Amer. Acad. of Arts and Sci., 66, pp. 185-233, 1931.
39. Bridgman, P.W., "The Pressure-Volume-Temperature Relations of the Liquid, and the Phase Diagram of Heavy Water," Jl. of Chem. Phys., 3, pp. 597-605, 1935.
40. Kennedy, G.C., "Pressure-Volume-Temperature Relations in Water at Elevated Temperatures and Pressures," Amer. Jl. of Sci., 248, pp. 540-564, 1950.

41. Keenan, J.H., and Keyes, F.G., Thermodynamic Properties of Steam, John Wiley and Sons, Inc., New York, 1936.
42. Farmer, I.W., "New Methods of Fracturing Rocks," Mining and Minerals Engineering, January 1965.
43. Chastovitin, P.A., and Cherkasov, N.E., "Mechanization of Working on Rocks During Construction of Tunnels," Transportation Construction, No. 6, pp. 15-19, 1960.
44. Bowden, F.P., et al., "A Discussion on Deformation of Solids by the Impact of Liquids, and its Relation to Rain Drop Damage in Aircraft and Missiles, to Blade Erosion in Steam Turbine, and to Erosion," Phil. Trans. Roy. Soc. of London, A, Vol. 260, pp. 73-315, July 1966.
45. Curtis, John S., "Some Limitations on the Performance of High Velocity Guns," Aerospace Operations Dept., GM Def. Res. Lab., Santa Barbara, Calif., CTN 64-03, August 1964.
46. Flagg, R.F., "The Application of Implosion Wave Dynamics to a Hypervelocity Launcher," U. of Toronto Inst. for Aerospace Studies, Rept. No. 125, June 1967.
47. Lunc, M., Norvak, H., and Smolenchi, D., "Accelerator for Jets Formed by Shaped Charges," Bull. Polish Acad. of Sci., Vol. 12, No. 5, p. 295, 1964.
48. Watson, J.D., "Implosion Driven Hypervelocity Launcher Performance Using Gaseous Detonation Waves," U. of Toronto Inst. for Aerospace Studies, Tech. Note No. 113, May 1967.
49. Herrmann, W., and Jones, A.H., "Survey of Hypervelocity Impact Information," MIT, ASRL Rept. 99-1, AD 267 289, September 1961.
50. Jones, A.H., et al., "Survey of Hypervelocity Impact Information II," ASRL Rept. 99-2, December 1963.
51. Birkhoff, Garrett, et al., "Explosives with Lined Cavities," Jl. of Appl. Phys., Vol. 19, pp. 563-582, June 1948.
52. Bjork, R.L., "Effect of Meteoroid Impact on Steel and Aluminum in Space," Rand paper No. P-1622.
53. Opik, E., "Research on the Physical Theory of Meteor Phenomena: I, Theory of the Formation of Meteor Craters," Acta et Comm., Univ. Tartuensis, 1936.

54. Rostoker, Norman, "The Formation of Craters by High Speed Particles," *Meteoritics*, Vol. I, p. 11, 1953.
55. Eichelberger, R.J., "Experimental Test of the Theory of Penetration by Metallic Jets," *Jl. of Appl. Phys.*, Vol. 27, p. 63, 1956.
56. Pack, D.C., and Evans, W.M., "Penetration by High-velocity (Munroe) Jets: I," *Proc. Phys. Soc.*, Vol. 64, pp. 298-302, 1951.
57. Whipple, F.L., Vistas in Astronautics 1958; The Meteoric Risk to Space Vehicles, pp. 115-124, Pergamon Press, New York, 1958.
58. Langton, N.H., "The Thermal Dissipation of Meteorites by a Bumper Screen," Bericht uber den V. Internationalen Astronautischen Kongres, August 1954.
59. Marnell, P., et al., "Hypervelocity Impact - A Series Solution," Seventh Hypervelocity Impact Symposium, Vol. III, February 1965.
60. Bjork, R.L., "Numerical Solution of the Axially Symmetric Hypervelocity Impact Process, Involving Iron," *Proc. Fifth Symp. on Hypervel. Impact*, Vol. 2, Chicago 1958.
61. Taylor, G.D., "The Formation of a Blast Wave by a Very Intense Explosion," *Proc. Roy. Soc.*, A201, p. 159, March 1950.
62. Ray, W.J., and Kirchner, H.P., "A Blast Wave Theory of Crater Formation in Semi-Infinite Targets," *Proc. Sixth Symp. on Hypervelocity Impact*, Vol. I, Pt. 1, Denver 1961.
63. Davids, N., et al., "A Penetration Method for Determining Impact Yield Strength," Seventh Hypervelocity Impact Symposium, Vol. III, February 1965.
64. Riney, T.D., "Theory of High Speed Impact," Summary Report, APGC-TDR-20, March 1962.
65. Wall, J.K., "Penetration of High Speed Projectiles into Semi-Infinite Targets (Normal Impact)," Douglas Aircraft Co., Rept. No. CH. 39353, January 1963.
66. Hopkins, H.G., and Kolsky, H., "Mechanics of Hypervelocity Impact Solids," Fifth Symposium Hypervelocity Impact, Vol. I, Pt. 1, 1960.
67. Denardo, B.P., et al., "Projectile Size Effects on Hypervelocity Impact Craters in Aluminum," Ames Research Center, NASA TND-4067, July 1967.

68. Kinslow, R., "Observations of Hypervelocity Impact on Transparent Plastic Targets," Seventh Hypervelocity Impact Symposium, Vol. II, pp. 49-108, February 1965.
69. Christman, D.R., et al., "Penetration Mechanisms of High Velocity Rods," Seventh Hypervelocity Impact Symposium, Vol. II, pp. 169-226, 1965.
70. Holloway, L.S., "Observations of Crater Growth in Wax," BRL, Min. Rept. No. 1526, October 1963.
71. Dignam, J.F., and Rockowitz, M., "A Study to Optimize the Damage Due to Hypervelocity Impact," RAP-TM-63-57, R & ARD, AVCO, July 1963.
72. Palmer, E.P., and Turner, G.H., "Energy Partitioning in High Velocity-Impact Cratering in Lead," Seventh Hypervelocity Impact Symposium, Vol. V, pp. 13-50, February 1965.
73. Walsh, J.M., and Johnson, W.E., "On the Theory of Hypervelocity Impact," Seventh Hypervelocity Impact Symposium, Vol. II, pp. 1-76, February 1965.
74. Riney, T.D., and Heyda, J.F., "Hypervelocity Impact Calculations," Seventh Hypervelocity Impact Symposium, Vol. II, pp. 77-186, February 1965.
75. Rosen, F.D., and Sully, C.N., "Impact Flash Investigations to 15.4 km/sec," Seventh Hypervelocity Impact Symposium, Vol. II, pp. 109-141, February 1965.
76. Dietrich, A.M., et al., "Calculation of Maximum Hypervelocity Impact Damage from Material Properties," Seventh Hypervelocity Impact Symposium, Vol. V, pp. 1-12, February 1965.
77. Gehring, J.W., et al., "Experimental Studies of Impact Phenomena and Correlation with Theoretical Models," Seventh Hypervelocity Impact Symposium, Vol. V, pp. 161-212, February 1965.
78. Sorensen, Neil R., "Systematic Investigation of Crater Formation in Metals," Seventh Hypervelocity Impact Symposium, Vol. II, pp. 281-326, 1965.
79. Diedrich, J.H., et al., "Brittle Behavior of Beryllium, Graphite and Lucite under Hypervelocity Impact," Proc. Seventh Hypervelocity Impact Symposium, Vol. VI, pp. 27-47, 1965.
80. Fish, R.H., and Summers, J.L., "The Effect of Material Properties on Threshold Penetration," Proc. Seventh Hypervelocity Impact Symposium, Vol. II, pp. 1-27, February 1965.

81. Bouma, D.D., and Burkitt, W.C., "Multivariable Analysis of the Mechanics of Penetration of High Speed Particles," Martin Marietta Corp., NASA CR-664, December 1966.
82. Moore, H.J., and Lugn, R.V., "Experimental Hypervelocity Impact Craters in Rock," Fifth Symposium on Hypervelocity Impact, Vol. I, Pt. 2, pp. 625-643, April 1962.
83. Gault, D.E., and Hietowit, E.D., "The Partition of Energy for Hypervelocity Impact Craters Formed in Rock," Sixth Symposium on Hypervelocity Impact, Vol. II, Pt. 2, August 1963.
84. Rice, M.H., et al., "Compression of Solids by Strong Shock Waves," Vol. VI, Academic Press, pp. 1-63.
85. Moore, H.J., et al., "Change of Effective Target Strength with Increasing Size of Hypervelocity Craters," Seventh Hypervelocity Impact Symposium, Vol. IV, pp. 35-46, February 1965.
86. Moore, H. J., et al., "Fluid Impact Craters and Hypervelocity-High Velocity Impact Experiments in Metals and Rock," Sixth Symposium on Hypervelocity Impact, Vol. II, Pt. 2, pp. 367-400, August 1963.
87. Lewis, R.S., and Clark, G.B., "Application of Explosive Charges to Mining Operations: Tests on Steel and Rock," Bull. No. 1, U. of Utah, Vol. 37, No. 5, 1946.
88. Clark, G.B., "Studies of the Design of Shaped Explosive Charges and Their Effect in Breaking Concrete Blocks," AIME Tech. Publ. No. 2157, May 1947.
89. Pugh, E.M., et al., "Theory of Jet Formation by Charges with Lined Conical Cavities," JI. of Appl. Phys., Vol. 23, No. 5, pp. 532-536, May 1962.
90. Austin, C.F., "Lined Cavity Shaped Charges and Their Use in Rock and Earth Materials," Bull. 69, Bur. of M & M Res., New Mexico Inst. of Min. & Tech., 1959.
91. Poulter, T.C., and Caldwell, B.M., "The Development of Shaped Charges for Oil Well Completion," Paper No. 680-G, Petroleum Branch, AIME.
92. Eichelberger, R.J., "Re-examination of the Theories of Jet Formation and Penetration by Lined Cavity Charges," Ph.D. Thesis, Carnegie Inst. of Tech., May 1954.

93. Clark, G.B., and Bruckner, W.H., "Behavior of Metal Cavity Liners in Shaped Explosive Charges," AIME Tech. Paper 2158, May 1947.
94. Kolsky, H., "A Study of the Mechanism of Munroe Charges, Pt. II - Charges with Hemispherical Liners," Research Supplement 2-2, 1949.
95. Eichelberger, R.J., and Pugh, E.M., "Experimental Verification of the Theory of Jet Formation by Charges with Lined Conical Cavities," JI. of Applied Physics, Vol. 23, No. 5, pp. 537-542, May 1952.
96. Brimmer, R.A., "Manual for Shaped-Charge Design," NAVORD Report 1248, NOTS 311, August 1950.
97. Austin, C.F., "Use of Shaped Charges in Mining," Mining Congress Journal, pp. 56-61, July 1964.
98. Draper, H.C., et al., "Shaped Charges Applied to Mining, Pt. I, Drilling Holes for Blasting," Bur. of Mines, RI 4371, November 1948.
99. Felts, L.F., and Clark, G.B., "A Laboratory Method of Determining the Thermodynamic Efficiency of High Explosives," Min. Eng., March 1956.
100. Merendino, A., et al., "A Method of Obtaining a Massive Hypervelocity Pellet from a Shaped Charge Jet," BRL Mem. Rept. MP/1508, August 1963.
101. Sykes, W.G., and Vrablik, E.A., "Development of an Explosive System for Accelerating a Metal Pellet," AFCRL 63-246, January 1963.
102. James, H.J., and Buchanan, J.S., "Experimental Studies of the Penetration of Shaped Charge Jets," Fluid Symp. on Hypervelocity Impact, Vol. I, February 1959.
103. Mackenzie, A., and Dalrymple, E., "The Dependence of Dynamic Strength of Cylindrical Pressure Vessels on Geometrical Parameters," Picatinny Arsenal, Dover, New Jersey, Tech. Memo. No. 1026, AD 406 622, 1963.
104. Mackenzie, A., et al., "Design of Pressure Vessels for Confining Explosives," AD 467 730, Picatinny Arsenal, Dover, New Jersey, Tech. Memo No. 1643.
105. Daugherty, J.F., "Design and Fabrication of a One Million PSI Ultra High Pressure Chamber," Final Report, Pressure Science Inc., Beltsville, Md., Contract DA-36-038-AMC-1818.

106. Spillers, W.R., "Orthotropic Viscoelastic Thick-Walled Tube," AD 614 978, ONR Tech. Rept. No. 9 CU-9-61-ONR 266(78) CE, September 1961.
107. Seely, F.B., and Smith, J.O., Advanced Mechanics of Materials, 2nd Ed., John Wiley and Sons, New York, 1952.
108. Berman, I., "Design and Analysis of Commercial Pressure Vessels to 500,000 PSI," Trans. of ASME, Jl. of Basic Eng., pp. 500-508, June 1966.
109. Faupel, J.H., "Some Considerations of the Mechanics and Design Limitations of Autofrettage," Jl. Franklin Institute, pp. 475-489, June 1960.
110. Prager, W., and Hodge, Jr., P.G., Theory of Perfectly Plastic Solids, John Wiley & Sons, New York 1946.
111. Jorgensen, S.M., "Overstrain and Bursting Strength of Thick-Walled Cylinders," Trans. of ASME, pp. 561-570, April 1958.
112. Jorgensen, S.M., "Overstrain Tests on Thick-Walled Cylinders," Jl. of Eng. for Industry, ASME, pp. 103-121, May 1960.
113. Crossland, B., and Bones, J.A., "Behavior of Thick-Walled Steel Cylinders Subjected to Internal Pressure," Jl. Mech. Eng., pp. 777-803, 1958.
114. Dawson, D.C., "Residual Bore Stress in an Autofrettaged Cylinder Constructed of a Strain Hardening Material," AD 626 927, NOL TR 64-25, December 1964.
115. Nadai, A., Theory of Flow and Fracture of Solids, Vol. I, McGraw-Hill, 1950.
116. Faupel, J.H., "Yield and Bursting Characteristics of Heavy-Wall Cylinders," Trans. ASME, pp. 1031-1064, July 1956.
117. Burrows, R.R. Michel, and Rankin, A.W., "A Wall-Thickness Formula for High-Pressure, High-Temperature Piping," Trans. ASME, pp. 427-444, April 1954.
118. Bailey, R.W., "Thick-Walled Tubes and Cylinders Under High Pressure and Temperature," Engineering, pp. 772-820, June 1930.
119. Maclaughlin, Thomas F., "Photoelastic Stress Analysis of Thick-Walled Closed-End Cylinders," Bener Labs., U.S. Army Weapons Command, Watervliet Arsenal, Rept. No. WVT-6514, AD 463 006, March 1965.

120. Becker, S.J., and Mollick, L., "The Theory of the Ideal Design of a Compound Vessel," *Jl. of Eng. for Industry, Trans. ASME*, pp. 136-142, May 1960.
121. Huddleston, Roy L., "Design of Minimum Wall-Thickness Multiregion High-Pressure Cylinders," *ASME*, 64-WA/PT-8, August 1964.
122. Huang, N.C., and Lee, E.H., "On Elastic Filament Reinforcement of a Viscoelastic Cylinder," *Stanford University, Div. of Eng. Mech., Tech. Rept. No. 168, AD 812 372*, February 1967.
123. Darms, F.J., and Molho, R., "Optimum Filament-Wound Construction for Cylindrical Pressure Vessels," *Tech. Doc. Rept. No. ASD-TDR-62-878, AD 403 517*, August 1962.
124. Angerman, R.E., "Fabrication of Large Diameter Titanium Pressure Vessels by the Spiral Wrap Method Covering the Period 1 January 1961 through 31 March 1961," *Rept. No. 2, Borg-Warner Corp., Kalamazoo, Mich., Contract DA-20-018-ORD-22890, AD 256 790*, April 1961.
125. Angerman, R.E., and Dalm, R.K., "Fabrication of Large Diameter Titanium Pressure Vessels by the Spiral Wrap Method Covering the period 1 January 1962 through 31 March 1962," *Rept. No. 6, Borg-Warner Corp., Kalamazoo, Mich., Contract DA-20-018-ORD-22890, AD 275 559*, April 1962.
126. Angerman, R.E., and Dalm, R.K., "Fabrication of Large Diameter Titanium Pressure Vessels by the Spiral Wrap Method Covering the Period 1 April 1962 through 30 June 1962," *Rept. No. 7, Borg-Warner Corp., Kalamazoo, Mich., Contract DA-20-018-ORD-22890, AD 281 726*, July 1962.
127. Angerman, R.E., and Dalm, R.K., "Fabrication of Large Diameter Titanium Pressure Vessels by the Spiral Wrap Method Covering the Period 1 October 1962 through 15 February 1963," *Rept. No. 9, Borg-Warner Corp., Kalamazoo, Mich., Contract DA-20-018-ORD-22890, AD 402 763*, March 1963.
128. Bridgman, P.W., *Proc. Amer. Acad. Arts & Sci.*, Vol. 74, p. 425, 1942.
129. Bridgman, P.W., *Proc. Amer. Acad. Arts & Sci.*, Vol. 76, p. 55, 1948.
130. Hu, L.W., and Schutzler, J.C., "Cascade Arrangement in Spherical Vessel Design for Nuclear Power Reactors," *Nuclear Eng. and Design*, Vol. 3, pp. 412-420, 1966.
131. Berman, I., "Design and Analysis of Commercial Pressure Vessels to 500,000 PSI," *Trans. ASME, Jl. Basic Eng.*, pp. 500-508, June 1966.

132. Langer, B.T., and Harding, W.L., "Material Requirements for Long-Life Pressure Vessels," *Jl. of Eng. for Power, Trans. ASME*, pp. 403-410, October 1964.
133. Schwartz, I.A., et al., "Notch Toughness Properties of Pressure Vessel Steels," AD 811 253, Rept. No. TR 67-021, Eng. Div. Mil. Construction, Chief of Eng., U.S. Army, Washington, D.C., February 1967.
134. Pellini, W.S., and Puzak, P.P., "Practical Considerations in Applying Laboratory Fracture Test Criteria to the Fracture-Safe Design of Pressure Vessels," U.S. Naval Res. Lab., Washington, D.C., AD 426 431, November 1963.
135. Crossland, B., et al., "The Strength of Thick-Walled Cylinders," *Jl. of Eng. for Industry, Trans. ASME*, pp. 95-114, May 1959.
136. Tiffany, C.F., "Investigation of Low Cycle Fatigue Failures Using Applied Fracture Mechanics," Progress Rept., The Boeing Co., Seattle, Wash., Contract AF 33(657)-10251, AD 410 470.
137. Mills, E.J., et al., "Design Performance Fabrication, and Material Considerations for High-Pressure Vessels," Battelle Mem. Inst., Contract No. DA-01-021-AMC-203(2), AD 603 694, 1964.
138. Goodman, J.W., "Final Report on Pressure Vessel Design Criteria," Space Technology Labs. Rept. STL/TR-60-000-19427, AFBMD-TR-61-9, AD 264 608, 1960.
139. Ingraham, J.M., "Transitional Behavior of High-Strength Steel Pressure Vessels," AD 407 432, Watertown Arsenal, Watertown, Mass., Tech. Rept., WAL TR 110.9/1, May 1963.
140. Beaverson, A., "The Design of Pressure Chambers, Part 2, Pressure Research Notes," Pressure Tech. Corp. of America, Vol. 4, No. 6, 1966.
141. Timoshenko, S., and Goodier, J.N., Theory of Elasticity, 2nd Ed., McGraw-Hill Book Co., New York, 1951.
142. Love, A.E.H., A Treatise on the Mathematical Theory of Elasticity, 4th Ed.(1927), Dover Publications, New York, 1944.
143. Timoshenko, S., Strength of Materials, Part 2, Advanced Theory and Problems, 3rd Ed., D. Van Nostrand Co., New York, 1956.
144. Hu, L.W., et al., "Effects of Triaxial Stresses on Mechanical Properties of Metals under High Pressure," Penn. State Univ., University Park, Pa., Contract AF 49(638)-676, AD 266 887.

145. Siegel, A.E., "The Theory of High Speed Guns," AGARDOGRAPH 91, May 1965.
146. Heybey, W., "Significant Parameters for the Expansion of Propellant Gases in an Idealized Gun," Naval Ord. Rept. 1582, February 1951.
147. Richardson, Arons and Halverston, ---Jl. of Chem. Phys., Vol. 15, p. 785, 1947.